Muon $(g - 2)$ Conceptual Design Report

E989 Collaboration

Thursday 3rd January, 2013

2

13:55

DISCLAIMER

This work was prepared as an account of work sponsored by an agency of the United States Government. Neither the United States Government nor any agency thereof, nor any of their employees, nor any of their contractors, subcontractors, or their employees makes any warranty, express or implied, or assumes any legal liability or responsibility for the accuracy, completeness, or any third partys use or the results of such use of any information, apparatus, product, or process disclosed, or represents that its use would not infringe privately owned rights. Reference herein to any specific commercial product, process, or service by trade name, trademark, manufacturer, or otherwise, does not necessarily constitute or imply its endorsement, recommendation, or favoring by the United States Government or any agency thereof or its contractors or subcontractors. The views and opinions of authors expressed herein do not necessarily state or reflect those of the United States Government or any agency thereof.

Executive Summary

This Conceptual Design Report details a new experiment for Fermilab to measure the muon anomalous magnetic dipole moment, or anomaly, at least a factor of four more precisely than the E821 collaboration did at the Brookhaven AGS. The muon anomaly a_μ is a low-energy observable, which can be both measured and computed to high precision, with both theory and experiment having reached the sub-part-per-million (ppm) level of precision. For many years, a_μ has played an important role in constraining models of "New Physics" beyond the standard model, and will continue to do so in the LHC era. The Standard-Model value has contributions from quantum electrodynamics (QED), the weak interaction, and from strongly interacting particles in vacuum polarization and "light-by-light" scattering diagrams.

The present experimental value appears to be larger than the expected Standard-Model value by greater than three standard deviations, which could be a harbinger of New Physics, and strongly motivates the new experiment. In addition to the expected experimental improvement of a factor of four, the uncertainly on the Standard-Model value will also be improved. One very important recent theoretical development is that lattice calculations are becoming relevant in the determination of the strong-interaction contributions.

BNL E821 has been a very high-impact experiment, with over 2000 citations to their four major papers, and over 2200 citations to all of those reporting physics results.
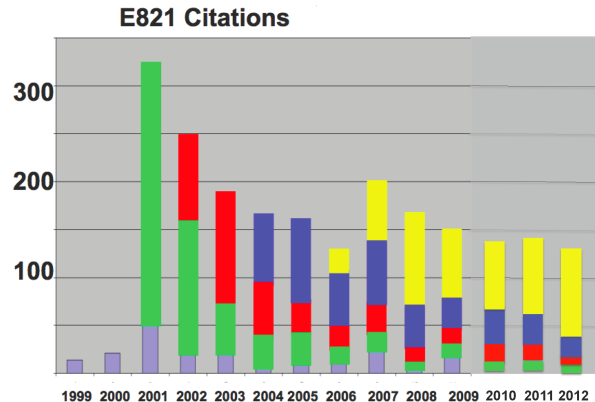
The experiment will also be optimised to improve significantly on the CP-forbidden electric dipole moment (EDM) of the muon. This presents a unique opportunity to search for an EDM of a second-generation particle. With proper design, the EDM sensitivity could reach two orders of magnitude beyond the present limit of $d_\mu < 1.8 \times 10^{-18}\,e$cm obtained by BNL E821.

A number of major components from E821 will be relocated to Fermilab and reused. The precision 700 T superconducting storage ring magnet built at Brookhaven will be relocated to Fermilab and installed in a new building on the Muon Campus. An 8 GeV proton beam from the Booster Accelerator will be injected into the recycler ring, rebunched, and one bunch at at time will be extracted to a a new pion production target at the location of the former antiproton production target. The resulting pion beam will be transported to the repurposed antiproton debuncher ring, now called the Delivery Ring, which will be used as

a 1,900 m decay line. The resulting muon beam will be extracted from the Delivery Ring and brought to the new MC1 building and injected into the muon storage ring. The MC1 building will be a general purpose building, suitable for the $(g-2)$ experiment, as well as for future experiments on the muon campus.

While the storage ring magnet, power supply, and vacuum chambers are being reused, the fast muon kicker, the electrostatic quadrupole system, the field monitoring and control system, the detectors, electronics, data acquisition system will all be upgraded.

...

(includes intro, precision goal, scope, capabilities, cost and schedule)

Contents

Chapter 1

Project Overview

ch:overview

1.1 Mission and Scope

1.1.1 Muon Beam

1.1.2 Storage Ring

1.1.3 Precision Magnetic Field

1.1.4 Detectors

1.2 $(g-2)$ and the Muon Campus

1.3 Conventional Facilities

1.4 Organization

1.4.1 Management

1.4.2 WBS

1.4.3 Controls

1.4.4 Quality Assurance

1.4.5 ES&H

1.4.6 Configuration Management

1.4.7 Risk Management

1.4.8 Cost and Schedule

1.5 References

Chapter 2

Introduction and Physics Motivation

2.1 Introduction

2.1.1 Magnetic Dipole Moments

The study of magnetic moments of subatomic particles grew up with the development of quantum mechanics. For fermions the magnetic dipole moment (MDM) is related to the spin by

$$\vec{\mu} = g \frac{Qe}{2m} \vec{s}.$$

(2.1) `eq:gfact`

where $Q = \pm 1$ and $e > 0$. Our modern interpretation of the Stern-Gerlach experiments [1] is that their observation that: "to within 10% the magnetic moment of the silver atom is one Bohr magneton" was telling us that the g-factor of the un-paired electron is equal to 2. However, reaching this conclusion required the discovery of spin [3], quantum mechanics [4] along with with Thomas' relativistic correction [5]. Phipps and Taylor [6] repeated the Stern-Gerlach experiment in hydrogen, and mentioned the electron spin explicitly. One of the great successes of Dirac's relativistic theory [7] was the prediction that $g \equiv 2$.

For some years, the experimental situation remained the same. The electron had $g = 2$, and the Dirac equation seemed to describe nature. Then a surprising and completely unexpected result was obtained. In 1933, against the advice of Pauli who believed that the proton was a pure Dirac particle [8], Stern and his collaborators [9] showed that the g-factor of the proton was ~ 5.5, not the expected value of 2. Even more surprising was the discovery in 1940 by Alvarez and Bloch [10] that the neutron had a large magnetic moment.

In 1947, motivated by measurements of the hyperfine structure in hydrogen that obtained splittings larger than expected from the Dirac theory [11, 12, 13], Schwinger [14] showed that from a theoretical viewpoint these "discrepancies can be accounted for by a small additional electron spin magnetic moment" that arises from the lowest-order radiative correction to the Dirac moment[1],

$$\frac{\delta\mu}{\mu} = \frac{1}{2\pi} \frac{e^2}{\hbar c} = 0.001162.$$

(2.2)

---

[1]A misprint in the original paper has been corrected here.

It is useful to break the magnetic moment into two terms:

$$\mu = (1 + a)\,\frac{e\hbar}{2m}, \quad \text{where} \quad a = \frac{(g-2)}{2}. \tag{2.3}$$

The first term is the Dirac moment, 1 in units of the appropriate magneton $e\hbar/2m$. The second term is the anomalous (Pauli) moment [15], where the dimensionless quantity a (Schwinger's $\delta\mu/\mu$) is sometimes referred to as the *anomaly*.

2.1.2 The Muon

The muon was first observed in a Wilson cloud chamber by Kunze[16] in 1933, where it was reported to be "a particle of uncertain nature." In 1936 Anderson and Neddermeyer[17] reported the presence of "particles less massive than protons but more penetrating than electrons" in cosmic rays, which was confirmed in 1937 by Street and Stevenson[18], Nishina, Tekeuchi and Ichimiya[19], and by Crussard and Leprince-Ringuet[20]. The Yukawa theory of the nuclear force had predicted such a particle, but this "mesotron" as it was called, interacted too weakly with matter to be the carrier of the strong force. Today we understand that the muon is a second generation lepton, with a mass about 207 times the electron's. Like the electron, the muon obeys quantum electrodynamics, and can interact with other particles through the electromagnetic and weak forces. Unlike the electron which appears to be stable, the muon decays through the weak force predominantly by $\mu^- \to e^-\nu_\mu\bar{\nu}_e$. The muon's long lifetime of $\simeq 2.2~\mu$s permits precision measurements of its mass, lifetime, and magnetic moment.

2.1.3 The Muon Magnetic Moment

The magnetic moment of the muon played an important role in the discovery of the generation structure of the Standard Model (SM). The pioneering muon spin rotation experiment at the Nevis cyclotron observed parity violation in muon decay [21], and also showed that g_μ was consistent with 2. Subsequent experiments at Nevis [24] and CERN [25] showed that $a_\mu \simeq \alpha/(2\pi)$, implying that in a magnetic field, the muon behaves like a heavy electron. Two additional experiments at CERN required that contributions from higher-order QED [26], and then from virtual hadrons [27] be included into the theory in order to reach agreement with experiment.

2.1.4 The Muon Electric Dipole Moment

Dirac [7] discovered an electric dipole moment (EDM) term in his relativistic electron theory. Like the magnetic dipole moment, the electric dipole moment must be along the spin. We can write an expression similar to Eq. (2.1),

$$\vec{d} = \eta\left(\frac{Qe}{2mc}\right)\vec{s}, \tag{2.4}$$

where η is a dimensionless constant that is analogous to g in Eq. (2.1). While magnetic dipole moments (MDMs) are a natural property of charged particles with spin, electric dipole moments (EDMs) are forbidden both by parity and by time reversal symmetry.

The search for an EDM dates back to the suggestion of Purcell and Ramsey [28] in 1950, well in advance of the paper by Lee and Yang [29], that a measurement of the neutron EDM would be a good way to search for parity violation in the nuclear force. An experiment was mounted at Oak Ridge [30] soon thereafter that placed a limit on the neutron EDM of $d_n < 5 \times 10^{-20}$ e-cm, although the result was not published until after the discovery of parity violation.

Once parity violation was established, Landau [31] and Ramsey [32] pointed out that an EDM would violate both P and T symmetries. This can be seen by examining the Hamiltonian for a spin one-half particle in the presence of both an electric and magnetic field,

$$\mathcal{H} = -\vec{\mu} \cdot \vec{B} - \vec{d} \cdot \vec{E}. \tag{2.5}$$

The transformation properties of $\vec{E}$, $\vec{B}$, $\vec{\mu}$ and $\vec{d}$ are given in Table 2.1.4, and we see that while $\vec{\mu} \cdot \vec{B}$ is even under all three symmetries, $\vec{d} \cdot \vec{E}$ is odd under both P and T. Thus the existence of an EDM implies that both P and T are not good symmetries of the interaction Hamiltonian, Eq. (2.5). The EDM is a CP-odd quantity, and if observed, would be the manifestation of a new source of CP violation. The search for a muon EDM provides a unique opportunity to search for an EDM of a second-generation particle.

Table 2.1: Transformation properties of the magnetic and electric fields and dipole moments.

	$\vec{E}$	$\vec{B}$	$\vec{\mu}$ or $\vec{d}$
P	-	+	+
C	-	-	-
T	+	-	-

Concerning these symmetries, Ramsey states [32]:

> "However, it should be emphasized that while such arguments are appealing from the point of view of symmetry, they are not necessarily valid. Ultimately the validity of all such symmetry arguments must rest on experiment."

Fortunately this advice has been followed by many experimental investigators during the intervening 50 years. Since the Standard Model CP violation observed in the neutral kaon and B-meson systems is inadequate to explain the predominance of matter over antimatter in the universe, the search for new sources of CP violation beyond that embodied in the CKM formalism takes on a certain urgency. Searches for a permanent electric dipole moment of the electron, neutron, and of an atomic nucleus have become an important part of the search for physics beyond the Standard Model. The present limits on subatomic EDMs is given in Table 2.1.4.

Table 2.2: EDM Limits for various systems

Particle	EDM Limit $(e\text{-cm})$	SM value $(e\text{-cm})$
p [33]	7.9×10^{-25}	
n [34]	2.9×10^{-26}	$\simeq 10^{-32}$
^{199}Hg [33]	3.1×10^{-29}	$\simeq 10^{-32}$
e^{-} [35]	1.05×10^{-27}	$< 10^{-41}$
μ [36]	1.8×10^{-19}	$< 10^{-38}$

`tb:EDMs`

2.2 The Experimental Technique

2.2.1 The Spin Equations

Measurements of magnetic and electric dipole moments make use of the torque on a dipole in an external field:

$$\vec{\tau} = \vec{\mu} \times \vec{B} + \vec{d} \times \vec{E}, \tag{2.6}$$

`eq:torque`

where we include the possibility of an electric dipole moment (EDM). Except for the original Nevis spin rotation experiment, the muon MDM experiments inject a beam of polarized muons into a magnetic field and measure the rate at which the spin[2] turns relative to the momentum, $\vec{\omega}_a = \vec{\omega}_S - \vec{\omega}_C$, where S and C stand for spin and cyclotron. These two frequencies are given by

$$\omega_S = -g\frac{Qe}{2m}B - (1 - \gamma)\frac{Qe}{\gamma m}B; \tag{2.7}$$

$$\omega_C = -\frac{Qe}{m\gamma}B; \tag{2.8}$$

$$\omega_a = \omega_S - \omega_C = -\left(\frac{g-2}{2}\right)\frac{Qe}{m}B = -a\frac{Qe}{m}B \tag{2.9}$$

`eq:diffreq1`

(where $e > 0$ and $Q = \pm 1$). There are two important features of ω_a: (i) It only depends on the anomaly rather than on the full magnetic moment; (ii) It depends linearly on the applied magnetic field.

To measure the anomaly, it is necessary to measure ω_a, and to determine the magnetic field B. The relevant quantity is $\langle B \rangle_{\text{muon distribution}}$ *viz.*

$$\langle B \rangle = \int M(r,\theta)B(r,\theta)rdrd\theta, \tag{2.10}$$

`eq:average-`

where the magnetic field $B(r,\theta)$ is expressed as the multipole expansion

$$B(r,\theta) = \sum_{n=0}^{\infty} r^n \left[c_n \cos n\theta + s_n \sin n\theta\right], \tag{2.11}$$

`eq:B-multip`

---

[2]The term 'spin' is often used in place of the more accurate term 'polarization'

and the muon distribution is expressed in terms of moments

$$M(r, \theta) = \sum [\gamma_m(r) \cos m\theta + \sigma_m(r) \sin m\theta].$$ (2.12) `eq:M-multip`

We find the usual coupling, multipole by multipole, in the expression for $\langle B \rangle$. To determine $\langle B \rangle$ to sub-part-per-million (ppm) precision, one either needs excellent knowledge of the multipole and moment distributions for B and M; or care must be taken to minimize the number of terms, with only the leading term being large, so that only the first few multipoles are important. This was achieved in the most recent experiment [39] by using a circular beam aperture, and making a very uniform dipole magnetic field.

However there is one important issue to be solved: How can the muon beam be confined to a storage ring if significant magnetic gradients cannot be used to provide vertical focusing? The answer to this question was discovered by the third CERN collaboration [27], which used an electric quadrupole field to provide vertical focusing. Of course, a relativistic particle feels a motional magnetic field proportional to $\vec{\beta} \times \vec{B}$, but the full relativistic spin equation contains a cancellation as can be seen below. Assuming that the velocity is transverse to the magnetic field ($\vec{\beta} \cdot \vec{B} = 0$), one obtains [5, 37]

$$\vec{\omega}_{a\eta} = \vec{\omega}_a + \vec{\omega}_\eta = -\frac{Qe}{m}\left[a_\mu \vec{B} + \left(a_\mu - \left(\frac{m}{p}\right)^2\right)\frac{\vec{\beta} \times \vec{E}}{c}\right] - \eta\frac{Qe}{2m}\left[\frac{\vec{E}}{c} + \vec{\beta} \times \vec{B}\right].$$ (2.13) `eq:omega-a-`

We have included the possibility of an electric dipole moment (EDM), as well as a magnetic one. There are both motional magnetic and electric fields in this equation – the terms which are proportional to $\vec{\beta} \times \vec{E}$ and $\vec{\beta} \times \vec{B}$ respectively.

The expression for ω_a is

$$\vec{\omega}_a = -\frac{Qe}{m}\left[a_\mu \vec{B} + \left(a_\mu - \left(\frac{m}{p}\right)^2\right)\frac{\vec{\beta} \times \vec{E}}{c}\right].$$ (2.14) `eq:omegaa`

For the "magic" momentum $p_{magic} = m/\sqrt{a} \simeq 3.09$ GeV/c ($\gamma_{magic} = 29.3$), the second term vanishes, and the electric field does not contribute to the spin motion relative to the momentum.[3] Note that if $g = 2$, then $a = 0$ and the spin would follow the momentum, turning at the cyclotron frequency.

2.2.2 Overview of the Experimental Method

Muons are produced in the weak pion decay

$$\pi^{\mp} \to \mu^{\mp} + \bar{\nu}_\mu(\nu_\mu).$$ (2.15)

Since the antineutrino (neutrino) is right-handed (left-handed) the μ^- (μ^+) is left-handed (right-handed). A beam of polarized muons can be obtained from a beam of pions by selecting the highest-energy muons (a "forward beam") or by selecting the lowest-energy muons (a

---

[3]Small corrections to the measured frequency must be applied since $\vec{\beta} \cdot \vec{B} \simeq 0$ and not all muons are at the magic momentum. These are discussed in Chapter 9.

"backward beam"), where forward or backward refers to whether the decay was forward of backward in the center-of-mass frame relative to the pion momentum. Polarizations greater than 90% are easily obtained in such beams. The dominant muon decay is

$$\mu^{\mp} \to e^{\mp} + \nu_\mu(\bar{\nu}_\mu) + \bar{\nu}_e(\nu_e) \tag{2.16}$$

which also violates parity.

Since the kinematics of muon decay are central to the measurements of a_μ, we discuss the general features in this section. Additional details are given in Ref. [52]. From a beam of pions traversing a straight beam-channel consisting of focusing and defocusing elements (FODO), a beam of polarized, high energy muons can be produced by selecting the "forward" or "backward" decays. The forward muons are those produced, in the pion rest frame, nearly parallel to the pion laboratory momentum and are the decay muons with the highest laboratory momenta. The backward muons are those produced nearly anti-parallel to the pion momentum and have the lowest laboratory momenta. The forward μ^- (μ^+) are polarized along (opposite) their lab momenta respectively; the polarization reverses for backward muons. The E821 experiment used forward muons, as will E989, the difference being the length of the pion decay line, which in E989 will be 1,900 m.

The pure $(V - A)$ three-body weak decay of the muon, $\mu^- \to e^- + \nu_\mu + \bar{\nu}_e$ or $\mu^+ \to e^+ + \bar{\nu}_\mu + \nu_e$, is "self-analyzing", that is, the parity-violating correlation between the directions in the muon rest frame (MRF) of the decay electron and the muon spin can provide information on the muon spin orientation at the time of the decay. When the decay electron has the maximum allowed energy in the MRF, $E'_{\max} \approx (m_\mu c^2)/2 = 53$ MeV. The neutrino and anti-neutrino are directed parallel to each other and at 180° relative to the electron direction. The $\nu\bar{\nu}$ pair carry zero total angular momentum; the electron carries the muon's angular momentum of 1/2. The electron, being a lepton, is preferentially emitted left-handed in a weak decay, and thus has a larger probability to be emitted with its momentum *anti-parallel* rather than parallel to the μ^- spin. Similarly, in μ^+ decay, the highest-energy positrons are emitted *parallel* to the muon spin in the MRF.

In the other extreme, when the electron kinetic energy is zero in the MRF, the neutrino and anti-neutrino are emitted back-to-back and carry a total angular momentum of one. In this case, the electron spin is directed opposite to the muon spin in order to conserve angular momentum. Again, the electron is preferentially emitted with helicity -1, however in this case its momentum will be preferentially directed *parallel* to the μ^- spin. The positron, in μ^+ decay, is preferentially emitted with helicity +1, and therefore its momentum will be preferentially directed *anti-parallel* to the μ^+ spin.

With the approximation that the energy of the decay electron $E' >> m_e c^2$, the differential decay distribution in the muon rest frame is given by[23],

$$dP(y', \theta') \propto n'(y') \left[1 \pm \mathcal{A}(y') \cos\theta'\right] dy' d\Omega' \tag{2.17}$$

where y' is the momentum fraction of the electron, $y' = p'_e/p'_{e\ \max}$, $d\Omega'$ is the solid angle, $\theta' = \cos^{-1}(\hat{p}'_e \cdot \hat{s})$ is the angle between the muon spin and $\vec{p}'_e$, $p'_{e\ \max} c \approx E'_{max}$, and the $(-)$ sign is for negative muon decay. The number distribution $n(y')$ and the decay asymmetry $\mathcal{A}(y')$ are given by

$$n(y') = 2y'^2(3 - 2y') \quad \text{and} \quad \mathcal{A}(y') = \frac{2y' - 1}{3 - 2y'}. \tag{2.18}$$

Note that both the number and asymmetry reach their maxima at $y' = 1$, and the asymmetry changes sign at $y' = \frac{1}{2}$, as shown in Figure 2.1(a).

(a) Muon Rest Frame   (b) Laboratory Frame
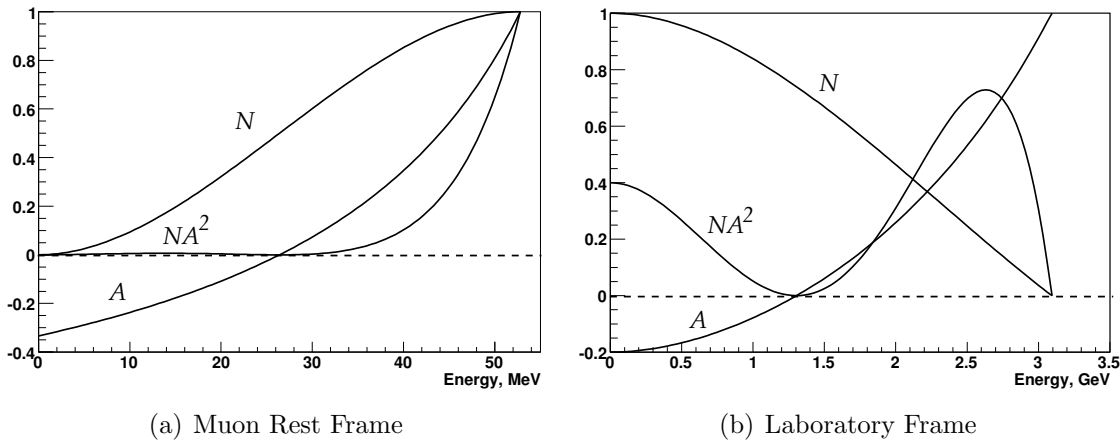
Figure 2.1: Number of decay electrons per unit energy, N (arbitrary units), value of the asymmetry A, and relative figure of merit NA^2 (arbitrary units) as a function of electron energy. Detector acceptance has not been incorporated, and the polarization is unity. For the third CERN experiment and E821, $E_{max} \approx 3.1$ GeV ($p_\mu = 3.094$ GeV/c) in the laboratory frame.

The CERN and Brookhaven based muon $(g-2)$ experiments stored relativistic muons of the magic momentum in a uniform magnetic field, which resulted in the muon spin precessing with constant frequency $\vec{\omega}_a$, while the muons traveled in circular orbits. If *all* decay electrons were counted, the number detected as a function of time would be a pure exponential; therefore we seek cuts on the laboratory observable to select subsets of decay electrons whose numbers oscillate at the precession frequency. The number of decay electrons in the MRF varies with the angle between the electron and spin directions, the electrons in the subset should have a preferred direction in the MRF when weighted according to their asymmetry as given in Equation 2.17. At $p_\mu \approx 3.094$ GeV/c the directions of the electrons resulting from muon decay in the laboratory frame are very nearly parallel to the muon momentum regardless of their energy or direction in the MRF. The only practical remaining cut is on the electron's laboratory energy. An energy subset will have the desired property: there will be a net component of electron MRF momentum either parallel or antiparallel to the laboratory muon direction. For example, suppose that we only count electrons with the highest laboratory energy, around 3.1 GeV. Let $\hat{z}$ indicate the direction of the muon laboratory momentum. The highest-energy electrons in the laboratory are those near the maximum MRF energy of 53 MeV, and with MRF directions nearly parallel to $\hat{z}$. There are more of these high-energy electrons when the μ^- spins are in the direction opposite to $\hat{z}$ than when the spins are parallel to $\hat{z}$. Thus the number of decay electrons reaches a maximum when the muon spin direction is opposite to $\hat{z}$, and a minimum when they are parallel. As the spin precesses the number of high-energy electrons will oscillate with frequency ω_a. More generally, at laboratory energies above ~ 1.2 GeV, the electrons have a preferred average MRF direction parallel to $\hat{z}$ (see Figure 2.1). In this discussion, it is assumed that the

spin precession vector, $\vec{\omega}_a$, is independent of time, and therefore the angle between the spin component in the orbit plane and the muon momentum direction is given by $\omega_a t + \phi$, where ϕ is a constant.

Equations 2.17 and 2.18 can be transformed to the laboratory frame to give the electron number oscillation with time as a function of electron energy,

$$N_d(t, E) = N_{d0}(E)e^{-t/\gamma\tau}[1 + A_d(E)\cos(\omega_a t + \phi_d(E))], \qquad (2.19) \quad \boxed{\texttt{eq:fivepd}}$$

or, taking all electrons above threshold energy E_{th},

$$N(t, E_{th}) = N_0(E_{th})e^{-t/\gamma\tau}[1 + A(E_{th})\cos(\omega_a t + \phi(E_{th}))]. \qquad (2.20) \quad \boxed{\texttt{eq:fivep}}$$

In Equation 2.19 the differential quantities are,

$$A_d(E) = \mathcal{P}\frac{-8y^2 + y + 1}{4y^2 - 5y - 5}, \quad N_{d0}(E) \propto (y - 1)(4y^2 - 5y - 5), \qquad (2.21)$$

and in Equation 2.20,

$$N(E_{th}) \propto (y_{th} - 1)^2(-y_{th}^2 + y_{th} + 3), \qquad A(E_{th}) = \mathcal{P}\frac{y_{th}(2y_{th} + 1)}{-y_{th}^2 + y_{th} + 3}. \qquad (2.22)$$

In the above equations, $y = E/E_{max}$, $y_{th} = E_{th}/E_{max}$, $\mathcal{P}$ is the polarization of the muon beam, and E, E_{th}, and $E_{max} = 3.1$ GeV are the electron laboratory energy, threshold energy, and maximum energy, respectively.
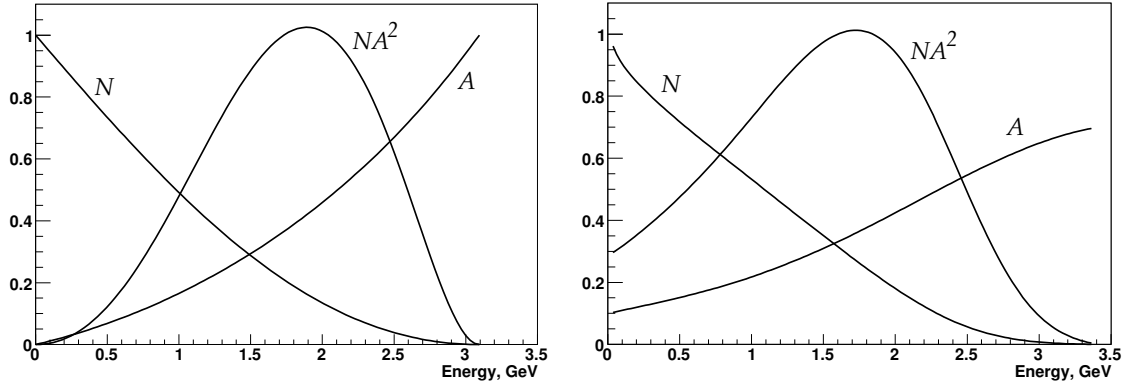
(a) No detector acceptance or energy resolution included   (b) Detector acceptance and energy resolution included

Figure 2.2: The integral N, A, and NA^2 (arbitrary units) for a single energy-threshold as a function of the threshold energy; (a) in the laboratory frame, not including and (b) including the effects of detector acceptance and energy resolution for the E821 calorimeters discussed below. For the third CERN experiment and E821, $E_{max} \approx 3.1$ GeV ($p_\mu = 3.094$ GeV/c) in the laboratory frame.

$\boxed{\texttt{integral\_na}}$

The fractional statistical error on the precession frequency, when fitting data collected over many muon lifetimes to the five-parameter function (Equation 2.20), is given by

$$\delta\epsilon = \frac{\delta\omega_a}{\omega_a} = \frac{\sqrt{2}}{2\pi f_a \tau_\mu N^{\frac{1}{2}} A}. \qquad (2.23) \quad \boxed{\texttt{eq:fracterr}}$$

where N is the total number of electrons, and A is the asymmetry, in the given data sample. For a fixed magnetic field and muon momentum, the statistical figure of merit is NA^2, the quantity to be maximized in order to minimize the statistical uncertainty.

The energy dependencies of the numbers and asymmetries used in Equations 2.19 and 2.20, along with the figures of merit NA^2, are plotted in Figures 2.1 and 2.2 for the case of E821. The statistical power is greatest for electrons at 2.6 GeV (Figure 2.1). When a fit is made to all electrons above some energy threshold, the optimal threshold energy is about 1.7-1.8 GeV (Figure 2.2).

The resulting arrival-time spectrum of electrons with energy greater than 1.8 GeV from the final E821 data run is shown in Fig. 2.3. While this plot clearly exhibits the expected features of the five-parameter function, a least-square fit to these 3.6 billion events gives an unacceptably large chi-square. A number of small effects must be taken into account to obtain a reasonable fit, which will be discussed in detail in the section on systematic errors.
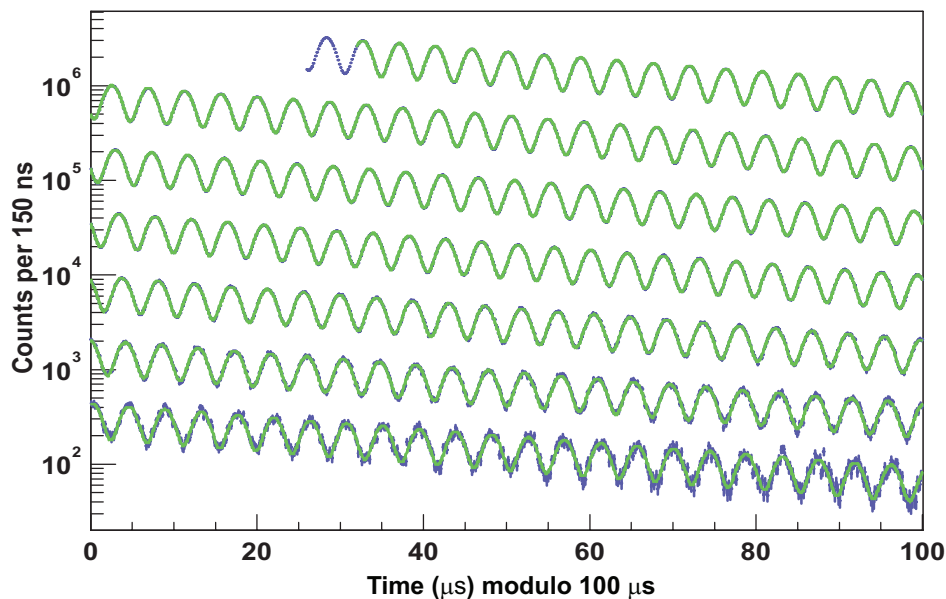
Figure 2.3: Histogram, modulo 100 μ s, of the number of detected electrons above 1.8 GeV for the 2001 data set as a function of time, summed over detectors, with a least-squares fit to the spectrum superimposed. Total number of electrons is 3.6×10^9. The data are in blue, the fit in green.

2.2.3 The Magnetic Field

The rate at which the muon spin turns relative to its momentum (Eq. 2.14) depends on the anomaly a_μ and on the average magnetic field given by Eq. 2.10. Thus the determination of

a_μ to sub-tenths of a ppm requires that both ω_a and $\langle B \rangle$ be determined to this level. The muon beam is confined to a cylindrical region of 9 cm diameter, which is 44.7 m in length. The volume of this region is $\simeq 1.14$ m^3 or $\simeq 40$ ft^3, which sets the scale for the magnetic field measurement and control. The E989 goal is to know the magnetic field averaged over the muon distribution to an uncertainty of ± 70 parts per billion (ppb).

The problem breaks into several pieces:

1. Producing as uniform magnetic field as possible by shimming the magnet.

2. Stabilizing B in time at the sub-ppm level by feedback, with mechanical and thermal stability.

3. Monitoring B to the 20 ppb level around the storage ring during data collection.

4. Periodically mapping the field throughout the storage region and correlating the field map to the monitoring information without turning off the magnet between data collection and field mapping. It is essential that the magnet not be powered off unless absolutely necessary.

5. Obtaining an absolute calibration of the B-field relative to the Larmor frequency of the free proton.

The only magnetic field measurement technique with the sensitivity needed to measure and control the B-field to the tens of ppb is nuclear magnetic resonance (NMR). Pulsed NMR was used, where a $\pi/2$ RF pulse rotated the spins and the resulting free-induction decay (FID) was detected by a pickup coil around the sample. The E821 baseline design used the NMR of protons in a water sample with a CuSO$_4$ additive that shortened the relaxation time, with the probes tuned to operate in a 1.45 T field. When the water evaporated from a few of the probes, the water was replaced with petrolium jelly, which the added features of a smaller sensitivity to temperature changes and no evaporation.

Special nuclear magnetic resonance (NMR) probes [41, 39] were used in E821 to measure and monitor the magnetic field during the experimental data collection.[4] Three types of probes were used: a spherical water probe that provided the absolute calibration to the free proton; cylindrical probes that were used monitor the field during data collection and in an NMR trolley to map the field; and a smaller spherical probe which could be plunged into the muon storage region by means of a bellows system to transfer the absolute calibration to the trolley probes. A collection of 378 cylindrical probes placed in symmetrically machined grooves on the top and bottom of the muon beam vacuum chamber gave a point to point measure of the magnetic field while beam was in the storage ring. Probes at the same azimuthal location but different radii gave information on changes to the quadrupole component of the field at that location.

The field mapping trolley contained 17 cylindrical probes arranged in concentric circles as shown in Figure 2.4. At several-day intervals during the running periods, the beam was turned off, and the field mapping trolley was driven around inside of the evacuated beam chamber measuring the magnetic field with each of the 17 trolley probes at 6,000

---

[4]The probes are described in Chapter 12

locations around the ring. One of the resulting field maps, averaged over azimuth, is shown in Figure 2.4(b).

(a)   (b)
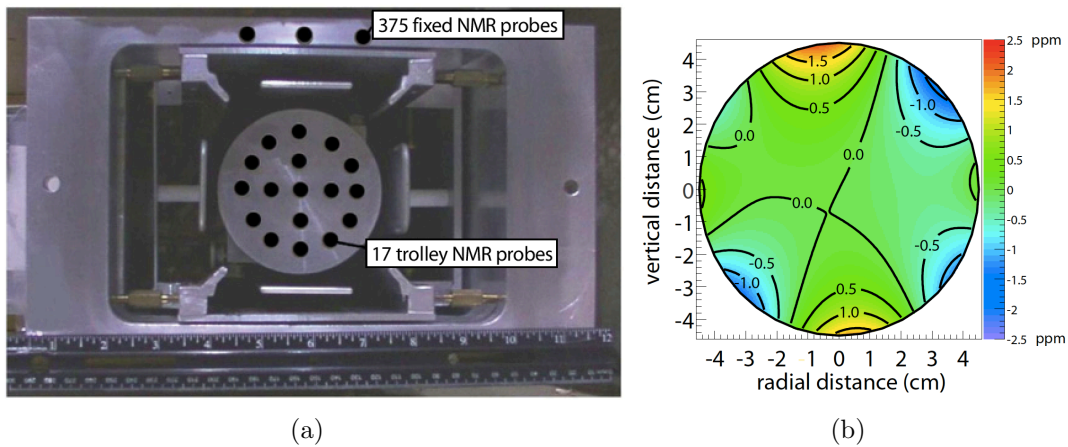
Figure 2.4: (a)The electrostatic quadrupole assembly inside a vacuum chamber showing the NMR trolley sitting on the rails of the cage assembly. Seventeen NMR probes are located just behind the front face in the places indicated by the black circles. The inner (outer) circle of probes has a diameter of 3.5 cm (7 cm) at the probe centers. The storage region has a diameter of 9 cm. The vertical location of three of the 180 upper fixed probes is also shown. An additional 180 probes are located symmetrically below the vacuum chamber. (Reprinted with permission from [39]. Copyright 2006 by the American Physical Society.) (b) A contour plot of the magnetic field averaged over azimuth, 0.5 ppm intervals.

The absolute calibration utilizes a probe with a spherical water sample [42]. The Larmor frequency of a proton in a spherical water sample is related to that of the free proton through $f_{\rm L}({\rm sph} - {\rm H_2O}, T) = [1 - \sigma({\rm H_2O}, T)] f_{\rm L}({\rm free})$, [43, 44] where $\sigma({\rm H_2O}, T) = 25.790(14) \times 10^{-6}$ is from the diamagnetic shielding of the proton in the water molecule, determined from [45]

$$\sigma({\rm H_2O}, 34.7^\circ C) = 1 - \frac{g_p({\rm H_2O}, 34.7^\circ C)}{g_J(H)} \frac{g_J(H)}{g_p(H)} \frac{g_p(H)}{g_p({\rm free})} . \tag{2.24}$$

The terms are: the ratio of the g-factors of the proton in a spherical water sample to that of the electron in the hydrogen ground state $(g_J(H))$ [45]; the ratio of electron to proton g-factors in hydrogen [46]; the bound-state correction relating the g-factor of the proton bound in hydrogen to the free proton [47, 48]. The temperature dependence is from Reference [49]. An alternate absolute calibration would be to use an optically pumped ^{3}He NMR probe [50]. This has several advantages: the sensitivity to the probe shape is negligible, and the temperature dependance is also negligible. This option is being explored for E989.

The calibration procedure used above permits the magnetic field to be expressed in terms of the Larmor frequency of a free proton, ω_p. The magnetic field is weighted by the muon distribution, and also averaged over the running time weighed by the number of stored muons to determine the value of ω_p which is combined with the average ω_a to determine a_μ. The reason for the use of these two frequencies, rather than B measured in tesla can be

understood from Eq. 2.14. To obtain a_μ from this relationship requires precise knowledge of the muon charge to mass ratio.

To determine a_μ from the two frequencies ω_a and ω_p, we use the relationship

$$a_\mu = \frac{\omega_a/\omega_p}{\lambda_+ - \omega_a/\omega_p} = \frac{\mathcal{R}}{\lambda_+ - \mathcal{R}} \,, \qquad (2.25) \quad \boxed{\texttt{eq:lambda}}$$

where the ratio

$$\lambda_+ = \mu_{\mu^+}/\mu_p = 3.183\,345\,137\,(85) \qquad\qquad (2.26)$$

is the muon-to-proton magnetic moment ratio [51] measured from muonium (the $\mu^+ e^-$ atom) hyperfine structure[53]. Of course, to use λ_+ to determine a_{μ^-} requires the assumption of *CPT* invariance, *viz.* ($a_{\mu^+} = a_{\mu^-}$; $\lambda_+ = \lambda_-$). The comparison of $\mathcal{R}_{\mu^+}$ with $\mathcal{R}_{\mu^-}$ provides a *CPT* test. In E821

$$\Delta\mathcal{R} = \mathcal{R}_{\mu^-} - \mathcal{R}_{\mu^+} = (3.6 \pm 3.7) \times 10^{-9} \qquad (2.27) \quad \boxed{\texttt{eq:DeltaR}}$$

2.2.4   Previous Measurements and Results

Measurement of a_μ

The E821 Collaboration working at the Brookhaven Laboratory AGS used an electric quadrupole field to provide vertical focusing in the storage ring, and shimmed the magnetic field to ± 1 ppm uniformity on average. The storage ring was operated at the "magic" momentum, $p_{magic} = 3.094$ GeV/c, ($\gamma_{magic} = 29.3$), such that $a_\mu = (m/p)^2$ and the electric field did not contribute to ω_a.[5] The result is [38, 39]

$$a_\mu^{\mathrm{E821}} = 116\,592\,089(54)_{stat}(33)_{syst}(63)_{tot} \times 10^{-11} \quad (\pm 0.54\,\mathrm{ppm}). \qquad (2.28) \quad \boxed{\texttt{eq:E821-res}}$$

The results from E821 are shown in Fig. 2.5 along with the Standard-Model value which is discussed below in section 2.3
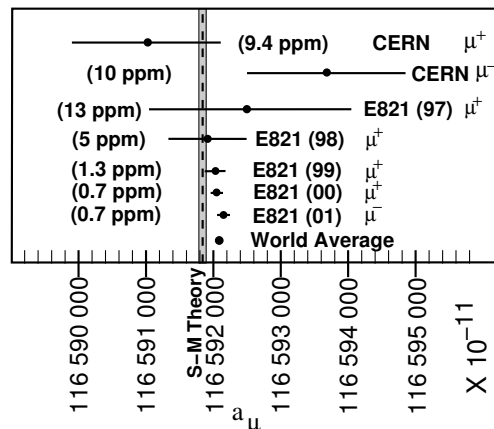
Figure 2.5: Measurements of a_μ along with the SM value given above. $\boxed{\texttt{fg:SM-Exp}}$

---

[5]The magic momentum was first employed by the third CERN collaboration [27].

2.2.5 Measuring the Muon EDM: d_μ

If an EDM is present, the measured frequency is the vector sum of two terms: the spin motion from the torques $\vec{\mu} \times \vec{B}$ and from $\vec{d} \times \vec{E}$, as shown in Eq. 2.13; $\vec{\omega}_{a\eta} = \vec{\omega}_a + \vec{\omega}_\eta$. The first term comes from the anomalous magnetic moment, a, and the second from the electric dipole moment. The motional electric field is much larger than any electric field in the lab, so the observed frequency $\vec{\omega}$ is (essentially) the vector sum of two orthogonal angular frequencies, $\vec{\omega}_a$ and $\vec{\omega}_\eta$. These two frequencies are shown in Fig. 2.6, where the EDM related frequency ω_η is greatly exaggerated.
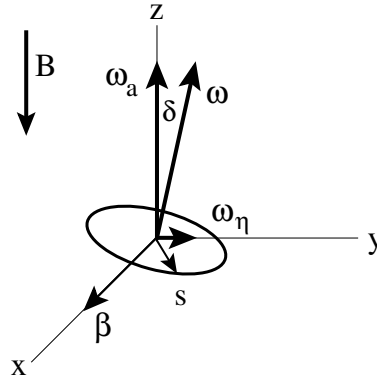
Figure 2.6: The two frequencies present if the muon has both a magnetic and electric dipole moment (not to scale). Note that the EDM ω_η is much smaller than ω_a. The muon spin precession plane is tilted by an angle proportional to the particle's EDM value. The tilt is highest for small $(g-2)$ frequencies.

Thus there are *two* effects due to an electric dipole moment:

1. The observed frequency is the vector sum of ω_a and ω_η so the magnitude of the observed frequency is increased from ω_a to

$$\omega_{a\eta} \simeq \sqrt{\omega_a^2 + \omega_\eta^2} = \omega_a \sqrt{1 + \left(\frac{\eta\beta}{2a}\right)^2} \qquad (2.29)$$

2. The spin precession plane is tilted (everywhere around the ring) by a (very small) angle

$$\delta = \tan^{-1}\frac{\omega_\eta}{\omega_a} = \tan^{-1}\left(\frac{\eta\beta}{2a}\right) \qquad (2.30)$$

as shown in Fig. 2.6

The tilting of the spin precession plane everywhere around the ring, is very much like there is a net radial magnetic field which when integrated around the ring is not zero. In a ring with a purely magnetic field, the average radial B-field for a stored particle is zero, since the particle adjusts its vertical position in the focusing system to ensure this. However, in the presence of other forces, like vertical E-fields, gravity, etc., this is not strictly true and must

be taken into account for systematic error estimation. A major tool against these types of systematic errors, which is only possible in a dedicated EDM storage ring experiment, would be the ability to inject into the storage ring both in a clockwise (CW) and counterclockwise (CCW) sense, where the non-magnetic forces are kept the same while the EDM signal changes sign.

The tipping of the plane of precession around the ring has an important implication for the resulting decay positrons. As the muon spin turns with the frequency ω_a, following the circle shown in Fig. 2.6, the EDM causes an up-down oscillation of the muon spin which is out of phase by $\pi/2$ with the $(g-2)$ precession. Thus the trajectories of the decay positrons (electrons) will oscillate between upward-going to downward-going with the frequency ω_a out of phase with ω_a. It was this effect which was searched for in the third $(g-2)$ experiment at CERN, and in E821 at Brookhaven. At CERN one detector station was outfitted with two scintillators, one just above the mid-plane, one just below.

Assuming the gain and acceptance of the upper and lower detectors are equal and the storage ring and vertical detector mid-plane are identical, the number of electrons above (+) or below (-) the mid-plane is given by[36]

$$N^{\pm}(t) \propto [1 \mp A_\eta \sin(\omega t + \phi) + A_\mu \cos(\omega t + \phi)] \tag{2.31}$$

where A_η is proportional to d_μ. A major source of systematic error arises if there is an offset between the average vertical position of the beam and the position of the boundary between the upper and lower detectors.

In E821, three separate methods were used to search for the up-down oscillations[36]. Five-element hodoscopes were placed in front of about half of the 24 electron calorimeters, and the vertical centroid of the decay electron distribution was fit as a function of time. Five calorimeter stations had finer-grained hodoscopes which also provided the vertical electron distribution of decay electrons as a function of time. One of the stations was equipped with a straw tube array that gave both x and y information, so that the electron tracks could be fit to search for the oscillation in upward- and downward-going tracks. These "traceback" chambers were primarily designed to provide information on the muon distribution in the storage ring[36], but turned out to be a powerful tool to search for the EDM signal. No evidence for an up-down oscillation was seen, and the result is[36]

$$d_\mu = (0.1 \pm 0.9) \times 10^{-19} e-\text{cm}; \quad |d_\mu| < 1.9 \times 10^{-19} e-\text{cm} \ (95\% \ \text{C.L.}), \tag{2.32}$$

a factor of five smaller than the previous limit.

2.3   The Standard-Model Value of a_μ

In this section we present the standard model (SM) theory of the muon anomalous magnetic moment (anomaly). In the following section we discuss physics beyond the standard model (BSM) that could contribute to the anomaly at a measurable level. The conclusion is that muon $(g-2)$ will play a powerful role in the interpretation of new phenomena that might be discovered at the LHC. If new phenomena are not discovered there, then muon $(g-2)$ becomes even more important, since it would provide one of the few remaining ways to search for new physics at the TeV scale.

2.3.1 Introduction

The magnetic moment of the muon (or electron), which is aligned with its spin, is given by

$$\vec{\mu} = g\frac{Qe}{2m_{\mu,e}}\vec{s}, \qquad \underbrace{g = 2}_{\text{Dirac}}(1 + a_\mu);$$

(2.33)

where the quantity g is exactly 2 in the Dirac theory, $Q = \pm 1$ with e a positive number. The small number a, the anomaly, arises from quantum fluctuations, with the largest contribution coming from the single loop diagram in Fig. 2.7(a). This contribution was first calculated by Schwinger [14], who obtained $a = (\alpha/2\pi) = 0.00116\cdots$. These calculations have been extended to higher powers in α/π, with the fourth- $(\alpha/\pi)^2$ and sixth-order $(\alpha/\pi)^3$ contributions having been carried out analytically.
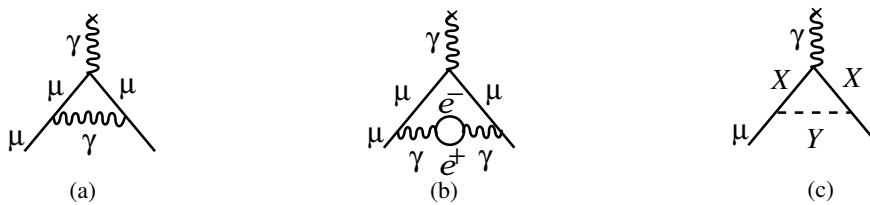
Figure 2.7: The Feynman graphs for: (a) The lowest-order (Schwinger) contribution to the lepton anomaly ; (b) The vacuum polarization contribution, which is one of five fourth-order, $(\alpha/\pi)^2$, terms; (c) The schematic contribution of new particles X and Y that couple to the muon.

The electron anomaly is relatively insensitive to heavier physics, so in principle the 0.03 ppb measurement of the electron anomaly [80] should provide a test of QED, but the few ppb precision of the *independent* measurements of α prevents this comparison. Alternately, one can accept that QED is valid and use the electron anomaly to determine the most precise measurement of α [81].

The muon anomaly is an entirely different case. The relative contribution to the muon anomaly of heavier virtual particles goes as $(m_\mu/m_e)^2 \simeq 43,000$, so with much less precision when compared with the electron, the muon anomaly is sensitive to mass scales in the several hundred GeV region. This not only includes the expected contribution of the W and Z bosons, but perhaps contributions from new, as yet undiscovered, particles such as the supersymmetric partners of the electro-weak gauge bosons (see Fig. 2.7(c)).

The standard-model value of a_μ has three contributions from radiative processes: QED loops containing leptons (e, μ, τ) and photons; loops containing hadrons in vacuum polarization loops where the e^+e^- pair in Fig 2.7(b) is replaced by hadrons; and weak loops involving the weak gauge bosons W, Z, and Higgs such as is shown in Fig. 2.7(c) where $X = W$ and $Y = \nu$, or $X = \mu$ and $Y = Z$. Thus

$$a_\mu^{\text{SM}} = a_\mu^{\text{QED}} + a_\mu^{\text{hadronic}} + a_\mu^{\text{weak}}.$$

(2.34)

The QED and weak contributions to the muon anomaly are now well understood at the level needed for the comparison of Standard-Model theory with experiment.

The hadronic contribution must be determined from a dispersion relation using experimental data, namely the cross sections for electron-positron annihilation to hadrons. The determination of this contribution represents a worldwide effort which was driven primarily by the existence of BNL experiment E821. The possibility of a new Fermilab experiment has already stimulated further work that will certainly continue unabated if P989 turns into an approved and funded experiment.

2.3.2   QED Contribution

The QED and electroweak contributions to a_μ are well understood. Recently the four-loop contribution has been updated and the full five-loop contribution has been calculated [79].

We take the numerical values from the review by Miller, et al, [88] with the QED contribution updated to the Höcker and Marciano [83]. The QED contribution to a_μ has been calculated through tenth order (five loops) [79]. The present value is

$$a_\mu^{\mathrm{QED}} = 116\ 584\ 718.951\ (0.009)(0.019)(0.007)(.077) \times 10^{-11} \qquad (2.35)$$

where the uncertainties are from the lepton mass ratios, the eight-order term, the tenth-order term, and the value of α taken from the ^{87}Rb atom $\alpha_(Rb)^-1 = 137.035\ 999\ 037(91)$ [0.66 ppb]. [82].

2.3.3   Weak contributions

The electroweak contribution (shown in Fig. 2.8) is now calculated through two loops [64, 65, 66, 67, 68]. The single loop result

$$
\begin{aligned}
a_\mu^{\mathrm{EW}(1)} &= \frac{G_F}{\sqrt{2}} \frac{m_\mu^2}{8\pi^2} \left\{ \underbrace{\frac{10}{3}}_{W} + \underbrace{\frac{1}{3}(1-4\sin^2\theta_W)^2 - \frac{5}{3}}_{Z} \right. \\
&\quad + \left. \mathcal{O}\left(\frac{m_\mu^2}{M_Z^2}\log\frac{M_Z^2}{m_\mu^2}\right) + \frac{m_\mu^2}{M_H^2}\int_0^1 dx \frac{2x^2(2-x)}{1-x+\frac{m_\mu^2}{M_H^2}x^2} \right\} \\
&= 194.8 \times 10^{-11}, \qquad\qquad\qquad\qquad (2.36)
\end{aligned}
$$

was calculated by five separate groups shortly after the Glashow-Salam-Weinberg theory was shown by 't Hooft to be renormalizable. With the present limit on the Higgs boson mass, only the W and Z contribute to the lowest-order electroweak at a measurable level.

The two-loop weak contribution, (see Figs. 2.8(c-e) for examples) is negative, and the total electroweak contribution is [88]

$$a_\mu^{\mathrm{EW}} = 153(1)(1) \times 10^{-11} \qquad (2.37)$$

where the first error comes from hadronic effects in the second-order electroweak diagrams with quark triangle loops, and the latter comes from the uncertainty on the Higgs mass [66, 65, 64, 52]. The leading logs for the next-order term have been shown to be small [68]. The weak contribution is about 1.3 ppm of the anomaly, so the experimental uncertainty on a_μ of ± 0.54 ppm now probes the weak scale of the standard model.

(a)   (b)   (c)   (d)   (e)
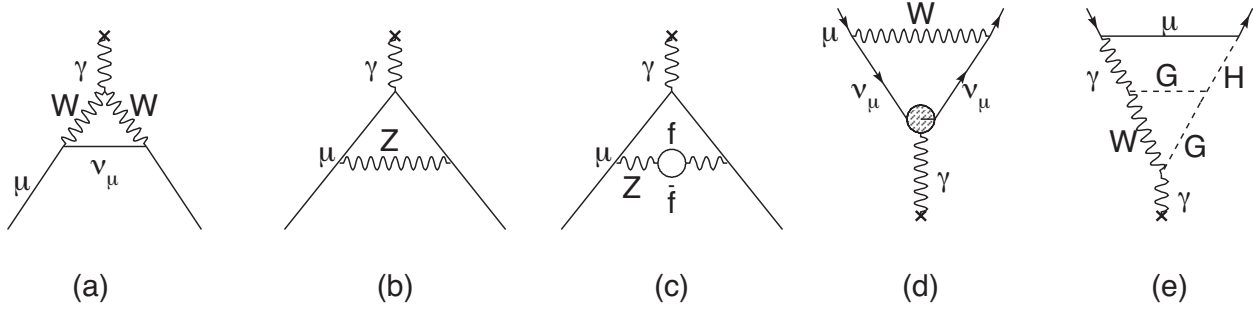
Figure 2.8: Weak contributions to the muon anomalous magnetic moment. Single-loop contributions from (a) virtual W and (b) virtual Z gauge bosons. These two contributions enter with opposite sign, and there is a partial cancellation. The two-loop contributions fall into three categories: (c) fermionic loops which involve the coupling of the gauge bosons to quarks, (d) bosonic loops which appear as corrections to the one-loop diagrams, and (e) a new class of diagrams involving the Higgs where G is the longitudinal component of the gauge bosons. See Ref. [52] for details. The $\times$ indicates the virtual photon from the magnetic field. `fg:weak`

Hadronic contribution

The hadronic contribution to a_μ is about 60 ppm of the total value. The lowest-order diagram shown in Fig. 2.9(a) dominates this contribution and its error, but the hadronic light-by-light contribution Fig. 2.9(e) is also important. We discuss both of these contributions below.

(a)   (b)   (c)   (d)   (e)
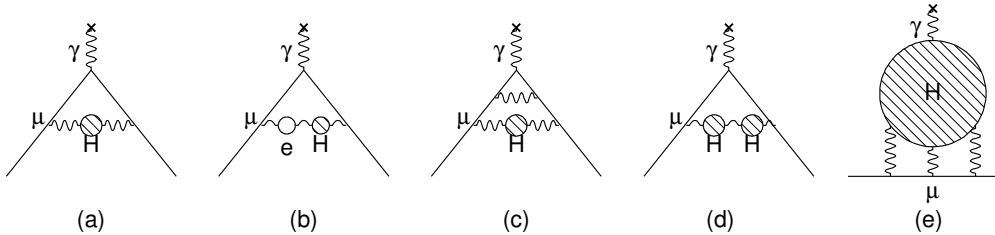
Figure 2.9: The hadronic contribution to the muon anomaly, where the dominant contribution comes from the lowest-order diagram (a). The hadronic light-by-light contribution is shown in (e). `fg:had`

The energy scale for the virtual hadrons is of order $m_\mu c^2$, well below the perturbative region of QCD. Thus it must be calculated from the dispersion relation shown pictorially in Fig. 2.10,

$$a_\mu^{\text{had;LO}} = \left(\frac{\alpha m_\mu}{3\pi}\right)^2 \int_{4m_\pi^2}^\infty \frac{ds}{s^2} K(s) R(s), \quad \text{where} \quad R \equiv \frac{\sigma_{\text{tot}}(e^+e^- \to \text{hadrons})}{\sigma(e^+e^- \to \mu^+\mu^-)}, \qquad (2.38)$$ `eq:dispersi`

using the measured cross sections for $e^+e^- \to$ hadrons as input, where $K(s)$ is a kinematic factor ranging from -0.63 at $s = 4m_\pi^2$ to 1 at $s = \infty$. This dispersion relation relates the

bare cross section for e^+e^- annihilation into hadrons to the hadronic vacuum polarization contribution to a_μ. Because the integrand contains a factor of s^{-2}, the values of $R(s)$ at low energies (the ρ resonance) dominate the determination of $a_\mu^{\mathrm{had;LO}}$, however at the level of precision needed, the data up to 2 GeV are very important. This is shown in Fig. 2.11, where the left-hand chart gives the relative contribution to the integral for the different energy regions, and the right-hand gives the contribution to the error squared on the integral. The contribution is dominated by the two-pion final state, but other low-energy multi-hadron cross sections are also important.
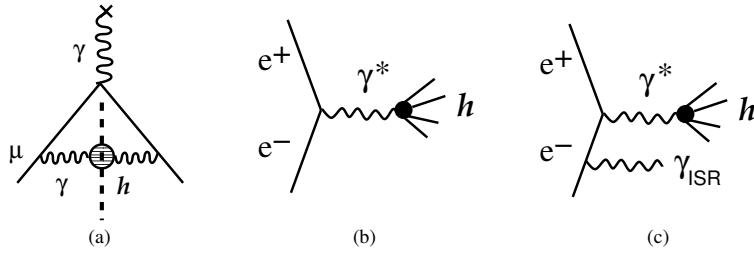
Figure 2.10: (a) The "cut" hadronic vacuum polarization diagram; (b) The e^+e^- annihilation into hadrons; (c) Initial state radiation accompanied by the production of hadrons.
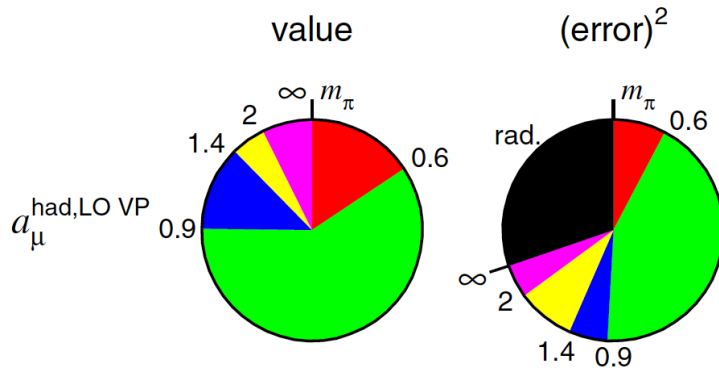
Figure 2.11: Contributions to the dispersion integral, and to the error on the dispersion integral. Taken from Hagirawa, et al., [58]

These data for e^+e^- annihilation to hadrons are also important as input into the determination of $\alpha_s(M_Z)$ and other electroweak precision measurements, including the limit on the Higgs mass [84]. After the discussion of the determination of the hadronic contribution, we will return to the implications on M_H.

In the 1980s when E821 was being proposed at Brookhaven, the hadronic contribution was know to about 10 ppm. It now is known to about 0.4 ppm. This improvement has come from the hard work of many experimental and theoretical physicists. The low energy e^+e^- data of the 80s have been replaced by very precise data from the CMD2 and SND collaborations in Novosibirsk, the KLOE collaboration at Frascati, and the BaBar collaboration at SLAC.

The new VEPP-2000 collider in Novosibirsk has been operational for several years, with two upgraded detectors, CMD-3 and SND-2000. This new facility will permit both energy scans, and the use of initial-state radiation to measure cross sections up to 2.0 GeV. Additional data on multi-hadron final states are expected from the Belle detector at KEK.

In addition to the collider experiments, significant theoretical work has been carried out in generating the radiator functions used in the initial-state radiation (ISR) experiments at Frascati and BaBar [94, 95], as well as on the hadronic light-by-light contribution shown in Fig. 2.9(e).

The worldwide effort to improve our knowledge of the hadronic contribution continues to this day. The most recent $\pi\pi$-final state measurements were reported by the BaBar [96] and KLOE [99, 100] collaborations. An independent analysis of KLOE data using the direct measurement of $\sigma e^+ e^- \to \pi^+ \pi^- / \sigma e^+ e^- \to \mu^+ \mu^-$, which agreed well with their previous analysis using the luminosity measurement and QED calculations, was reported at Tau2012 [101]

Muon $(g-2)$, and the determination of the hadronic contribution continues to feature prominently in the international workshops Tau [97] and PHIPSI [98], where sessions were devoted to all issues around muon $(g-2)$. We emphasize that while this is a difficult subject, progress will continue to be made, provided that a new experiment does indeed go forward at Fermilab.

Lowest- and next-lowest-order hadronic contribution

The cross sections at low energies dominate the dispersion relation, and until recently the low-energy electron-positron storage rings in Novosibirsk and Frascati provided the bulk of the new measurements. The Novosibirsk experiments CMD2 (cryogenic magnetic detector) and SND (spherical neutral detector) collected data using the traditional $e^+ e^-$ energy scan. The KLOE experiment ran at a fixed energy around 1 GeV, either on the ϕ-resonance or just below it, using initial-state radiation to lower the collision energy and provide the full energy range in a single measurement (see Fig. 2.10(c)). The BaBar experiment also used the ISR technique, but operated at a much higher energy at or near the $\Upsilon 4s$, which easily permitted observation of the ISR photon. At Tau2012 the Belle experiment reported new results on the $\pi^+ \pi^- \pi^0$ final state [102] using ISR data. The ISR (sometimes called "radiative return") technique is possible because of the development of the necessary theory [94, 95], which provides the effective virtual photon spectrum, called the "radiator function."

While the KLOE experiment was limited to the $\pi\pi\gamma$ channel, the higher energy of the PEP-2 collider permitted BaBar to detect the ISR photon and to measure many multiple hadron final states along with the $\pi\pi\gamma$ final state, thus providing important data from channels which were either very imprecise, or simply not available before. The first $\pi^+ \pi^-$ data from BaBar were released in August 2009 [96], and covered the energy range from threshold to 3 GeV. Unlike the other experiments that used a calculated $\mu\mu$ cross section for the denominator in Eq. (2.38), the BaBar experiment measured the $\mu\mu$ production directly and took the ratio of experimental numbers to determine $R(s)$ directly. This had the benefit of canceling a number of systematic errors, and significantly lowered the uncertainty on the cross section. If BaBar had used the calculated $\mu\mu$ cross section, the cross section errors would have been at the $\sim 5\%$ level, much too large to be useful in the determination of a_μ^{had}.

Published cross sections from the BaBar, KLOE, CMD2 and SND experiments are shown
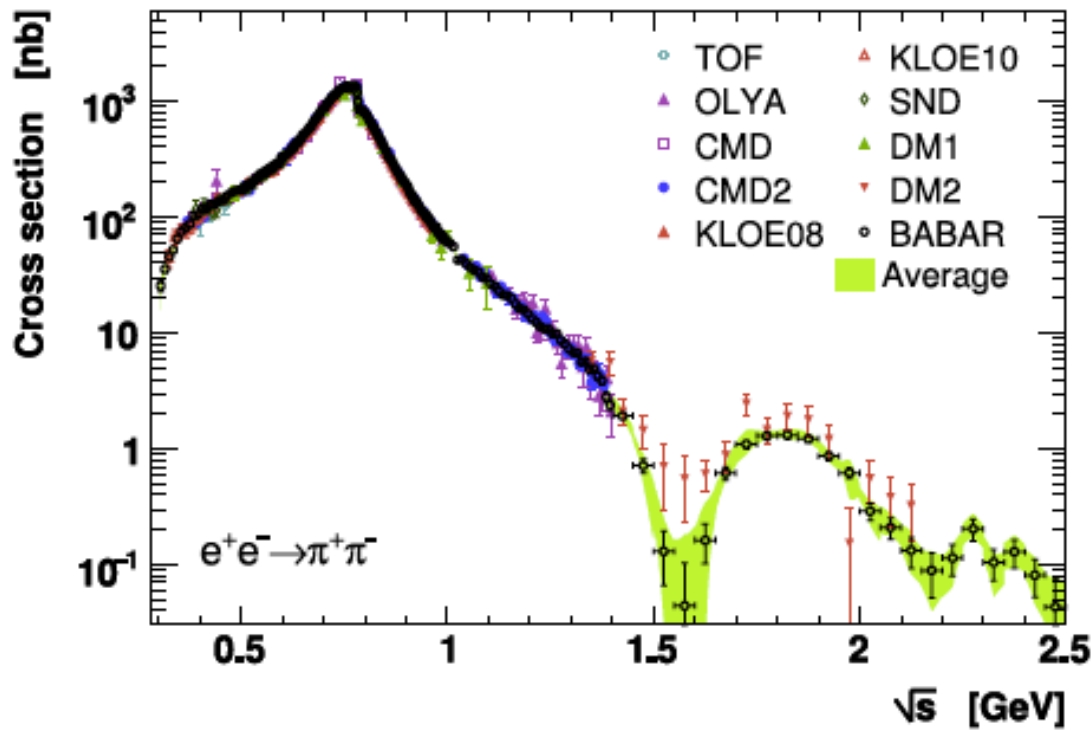
(a)
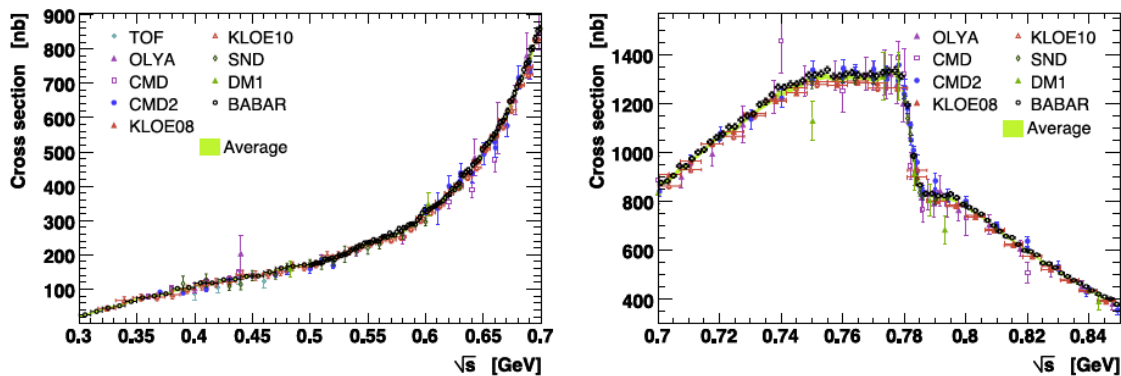
(b)

Figure 2.12: The $\pi\pi$ cross section from BaBar, CMD2, KLOE and SND. The lower left-hand figure shows the threshold region, the right-hand figure shows a blowup of the ρ resonance region. The sharp cusp comes from $\rho - \omega$ interference.

in Fig. 2.12. The KLOE re-analysis of their small-angle data using the ratio of the $\pi\pi$ $\mu\mu$ cross sections, compared large-angle data[100], and are displayed in Fig. 2.13 as the pion

form factor F_π, which is related to the cross section by

$$\sigma_{e^+e^-\to\pi^+\pi^-} = \frac{\pi\alpha^2}{3s}\beta_\pi^3|F_\pi|^2.$$ (2.39)

They were analyzed by a different group of collaborators who worked independently from those involved in the the KLOE08 [99] analysis.
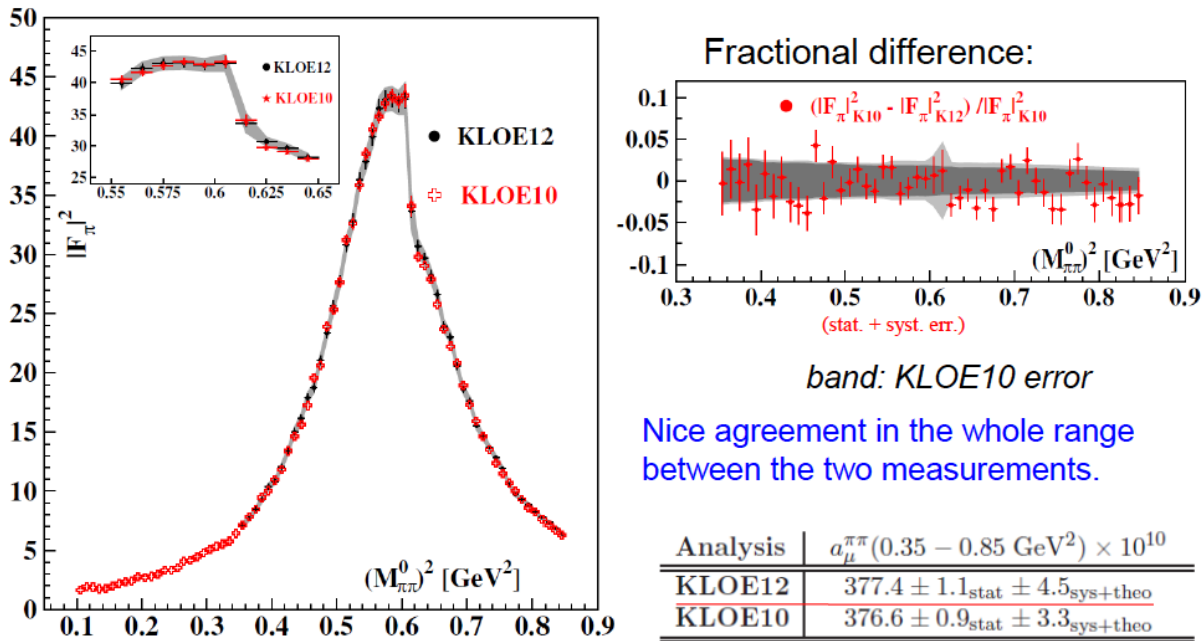
Figure 2.13: The pion form factor $|F_\pi|^2$ from KLOE2010 [100] and the re-analysis of the 2008 data [99] using the cross-section ratio described above [101]. The right-hand side shows the fractional difference between the two analyses.

`fg:KLOE0812`

Two recent analyses [57, 58] of the e^+e^- hadroproduction data obtained:

$$a_\mu^{\mathrm{had;LO}} = (6\,923 \pm 42 \times 10^{-11}.$$ (2.40)   `eq:hvp1-pub`
$$a_\mu^{\mathrm{had;LO}} = (6\,949 \pm 43 \times 10^{-11}.$$ (2.41)   `eq:hvp2-pub`
(2.42)

Important earlier global analyses include those of HMNT [85], Davier, et al., [86], Jegerlehner [87].

The most recent evaluation of the next-order hadronic contribution shown in Fig. 2.9(b-d) `fg:had` can also be determined from a dispersion relation, and the result is [58] `Hagiwara:2011`

$$a_\mu^{\text{had:NLO})} = (-98.4 \pm 0.6_{\text{exp}} \pm 0.4_{\text{rad}}) \times 10^{-11}. \qquad (2.43) \quad \boxed{\texttt{exphvpnlo}}$$

$a_\mu^{\text{had;LO}}$ from hadronic τ decay

The value of $a_\mu^{\text{had;LO}}$ from threshold up to m_τ could in principle be obtained from hadronic τ^- decays (See Fig. 2.9), `fg:had` provided that the necessary isospin corrections are known. This was first demonstrated by Almany, Davier and Höcker [89]. `adh` In the absence of second-class currents, hadronic τ decays to an *even* number of pions such as $\tau^- \to \pi^-\pi^0\nu_\tau$ goes through the vector part of the weak current, and can be related to e^+e^- annihilation into $\pi^+\pi^-$ through the CVC hypothesis and isospin conservation (see Fig. 2.14) [89, 93]. `fg:hadprotah98` The τ-data only contain an isovector piece, and the isoscalar piece present in e^+e^- annihilation has to be put in "by hand" to evaluate $a_\mu^{\text{had;LO}}$. Until recently there were 3.5 to 4.5 standard deviation differences when e^+e^- data and the CVC hypothesis were used to determine the $\tau^- \to \nu_\tau\pi^-\pi^0$ or $\tau^- \to \nu_\tau 2\pi^-\pi^+\pi^0$ branching fractions, when compared with the experimental values. Thus until recently most authors [58, 88, 87] `Hagiwara:2011,Miller:2012,Jegerlehner:2009` concluded that there are unresolved issues, most likely incorrect isospin breaking corrections, that make it difficult to use the τ data on an equal footing with the e^+e^- data. New isospin corrections reduced the disagreement between the two methods [57]. `Davier11` However, none of the analyses using tau data have tried to combine the CVC determined part with that obtained from e^+e^- data. Were this to be done, the addition of the e^+e^- data would decrease the overall tau-based evaluation of to a_μ^{had}. Even so, the tau-based evaluation has to use e^+e^- data to determine the isoscalar part, so that the tau-based evaluation by Davier, et al., [57] `Davier11` can never be completely independent of the e^+e^- data.

More recently, Jegerlehner and Szafron [90] `Jegerlehner:2011` appear to have resolved this problem by calculating the correction from $\rho - \gamma$ mixing, which had not been included correctly in the previous evaluations. A subsequent hidden local symmetry calculation [91, 92] `Benayoun:2012a,Benayoun:2012b` further refines these ideas and includes the τ-data in a combined analysis. They conclude that their analysis yields a 4.7 to 4.9 σ difference with the Standard Model.

We should note that the theoretical uncertainties on the dispersion relation in Eq. (2.38), `eq:dispersion` which assumes analyticity and the optical theorem, are negligible. The cross section that enters in Eq. (2.38) `eq:dispersion` is the bare cross section, and some of the early experiments were not so careful in their reporting the data and being clear on what, if any radiative corrections were applied. All of the modern experiments are well aware of these issues, and their reported errors include any uncertainties introduced in determining the bare cross section.
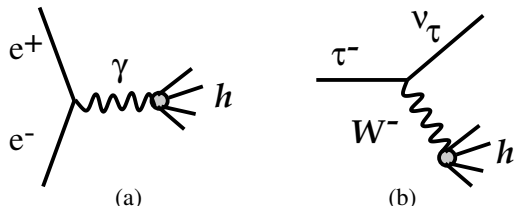
Figure 2.14: e^+e^- annihilation into hadrons (a), and hadronic τ decay (b).   `fg:hadprota`

Hadronic light-by-light contribution

The hadronic light-by-light contribution, (Fig. 2.9(e)) cannot at present be determined from data, but rather must be calculated using hadronic models that correctly reproduce the properties of QCD. A number of authors have calculated portions of this contribution, and recently a synthesis of all contributions has become available from Prades, de Rafael and Vainshtein [70][6], which has been agreed to by authors from each of the leading groups working in this field. They obtain

$$a_\mu^{\mathrm{HLbL}} = (105 \pm 26) \times 10^{-11} \, . \tag{2.44}$$

Additional work on this contribution is underway on a number of fronts, including on the lattice. A workshop was held in March 2011 at the Institute for Nuclear Theory in Seattle [71] which brought together almost all of the interested experts.

One important point should be made here. The main physics of the hadronic light-by-light scattering contribution is well understood. In fact, but for the sign error unraveled in 2002, the theoretical predictions for a_μ^{HLbL} have been relatively stable for more than ten years. We summarize with a quote from Eduardo de Rafael [74]:

> "For the time being, concerning the issue of errors, and after the work in PdeRV, I personally think that a 25% error on the HLbL is quite a generous one. One of my reasons is the fact that in the comparable HVP contribution—assuming that we did not have data from ee-annihilations nor tau-decays—I claim that from the underlying physics which we know, and using the same techniques as in the HLbL calculation, we are presently able to make there an estimate which, when compared to the one with data, turns out to be quite good: at the 10% to 15% level."

There is one calculation which used a Dyson-Schwinger approach, that appeared to strongly disagree with all of the other model calculations of the hadronic-light-by-light contribution [76]. However, recently these authors found several sign mistakes that change their result, moving it closer to other calculations [77].

At Tau2012, Blum reported that the lattice calculation of the hadronic-light-by-light contribution had started to see a signal [78]. "Signal may be emerging in the model ballpark:" Blum also had encouraging words about the precision that the lattice might reach on the lowest-order hadronic contribution.

In addition to the theoretical work on the HLbL, a new facility is being commissioned at DAϕNE which will provide tagged virtual photons for $\gamma^*\gamma^*$ physics. Both high- and low-energy taggers are being constructed on both sides of the interaction region to detect and measure the scattered electron and positron. Thus a coincidence between the scattered electrons and a π^0 would provide information on $\gamma^*\gamma^* \to \pi^0$, etc. [75], and will provide experimental constraints on the models used to calculate the hadronic light-by-light contribution.

---

[6]This compilation is generally referred to as the "Glasgow Consensus" since it grew out of a workshop in Glasgow in 2007.

2.3.4 Summary of the Standard-Model Value and Comparison with Experiment

We determine the SM value using the new QED calculation from Aoyama [79]; the electroweak from Ref. [88], the hadronic light-by-light contribution from the "Glasgow Consensus" [70]; and lowest-order hadronic contribution from Davier, et al., [57], or Hagawara et al., [58], and the higher-order hadronic from Ref. [58] A summary of these values is given in Table 2.3.

Table 2.3: Summary of the Standard-Model contributions to the muon anomaly. Two values are quoted because of the two recent evaluations of the lowest-order hadronic vacuum polarization.

	Value ($\times 10^{-11}$) units
QED ($\gamma + \ell$)	$116\,584\,718.951 \pm 0.009 \pm 0.019 \pm 0.007 \pm 0.077_\alpha$
HVP(lo) [57]	$6\,923 \pm 42$
HVP(lo) [58]	$6\,949 \pm 37$
HVP(ho) [58]	-98.4 ± 0.7
HLbL	105 ± 26
EW	$153 \pm 1 \pm 1$
Total SM [57]	$116\,591\,802 \pm 42_{\text{H-LO}} \pm 26_{\text{H-HO}} \pm 2_{\text{other}} \ (\pm 49_{\text{tot}})$
Total SM [58]	$116\,591\,828 \pm 37_{\text{H-LO}} \pm 26_{\text{H-HO}} \pm 2_{\text{other}} \ (\pm 45_{\text{tot}})$

This SM value is to be compared with the combined a_μ^+ and a_μ^- values from E821 [39] corrected for the revised value of λ as mentioned above:

$$a_\mu^{\text{E821}} = (116\,592\,089 \pm 63) \times 10^{-11} \quad (0.54\,\text{ppm}), \tag{2.45}$$

which give a difference of

$$\Delta a_\mu(\text{E821} - \text{SM}) = (287 \pm 80) \times 10^{-11} \tag{2.46}$$
$$= (261 \pm 78) \times 10^{-11} \tag{2.47}$$
$$\tag{2.48}$$

depending on which evaluation of the lowest-order hadronic contribution that is used [57, 58]. This comparison is shown graphically in Fig. 2.5.

This difference of 3.2 to 3.6 standard deviations is tantalizing, but we emphasize that whatever the final agreement between the measured and SM value turns out to be, it will have significant implications on the interpretation of new phenomena that might be found at the LHC and elsewhere. This point is discussed in detail below.

The present theoretical error is dominated by the uncertainty on the lowest-order hadronic contribution and uncertainty on the hadronic light-by-light contribution (see Table 2.3). The lowest-order hadronic contribution could be reduced to 25×10^{-11} based on the analysis of existing data and on the data sets expected from future efforts, e.g. VEPP-2000 in

Novosibirsk and BESS3. When combined with future theoretical progress on the hadronic light-by-light contribution, the total SM error could reach 30×10^{-11}.

With the proposed experimental error of $\pm 16 \times 10^{-11}$, the combined uncertainty for the difference between theory and experiment could be as small as $\pm 34 \times 10^{-11}$, which is to be compared with the $\pm 81 \times 10^{-11}$ in Eq. (2.48).

$R(s)$ measurements and the Higgs mass, M_H

If the hadronic cross section that enters into the dispersion relation of Eq. (2.38) were to increase significantly from the value obtained in the published papers of CMD2, SND and KLOE, then as pointed out by Passera, Marciano and Sirlin [84], it would have significant implications for the limit on the mass of the Higgs boson. The value of $\Delta\alpha_{\text{had}}^{(5)}(M_Z)$ depends on the *same* measured cross-sections that enter into Eq. (2.38),

$$\Delta\alpha_{\text{had}}^{(5)}(M_Z) = \frac{M_Z^2}{4\alpha\pi^2} P \int_{4m_\pi^2}^{\infty} ds \frac{\sigma(s)}{M_Z^2 - s} \, . \tag{2.49}$$

The present bound of $M_H \leq 150$ GeV (95% C.L.) changes if $\Delta\alpha_{\text{had}}(M_Z)$ changes. Assuming that the hadronic contribution to a_μ is increased by the amount necessary to remove the difference between the experimental and theoretical values of a_μ, the effect on M_H is to move the upper bound down to $\simeq 130$ GeV. Given the experimental limit $M_H > 114.4$ GeV (95% C.L.), this significantly narrows the window for the Higgs mass. The details depend on the *s*-region assumed to be incorrect in the hadronic cross section. A much more complete discussion is given in Ref. [84].

Now that a "Higgs-like" particle has been discovered at the LHC, could one make a statement on limits on the hadronic contribution? When asked this question at the Tau2012 workshop, Passera replied that he didn't know the answer but W. Marciano had also asked the same question.

2.3.5 Expected Improvements in the Standard-Model Value

Much experimental and theoretical work is going on worldwide to refine the hadronic contribution. The theory of $(g-2)$, relevant experiments to determine the hadronic contribution, including work on the lattice, have featured prominently in the series of tau-lepton workshops and PHIPSI workshops which are held in alternate years.

Over the development period of our new experiment, we expect further improvements in the SM-theory evaluation. This projection is based on the following developments and facts:

- **Novosibirsk:** The VEPP2M machine has been upgraded to VEPP-2000. The maximum energy has been increased from $\sqrt{s} = 1.4$ GeV to 2.0 GeV. Additionally, the SND detector have been upgraded and the CMD2 detector was replaced by the much-improved CMD3 detector. The cross section will be measured from threshold to 2.0 GeV using an energy scan, filling in the energy region between 1.4 GeV, where the previous scan ended, up to 2.0 GeV, the lowest energy point reached by the BES collaboration in their measurements. See Fig. 2.11 for the present contribution to the overall error from this region. Engineering runs began in 2009, and data collection

started in 2011. So far two independent energy scans between 1.0 and 2.0 GeV were performed in 2011 and 2012. The peak luminosity of 3×10^{31} 1/cm²s was achieved, which is limited by the positron production rate. The new injection facility, scheduled to be commissioned during the 2013-2014 upgrade, should permit the luminosity to reach $10^3 2$ 1/cm²s. Data collection is expected to be resumed by the end of 2012 with new energy scan at energies below 1.0 GeV. The goal of experiments at VEPP-2000 is to achieve a systematic error 0.3-0.5% in $\pi^+\pi^-$ channel with negligble statistical error in the integral. The high statistics, expected at VEPP-2000, should allow a detailed comparison of the measured cross-sections with ISR results at BaBar and DAϕNE. After the upgrade, experiments at VEPP-2000 plan to take a large amount of data at 1.8-2 GeV, around $N\bar{N}$ threshold. This will permit ISR data with the beam energy of 2 GeV, which is between the PEP2 energy at the $\Upsilon(4s)$ and the 1 GeV ϕ energy at the DAϕNE facility in Frascati. The dual ISR and scan approach will provide an important cross check on the two central methods to determine HVP.

- **KLOE:** The KLOE collaboration has just reported the analysis of their 2008 data set using the experimental ratio $\pi\pi/\mu\mu$ final states, rather than the luminosity to get the cross sections [101]. In the future, they will begin the program of two-photon physics will be ramping up, which will provide experimental input to the hadronic light-by-light theory.

- **BaBar:** A significant amount of new data exists from BaBar, which can be used to provide another ISR measurement from threshold to 3 GeV. It is not at all clear that the Collaboration will be able to take on the analysis challenge.

- **Belle:** Some work on ISR measurements of $R(s)$ is going on in multi-hadron channels. These studies will complement those completed at BaBar and provide an important check.

- **Calculations on the Lattice for Lowest-Order HVP:** With the increased computer power available for lattice calculations, it may be possible for lattice calculations to contribute to our knowledge of the lowest-order hadronic contribution. Blum and his collaborators are continuing to work on the lowest-order contribution, Several groups, UKQCD (Edinburg), DESY-Zeuthen (Renner and Jansen), and the LSD (lattice strong dynamics) group in the US are all working on the lowest-order contribution.

- **Calculations on the Lattice of Hadronic Light-by-Light:** The hadronic light-by-light contribution has a magnitude of $(105 \pm 26) \times 10^{-11}$, ~ 1 ppm of a_μ. A modest calculation on the lattice would have a large impact. Blum and his collaborators at BNL, RIKEN and Nagoya are working on HLbL, and are beginning to see a signal.

2.4 Physics Beyond the Standard Model

For many years, the muon anomaly has played an important role in constraining physics beyond the standard model [55, 56, 106, 109]. The almost 1500 citations to the major E821

papers [39, 38, 63, 62], with 111 by July 2012, demonstrates that this role continues. The citations are shown as a function of year in Fig. 2.15. As discussed in the previous section (see Eq. (2.48)), the present Standard-Model value is smaller than the experimental value by $\Delta a_\mu(\text{E821} - \text{SM}) = (255 \pm 80) \times 10^{-11}$.
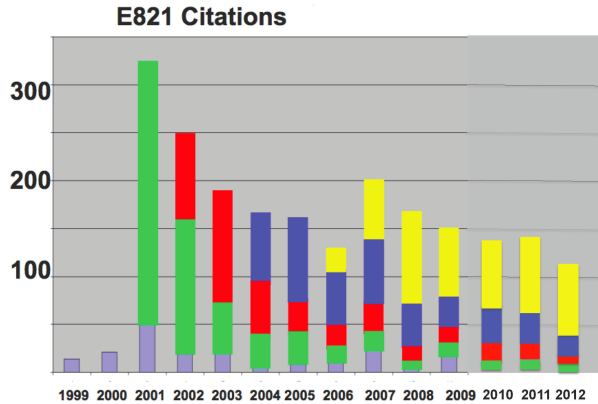
E821 Citations

Figure 2.15: Citations by year to the E821 papers reporting physics results as of July 2012: light blue [60] plus [61]; green [62]; red [63]; blue [38]; and yellow the Physical Review article [39].

In this section, we discuss how the muon anomaly provides a unique window to search for physics beyond the standard model. If new physics is discovered at the LHC, then a_μ will play an important role in sorting out the interpretation of those discoveries. In the sections below, examples of constraints placed on various models that have been proposed as extensions of the standard model are discussed. However, perhaps the ultimate value of an improved limit on a_μ, will come from its ability to constrain the models that we have not yet invented.

Overview

The LHC experiments have just begun operation, thus taking the next major energy step forward in directly probing physics at the TeV scale. This scale appears to be a crucial scale in particle physics. It is linked to electroweak symmetry breaking, and many arguments indicate that radically new concepts such as supersymmetry, extra dimensions, technicolor, or other new interactions, could be realized at this scale. Cold dark matter particles could have weak-scale/TeV-scale masses, and models of Grand Unification prefer the existence of supersymmetry at the TeV scale. TeV-scale physics could be very rich, and the LHC is designed to discover physics beyond the standard model. Independent of whether the LHC establishes physics beyond the SM or produces the SM Higgs and nothing else, complementary experiments are needed in the quest to understand the TeV scale. This need is highlighted by the unprecedented complexity of the LHC accelerator and experiments, the involved initial and final states, and the huge backgrounds at the LHC.

The muon $(g-2)$, together with searches for charged lepton flavor violation, electric

dipole moments, and rare decays, provides such a complementary tool to probe the high-energy frontier.

The complementarity between these different measurements can be easily seen. $g-2$ corresponds to a flavor- and CP-conserving interaction which is sensitive to and potentially enhanced by chirality flips. Many high-energy collider observables are insensitive to chirality flips. Many other low-energy observables are chirality-flipping but flavor-violating (b- or K-decays, $\mu \to e$ conversion, etc) or CP-violating (electric dipole moments). Furthermore, while $g-2$ is sensitive to leptonic couplings, b- or K-physics more naturally probe the hadronic couplings of new physics. If charged lepton-flavor violation exists, observables such as $\mu \to e$ conversion can only determine a combination of the strength of lepton-flavor violation and the mass scale of new physics. In that case, $g-2$ can help to disentangle the nature of the new physics.

The role of $g-2$ as a discriminator between very different standard model extensions is well illustrated by a relation discussed by Czarnecki and Marciano [56] that holds in a wide range of models as a result of the chirality-flipping nature of $g-2$: If a new physics model with a mass scale Λ contributes to the muon mass $\delta m_\mu(\text{N.P.})$, it also contributes to a_μ, and the two contributions are related as

$$a_\mu(\text{N.P.}) = \mathcal{O}(1) \times \left(\frac{m_\mu}{\Lambda}\right)^2 \times \left(\frac{\delta m_\mu(\text{N.P.})}{m_\mu}\right). \qquad (2.50)$$

The ratio $C(\text{N.P.}) \equiv \delta m_\mu(\text{N.P.})/m_\mu$ is typically between $\mathcal{O}(\alpha/4\pi)$ (for perturbative contributions to the muon mass) and $\mathcal{O}(1)$ (if the muon mass is essentially due to radiative corrections). Hence the contributions to a_μ are highly model dependent.

It is instructive to classify new physics models as follows:

- Models with $C(\text{N.P.}) \simeq 1$: In such models the muon mass is essentially generated by radiative effects at some scale Λ. A variety of such models have been discussed in [56], including extended technicolor or generic models with naturally vanishing bare muon mass. In these models the new physics contribution to a_μ can be very large,

$$a_\mu(\Lambda) \simeq \frac{m_\mu^2}{\Lambda^2} \simeq 1100 \times 10^{-11} \left(\frac{1 \text{ TeV}}{\Lambda}\right)^2. \qquad (2.51)$$

  and the difference Eq. (2.48) can be used to place a lower limit on the new physics mass scale, which is in the few TeV range [110].

- Models with $C(\text{N.P.}) = \mathcal{O}(\alpha/4\pi)$: In such models a difference as large as Eq. (2.48) is very hard to accommodate unless the mass scale is very small, of the order of M_Z. If any of these are realized in Nature, the new measurement of a_μ would be expected to agree with the standard model value within approximately $\pm 34 \times 10^{-11}$, the projected sensitivity of the combined standard model plus experiment sensitivity. Conversely, if the future a_μ-measurement establishes a definite deviation from the standard model prediction, such models will all be conclusively ruled out. There are many well-motivated models of this kind, e.g. models with extra weakly interacting gauge bosons Z', W', certain models with extra dimensions, and variants of Little Higgs models. As examples, the contributions to a_μ in a model with $\delta = 1$ (or 2)

universal extra dimensions [111] and the Littlest Higgs model with T-parity [112] are
given by

$$a_\mu(\text{UED}) \simeq -5.8 \times 10^{-11}(1 + 1.2\delta)S_{\text{KK}}, \tag{2.52}$$

$$a_\mu(\text{LHT}) < 12 \times 10^{-11} \tag{2.53}$$

with $|S_{\text{KK}}| \lesssim 1$ [111]. In both cases, the models predict observable effects at the LHC,
which are hard to distinguish from e.g. supersymmetry at the LHC. Many other models
with extra weakly interacting particles give similar results [113].

- Models with intermediate values for $C(\text{N.P.})$ and mass scales around the weak scale:
  In such models, contributions to a_μ could be as large as Eq. (2.48) or even larger,
  or smaller, depending on the details of the model. This implies that a more precise
  a_μ-measurement will have significant impact on such models and can even be used to
  measure model parameters. Supersymmetric models are the most well-known exam-
  ples, so muon $g-2$ would have substantial sensitivity to the supersymmetric particles.
  Compared to generic perturbative models, supersymmetry provides an enhancement
  to $C(\text{SUSY}) = \mathcal{O}(\tan\beta \alpha/4\pi)$ and to $a_\mu(\text{SUSY})$ by a factor $\tan\beta$ (the ratio of the vac-
  uum expectation values of the two Higgs fields). The SUSY diagrams for the magnetic
  dipole moment, the electric dipole moment, and the lepton-number violating conver-
  sion process $\mu \to e$ in the field of a nucleus are shown pictorially in Fig. 2.16. In a
  model with SUSY masses equal to Λ the supersymmetric contribution to a_μ is given
  by [56]

  $$a_\mu(\text{SUSY}) \simeq \text{sgn}(\mu)\,130 \times 10^{-11}\,\tan\beta\,\left(\frac{100\text{ GeV}}{\Lambda}\right)^2 \tag{2.54}$$

  which indicates the dependence on $\tan\beta$, and the SUSY mass scale, as well as the sign
  of the SUSY μ-parameter. The formula still approximately applies even if only the
  lighter smuon and chargino masses are of the order Λ but e.g. squarks and gluinos are
  much heavier. Thus muon $g-2$ is sensitive to SUSY models with SUSY masses in the
  few hundred GeV range, even if $\tan\beta$ is as low as around 10. Conversely, such SUSY
  models could provide an explanation of the deviation in Eq. (2.48).

  There are many non-supersymmetric models of this kind, too. The most well-known are
  variants of Randall-Sundrum models [114, 115, 116] and large extra dimension models
  [117]. In these models, large contributions to a_μ are possible, but the theoretical eval-
  uation is difficult because of cutoff dependences. Further examples include scenarios of
  unparticle physics [118, 119] (here a more precise a_μ-measurement would constrain the
  unparticle scale dimension and effective couplings), Hidden Sector models of Ref. [120]
  or a model with the discrete flavor symmetry group T' and Higgs triplets [121] (here
  a more precise a_μ-measurement would constrain Hidden Sector/Higgs triplet masses
  and couplings), or the model proposed in Ref. [122], which implements the idea that
  neutrino masses, leptogenesis and the deviation in a_μ all originate from dark matter
  particles. In the latter model, new leptons and scalar particles are predicted, and
  a_μ provides significant constraints on the masses and Yukawa couplings of the new
  particles.

The following types of new physics scenarios are quite different from the ones above:
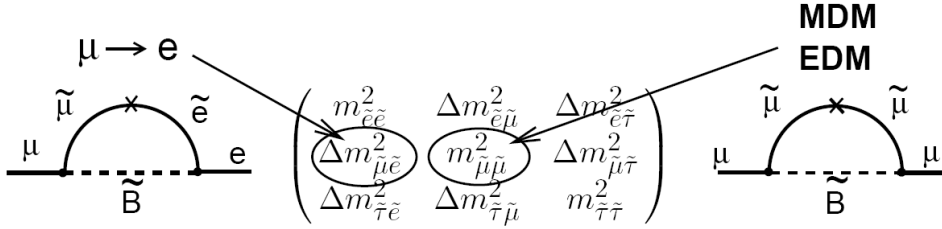
Figure 2.16: The supersymmetric contributions to the anomaly, and to $\mu \to e$ conversion, showing the relevant slepton mixing matrix elements. The MDM and EDM give the real and imaginary parts of the matrix element, respectively. The $\times$ indicates a chirality flip. `fg:susy`

- Models with extended Higgs sector but without enhanced Yukawa couplings: Among these models are the usual two-Higgs-doublet models or the Shadow Higgs scenario `lltan:2009xn` of Ref. [123]. The contribution of such models to a_μ is suppressed by two additional powers of the muon Yukawa coupling, corresponding to $a_\mu(\text{N.P.}) \propto m_\mu^4/\Lambda^4$ at the one-loop level. Two-loop effects from Barr-Zee diagrams can be larger, but typically the contributions to a_μ are negligible in these models.

- Models with additional light particles with masses below the GeV-scale: examples are provided by the secluded U(1) model of Ref. [124] `Pospelov:2008zw` or the more general models discussed in Ref. [125], `Essig:2009nc` where additional light neutral gauge bosons can affect electromagnetic interactions. These models are difficult to study at the LHC, but they can lead to contributions to a_μ which are of the same order as the deviation in Eq. (2.48). `eq:Delta` Hence the new $g-2$ measurement will provide an important test of such models.

To summarize: many well-motivated models can accomodate larger contributions to a_μ — if any of these are realized $g-2$ can be used to constrain model parameters; many well-motivated new physics models give tiny contributions to a_μ and would be disfavored if the more precise $g-2$ measurement confirms the deviation in Eq. (2.48). `eq:Delta` There are also examples of models which lead to similar LHC signatures but which can be distinguished using $g-2$.

In the following we discuss in more detail how a_μ will be useful in understanding TeV-scale physics in the event that the LHC established the existence of physics beyond the standard model [126]. `PhysicsCaseWP`

a_μ as a benchmark for models of new physics

It has been established that the LHC is sensitive to virtually all proposed weak-scale extensions of the standard model, ranging from supersymmetry (SUSY), extra dimensions and technicolor to little Higgs models, unparticle physics, hidden sector models and others. However, even if the existence of physics beyond the standard model is established, it will be far from easy for the LHC alone to identify which of these — or not yet thought of — alternatives is realized. Typically LHC data will be consistent with several alternative models. The measurement of a_μ to 16×10^{-11} will be highly valuable in this respect since it will provide a benchmark and stringent selection criterion that can be imposed on any model that is tested at the LHC.

For example, a situation is possible where the LHC finds many new heavy particles which are compatible with both minimal-supersymmetric and universal-extra-dimension model predictions [127], or both minimal-supersymmetric and and Littlest Higgs model predictions [112]. The muon $g-2$ would especially aid in the selection since UED or Littlest Higgs models predict a tiny effect to a_μ, while SUSY effects are usually much larger.

On the other hand, a situation where the LHC finds no physics beyond the standard model but the a_μ measurement establishes a deviation, might be a signal for models such as the secluded U(1) model, with new light particles, or for unparticle physics effects, which are hard to identify at the LHC.

Next consider the situation that extra dimensions are realized in the form of a Randall-Sundrum or ADD model. In that case, the a_μ measurement will not only help to constrain model parameters. Since the a_μ predictions in these models strongly depend on the details of the physics of the extra dimensions, the a_μ measurement will also help to identify and test these details.

Within the framework of SUSY there are many different well-motivated scenarios that are not always easy to distinguish at the LHC. Fig. 2.17 shows a graphical distribution of the 10 Snowmass Points and Slopes model benchmark predictions [128] for a_μ(SUSY). They range considerably and can be positive and negative, due to the factor sgn(μ) in Eq. 2.54, where this sign would be particularly difficult to determine at LHC, even if SUSY were to be discovered. The discriminating power of an improved $g-2$ measurement—even if the actual value of Δa_μ turned out to be smaller—is evident from Fig. 2.17.

(a)   (b)
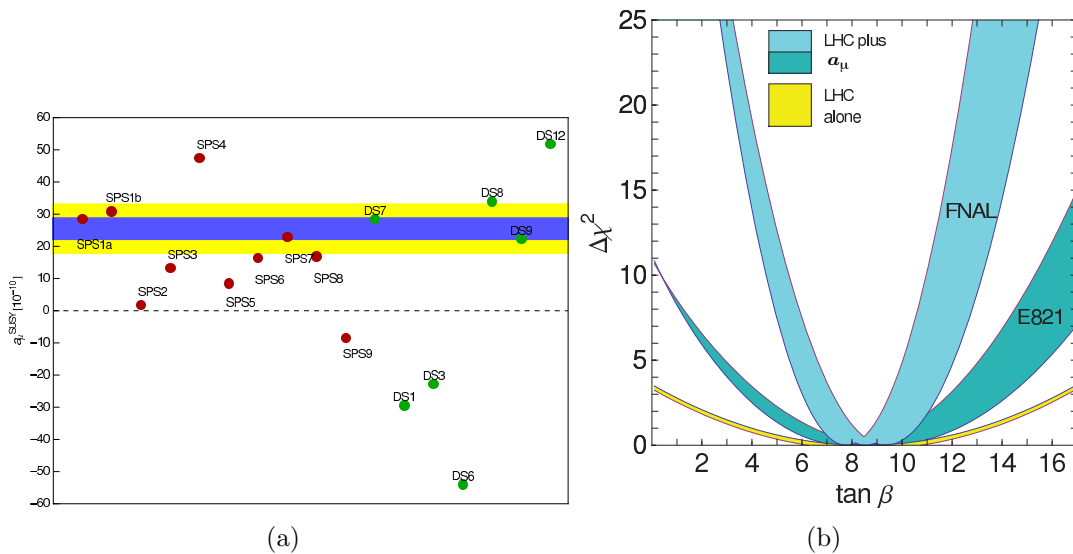
Figure 2.17: (a) SUSY contributions to a_μ for the SPS benchmark points (red), and for the "degenerate solutions" from Ref. [107]. (b) Possible future $\tan\beta$ determination assuming that a slightly modified MSSM point SPS1a (see text) is realized. The bands show the $\Delta\chi^2$ parabolas from LHC-data alone (yellow) [134], including the a_μ with current precision (dark blue) and with prospective precision (light blue). The width of the blue curves results from the expected LHC-uncertainty of the parameters (mainly smuon and chargino masses) [134].

A final example concerns the restriction of special, highly constrained models of new physics such as the constrained MSSM (CMSSM). The CMSSM has only four free continuous parameters. One precise measurement such as the future determination of Δa_μ effectively fixes one parameter as a function of the others and thus reduces the number of free parameters by one. A large number of recent analyses have made use of this feature, see e.g. Refs. [T29]. In fact, the CMSSM is very sensitive not only to the a_μ but also to the dark matter (which in this model is assumed to consist of neutralinos) relic density. As shown in Fig. 2.18, both observables lead to orthogonal constraints in CMSSM parameter space, and therefore imposing both constraints leaves only two free parameters and thus allows for very stringent tests of the CMSSM at the LHC. From Fig. 2.18(a) we see that in this model, there is little room left for $\tan\beta = 10$.

a_μ is sensitive to quantities that are difficult to measure at the LHC

For unraveling the mysteries of TeV-scale physics it is not sufficient to determine which type of new physics is realized, but it is necessary to determine model parameters as precisely as possible. Here the complementarity between the LHC and precision experiments such as a_μ becomes particularly important. A difficulty at the LHC is the indirect relation between LHC observables (cross sections, mass spectra, edges, etc) and model parameters such as masses and couplings, let alone more underlying parameters such as supersymmetry-breaking parameters or the μ-parameter in the MSSM. Generally, the LHC Inverse problem [T31] states that several different points in the supersymmetry parameter space can give rise to indistinguishable LHC signatures. It has been shown that a promising strategy is to determine the model parameters by performing a global fit of a model such as the MSSM to all available LHC data. However, recent investigations have revealed that in this way typically a multitude of almost degenerate local minima of χ^2 as a function of the model parameters results [132]. Independent observables such as the ones available at the proposed International Linear Collider [133] or a_μ will be highly valuable to break such degeneracies, and in this way to unambiguously determine the model parameters.

In the following we provide further examples for the complementarity of LHC and a_μ for the well-studied case of the MSSM. Two central parameters which are related to electroweak symmetry breaking are the μ-parameter and $\tan\beta$, the ratio of the two Higgs vacuum expectation values. According to Eq. 2.54 the MSSM contributions to a_μ are highly sensitive to both $\text{sign}(\mu)$ and $\tan\beta$. Therefore, a future improved a_μ measurement has the potential to establish a definite positive or negative sign of the μ-parameter in the MSSM, which would be a crucial piece of information. The LHC has a weaker and less direct sensitivity to these two parameters. Combining LHC measurements with a_μ can lead to a good determination of $\tan\beta$.

One should note that even if better ways to determine $\tan\beta$ at the LHC alone might be found, an independent determination using a_μ will still be highly valuable, as $\tan\beta$ is one of the central MSSM parameters; it appears in all sectors and in almost all observables. In non-minimal SUSY models the relation between $\tan\beta$ and different observables can be modified. Therefore, measuring $\tan\beta$ in different ways, e.g. using certain Higgs- or b-decays at the LHC or at b-factories and using a_μ, would constitute a non-trivial and indispensable test of the universality of $\tan\beta$ and thus of the structure of the MSSM.
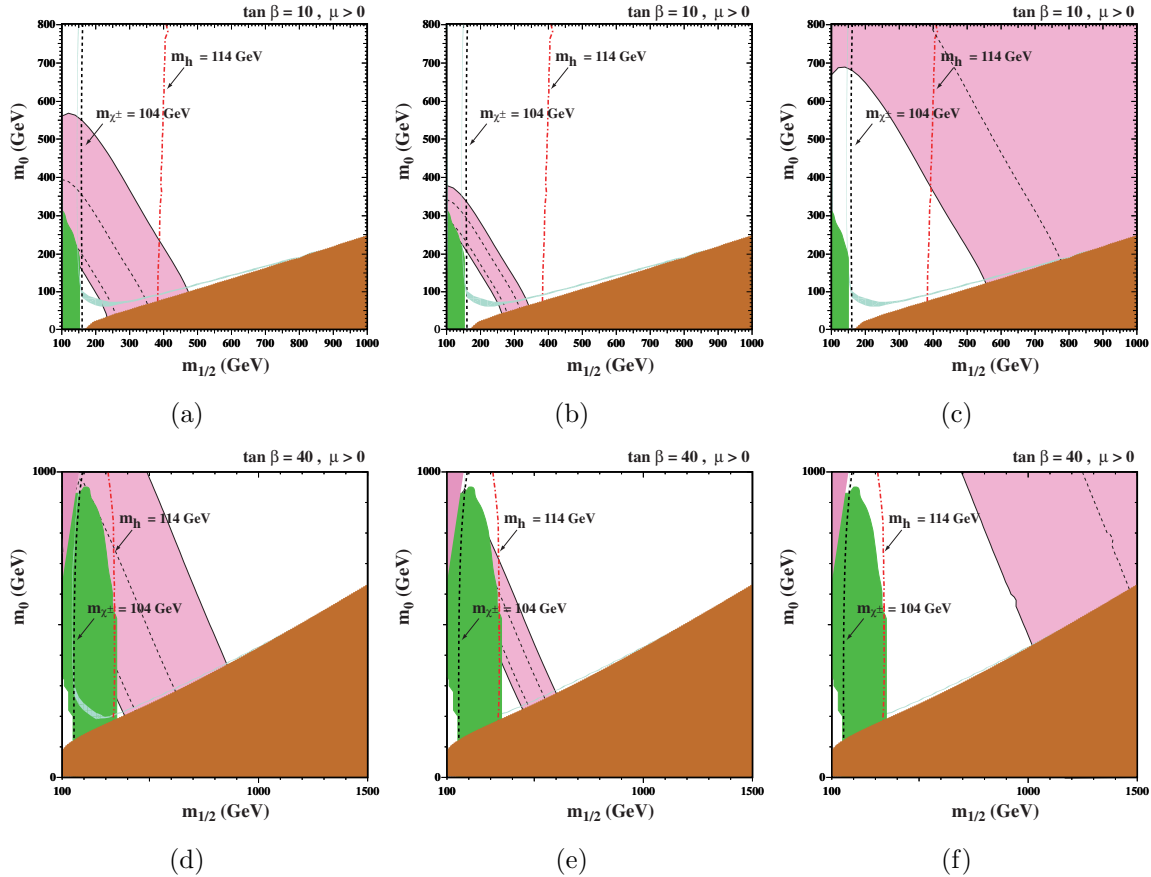
Figure 2.18: The m_0(scalar mass)–$m_{1/2}$(gaugino mass) plane of the CMSSM parameter space for $\tan\beta = (10; 40)$, $A_0 = 0$, $\text{sgn}(\mu) = +$:

(a;d) The $\Delta a^{(\text{today})} = 255(80) \times 10^{-11}$ between experiment and standard-model theory is from Ref. [108]. The brown wedge on the lower right is excluded by the requirement the dark matter be neutral. Direct limits on the Higgs and chargino $\chi^{\pm}$ masses are indicated by vertical lines, with the region to the left excluded. Restrictions from the WMAP satellite data are shown as a light-blue line. The $(g-2)$ 1 and 2-standard deviation boundaries are shown in purple. The green region is excluded by $b \to s\gamma$. (b;e) The plot with $\Delta a_\mu = 255(34) \times 10^{-11}$. (c;f) The same errors as (b), but $\Delta a_\mu = 0$. (Figures courtesy of K. Olive, following Ref. [130])

In the event that SUSY is discovered, we give an illustration of a $\tan\beta$ measurement and consider a case similar to the one discussed in Ref. [132]. We assume that the deviation $\Delta a_\mu = 255 \times 10^{-11}$ is real and that an MSSM parameter point SPS1a* is realized, where SPS1a* is defined in the same way as SPS1a [128] except that $\tan\beta = 8.5$. With this assumption, the comprehensive LHC-analysis of [132] for SPS1a can be taken over, and the LHC would find many SUSY particles and measure many SUSY parameters rather well. Only $\tan\beta$ can be determined rather poorly with an uncertainty of ± 4.5. In such a situation one can study the MSSM prediction for a_μ as a function of $\tan\beta$ (all other parameters are known from the global fit to LHC data) and compare it to the measured value, in particular after

an improved measurement. As can be seen from Fig. 2.19, using today's value for a_μ would
improve the determination of $\tan\beta$, but the improvement will be even more impressive after
a future more precise a_μ measurement. Should such a scenario unfold, as the SUSY masses
become better measured, the measure of $\tan\beta$ from a_μ would improve further. A similar but
more comprehensive study in [134], where a_μ has been incorporated into the global fit and
error correlations can be controlled better, confirms this role of a_μ as an excellent observable
to measure $\tan\beta$. In Ref. [134], the precision of $\tan\beta$ increases by a factor two already if
today's a_μ is included in the fit, so a 3–4-fold improvement can be expected if LHC-data is
combined with the future a_μ measurement.
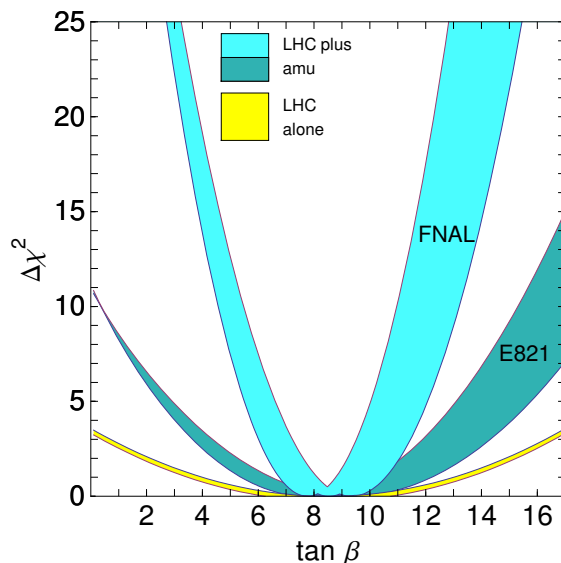
Figure 2.19: Possible future $\tan\beta$ determination from the measurement of a_μ, assuming that
the MSSM point SPS1a* (see text) is realized. The yellow band is from LHC alone which
gives $\tan\beta^{\text{LHC fit}} = 8.5 \pm 4.5$, taking over the SPS1a analysis of Refs. [132, 134]. The darker
blue band labelled E821 assumes $\Delta a_\mu = (255 \pm 80) \times 10^{-11}$, which comes from the present
values for a_μ and the Standard-Model contribution, the lighter blue band labelled FNAL
corresponds to $\Delta a_\mu^{\text{future}} = (255 \pm 34) \times 10^{-11}$. The blue bands show $\Delta\chi^2 = \left(\frac{a_\mu^{MSSM}(\tan\beta) - a_\mu^{\text{exp}}}{\{80; 34\} \times 10^{-11}} \right)^2$
as a function of $\tan\beta$, where in $a_\mu^{\text{MSSM}}(\tan\beta)$ all parameters except $\tan\beta$ have been set to
the values determined at the LHC. The width of the blue curves results from the expected
LHC-uncertainty of the parameters (mainly smuon masses and M_2, μ) [134]. The plot shows
that the precision for $\tan\beta$ that can be obtained using a_μ is limited by the precision of
the other input parameters but is still much better than the determination using LHC data
alone.

At the 2007 Glasgow $g-2$ Workshop [54], Martin and Wells presented an update of their
so-called "superconservative analysis" [136], where a very conservative 5σ band around the
observed difference Eq. (2.48) and the general supersymmetric standard model are consid-
ered. Surprisingly, it could be shown that even this mild assumption leads to regions of

parameter space which are excluded by $g-2$ and nothing else. Hence, $g-2$ provides complementary information to collider, dark matter, or other low-energy observables. An improved $g-2$ measurement will be very useful—independent of the actual numerical result.

In a similar spirit, Berger, Gainer, Hewett and Rizzo [137] discussed "supersymmetry without prejudice." First a large set of supersymmetry parameter points ("models") in a 19-dimensional parameter space was identified, which was in agreement with many important existing experimental and theoretical constraints. Then the implications for observables such as $g-2$ were studied. The result for $g-2$ was rather similar to Fig. 2.17, although the context was far more general: the entire range $a_\mu^{\mathrm{SUSY}} \sim (-100 \ldots +300) \times 10^{-11}$ was populated by a reasonable number of "models." Therefore, a precise measurement of $g-2$ to $\pm 16 \times 10^{-11}$ will be a crucial way to rule out a large fraction of models and thus determine supersymmetry parameters.

The anomalous magnetic moment of the muon is sensitive to contributions from a wide range of physics beyond the standard model. It will continue to place stringent restrictions on all of the models, both present and yet to be written down. Assuming that we will be so fortunate as to discover new phenomena in the LHC era, a_μ will constitute an indispensable tool to discriminate between very different types of new physics, especially since it is highly sensitive to parameters which are difficult to measure at the LHC. If we are unfortunate, then it represents one of the few ways to probe physics beyond the standard model. In either case, it will play an essential and complementary role in the quest to understand physics beyond the standard model at the TeV scale. This prospect is what motivates our collaboration to push forward with a new measurement.

References

[ern-Gerlach] [1] O. Stern, Z. Phys. **7**, 249 (1921);

[Gerlach22] [2] W. Gerlach and O. Stern, , Z. Phys. **8**, 110 (1922); Z. Phys. **9** and 349(1922), Z. Phys. **9**, 353 (1924); W. Gerlach and O. Stern, Ann. Phys. **74**, 673 (1924).

[UG25] [3] G.E. Uhlenbeck and S. Goudsmit, Naturwissenschaften **47**, 953 (1925); G.E. Uhlenbeck and S. Goudsmit, Nature **117** (1926) 264.

[rodinger-26] [4] E. Schrödinger, Ann. Phys. **79** (1926) 361.

[Thomas26] [5] L.H. Thomas, Nature **117**, (1926) 514 and Phil. Mag. **3** (1927) 1.

[phipps27] [6] T.E. Phipps and J.B. Taylor, Phys. Rev. **29**, 309 (1927).

[Dirac28] [7] P.A.M. Dirac, Proc. R. Soc. (London) **A117**, 610 (1928), and **A118**, 351 (1928). See also, P.A.M. Dirac, *The Principles of Quantum Mechanics*, 4th edition, Oxford University Press, London, 1958.

[Tomonaga] [8] Sin-itiro Tomonaga, *The Story of Spin*, translated by Takeshi Oka, U. Chicago Press, 1997.

[sternp] [9] R. Frisch and O. Stern, Z. Phys. **85**, 4 (1933), and I. Estermann and O. Stern, Z. Phys. **85**, 17 (1933).

[nmdm] [10] Luis W. Alvarez and F. Bloch, Phys. Rev. **57**, 111 (1940).

[nafe] [11] J.E. Nafe, E.B. Nelson and I.I. Rabi Phys. Rev. **71**, 914(1947).

[nagel] [12] D.E. Nagel, R.S. Julian and J.R. Zacharias, Phys. Rev. **72**, 971 (1947).

[kf1] [13] P. Kusch and H.M Foley, Phys. Rev **72**, 1256 (1947).

[winger:1948] [14] J. Schwinger, Phys. Rev. **73**, 416L (1948), and Phys. Rev. **76** 790 (1949). The former paper contains a misprint in the expression for a_e that is corrected in the longer paper.

[Bethe57] [15] Hans A. Bethe and Edwin E. Salpeter, *Quantum Mechanics of One- and Two-Electron Atoms*, Springer-Verlag, (1957), p. 51.

[kunze] [16] See Figure 5 in Paul Kunze, Z. Phys. **83**, 1 (1933).

`Ned` [17] Carl D. Anderson and Seth H. Neddermeyer, Phys. Rev. **50** (1936) 263, and Seth H. Neddermeyer and Carl D. Anderson, Phys. Rev. **51** (1937) 844.

`Street` [18] J.C. Street, E.C. Stevenson, Phys. Rev. **52** (1937) 1003.

`Nishina` [19] Y. Nishina, M. Tekeuchi and T. Ichimiya, Phys. Rev. **52** (1937) 1198.

`Crussard` [20] M.M. Jean Crussard and L. Leprince-Ringuet, Compt. Rend. **204** (1937) 240.

`Garwin57` [21] Garwin RL, Lederman LM, Weinrich M, Phys. Rev. 105:1415 (1957)

`Friedman57` [22] J.I. Friedman and V.L. Telegdi, Phys. Rev. **105**, 1681 (1957).

`onopinski59` [23] E.J. Konopinski, Ann. Rev. Nucl. Sci. **9** 99, (1959).

`Garwin60` [24] Garwin RL, Hutchinson DP, Penman S, Shapiro G, Phys. Rev. 118:271 (1960)

`Charpak61` [25] Charpak G, et al. Phys. Rev. Lett. 6:28 (1961), Nuovo Cimento. 22:1043 (1961), Phys. Lett. 1:16 (1962), Nuovo Cimento. 37:1241 (1965) and Charpak G. et al. Phys. Lett. 1:16 (1962)

`cern2` [26] Bailey J, et al. Phys. Lett. 28B:287 (1968). Additional details can be found in Bailey J, et al. Nuovo Cimento. A9:369 (1972) and references therein.

`Bailey79` [27] Bailey J, et al. Nucl. Phys. B150:1 (1979)

`purcell50` [28] E.M. Purcell and N.F. Ramsey, Phys. Rev. **78**, 807 (1950).

`Lee-56i` [29] T.D. Lee and C.N. Yang, Phys. Rev. **104** (1956) 254.

`smith57` [30] J.H. Smith, E.M. Purcell and N.F. Ramsey, Phys. Rev. **108**, 120 (1957).

`landau57` [31] L. Landau, Nucl. Phys. **3**, 127 (1957).

`ramsey58` [32] N.F. Ramsey Phys. Rev. **109**, 225 (1958).

`iffith:2009` [33] W.C. Griffith, et al., Phys. Rev. Lett. **102**, 101601 (2009).

`Baker:2006` [34] C.A. Baker, et al., Phys. Rev. Lett. **97**, 131801 (2006).

`Hudson:2011` [35] J.J. Hudson, et al., Nature **473**, 493 (2011).

`ennett:2009` [36] G.W. Bennett, et al., Phys. Rev. **D 80**, 052008 (2009).

`Bargmann59` [37] Bargmann V, Michel L, Telegdi VL, Phys. Rev. Lett. 2:435 (1959)

`nett:2004xx` [38] Bennett GW, et al. (The $g - 2$ Collab.) Phys. Rev. Lett. 92:161802 (2004)

`ennett:2006` [39] Bennett GW, et al.(The $g - 2$ Collab.) Phys. Rev. D, 73:072003 (2006)

`Wu57` [40] C.S. Wu, E. Ambler, R.W. Hayward, D.D. Hoppes, R.P. Hudson, Phys. Rev. **105**, 1413 (1957).

`nmr` [41] Prigl R *et al.*, *Nucl. Inst. Methods Phys. Res.* A374:118 (1996)

`fei` [42] Fei X, Hughes V, Prigl R, *Nucl. Inst. Methods Phys. Res.* A394:349 (1997)

`abragam` [43] Abragam A. In *Principles of Nuclear Magnetism'*, p. 173-178. Oxford U. Press, (1961)

`mohr-mu` [44] Mohr PJ, Taylor BH, *Rev. Mod. Phys.* 77:1 (2005)

`phillips` [45] Phillips WD, et al. *Metrologia* 13:179 (1979)

`winkler` [46] Winkler PF, Kleppner D, Myint T, Walther FG, *Phys. Rev.* A5:83 (1972)

`lamb41` [47] Lamb Jr. WE. *Phys. Rev.* 60:817 (1941)

`grotch` [48] Grotch H, Hegstrom RA. *Phys. Rev.* A4:59 (1971)

`Petley-1984` [49] B.W. Petley et al. *Metrologia.***20**, 81 (1984)

`lowers-1993` [50] J.L. Flowers, B.W. Petley and M.G. Richards, Metrologia **30**, 75 (1993).

`CODATA08` [51] Mohr PJ, Taylor BN, Newell DB, (CODATA recommended values). *Rev. Mod. Phys.* 80:633 (2008)

`Miller:07` [52] James P. Miller, Eduardo de Rafael and B. Lee Roberts, Rept. Prog. Phys. **70**, 795-881, 2007.

`Liu` [53] W. Liu et al., Phys. Rev. Lett. **82**, 711 (1999).

`gowworkshop` [54] Topical Workshop on The Muon Magnetic Dipole Moment; Oct. 2007 School of Physics and Astronomy, The University of Glasgow. See: www.ippp.dur.ac.uk/old/MuonMDM/.

`kinmar` [55] T. Kinoshita and W.J. Marciano in *Quantum Electrodynamics* (Directions in High Energy Physics, Vol. 7), ed. T. Kinoshita, (World Scientific, Singapore, 1990), p. 419.

`czmar` [56] Andrzej Czarnecki and William J. Marciano, Phys. Rev. **D64** 013014 (2001).

`Davier11` [57] Davier M, et al.M. Davier1, A. Hoecker2,a, B. Malaescu1,b, Z. Zhang1 Eur. Phys. J. C 71:1515 (2011), erratum Eur. Phys. J. C 72:1874 (2012).

`giwara:2011` [58] Koru Hagiwara, Ruofan Liao, Alan D. Martin, Daisuke Nomura and Thomas Teubner, J. Phys. G**38**, 085003 (2011).

`Feng:2011` [59] Xu Feng, Karl Jansen, Marcus Perschlies and Dru B. Renner, Phys. Rev. Lett. 107 081802 (2011).

`arey:1999dd` [60] The $g - 2$ Collaboration: R.M. Carey et al., Phys. Rev. Lett. **82**, 1632 (1999).

`rown:2000sj` [61] The $g - 2$ Collaboration: H.N. Brown et al., Phys. Rev. D **62**, 091101 (2000).

`rown:2001mg` [62] The $g - 2$ Collaboration: H.N. Brown et al., Phys. Rev. Lett. **86**, 2227 (2001).

`nett:2002jb` [63] The $g - 2$ Collaboration: G.W. Bennett et al., Phys. Rev. Lett. **89**, 101804 (2002); Erratum-ibid. **89**, 129903 (2002).

`CKM96` [64] A. Czarnecki, B. Krause and W.J. Marciano, Phys. Rev. Lett. **76** (1996) 3267.

`PPdR95` [65] S. Peris, M. Perrottet and E. de Rafael, Phys. Lett. **B355** (1995) 523.

`CKM95` [66] A. Czarnecki, B. Krause and W. Marciano, Phys. Rev. **D52** (1995) R2619.

`CMV03` [67] A. Czarnecki, W.J. Marciano and A. Vainshtein, Phys. Rev. **D67** (2003) 073006. A. Czarnecki, W.J. Marciano and A. Vainshtein, Phys. Rev. **D67** (2003) 073006.

`CM-LM` [68] Andzrej Czarnecki and William J. Marciano in *Lepton Dipole Moments*, ed. B. Lee Roberts and William J. Marciano, Advanced Series on Directions in High Energy Physics, Vol. 20, World Scientific, 2010 p. 11 and references therin.

`Miller2010` [69] Miller JP, Roberts BL, Jungmann K. *Lepton Dipole Moments*, ed Roberts BL, Marciano WJ, p.333. World Scientific (2010)

`Prades:2010` [70] Prades J, Rafael E. de, Vainshtein A. *Lepton Dipole Moments*, ed Roberts BL, Marciano WJ, World Scientific (2010), p.303; and arXiv:0901.0306v1 [hep-ph].

`INT:2011` [71] http://www.int.washington.edu/PROGRAMS/11-47w/

`ckinger2010` [72] Stöckinger D. *Lepton Dipole Moments*, ed Roberts BL, Marciano WJ, p.393. World Scientific (2010)

`dsreview` [73] Stöckinger D, *J. Phys.G G* 34:R45 (2007)

`EdRpc2010` [74] Eduardo de Rafael, private communication.

`KLOE-2` [75] G. Amelino-Camelia, et al., (KLOE-2 Collaboration) arXiv:1003.3868v1 [hep-ex] March 2010.

`Goecke:2011` [76] Tobias Goecke, Christian S. Fischer, Richard Williams Phys. Rev. **D83**, 094006 (2011).

`fischer-pc` [77] C. Fischer, private communication, October 2012.

`Blum:2012` [78] . Tom Blum, The 12th International Workshop on Tau Lepton Physics, 17-21 September 2012,Nagoya University.

`oyama1:2012` [79] Tatsumi Aoyama, Masashi Hayakawa, Toichiro Kinoshita, Makiko Nio. May 2012. May 2012, arXiv:1205.5370 [hep-ph], Phys. Rev. Lett. **109**, 111808 (2012).

`Hanneke08` [80] D. Hanneke, S. Fogwell and G. Gabrielse, Phys. Rev. Lett. 100, 120801 (2008).

`oyama2:2012` [81] rTatsumi Aoyama, Masashi Hayakawa, Toichiro Kinoshita, Makiko Nio. May 2012, e-Print: arXiv:1205.5368 [hep-ph], Phys. Rev. Lett. **109**, 111807 (2012).

`endira:2011` [82] R. Bouchendira, P. Clade, S. Guellati-Khelifa, F. Nez, and F. Biraben, Phys. Rev. Lett. 106, 080801 (2011).

`pdg-HM2009` [83] A. Höcker and W.J. Marciano, Particle Data Group, Review *THE MUON ANOMA-LOUS MAGNETIC MOMENT* Updated July 2009, http://pdg.lbl.gov/

`Passera08` [84] M. Passera, W.J. Marciano and A. Sirlin, Phys. Rev. **D 78**, 013009 (2008).

`HMNT07` [85] K. Hagiwara, A.D. Martin, D. Nomura and T. Teubner, Phys. Lett. **B649** 173 (2007).

`Davier07` [86] M. Davier, hep-ph/0701163v2, Jan. 2007.

`lehner:2009` [87] Fred Jegerlehner and Andreas Nyffeler, Phys.Rept. **477** 1 ((2009)

`Miller:2012` [88] James P. Miller, Eduardo de Rafael, B. Lee Roberts and Dominik Stöckinger, Ann. Rev. Nucl. Part. Sci. 62, 237 (2012).

`adh` [89] R. Alemany, M. Davier and A. Höcker, Eur.Phys.J. **C2** 123 (1998).

`lehner:2011` [90] Fred Jegerlehner, Robert Szafron, Eur.Phys.J. C71 (2011) 1632.

`ayoun:2012a` [91] M. Benayoun, P. David, L. DelBuono, F. Jegerlehner, Eur. Phys. J. **C72** (2012) 1848.

`ayoun:2012b` [92] M. Benayoun, P. David, L. DelBuono, F. Jegerlehner, arXiv:1210.7184v2 [hep-ph] 9 Nov 2012.

`dh98` [93] M. Davier and A. Höcker, Phys. Lett.**B435**, 427 (1998).

`phokhara` [94] S. Binner, J.H. Kühn and K. Melnikov, Phys. Lett. **B 459**, 279 (1999).

`radiomc` [95] S. Actis, et al., (Working Group on Radiative Corrections and Monte Carlo Generators for Low Energies), arXiv0912.0749, Dec. 2009, submitted to Eur. Phys. J. **C**.

`BaBar09` [96] BABAR Collaboration, B. Aubert et al., Phys. Rev. Lett. 103:231801 (2009).

`tau08-12` [97] http://tau08.inp.nsk.su/ ; http://www.hep.manchester.ac.uk/TAU2010 ; http://tau2012.hepl.phys.nagoya-u.ac.jp/

`PHIPSI` [98] http://phipsi11.inp.nsk.su/

`rosino:2009` [99] F. Ambrosino et al., (KLOE Collaboration), Phys. Lett. **B 670**, 285 (2009).

`rosino:2011` [100] F. Ambrosino et al., (KLOE Collaboration), Phys. Lett. **B 700**, 102 (2011).

`LOE-Tau2012` [101] Giuseppe Mandaglio, The 12th International Workshop on Tau Lepton Physics, 17-21 September 2012,Nagoya University.

`Crnkovic` [102] Jason Crnkovic, The 12th International Workshop on Tau Lepton Physics, 17-21 September 2012,Nagoya University.

`blum` [103] T. Blum, Phys. Rev. Lett. **91**, 052001-1 (2003).

`blum2` [104] T. Blum, Nucl. Phys. Proc. Suppl. **129**, 904-906,2004, and arXiv hep-lat/0310064,

`blumpc` [105] T. Blum, private communication, February 2012.

`Davier:04` [106] M. Davier and W.J. Marciano, Ann. Rev. Nucl. Part. Phys. **54**, 115 (2004).

`Adam:2010uz` [107] Adam C, Kneur J -L, Lafaye R, Plehn T, Rauch M, Zerwas D. *Eur. Phys. J. C* 71:1520 (2011)

`Rafael:2008` [108] Eduardo de Rafael *Present Status of the Muon Anomalous Magnetic Moment*; To appear in the proceedings of 14th High-Energy Physics International Conference in Quantum Chromodynamics (QCD 08), Montpellier, France, 7-12 Jul 2008. e-Print: arXiv:0809.3085.

`ed` [109] The articles listed in the SPIRES citations to Ref. [62] contain many different models beyond the standard model.

`elp` [110] E. Eichten, et al., Phys. Rev. Lett. **45**, 225 (1980), K. Lane, arXiv hep-ph/0102131, 2001.

`AppelqDob` [111] T. Appelquist and B. A. Dobrescu, "Universal extra dimensions and the muon magnetic moment," Phys. Lett. B **516** (2001) 85 [arXiv:hep-ph/0106140].

`anke:2007db` [112] M. Blanke, A. J. Buras, B. Duling, A. Poschenrieder and C. Tarantino, JHEP **0705** (2007) 013 [arXiv:hep-ph/0702136].

`rlehnerBook` [113] Friedrich Jegerlehner, The Anomalous Magnetic Moment of the Muon, Springer Tracts in Modern Physics Vol. 226.

`iasl:2000my` [114] H. Davoudiasl, J. L. Hewett and T. G. Rizzo, Phys. Lett. B **493** (2000) 135 [arXiv:hep-ph/0006097].

`Park:2001uc` [115] S. C. Park and H. S. Song, Phys. Lett. B **506** (2001) 99 [arXiv:hep-ph/0103072].

`Kim:2001rc` [116] C. S. Kim, J. D. Kim and J. H. Song, Phys. Lett. B **511** (2001) 251 [arXiv:hep-ph/0103127].

`sser:1999yg` [117] M. L. Graesser, Phys. Rev. D **61** (2000) 074019 [arXiv:hep-ph/9902310].

`ung:2007zza` [118] K. Cheung, W. Y. Keung and T. C. Yuan, Phys. Rev. Lett. **99** (2007) 051803 [arXiv:0704.2588 [hep-ph]].

`nley:2008jg` [119] J. A. Conley and J. S. Gainer, arXiv:0811.4168 [hep-ph].

`Keen:2009ny` [120] D. McKeen, arXiv:0912.1076 [hep-ph].

`Ho:2010yp` [121] C. M. Ho and T. W. Kephart, arXiv:1001.3696 [hep-ph].

`mbye:2006zn` [122] T. Hambye, K. Kannike, E. Ma and M. Raidal, Phys. Rev. D **75** (2007) 095003 [arXiv:hep-ph/0609228].

`ltan:2009xn` [123] E. O. Iltan, arXiv:0901.0544 [hep-ph].

`elov:2008zw` [124] M. Pospelov, Phys. Rev. D **80** (2009) 095002 [arXiv:0811.1030 [hep-ph]].

ssig:2009nc [125] R. Essig, P. Schuster and N. Toro, Phys. Rev. D **80** (2009) 015003 [arXiv:0903.3941 [hep-ph]].

ysicsCaseWP [126] D. W. Hertzog, J. P. Miller, E. de Rafael, B. Lee Roberts and D. Stöckinger, arXiv:0705.4617 [hep-ph].

illieWebber [127] J. M. Smillie and B. R. Webber, JHEP **0510** (2005) 069 [arXiv:hep-ph/0507170].

SPS [128] B. C. Allanach *et al.*, *Proc. of the APS/DPF/DPB Summer Study on the Future of Particle Physics (Snowmass 2001)* ed. N. Graf, Eur. Phys. J. C **25** (2002) 113 [eConf **C010630** (2001) P125].

cmssm [129] R. Ruiz de Austri, R. Trotta and L. Roszkowski, JHEP **0605** (2006) 002 [arXiv:hep-ph/0602028]; JHEP **0704** (2007) 084 [arXiv:hep-ph/0611173]; JHEP **0707** (2007) 075 [arXiv:0705.2012]; B. C. Allanach, C. G. Lester and A. M. Weber, JHEP **0612** (2006) 065; B. C. Allanach, K. Cranmer, C. G. Lester and A. M. Weber, JHEP **0708**, 023 (2007); J. R. Ellis, S. Heinemeyer, K. A. Olive, A. M. Weber and G. Weiglein, JHEP **0708** (2007) 083; S. Heinemeyer, X. Miao, S. Su and G. Weiglein, JHEP **0808**, 087 (2008).

olive [130] J. R. Ellis, K. A. Olive, Y. Santoso and V. C. Spanos, Phys. Lett. **B 565** 176 (2003); John Ellis, Keith A. Olive, Yudi Santoso, and Vassilis C. Spanos, Phys. Rev. **D71** 095007 (2005), and references therein.

AKTW [131] N. Arkani-Hamed, G. L. Kane, J. Thaler and L. T. Wang, JHEP **0608**, 070 (2006) [arXiv:hep-ph/0512190].

Sfitter [132] R. Lafaye, T. Plehn, M. Rauch and D. Zerwas, arXiv:0709.3985 [hep-ph].

BGHLR [133] C. F. Berger, J. S. Gainer, J. L. Hewett, B. Lillie and T. G. Rizzo, arXiv:0712.2965 [hep-ph].

ehnRauchNew [134] M. Alexander, S. Kreiss, R. Lafaye, T. Plehn, M. Rauch, and D. Zerwas, Chapter 9 in M. M. Nojiri *et al.*, arXiv:0802.3672 [hep-ph].

RossSerna [135] G. Ross and M. Serna, arXiv:0704.1248 [hep-ph].

onservative [136] S. P. Martin and J. D. Wells, Phys. Rev. D **67**, 015002 (2003) [arXiv:hep-ph/0209309].

Hewett [137] C. F. Berger, J. S. Gainer, J. L. Hewett and T. G. Rizzo, arXiv:0812.0980 [hep-ph].

Chapter 3

Design Methodology for the New Experiment

ch:design

3.1 Lessons from E821

3.2 Requirements for E989

3.3 Simulation Tools

Chapter 4

Accelerator and Muon Delivery

In order to achieve a statistical uncertainty of 0.1 ppm, the total $(g-2)$ data set must contain at least 1.8×10^{11} detected positrons with energy greater than 1.8 GeV, and arrival time greater than 30 μs after injection into the storage ring. This is expected to require 4×10^{20} protons on target including commissioning time and systematic studies. For optimal detector performance, the number of protons in a single pulse to the target should be no more than 10^{12} and the number/fraction(?) of secondary protons transported into the muon storage ring should be less than ??. Data acquisition limits the time between pulses to be at least 10 ms. The revolution time of muons around the storage ring is 149 ns, and therefore the experiment requires the bunch length to be no more than $\sim$100 ns. Systematic effects on muon polarization limit the momentum spread dp/p of the secondary beam. Requirements and general accelerator parameters are given in Table 4.1.

Parameter	Design Value	Requirement	Unit
Total protons on target	2.3×10^{20}/year	4×10^{20}	protons
Interval between beam pulses	≥ 10	≥ 10	ms
Max bunch length (full width)	120 (95%)	< 149	ns
Intensity of single pulse on target	10^{12}	10^{12}	protons
Max Pulse to Pulse intensity variation	± 10	± 50	%
dp/p of pions accepted in decay line	2-5	2	%
Momentum of muon beam	3.094	3.094	GeV/c
Stored muons per 10^{12} proton on target	10^5 into inflector	≥ 6000	muons
dp/p of muons into ring	0.5	0.5	%
Fraction of beam into ring which is protons	1??	< 10??	%

Table 4.1: General beam requirements and design parameters. tb:genaccelreq

4.1 Overall Strategy

The $(g - 2)$ experiment at Fermilab is designed to take advantage of the infrastructure of the former Antiproton Source, as well as improvements to the Proton Source and the

conversion of the Recycler to a proton-delivery machine. It is also designed to share as much infrastructure as possible with the Mu2e experiment in order to keep overall costs low.

The Antiproton Accumulator will no longer be in use, and many of its components will be reused for the new and redesigned Muon beamlines. Stochastic cooling components and other infrastructure no longer needed in the Debuncher ring will be removed in order to improve the aperture, proton abort functionality will be added, and the ring will be renamed the Delivery Ring (DR). The former AP1, AP2, and AP3 beamlines will be modified and renamed M1, M2, and M3. The DR Accelerator Improvement Project (AIP) will provide upgrades to the Delivery Ring as well as aperture improvements to the P1, P2, and M1 lines needed for future muon experiments using 8 GeV protons, including $(g-2)$. The layout of the beamlines is shown in Fig. 4.1.
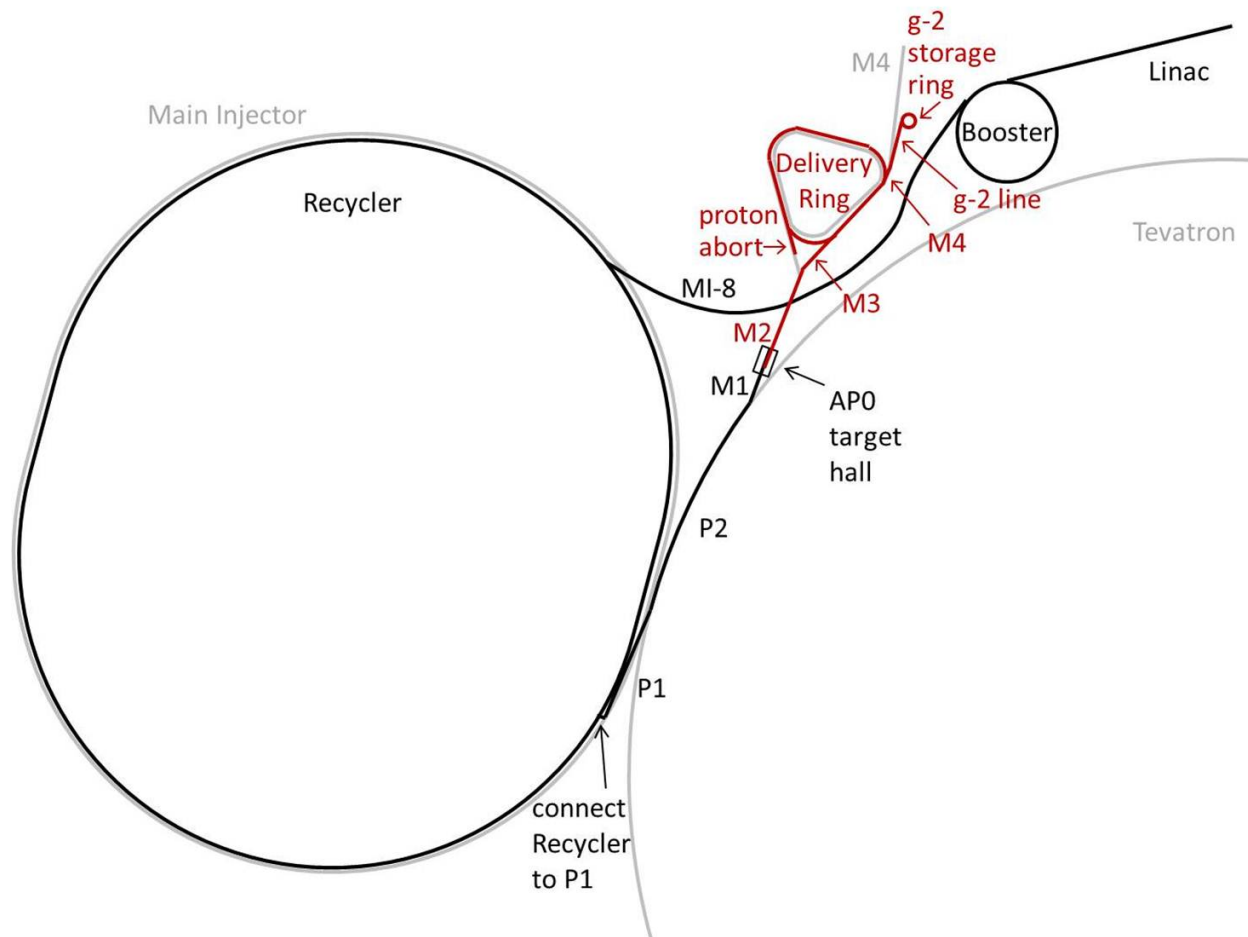
Figure 4.1: Path of the beam to $(g-2)$. Protons (black) are accelerated in the Linac and Booster, are re-bunched in the Recycler, and then travel through the P1, P2, and M1 lines to the AP0 target hall. Secondary beam (red) then travels through the M2 and M3 lines, around the Delivery Ring, and then through the M4 and $(g-2)$ lines to the muon storage ring.

The Proton Improvement Plan [1], currently underway, will allow the Booster to run at 15 Hz, at intensities of 4×10^{12} protons per Booster batch. Following the completion

of the Accelerator and NuMI Upgrades (ANU) subproject at Fermilab to prepare for the NOνA experiment [2], the Main Injector (MI) will run with a 1.333 s cycle time for its neutrino program, with twelve batches of beam from the Booster being accumulated in the Recycler and single-turn injected into the MI at the beginning of the cycle. While the NOνA beam is being accelerated in the MI, eight Booster batches will be available for experimental programs such as $(g-2)$ which use 8 GeV protons. The ANU subproject will also enable injection from the Booster into the Recycler. Extraction from the Recycler to the P1 beam line, required for $(g-2)$, will be implemented in the Recycler AIP.

Protons from the Booster with 8 GeV kinetic energy will be re-bunched into four smaller bunches in the Recycler and transported through the P1, P2, and M1 beamlines to a target at AP0. Secondary beam from the target will be collected using a focusing device, and positively-charged particles with a momentum of 3.11 GeV/c will be selected using a bending magnet. Secondary beam leaving the target station will travel through the M2 and M3 lines which are designed to capture as many muons with momentum 3.094 GeV/c from pion decay as possible. The beam will then be injected into the Delivery Ring. After several revolutions around the DR, essentially all of the pions will have decayed into muons, and the muons will have separated in time from the heavier protons. A fast kicker will then be used to abort the protons, and the muon beam will be extracted into the new M4 line, and finally into the new $(g-2)$ beam line which leads to the $(g-2)$ storage ring. Note that the M3 line, Delivery Ring, and M4 line are also designed to be used for 8 GeV proton transport by the Mu2e experiment.

The expected number of muons transported to the storage ring, based on target-yield simulations using the antiproton-production target and simple acceptance assumptions, is 1×10^5???. Beam tests were conducted using the existing Antiproton-Source configuration with total charged-particle intensities measured at various points in the beamline leading to the Debuncher, which confirmed the predicted yields to within a factor of two(???) [3]. More details are given in Sec. 4.4.1.

4.2   Protons from Booster

During the period when $(g-2)$ will take data, the Booster is expected to run with present intensities of 4×10^{12} protons per batch, and with a repetition rate of 15 Hz. In a 1.333 s Main-Injector super cycle, twelve Booster batches are slip-stacked in the Recycler and then accelerated in the MI and sent to NOνA. While the Main Injector is ramping, a time corresponding to eight Booster cycles, the Recycler is free to send 8 GeV (kinetic energy) protons to $(g-2)$. The RF manipulations of beam for $(g-2)$ in the Recycler (Sec. 4.3.1) allow $(g-2)$ to take every-other of the eight available Booster batches. Figure 4.2 shows the time structure of beam pulses to $(g-2)$.

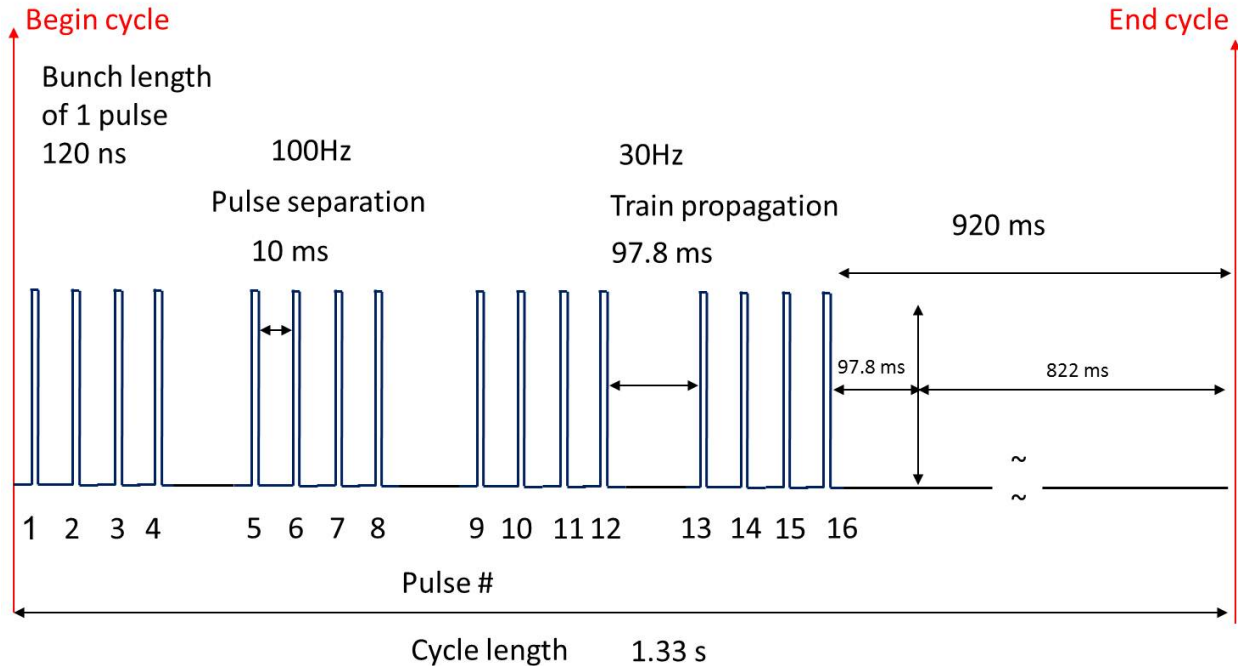The following section describes improvements needed to run the proton source reliably at 15 Hz.

Figure 4.2: Time structure of beam pulses to $(g-2)$. `fg:accel_pulsetrain`

`sct:PIP` ## 4.2.1   Proton Improvement Plan

The Fermilab Accelerator Division has undertaken a Proton Improvement Plan (PIP) [1]`accel_PIP` with the goals of maintaining viable and reliable operation of the Linac and Booster through 2025, increasing the Booster RF pulse repetition rate, and doubling the proton flux without increasing residual activation levels.

The replacement of the Cockroft-Walton pre-accelerator with an RFQ during the 2012 shutdown is expected to increase reliability of the pre-accelerator and to improve beam quality.

The Booster RF solid-state upgrade is necessary for reliable 15 Hz RF operations. This involves the replacement of 40-year-old electronics that are either obsolete, difficult to find, or unable to run at the required higher cycle-rate of 15 Hz, and will allow for easier maintenance, shorter repair times, and less radiation exposure to personnel. The solid-state upgrade will be completed in 2013.

Refurbishment of the Booster RF cavities and tuners, in particular, cooling, is also necessary in order to operate at a repetition rate of 15 Hz.

Other upgrades, replacements, and infrastructure improvements are needed for viable and reliable operation. Efforts to reduce beam loss and thereby lower radiation activation include improved methods for existing processes, and beam studies, e.g., aimed at finding and correcting aperture restrictions due to misalignment of components.

The proton flux through the Booster over the past two decades and projected into 2016 based on expected PIP improvements is shown in Fig. 4.3. `fg:accel_boosterflux`

The new PIP flux goal will double recent achievements and needs to be completed within five years. Figure 4.4 shows both the increase in flux as well as planned users. The goal `fg:accel_stuartplot`

of doubling the proton flux will be achieved by increasing the number of cycles with beam. The intensity per cycle is not planned to increase.

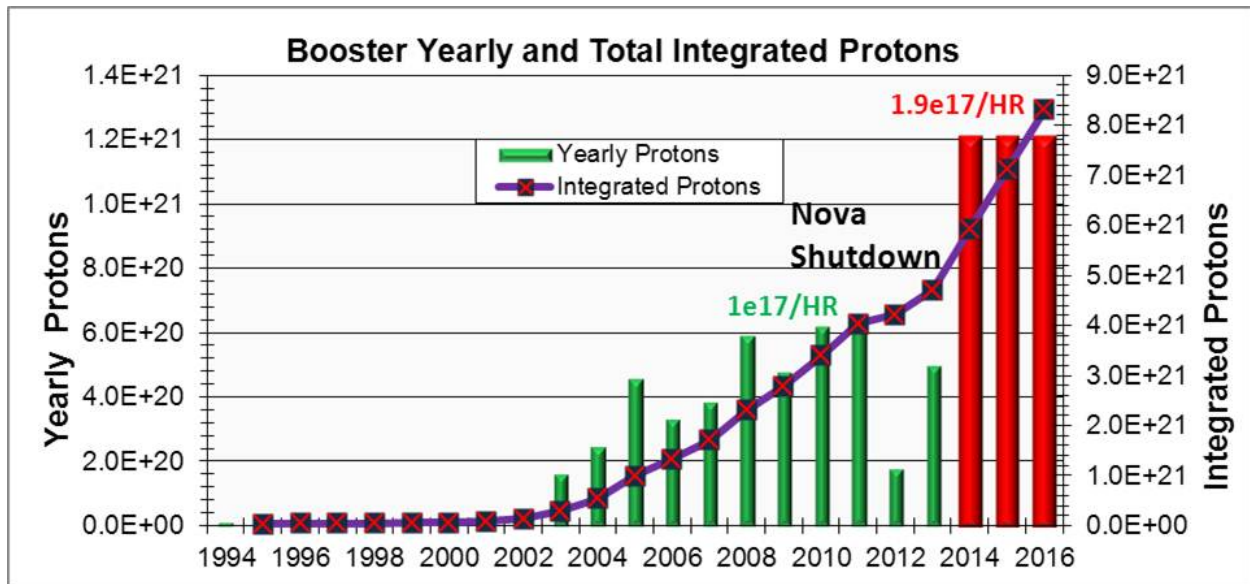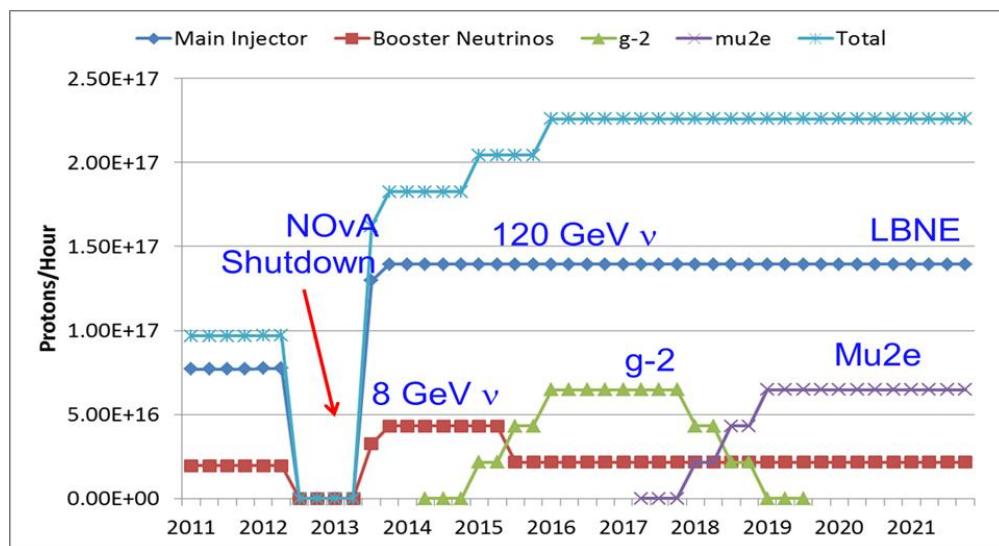Figure 4.3: Yearly and integrated proton flux (including PIP planned flux increase). fg:accel_booste

_stuartplot

Figure 4.4: Expectations for increases in the proton flux from the Proton Source needed for future experiments.

4.3 Recycler

The $(g-2)$ experiment requires a low number of decay positrons in a given segment of the detector, and therefore requires that the full-intensity $(4 \times 10^{12}$ protons) bunches be redistributed into four bunches of 1×10^{12} protons. These bunches should be spaced no closer than 10 ms to allow for muon decay and data acquisition in the detector. Because the revolution time of muons in the $(g-2)$ ring is 149 ns, and the time needed for the ring kicker to fire is XX, the longitudinal extent of the bunches should be no more than 120 ns. The Recycler modifications needed to achieve these requirements will be made under the Recycler AIP, and are described below.

4.3.1 Recycler RF

The proposed scheme for $(g-2)$ bunch formation [4] uses one RF system, 80 kV of 2.5 MHz RF. The design of the RF cavities will be based on that of existing 2.5 MHz cavities which were used in collider running, but utilizing active ferrite cooling. The ferrites of the old cavities and the old power amplifiers will be reused in the new system.

In order to avoid bunch rotations in a mismatched bucket, the 2.5 MHz is ramped "adiabatically" from 3 to 80 kV in 90 ms. Initially the bunches are injected from the Booster into matched 53 MHz buckets (80 kV of 53 MHz RF), then the 53 MHz voltage is turned off and the 2.5 MHz is turned on at 3 kV and then ramped to 80 kV. The first 2.5 MHz bunch is then extracted and the remaining three bunches are extracted sequentially in 10 ms intervals. The formation and extraction of all four bunches takes two Booster ticks or 133 ms. This limits the $(g-2)$ experiment to using four of the available eight Booster ticks in every Main-Injector super cycle.

Simulated 2.5 MHz bunch profiles are shown in Fig. 4.5. The 53 MHz voltage was ramped down from 80 to 0 kV in 10 ms and then turned off. The 2.5 MHz voltage was snapped to 3 kV and then adiabatically raised to 80 kV in 90 ms. The overall efficiency is 95%, and 95% of the beam captured is contained within 120 ns. The maximum momentum spread is $dp/p = \pm0.28\%$.

Although the Recycler is not yet configured to do such RF manipulations, by using the 2.5 MHz coalescing cavities in the Main Injector, the proposed bunch-formation scheme was tested with beam. In general, the agreement between simulations and data is very good. For illustration, the comparison between the beam measurements and the simulations for the case in which the 2.5 MHz voltage is ramped adiabatically from 3 to 70 kV in 90 ms is shown in Fig. 4.6.

Extraction from the Recycler and primary proton beam transport will be described in the beamline section, Sec. 4.5.
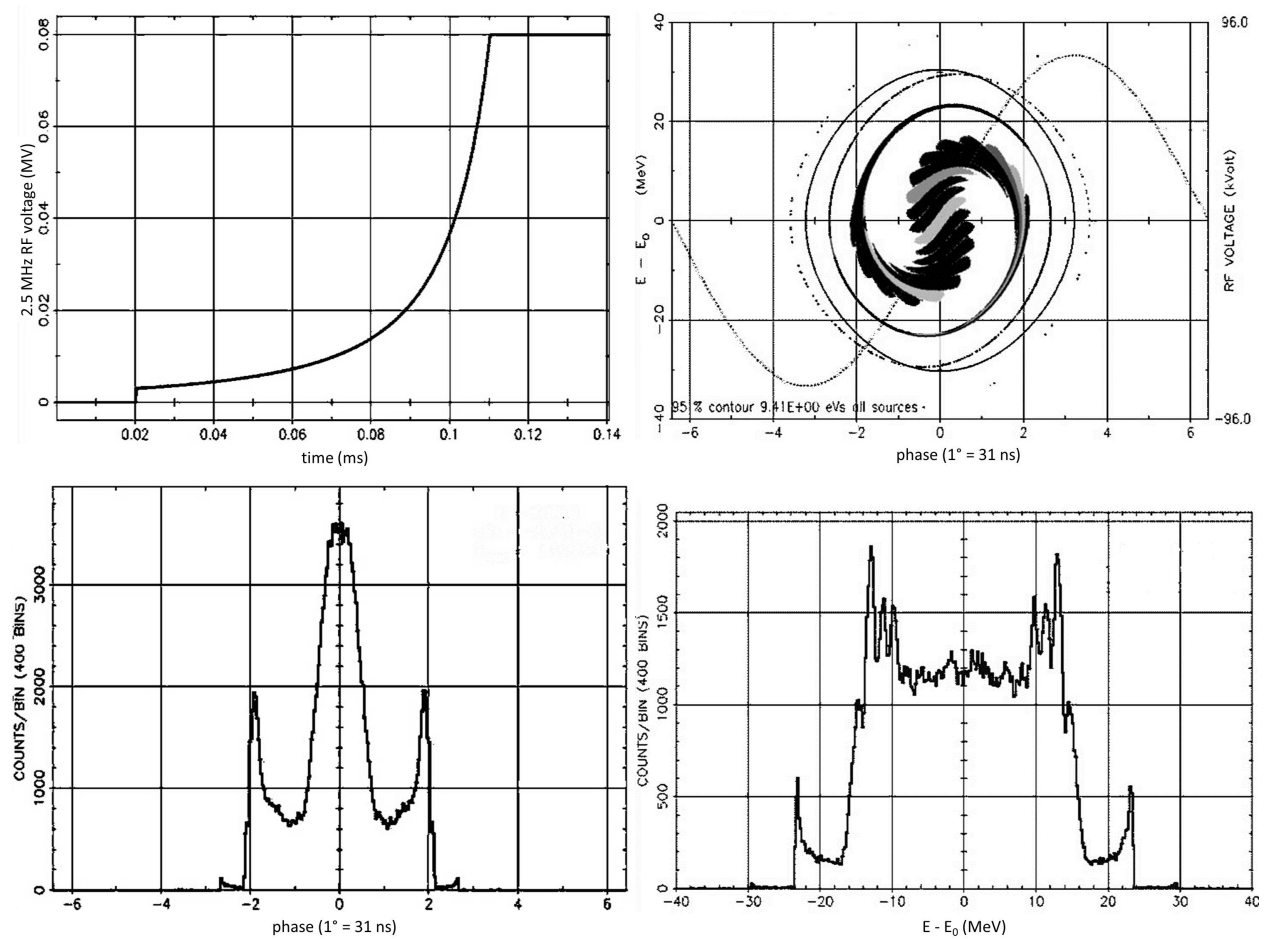
Figure 4.5: Results of RF simulations: 2.5 MHz voltage curve (upper left), phase space distribution (upper right), phase projection (lower left) and momentum projection (lower right).
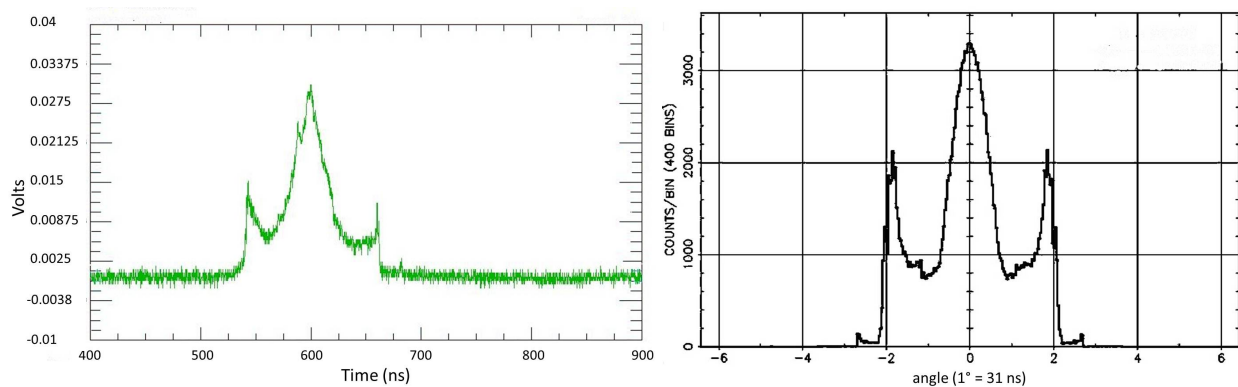
accel_RFsim

Figure 4.6: Comparison of beam profile (left) with simulation (right) for the case in which the 2.5 MHz voltage is ramped "adiabatically" from 3-70 kV in 90 ms. In both profiles, 95% of the particles captured are contained within 120 ns.

l_RFsimbeam

4.4   Target station

The $(g-2)$ production target station will reuse the existing target station that has been in operation for antiproton production for the Tevatron Collider for 23 years, while incorporating certain modifications. The $(g-2)$ target station will be optimized for maximum π^+ production per proton on target (POT) since the experiment will utilize muons from pion decay. Repurposing the antiproton target station to a pion production target station takes full advantage of a preexisting tunnel enclosure and service building with no need for civil construction. Also included are target vault water cooling and air ventilation systems, target systems controls, remote handling features with sound working procedures and a module test area. Figure 4.7 shows the current target-station (vault) layout. The overall layout of the target-vault modules will be unchanged from that used for antiproton production. The major differences in design will include different primary and secondary beam energies, polarity of the selected particles and pulse rate. Upgrades to pulsed power supplies, target design, pulsed-magnet design and the target dump are all considered.
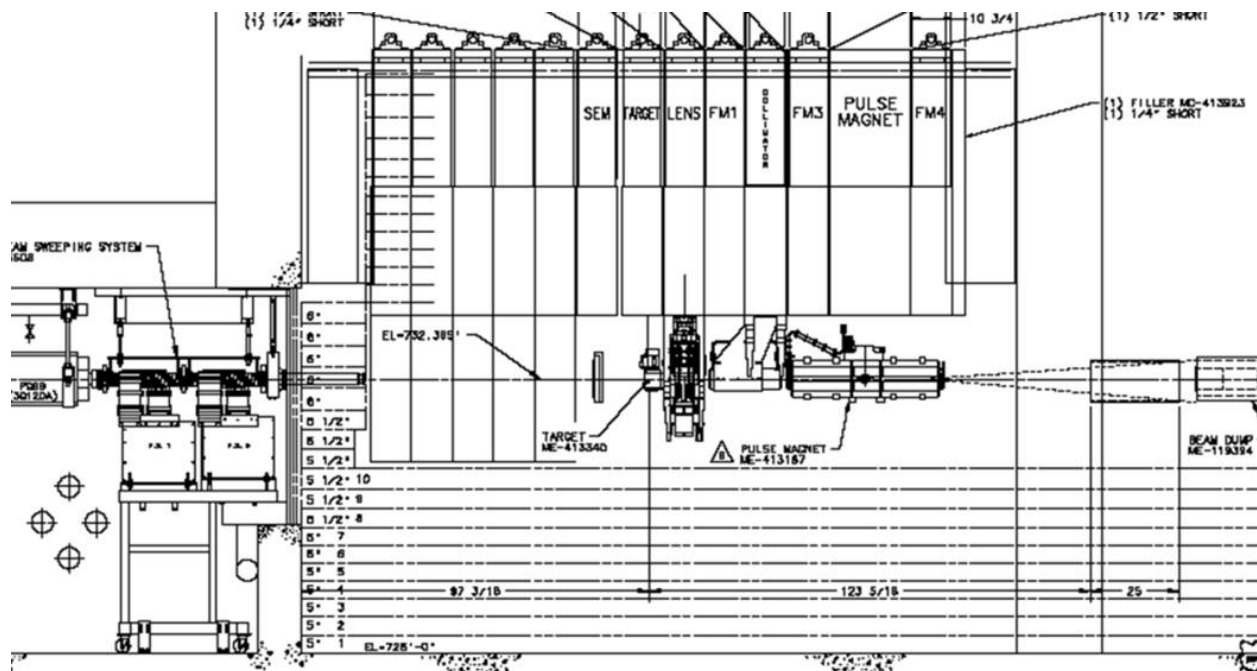
Figure 4.7: Layout of the $(g-2)$ target station. fg:accel_targetvault

The production target station consists of five main devices: the pion production target, the lithium lens, a collimator, a pulsed magnet, and a beam dump. Once the primary beam impinges on the target, secondaries from the proton-target interaction are focused by the lithium lens and then momentum-selected, centered around a momentum of 3.094 GeV/c, by a pulsed dipole magnet (PMAG). This momentum is the magic momentum needed to measure the muon anomalous magnetic moment in the downstream muon ring. The momentum-selected particles are bent 3° into a channel that begins the M2 beam line. Particles that are not momentum-selected will continue forward and are absorbed into the target-vault dump. An overview of some of the required beam design parameters for the $(g-2)$ target system

can be found in Table `tb:accel_targetparams` 4.2.

Parameter	FNAL $(g-2)$ 12 Hz
Intensity per pulse	10^{12} p
Total POT per cycle	16×10^{12} p
Number of pulses per cycle	16
Cycle length	1.33 s
Primary energy	8.89 GeV
Secondary energy	3.1 GeV
π^+ production / POT	0.9×10^{-5}
p production / POT	2.0×10^{-5}
μ^+ production / POT	0.007×10^{-5}
Beam power at target	17.2 kW
Beam size σ at target	0.15 mm
Selected particle	π^+
dp/p (PMAG selection)	5%

Table 4.2: Beam parameters for the target station. `tb:accel_targetparams`

One significant difference the $(g-2)$ production target station will have from the antiproton production target station is the pulse rate at which beam will be delivered to the target station. The $(g-2)$ production rate will need to accommodate 16 pulses in 1.33 s with a beam pulse-width of 120 ns. This is an average pulse rate of 12 Hz. The antiproton production pulse rate routinely operated at 1 pulse in 2.2 s or 0.45 Hz. This will be a challenging factor that can drive the cost of the design since the lithium lens and pulsed magnet will need to pulse at a significantly higher rate. Figure `fg:accel_pulsetrain` 4.2 shows the $(g-2)$ pulse scenario for pulsed devices and timing for proton beam impinging on the target.

4.4.1 The $(g-2)$ production target and optimization of production

`sct:target`

The current default target to be used for the $(g-2)$ experiment is the antiproton production target used at the end of the Tevatron Collider Run II. This target should be able to produce a suitable yield of approximately 1.0×10^{-5} π^+/POT. This target design has a long history of improvements for optimization and performance during the collider run. The target is constructed of a solid Inconel 600 core and has a radius of 5.715 cm with a typical chord length of 8.37 cm. The center of the target is bored out to allow for pressurized air to pass from top to bottom of the target to provide internal cooling to the Inconel core. It also has a cylindrical beryllium outer cover to keep Inconel from being sputtered onto the lithium lens from the impinging protons. The target has a motion control system that provides three-dimensional positioning with rotational motion capable of 1 turn in 45 s. This target and the target motion system need no modifications or enhancements to run for the $(g-2)$ experiment. Figure `fg:accel_targetphoto` 4.8 shows a drawing and a photo of the current target.

Summarize results of beam tests and comparison to simulation.
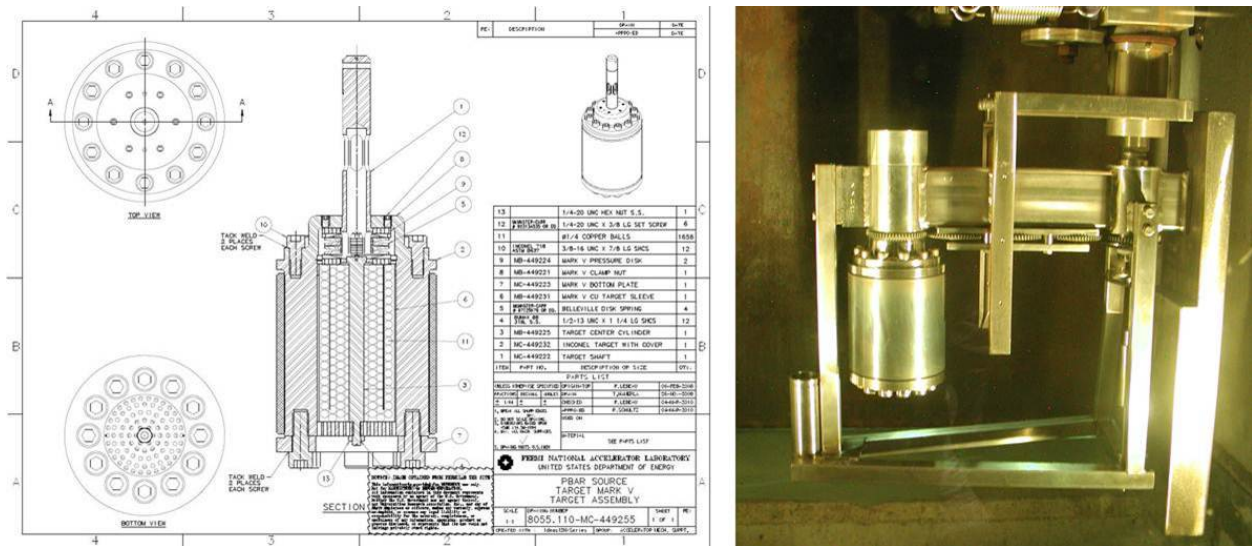
Figure 4.8: Current default target to be used for the $(g-2)$ target station. `fg:accel_targetphoto`

Even though this target is expected to produce a reasonable yield of about $10^{-5}\, \pi^+/\mathrm{POT}$ for the $(g-2)$ experiment, significant effort has been put into investigating a cost-effective, practical target design that will be optimized for pion production. Simulations have been conducted using MARS `accel_MARS` [6] to determine the optimal parameters, including impinging proton spot size at the target, target material, target length and thickness, and target orientation `accel_targetmarss` [7]. A graphical representation of the target system as implemented in the MARS15 code is shown `fg:accel_marstarget` in Fig. 4.9.
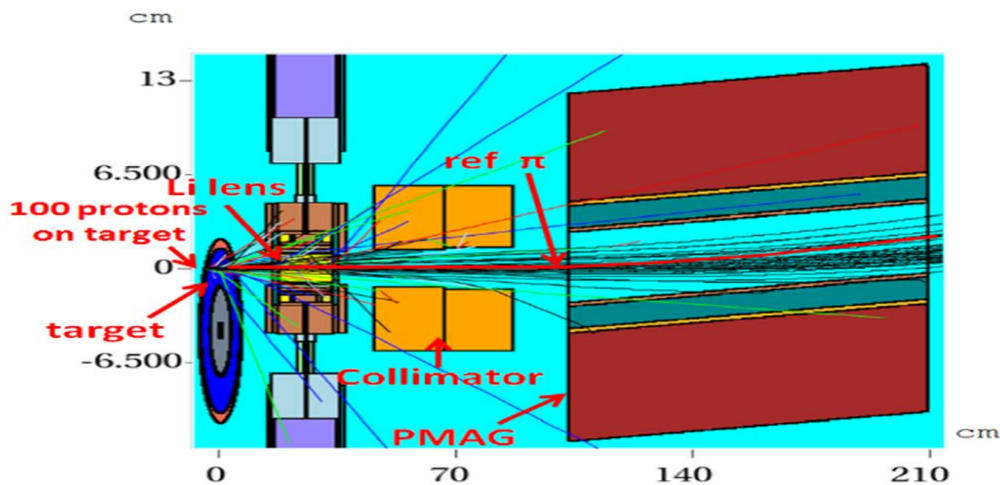
Figure 4.9: Graphical representation of target system used in MARS for simulated yield `_marstarget` results.

The spot size of the beam on the target is an important parameter in determining the pion yield. Initial values for the spot size were simply scaled from the $\sigma_x = \sigma_y = 0.15$ mm size of the beam for 120 GeV antiproton production to $\sigma_x = \sigma_y = 0.55$ mm for 8.9 GeV. Optimized results from the MARS simulations for the impinging-proton spot size can be seen

in Fig. 4.10. This plot shows the dependence of pion yield per POT on the beta function β at half distance into the target for the current default target. A reasonable range of expected β's which can be achieved is from 2.5 to 3.5 cm. The simulation result demonstrates that if the spot size is reduced from the original 0.55 mm to 0.15 mm, a 40-60% increase in pion production can be achieved [8] depending on β. These modifications are not directly made to the target station or target components but to the beam line just upstream of the target. Details of the beam line optics incorporating this optimization for pion yield can be found in Sec 4.5.4.
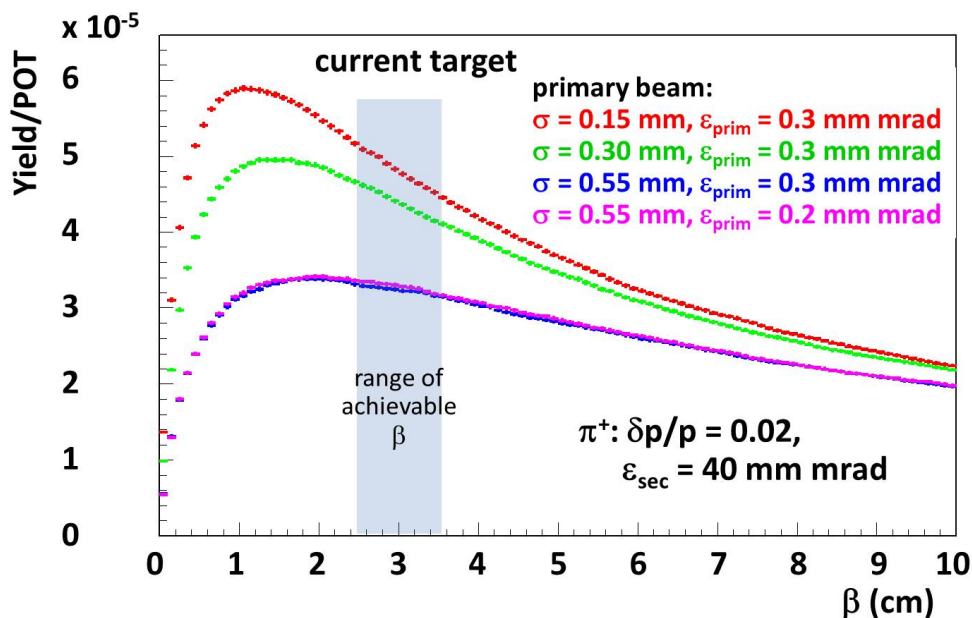
Figure 4.10: MARS simulation result for dependence of pion yield on β for different target spot sizes for a proton beam of emittance ε_{prim} and secondary beam momentum spread $dp/p = 0.02$ and emittance $\varepsilon_{sec} = 40$ mm mrad.

Also, optimizations concerning parameters for the target material, target length, and target width were also considered. First considered were optimizations to the target material. Three materials were simulated: Inconel, tantalum and carbon. Figure 4.11 illustrates the dependence of yield vs. β at the target for different materials with optimized lengths. Inconel and carbon are shown to have higher yields than tantalum. These results, combined with Fermilab's long history of building antiproton targets with Inconel, make Inconel the favored target material.

Next considering the dimensions of the target, Fig. 4.12a illustrates that a longer target will produce higher yields, while Fig. 4.12b demonstrates a weak dependence on the target thickness or radius. Therefore, the optimal pion production target may be a cylindrical rod with a length of 89 mm and a radius of 0.6 mm. However, to favor a more practical target design that will be able to be incorporated into the existing target mechanical and cooling systems, horizontal slabs made of Inconel of various heights were simulated. The output of the MARS simulation was then placed into G4beamline [9] in order to propagate particles
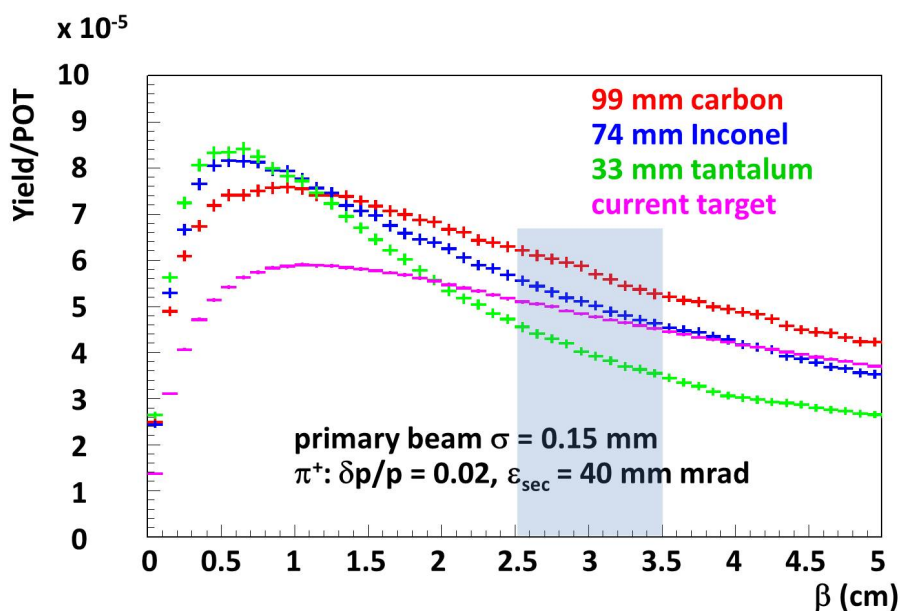
Figure 4.11: MARS simulation result for dependence of pion yield on β for different target materials. The length of the target is proportional to the interaction length of the material.

through the first four quadrupoles in the M2 beam line. Particles yields were tallied at the end of these quadrupoles with appropriate acceptance cuts for the elements. Figure 4.13 shows the pion yield for two optimized horizontal slab targets one of height 0.60 mm and the second of 0.75 mm. They are both approximately 107 mm long. Simulations for these slab targets show that a 22% and 14% gain in pion yield from optimized horizontal slabs can be obtained, respectively. Therefore, by combining the 40-60% increase from the reducing the target spot size and a 14 to 22% increase from an optimized target, a total increase of a factor of almost two in pion production may be achievable. This would be an estimated production rate of $2.0 \times 10^{-5} \pi^+$/POT with all the suggested improvements.

The actual details for the design of the alternate target are currently being worked out. However, it is preferred that the simulated horizontal slabs transition into target discs that could be mounted on a stacked-disc style target incorporating the simulated dimensions. In order to provide cooling to the target material, the target discs would be separated by discs of low Z material like beryllium or aluminum. Figure 4.14 is a picture of a proposed design of a target incorporating stacked target and cooling discs. The blue material represents discs of Inconel separated by the grey shaded areas which would be beryllium. One consideration for operating with the stacked discs that are very thin, approximately 0.6 mm, is the need for beam stability on the target. This may require improvements in upstream trim power supplies to achieve appropriate stability. There will be beam tests in 2013 in which a prototype stacked-disc target will be constructed and tested to narrow and confirm the design of the alternate target.
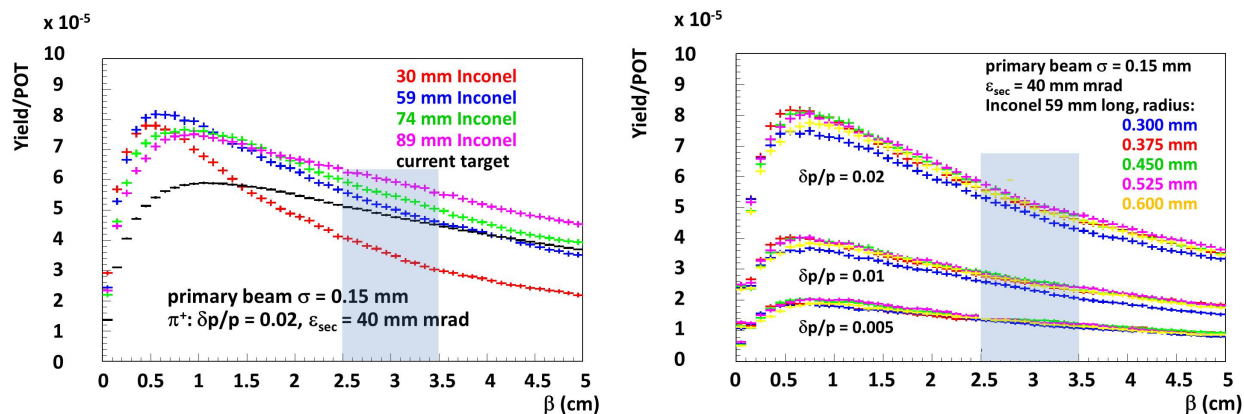
Figure 4.12: MARS simulation result for dependence of pion yield on β for different target lengths (a) and thicknesses (b).
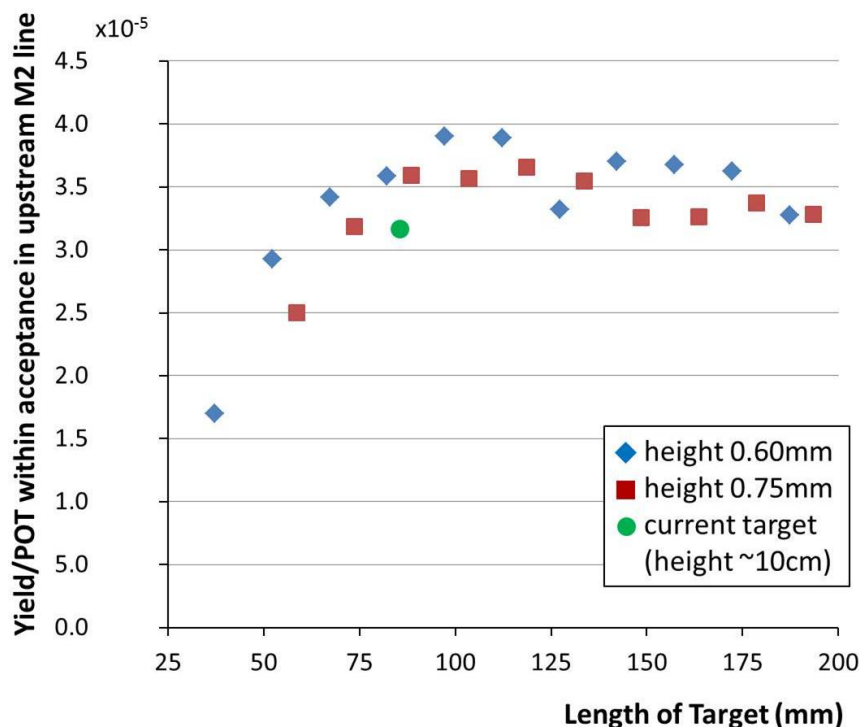
Figure 4.13: MARS/G4beamline predictions for number of pion secondaries from an Inconel target making it to the upstream M2 line as a function of target slab length for a slab of height 0.60 mm (with the upstream end of the target 56 mm from the lens focal point), a slab of height 0.75 mm (with the upstream end of the target 67 mm from the lens focal point), and the current target (assuming a chord length of 75 mm). The location of the target for a given height slab was optimized to give maximum yield. The spot size of beam on the target is taken to be 15 mm and the acceptance 40 mm mrad. A thin target of length 107 mm is predicted to give an increase in yield of 14-22% over the existing target.
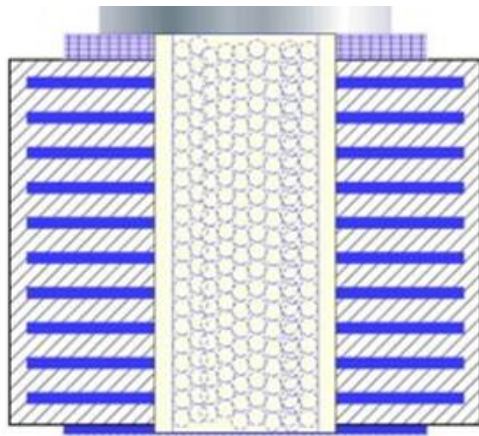
Figure 4.14: Proposal for new $(g-2)$ target design utilizing stacked thin slabs of Inconel (blue) separated by Beryllium (hashed grey). Target material air cooling channels are in the middle of the target.

l_alttarget

sct:M2M3

4.4.2 Focusing of secondaries from the target

The lithium collection lens is a 1 cm radius cylinder of lithium that is 15 cm long and carries a large current pulse that provides a strong isotropically focusing effect to divergent incoming secondaries after the initial interaction of impinging particles with the target [10]. accel_pbrookie
The lithium lens cylinder is contained within a toroidal transformer, and both lens and transformer are water cooled. Figure 4.15 is a drawing of the lithium lens depicting (a) the fg:accel_lensdrawing transformer and lens body, and (b) details of the lithium cylinder.

a)   b)
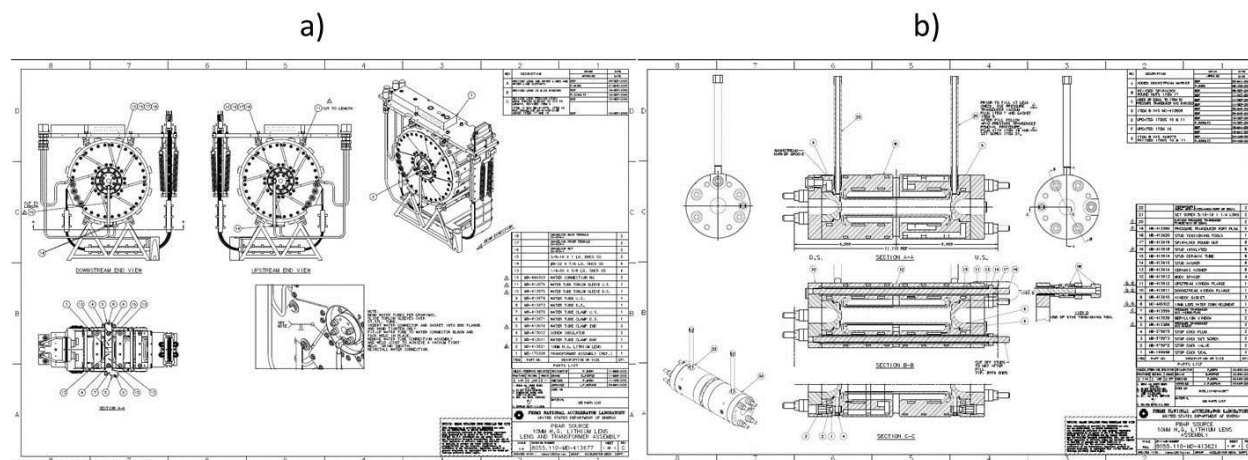
Figure 4.15: Drawing of the lithium lens and transformer (a) and the lithium cylinder body (b).

lensdrawing

During antiproton production for the Collider Run II, the lens pulsed at a peak current of 62 kA, which is equivalent to a gradient of 670 T/m at 8.9 GeV/c with a base pulse width of 400 μs. Scaling the lens gradient for use at 3.115 GeV/c for $(g-2)$ and in order to accommodate a similar range of focal lengths from the target to the lens of roughly 28 cm, the gradient required will be 230 T/m at a pulsed peak current of 22 kA with the tb:accel_lensparam same 400 μs pulse width. Table 4.3 provides an overview of required operating parameters. Accommodating the $(g-2)$ 12 Hz average pulse rate for the lithium lens is one of the biggest challenges and concerns for repurposing the antiproton target station for $(g-2)$. Even though peak current and gradient will be reduced by a factor of about 3, the pulse rate will increase by a factor of 24 compared to the operation for antiproton production. Resistive and beam heating loads, cooling capacity, and mechanical fatigue are all concerns that are warranted for running the lithium lens at the $(g-2)$ repetition rate.

Lens operation	Pulse width (μs)	Peak current (kA)	Gradient (T/m)	Pulses per day
Antiproton production	400	62.0	670	38,880
$(g-2)$ pion production	400	22.6	230	1,036,800

Table 4.3: Lithium lens operation parameters. tb:accel_lensparam

Therefore, in order to gain confidence that the lens will be able to run under these accel_ANSYS conditions, a preliminary ANSYS [11] analysis has been conducted. This analysis simulated

thermal and mechanical fatigue for the lens based on the pulse timing scenario in Fig 4.2 fg:accel_pulsetra and at a gradient of 230 T/m. These results were compared to results from a similar analysis for the lens operating under the antiproton-production mode of a gradient of 670 T/m at a pulse rate of 0.5 Hz [12]. Figure 4.16 (left) shows the ANSYS output thermal profile of a accel_lensansys fg:accel_ansystemp cutaway of the lens operating at 12 Hz. The lithium body corner is a temperature-sensitive location and should avoid lithium melting temperatures of 453.75 K. The corner temperature reaches a maximum temperature of 376 K. The plot on the right of Fig. 4.16 is the increase in fg:accel_ansystemp maximum temperature of the lithium over the 16 pulses, depicting a change in temperature of 22 K when the operating temperature has come to equilibrium. We conclude from this analysis that the lithium lens is adequately cooled to operate at the nominal $(g-2)$ pulse rate.
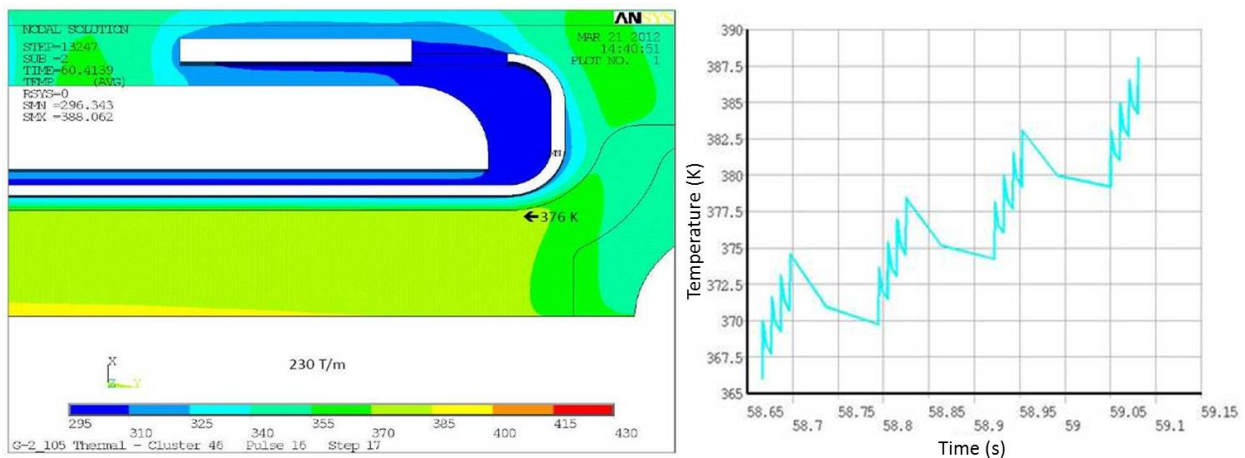
Figure 4.16: Simulated thermal profile from ANSYS for the lens operating at an average pulse rate of 12 Hz (left) depicting little beam heating and a corner temperature of 376 K. (Right) Plots showing lens temperature increase over the 16 pulses.

Mechanical fatigue was also assessed for the lithium lens. Figure 4.17 fg:accel_lensfatigue depicts a constant life fatigue plot developed for the lens from the ANSYS analysis. The two red lines represent upper and lower estimates of fatigue limits for the lens material. The red data points represent fatigues for gradients of 1000 T/m, 670 T/m, and two points at 230 T/m for a preload pressure of 3800 and 2200 psi, respectively. For the lens operating in the antiproton production conditions of 670 T/m, the mechanical fatigue was a large concern in the lens design. It appears that for the $(g-2)$ case, the mechanical fatigue will be a comparatively small concern.

This initial assessment of the lithium lens suggests that is should be able to operate at the $(g-2)$ repetition rate. However, since the operation of the lithium lens at the average 12 Hz rate is crucial, testing of the lens at 12 Hz is needed. Currently the lens is being pulsed in a test station at a 12 Hz rate in order to confirm that 1M pulses per day can be achieved and sustained over many months. Also, data from these tests can be used to confirm predictions of the ANSYS model.
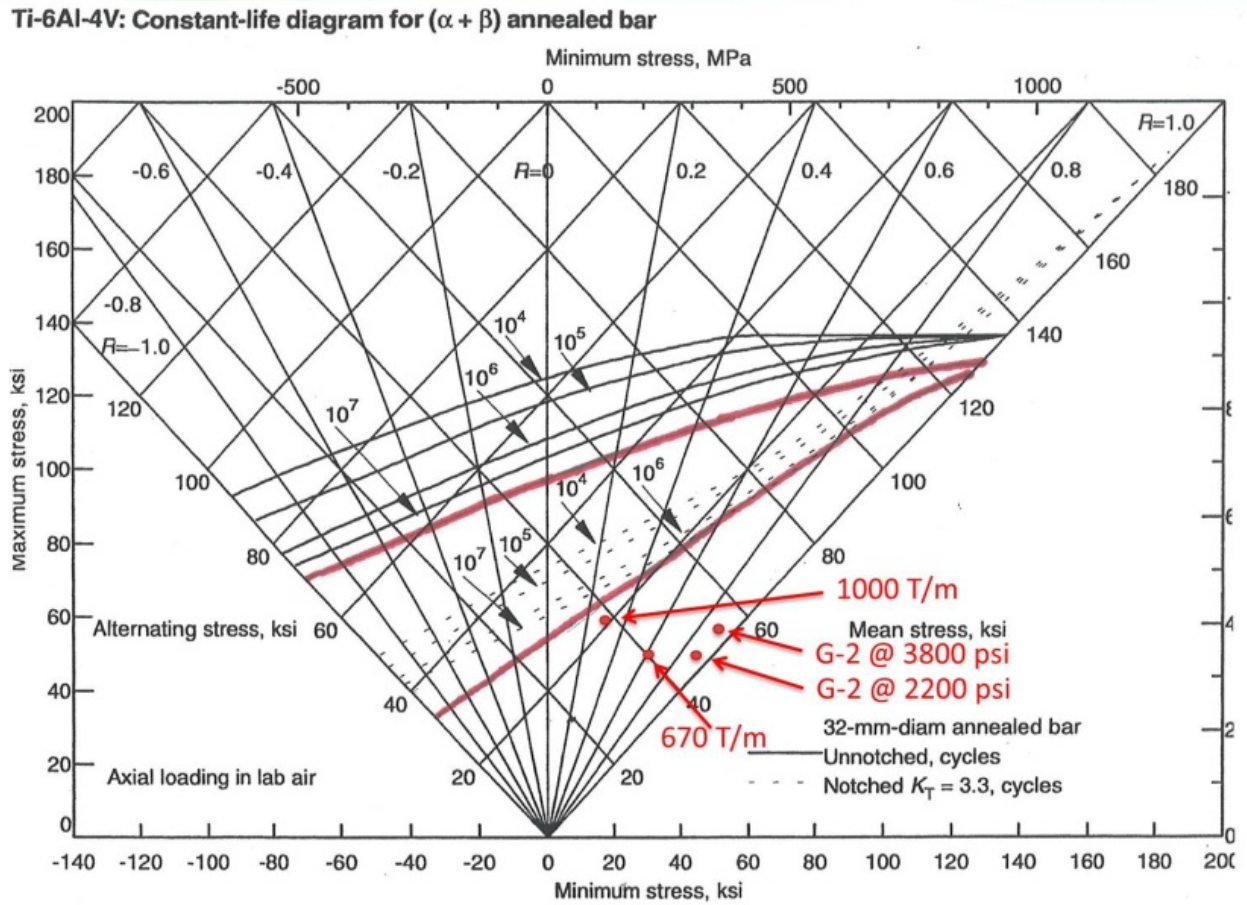
Figure 4.17: Constant-life fatigue plot of the lithium lens for antiproton and $(g-2)$ modes showing that mechanical fatigue for the $(g-2)$ pulse rate is a small concern.

lensfatigue

sct:pmag

4.4.3   Pulsed magnet (PMAG) and collimator

fg:accel_pmag

The pulsed magnet, shown in Fig. 4.18, selects 3.115 Gev/c positive particles and bends them $3°$ into the channel that begins the M2 beam line. The magnet will operate with a field of 0.53 T and is a 1.07 m long magnet with an aperture of 5.1 cm horizontally and 3.5 cm vertically. It is a single-turn magnet that has incorporated radiation-hard hardware such as ceramic insulation between the magnet steel and the single conductor bars, as well as Torlon-insulated bolts [10]. The pulsed magnet has a typical pulse width of 350 μs and similarly to the lithium lens, will need to accommodate the $(g-2)$ pulse rate shown in Fig. 4.2. The pulsed magnet is water cooled. In addition to the magnet currently in the target vault, there are three spares.

accel_pbrookie

fg:accel_pulsetrain
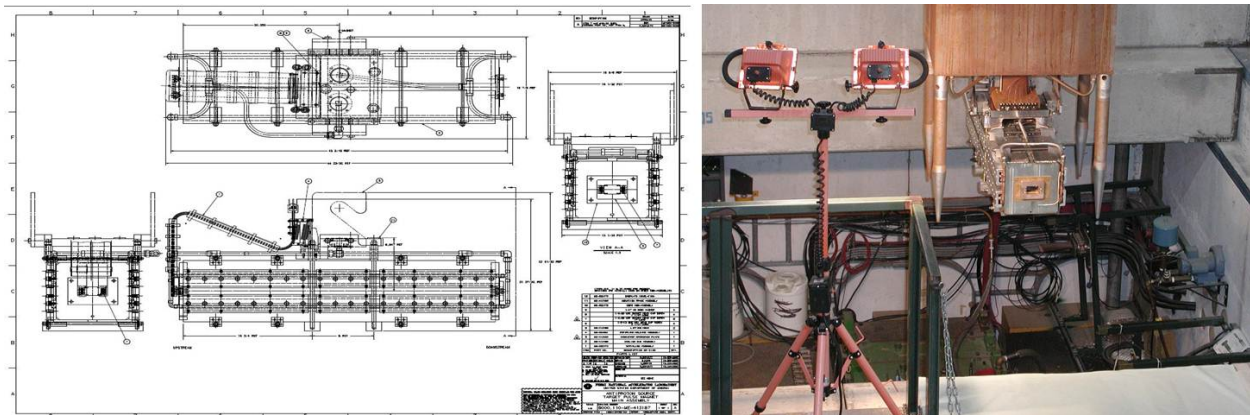
Figure 4.18: Pulsed magnet (PMAG) used for momentum-selection of pions. fg:accel_pmag

One consideration that may require a change to the pulsed magnet design is the fact that the polarity of the selected particles for $(g-2)$ is opposite that for antiproton production. MARS results predict that in the $(g-2)$ polarity, a negatively-charged particle may interact with the downstream end of the magnet, increasing the integrated radiation dose. MARS simulations estimate the integrated dose at the downstream end of PMAG to be down by a factor of 5 compared to the antiproton production case, but the repetition rate is increased by a factor of 24. Therefore, a new magnet design may be required. A C-magnet style pulsed magnet would prevent the negative particles from hitting the pulsed magnet thus reduce the likelihood of magnet failures.

In order to accommodate the $(g-2)$ pulse rate, the pulsed magnet power supply will also need to be modified or replaced with one similar to the new supply for the lithium lens with improved charging capability.

The collimator is located directly upstream of the pulsed magnet. The purpose of the collimator is to provide radiation shielding to the pulsed magnet to improve its longevity. It is a water-cooled copper cylinder 12.7 cm in diameter and 50.8 cm long. The hole through the center of the cylinder is 2.54 cm diameter at the upstream end, widening to a diameter of 2.86 cm at the downstream end. The existing collimator is currently planned to be used without modification.

sct:dump ## 4.4.4 Target station beam dump

The target-station beam dump absorbs particles which are not momentum-selected by the pulsed dipole magnet and continue straight ahead. The location of the beam dump can be seen in Fig. 4.19. The current beam dump has a graphite and aluminum core which is water cooled, surrounded by an outer steel box. The graphite core is 16 cm in diameter and 2 m in length, and is designed to handle a beam power of 80 kW [13]. The existing dump has a known water leak that developed at the end of the collider run. Therefore, consideration for replacing the beam dump will need to be made. The current plan is to replace the beam dump with an updated copy of the 80 kW beam dump. The maximum estimated beam energy load for $(g-2)$ would occur if $(g-2)$ takes advantage of extra cycles, running at a rate up to 18 Hz, during a hypothetical period when the NOνA experiment would not be able to operate, and would be 25 kW, which is easily accommodated with the current dump design.
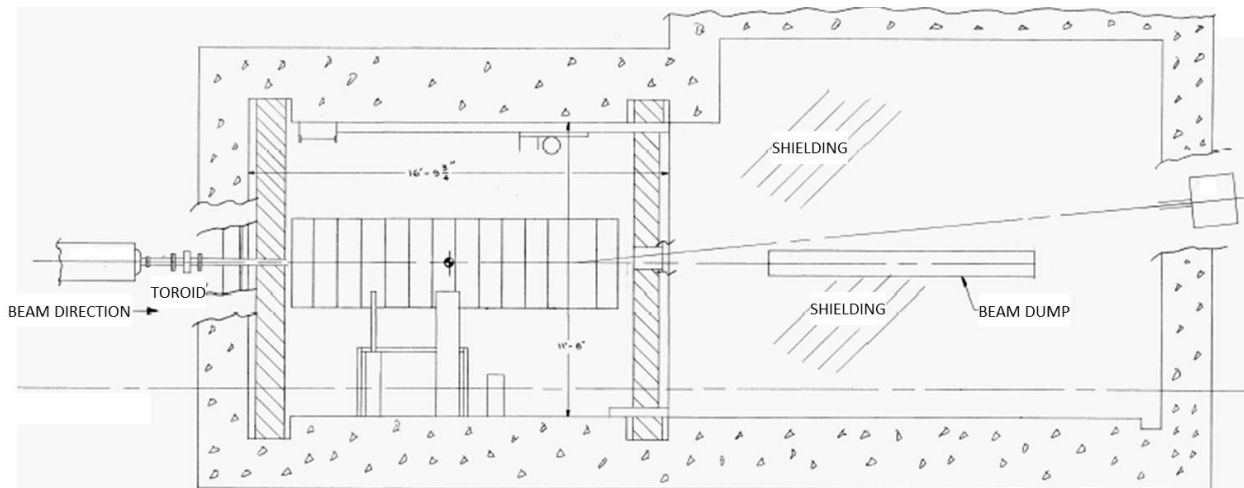
Figure 4.19: Layout of the target-station beam dump. fg:accel_dump

An alternative, shorter, cost-effective dump was also considered and designed at an operating capacity of 25 kW. This design resulted in a copper cylinder 2 ft long and 6 in in diameter, with copper cooling tubes vacuum-brazed around the outside of the cylinder (Fig. 4.20).
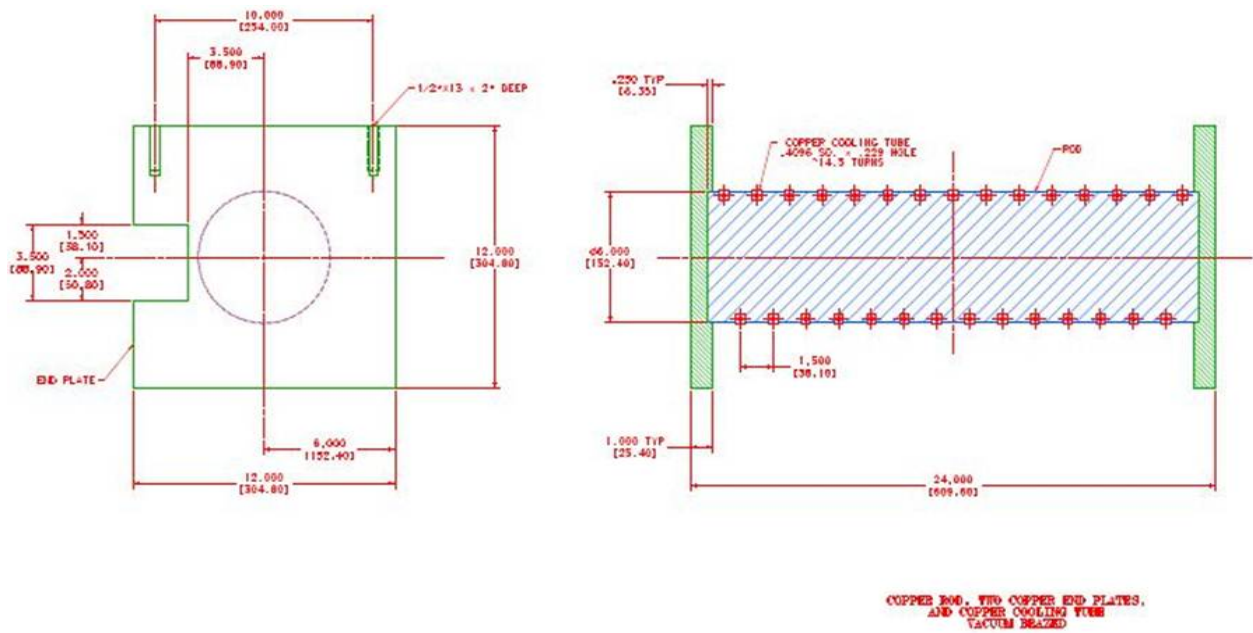
Figure 4.20: Alternate 25 kW dump made of a copper-core rod with copper water tubing water for cooling.

cel_altdump

4.5 Beam Transport Lines

4.5.1 Overview of $(g-2)$ beamlines

The existing tunnel enclosures and beamlines connecting the Recycler Ring to the Delivery Ring will be largely reused for $(g-2)$ operation. However, there are fundamental differences between the way the Rings and beamlines were operated for Collider Operation and how they will be used to support the Muon Campus. A high-intensity, 8 GeV kinetic energy proton beam will be transported to the AP0 Target Station in $(g-2)$ operation and to the Delivery Ring for the Mu2e experiment. The increase in intensity from Collider Operation in conjunction with the beam size of the 8 GeV beam will present challenges for efficient beam transfer. The beamlines downstream of the AP0 Target Station will need to be reconfigured to connect to the D30 straight section of the Delivery Ring. New extraction lines will be constructed to transport beam from the D30 straight section to the $(g-2)$ and Mu2e experiments. Careful planning is required for the D30 straight section of the Delivery Ring due to the presence of both the injection and extraction points. The extraction line will also need to support both single-turn extraction for $(g-2)$ and resonant extraction for Mu2e.

4.5.2 Beamline Changes from Collider Operation

During Pbar operation in Collider Run II, the P1 line connected to the Main Injector at the MI 52 location. The P1 line supported operation with three different beam energies, 150 GeV for protons to the Tevatron, 120 GeV for Pbar production and SY120 operation, and 8 GeV for protons and antiprotons to and from the Antiproton Source. The junction between the P1 and P2 lines occurs at F0 in the Tevatron enclosure. The P2 line ran at two different beam energies, 120 GeV for antiproton production and SY120 operation and 8 GeV for protons and antiprotons to and from the Antiproton Source. The P2, P3 (for SY120 operation), and AP-1 lines join at the F17 location in the Tevatron enclosure. The AP-1 line also operated at 120 GeV and 8 GeV, but is not used for SY120 operation. The AP-3 line only runs at a kinetic energy of 8 GeV. The AP-3 line connects with the AP-1 line in the Pre-Vault beam enclosure near the Target Vault and terminates at the Accumulator.

After the conversion from collider to NOνA and $(g-2)$ operation, the Recycler will become part of the proton transport chain and will connect directly with the Booster. There will be a new beamline connection between the Recycler Ring and the P1 line. The P1 line will become a dual energy line, with no further need to deliver 150 GeV protons with the decommissioning of the Tevatron. The P2 line will continue to operate at both 8 GeV for the Muon experiments and 120 GeV for SY120 operation. The AP-2 and AP-3 lines will need to be almost completely dismantled and reconfigured to support both the transport of muon secondaries via the Target Station for $(g-2)$ and protons via the target bypass for Mu2e. The $(g-2)$ 3.1 GeV secondary beamline emanating from the Target Station and the Mu2e 8 GeV primary beamline bypassing the Target Station will merge and follow a single line to the Delivery Ring. The new injection line will connect to the Delivery Ring in the D30 straight section. The extraction line also originates in the D30 straight section and has to be capable of supporting both resonant and single-turn extraction.

The beamlines that made up the Antiproton Source, those that have an "AP" prefix,

will be modified, reconfigured and renamed prior to $(g-2)$ operation. The AP-1 line will only operate at an energy of 8 GeV and will be renamed M1. The AP-1 line will be largely unchanged, with the exception of the replacement of some magnets to improve aperture. The AP-2 line will become two separate beamlines and no longer be continuous. The upstream end of the line is needed as a pion decay channel for the $(g-2)$ experiment and will be renamed M2. It will provide a connection from the Pbar AP0 Target Station to the M3 line. The downstream section of AP-2 will become the abort and proton removal line from the Delivery Ring. The old AP-3 line will be required to transport both 8 GeV beam for the Mu2e experiment and also a 3.1 GeV secondary beam for the $(g-2)$ experiment and will be renamed M3. The 18.5° right bend will be changed from a two to a three dipole configuration in order to avoid higher beta functions in this region. The M3 line will will also be modified to connect to the Delivery Ring (formerly Debuncher) instead of the Accumulator. The extraction line connecting the Delivery Ring to the experiments will be called M4. The $(g-2)$ line will branch from the M4 line in the "Left Bend" area. Figure 4.21 compares the Pbar beamline configuration with that proposed for $(g-2)$ and Mu2e operation. In general, the AP-1, AP-2 and AP-3 lines will refer to the old Pbar beamline configuration and M1, M2, M3, M4 and $g-2$ will refer to the beamline configuration for $(g-2)$ operation.
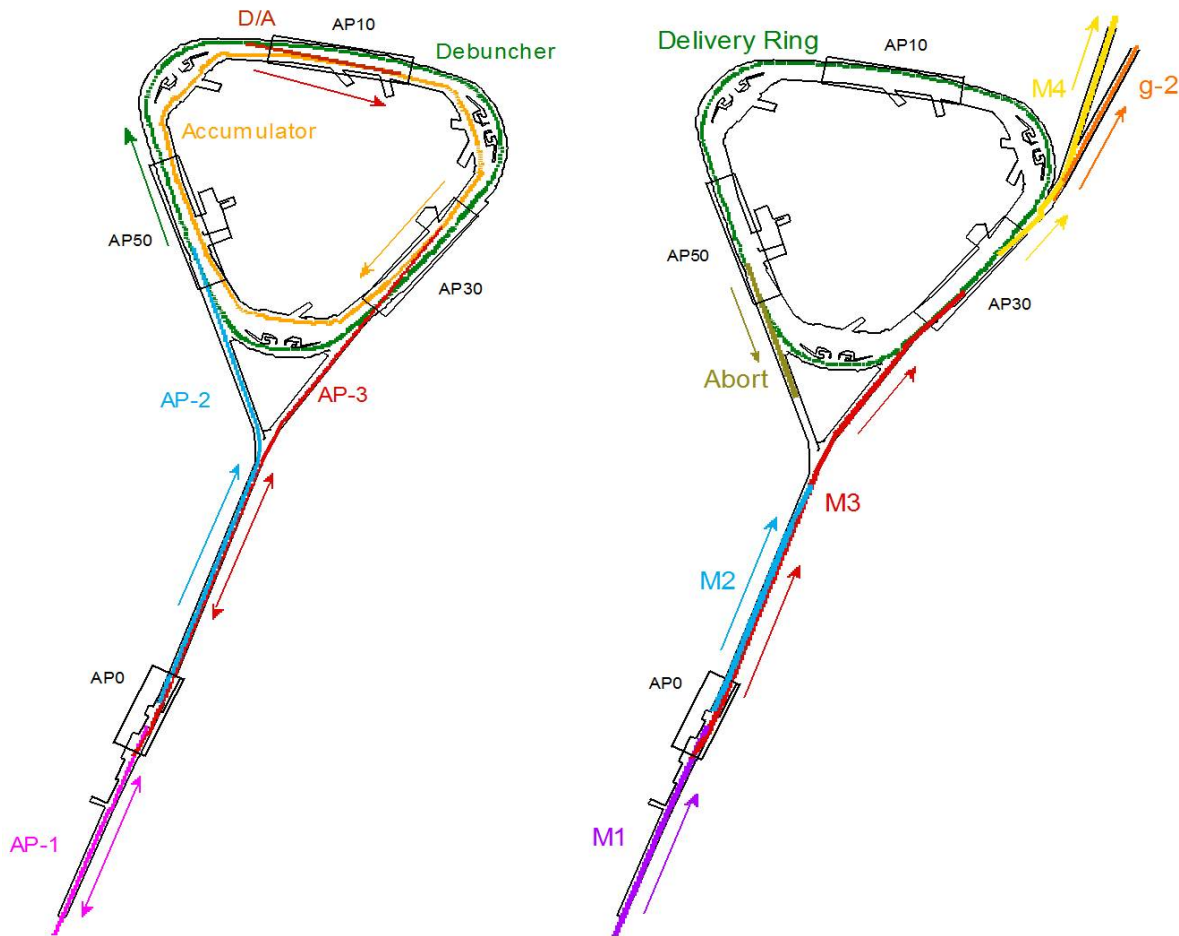
Figure 4.21: Layout of the Antiproton Source beamlines (left) and the reconfigured beamlines for $(g-2)$ operation (right).

Most of the common improvements to the beamlines and Delivery Ring that benefit Mu2e, $(g-2)$, and future experiments will be incorporated into an Accelerator Improvement Project (AIP). Table 4.4 summarizes which improvements are contained in the AIP, as well as those that will be managed as part of the Recycler Ring AIP, Mu2e and $(g-2)$ projects. Project Managers for the various projects will work closely together to ensure they interface properly. Virtually all of the work that is incorporated into the AIP's must be completed prior to beam operation to $(g-2)$.

Description	Project	Comment
Recycler RF upgrade	RR AIP	
Recycler extraction/P1 stub line	RR AIP	
P1,P2 and M1 aperture upgrade	DR AIP	**M1 final focus quadrupoles are $(g-2)$**
Reconfigure AP-2 and AP-3	**$(g-2)$**	**New lines are called M2 and M3**
Final focus to AP0 Target Station	**$(g-2)$**	
AP0 Target Station upgrades	**$(g-2)$**	
Beam transport instrumentation	DR AIP	
Beam transport controls	*Mu2e*	
Beam transport infrastructure	DR AIP	
Delivery Ring injection	DR AIP	
D30 straight section preparation	DR AIP	
Delivery Ring modification	DR AIP	
D.R. abort/proton removal	DR AIP	
Delivery Ring RF system	*Mu2e*	
Delivery Ring controls	*Mu2e*	
Delivery Ring instrumentation	DR AIP	*DCCT and Tune measure are Mu2e*
Resonant extraction from DR	*Mu2e*	
Fast extraction from DR	**$(g-2)$**	
Delivery Ring infrastructure	DR AIP	
Extraction line to split	**$(g-2)$**	**Upstream M4 line**
Extraction line from split to Mu2e	*Mu2e*	*Downstream M4, including extinction*
Extraction line from split to $(g-2)$	**$(g-2)$**	**Beamline to MC-1 building**

Table 4.4: Beam-line and Delivery-Ring upgrades and associated project: $(g-2)$ project, Mu2e project, Delivery Ring Accelerator Improvement Project (DR AIP), and Recycler Ring AIP (RR AIP).

4.5.3 Proton Beam Transport to the Target Station

Beam transport of the 8 GeV primary beam from the Recycler Ring (RR) to the Target Station closely resembles the scheme used to transport 120 GeV protons for antiproton production in Collider operation. The most notable differences are the change in beam energy and the switch from the Main Injector to the RR as the point of origin for the P1 line. The beamlines will be modified to 1) provide a connection between the RR and P1 line, 2) improve aperture to accommodate the larger beam size and intensity, and 3)

reconfigure the final focus region in order to reach the desired spot size on the production target. Table 4.5 lists the beamlines connecting the RR with the Target Station and their respective lengths.

Beam Line	Length (m)
RR to P1	43
P1	182
P2	212
AP-1 (M1)	144
RR to Target Total	581

Table 4.5: Recycler Ring to Target beam line lengths. `tb:accel_RRtotarget`

Recycler Ring to P1 line stub

Operation of $(g-2)$ and Mu2e requires the transport of protons from the RR rather than the Main Injector. A new transfer line from the RR to the P1 beamline will be constructed to facilitate proton beam transport from the RR to the Delivery Ring. This new beamline provides a way to deliver 8 GeV kinetic energy protons to the Delivery Ring, via the RR, using existing beam transport lines and without the need for new civil construction.

Beamline Design   The P1 line is lower in elevation than the RR, thus the beam will be extracted downward. This will be accomplished with a horizontal kicker that will displace beam into the field region of a Lambertson magnet that will bend beam down. The kickers are located immediately downstream of the RR 520 location and the Lambertson will be just downstream of the RR 522 location. Due to space limitations, only two vertical bend centers made up of the Lambertson and a dipole are used in the new line. An integer multiple of 360° in betatron phase advance between the two bending centers is required to cancel the vertical dispersion from the bends. The new beamline needs to intercept the existing P1 line in a location that doesn't disturb the extraction trajectory from the Main Injector, which will be retained for SY120 operation. That junction point will be located near quadrupole Q703.The angles of both the Lambertson and the vertical bending magnet (VBEND) were obtained by matching the site coordinates from the RR to P1 line using TRANSPORT [14] `accel_transport` code. Figure 4.22 shows the layout of the new line, with the existing P1 line drawn in red.

Figure 4.22: The new Recycler Ring to P1 connecting beamline. `fg:accel_RRtoP1`

Kickers   The $(g-2)$/Mu2e extraction kicker will be of the same design as the kickers used during collider operation, but will be potted instead of using Fluorinert for electrical insulation. The physical dimensions and properties of the kickers are listed in Table 4.6. `tb:accel_RRkicker` The plan is to reuse the ceramic vacuum chamber from old RR kicker magnets, which are slightly smaller than the standard RR vacuum chamber. The kicker system will be made up of two magnets producing 0.79 mrad each for a total kick of 1.58 mrad. The new kicker power supplies will be located in the MI-52 service building. Power supplies for the new beamline magnets will also be located at MI-52. This service building will be expanded to accommodate the new power supplies.

Recycler Extraction Kicker RKB-25	
Parameter	Value
Ferrite length	46.6 in
Case length	64.0 in
Insert length	67.78 in
Print number	ME-481284
Maximum strength (each)	0.279 kG m
Maximum kick (each)	0.94 mrad @ 8 GeV/c^2
Required kick (each)	0.79 mrad @ 8 GeV/c^2
Rise time, 3% - 97%	140 ns

Table 4.6: RR extraction kicker parameters. `tb:accel_RRkicker`

Lambertson   The Lambertson magnet will be rolled 2.7° and the vertical bend magnet -4.0° to provide a small horizontal translation in order to create the proper horizontal trajectory required to match the P1 line. The vertical dipole magnet is a 1.5 m "modified B-1" type that will provide a 21 mrad bend, matching the bend of the Lambertson. There will be two quadrupoles located between the Lambertson and vertical dipole magnets that make up the dogleg between the RR and P1 line. Due to space constraints, the quadrupoles are shifted downstream from their ideal locations by 0.25 m. A more detailed technical descrip-

tion of the design features of the new beam line stub can be found in Ref. [15]. Figure 4.23 shows the lattice functions for the entire RR to Target Station line.

Figure 4.23: LATTICE FUNCTIONS FOR RR TO TARGET STATION `fg:accel_protonlatti`

Recycler orbit   The RR extraction scheme incorporates a permanent horizontal 3-bump in the RR that displaces the circulating beam outward 25 mm at the upstream end of the Lambertson (RLAM). Figure 4.24 shows the trajectories of the circulating and extracted beams, including the horizontal bump at the Lambertson. The bump is created by horizontal trim dipoles at the 524, 522 and 520 locations. The extraction kickers displace the extracted beam inward 25 mm at the same location. This creates a separation of the RR circulating beam and extracted beam at the front face of the Lambertson of 50 mm.

Apertures   Lambertson magnets are typically one of the limiting apertures in a beamline. The Recycler extraction Lambertson has an adequate aperture for both the circulating and extracted beams. Figure 4.25 shows the footprint of both beams at the Lambertson for both a 10σ and 6σ beam size. The vertical bend magnet has a relatively small horizontal aperture, but is located where the horizontal beta functions are small. The horizontal acceptance of the vertical dipole is actually larger than that of the Lambertson, despite the smaller physical aperture. The quadrupole and trim magnets are modeled after those in the Recycler and have good apertures.
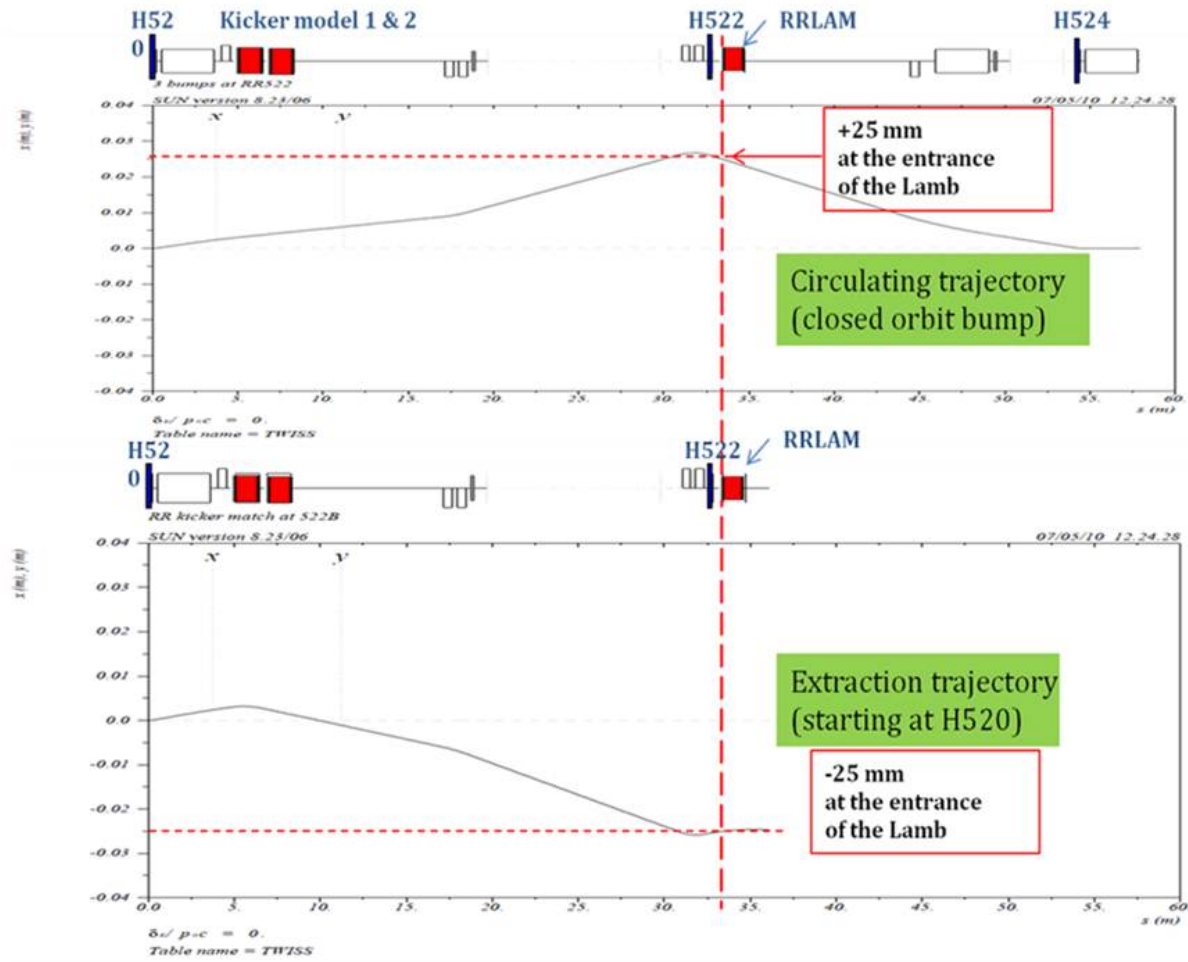
Figure 4.24: Horizontal trajectories for circulating and extracted beam from the RR. `fg:accel_proton`
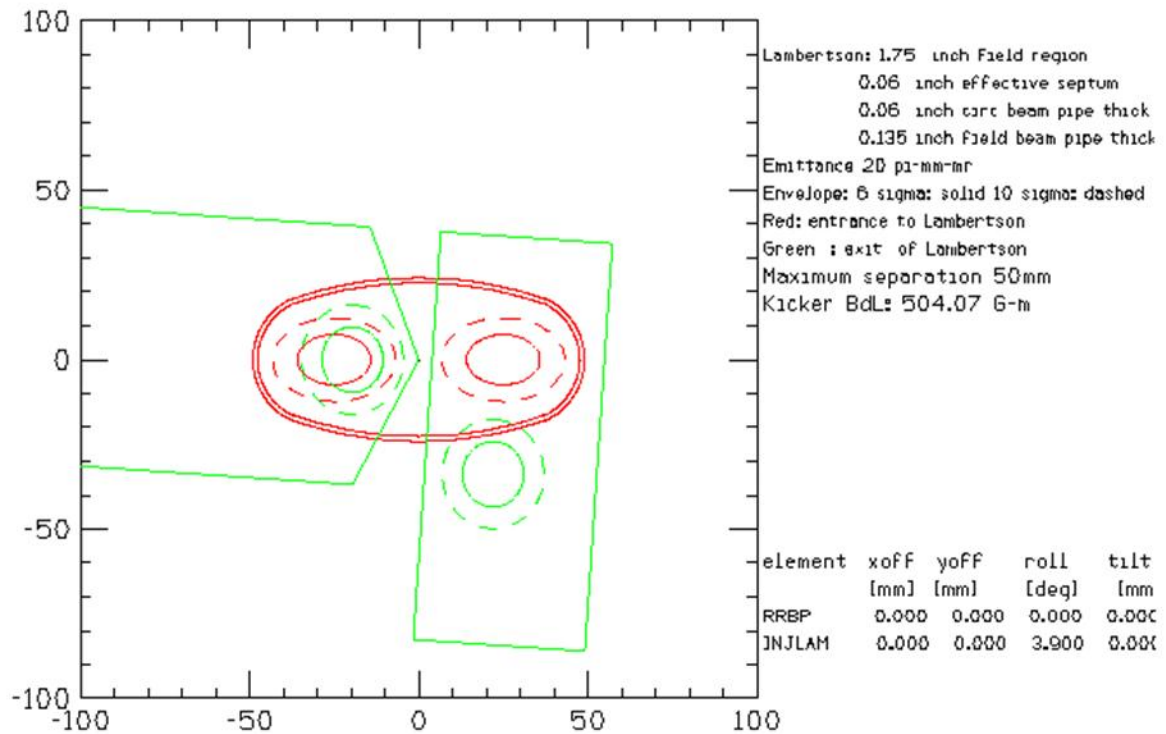
Figure 4.25: Beam sizes at the entrance (red) and exit (green) of the extraction Lambertson. The dashed outline represents 10σ and the solid outline 6σ beam for a normalized emittance

accel_RRlam   of 18 π-mm-mrad.

4.5.4 P1, P2 and AP-1 Aperture Improvements

The increased intensity and beam size planned for muon operation will lead to unacceptably high beam loss unless apertures are improved in the P1, P2 and AP-1 lines. Limiting apertures were identified during Collider Run II when evaluating possible improvements, simplifying the process of identifying locations. The elimination of AP-1 120 GeV operation for antiproton stacking provides an opportunity to improve the aperture with weaker magnets that previously were not practical for use as replacements.

The introduction of the P1-line stub has eliminated several aperture restrictions that were associated with Main Injector extraction. In particular, the vertical C-magnets that follow the MI-52 Lambertson will be avoided with the new stub line. Most of the P1 line after the P1-line stub has good aperture, until the former junction area with the Tevatron. The vertical dipole at the 714 location was installed as a C-magnet because of its proximity with the Tevatron and has a small horizontal aperture. The decommissioning of the Tevatron allows the replacement of this magnet with a conventional dipole that will increase the horizontal acceptance by more than 50%. The new magnet must also be capable of producing enough field strength to operate at 120 GeV and support SY120 operation. The four Tevatron F0 Lambertsons will no longer be needed to inject protons into the Tevatron and can be removed to improve the aperture, also in the horizontal plane.

In addition to the improvements to physical aperture, a new quadrupole is proposed in the region presently occupied by the Tevatron injection Lambertsons at F0. The long drift space in the P1 and P2 lines required for Tevatron injection results in large excursions in dispersion throughout the beamlines. Unless the dispersion is reduced, the increased momentum spread created by RR bunch formation will cause high beam losses. The addition of a quadrupole (or quadrupoles) in this region will provide the means to improve the optics of the transport lines.

The P2 line will remain a dual-energy line supporting $(g-2)$ and SY120 operation, so the junction between the P2, AP-1, and P3 beamlines at F17 will remain. The aperture for both $(g-2)$ and SY120 operation will substantially improve with the proposed replacement of the F17 C-magnets with a large aperture CDA magnet that both beams will pass through. The B-3 dipole at the F-17 location will remain.

AP-1 will only operate at 8 GeV for $(g-2)$ operation, so the eight EPB magnets that make up the HV100 and HV102 string can be replaced with larger, weaker dipoles. The number of dipoles can be reduced from four to two in each string. The 1.5 m "modified B-1" magnets (formally known as MDC magnets) have a pole gap that is 2.25 in instead of 1.5 in and provides more than a factor of two increase in acceptance. Several trims will also be replaced or relocated to complete the aperture upgrade. The final-focus region at the end of AP-1 is described separately in the next section. Table 4.7 summarizes the proposed improvements to the physical apertures in the RR to Target Station lines. Reference [15] has a more detailed explanation of the devices used to improve the aperture and how the improvements will be implemented.

Location	Existing magnet	Proposed improvement
V714	C-magnet	1 B2 magnet
F0 Lambertsons	4 Lambertsons	Remove magnets
F17 (V)	B3 and two C-magnets	1 CDA (retain B3)
HV100	4 EPB dipoles	2 MDC
HV102	4 EPB dipoles	2 MDC

Table 4.7: Proposed aperture improvements for RR to Target Station beamlines. `tb:accel_protonap`

`focustarget` **Final Focus Region**

The desired spot size on the production target, a proton beam σ in both planes of 0.15 mm, is the same as what was used in antiproton production during collider operation. Because the beam momentum is 8.89 GeV/c for $(g-2)$ operation instead of the 120 GeV/c that was used for antiproton production, much smaller beta functions are required to achieve this spot size (0.068 m vs. 0.878 m, respectively). The larger beam size would also lead to beam loss and reduced transfer efficiency with the existing quadrupole magnets and lattice, due to their aperture, length, and busing configuration. The existing quadrupoles in the AP-1 line are 3Q120 magnets that are 120 in (3.048 m) long and have a 3 in (76 mm) circular aperture. One advantage that the reduced beam momentum provides is the greatly reduced quadrupole gradients required to focus the beam. Figure 4.26 shows a modified version of the scheme proposed in Ref. [16], where a quadrupole triplet replaces the last quadrupole, PQ9B, in the AP-1 line. Figure 4.26 shows the optics in the final 50 m of the AP-1 line where the final focus occurs. The PQ8A&B and PQ9A magnets are not powered and can be removed to improve aperture, if desired. The peak beta functions in the quadrupole triplet are reduced by shifting the magnets as close to the vault wall as possible. By removing the Beam Sweeping system used in Pbar operation and relocating toroid TOR109, the triplet can be shifted by more than 2 m (this configuration is shown in Fig. 4.26). It is also advantageous to use shorter quadrupole magnets in the triplet as another means of locating the magnets further downstream. There are two magnet options using available magnets that are under consideration. Both are relatively compact and have adequate apertures. The first is a 4Q16 – 4Q24 – 4Q16 (from BNL) grouping and the other is made up of an SQA – SQC – SQA (Pbar) combination. Even without the shorter magnets, the desired spot size of $\sigma_x = \sigma_y = 0.15$ mm can be achieved at the production target.
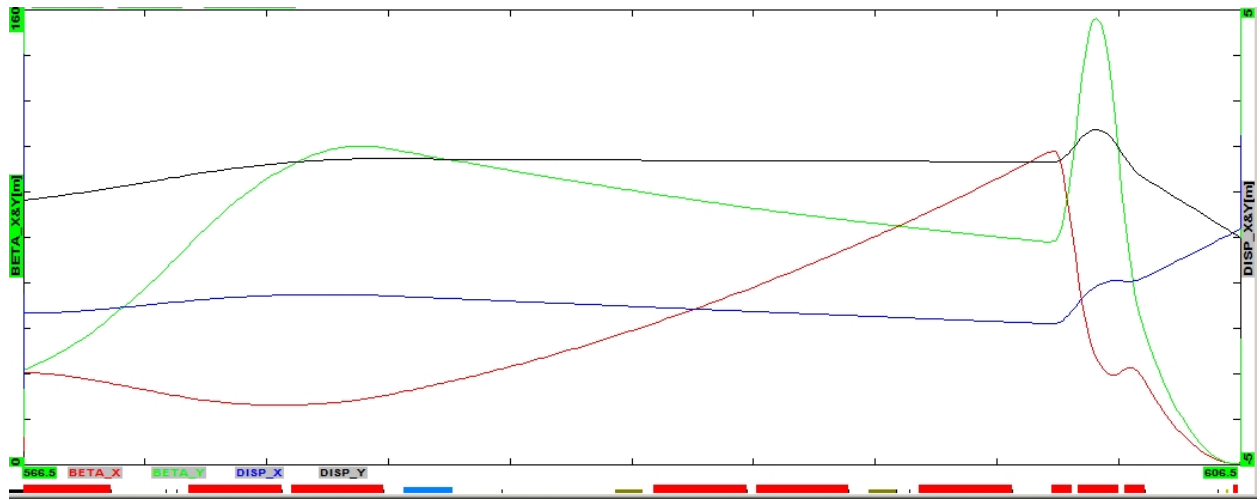
Figure 4.26: Beta functions (horizontal is red, vertical is green) and dispersion functions (horizontal is blue, vertical is black) for final focus region of AP-1 line.

_finalfocus

4.5.5   Pion to muon decay beam lines

4.5.6   Delivery Ring

The Pbar Debuncher ring will largely remain intact for $(g-2)$ operation and will be renamed the Delivery Ring for its new role in providing muons to the experiment. A considerable amount of equipment left over from Pbar operation will need to be removed from the Debuncher. Most of the equipment targeted for removal was used for stochastically cooling the antiproton beam during collider operation and is not needed for $(g-2)$. Some of these devices also have small apertures, so the ring acceptance will be improved with their removal. The cooling tanks in the D30 straight section also need to be removed to provide room for the new injection and extraction devices.

The Pbar Accumulator ring will not be needed for $(g-2)$ and Mu2e operation and will become a source of magnets, power supplies and other components for use in the reconfigured beamlines. In particular, the M4 (extraction) line will be largely made up of former Accumulator components. Some larger-aperture magnets will also be needed in the injection and extraction regions and will come from the Accumulator or other surplus sources.

Rings Lattice and Acceptance

The original design lattice for the Debuncher will be used for the Delivery Ring with few modifications. The lattice has a 3-fold symmetry with additional mirror symmetry in each of the three periods, with three zero-dispersion straight sections: D10, D30 and D50. The original lattice parameters were largely dictated by the requirements for Pbar stochastic cooling and the RF systems. The Debuncher was designed with a large transverse and longitudinal momentum acceptance in order to efficiently RF-debunch and stochastically cool antiprotons from the production target. This lattice design is also well suited for $(g-2)$ operation. During Collider Run II, the original lattice was distorted somewhat in order to reduce the beam size in the stochastic cooling tanks that had limiting apertures. Since these tanks will be removed, the lattice that will be used for the $(g-2)$ conceptual-design work will
fig:accel_DRlattice
revert back to the original Debuncher design lattice. Figure 4.27 shows the lattice functions for one period of the Debuncher.

It should be noted that the design acceptance of the Debuncher was 20 π-mm-mr. During the 25 years of Pbar operation, numerous aperture improvements were undertaken to boost the acceptance of the Debuncher. After the final Collider Run II aperture improvements were put in place in 2007, the measured acceptance of the Debuncher was as high as 33 π-mm-mr in both transverse planes. The $(g-2)$ design goal of a 40 π-mm-mr acceptance for the Delivery Ring, while reusing as much of the original equipment as possible, presents a difficult challenge.

The transverse acceptances of the Debuncher dipole, quadrupole, sextupole, and trim magnets are quite large. The smallest magnet acceptance is in the vertical plane of the dipoles and is approximately 54 π-mm-mr on one end, growing to 79 π-mm-mr on the other end. The dipoles have a 90 π-mm-mr or larger horizontal acceptance (90 π-mm-mr for the $\pm 2\%$ momentum spread and locations with the largest dispersion) and the other magnets have a 100 π-mm-mr or larger acceptance in both planes. Since the original Debuncher lattice will not be significantly changed for $(g-2)$ operation, the main Delivery-Ring magnets will
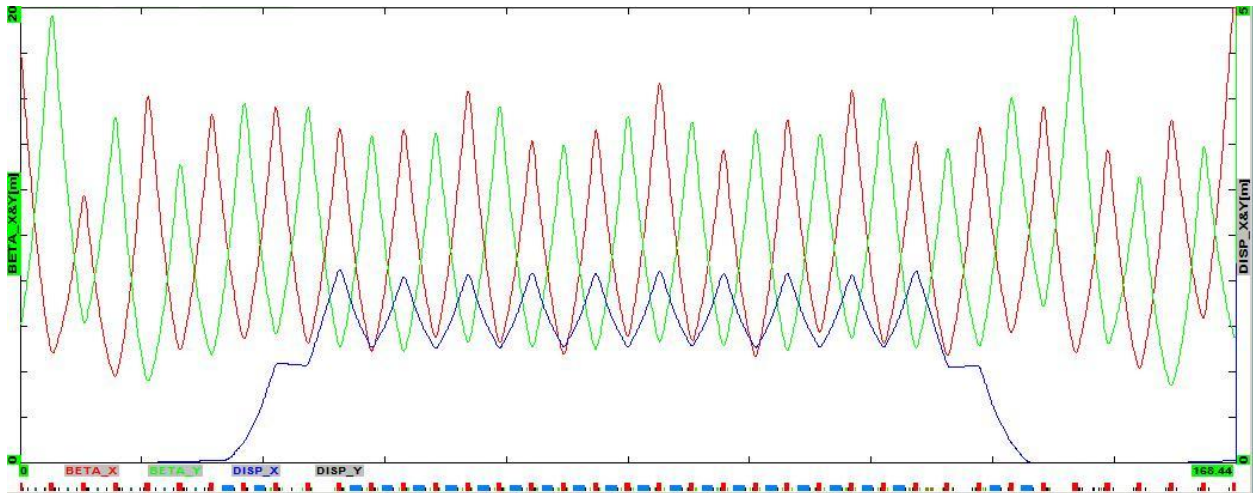
Figure 4.27: Debuncher/Delivery Ring lattice functions through 1/3 of the ring. β_x is in red, β_y in green, and horizontal dispersion in blue.

not be limiting apertures. In general, devices with a physical aperture of 50 mm or greater provide an acceptance of over 40 π-mm-mr in the Debuncher, and select locations can provide that acceptance for devices that have an aperture of 40 mm, as long as they are relatively short.

During Collider operation, the smallest physical apertures in the Debuncher came from stochastic cooling tanks, RF cavities, instrumentation, and devices used for injecting and extracting beam. Many of these devices will be removed as part of the repurposing of the Debuncher for the muon experiments. Some of these devices, most notably the kickers, will be retained in the interest of economy and/or complexity and lead-time of manufacture. Other devices, such as the injection septa, will be new devices with necessarily small physical apertures in order to provide enough bend strength.

During Collider Run II, the Band-4 stochastic cooling tanks were the limiting aperture in both planes of the Debuncher. The Band-4 tanks had a 38 mm physical aperture in the cooling plane, and there were both horizontal and vertical pick-up and kicker tanks in the D10 and D30 straights respectively. All of the stochastic cooling tanks will be removed prior to $(g-2)$ operation.

There is only one RF cavity planned for the Delivery Ring, which is needed to support Mu2e operation and will have an aperture similar to the Debuncher rotator cavities. Since the rotator cavities had an acceptance that was greater than 100 π-mm-mr, the new cavity will have ample aperture and need not be removed when switching from operating Mu2e to $(g-2)$. All RF cavities used for antiproton production will be removed prior to $(g-2)$ operation.

Many of the beam detectors used during Pbar operation had small physical apertures in order to improve sensitivity. Since the beam intensities when running $(g-2)$ are expected to be even smaller than those seen during Pbar operation, designers will need to be mindful of the aperture needs of the $(g-2)$ experiment. Similarly, when instrumentation is being considered for reuse in the Delivery Ring, the physical aperture and proposed tunnel location should be analyzed for adequate acceptance.

The transverse Schottky detectors used in the Debuncher had apertures that were only slightly larger than the Band-4 stochastic cooling pick-up. They were removed from the Debuncher during Run II, but have been reinstalled for use during $(g-2)$ and Mu2e studies. Although these Schottkys are slated for removal prior to $(g-2)$ operation, the Mu2e experiment may need a new device to monitor tunes during resonant extraction. If a new device is made, it will need to have adequate aperture for $(g-2)$ or will have to be removed when switching between the two experiments. The DCCT beam-intensity monitor will also be used by the Mu2e experiment. It is expected to have adequate aperture as long as it is located in the middle of a straight section half-cell, where the beam has a circular cross-section.

Both injection from the M3 line and extraction to the M4 line take place in the D30 straight section. Injection will be located in the upstream half of the straight section, and the pulsed magnetic septum and kicker magnets will have small apertures in order to provide adequate bending strength. The septum has a small aperture in both planes, while the kicker is primarily limited in the horizontal plane. The septum is a modified Booster-style (BSE) magnetic septum magnet. The septum modifications involve increasing the pole gap from 28 mm to 42 mm in order to greatly improve the horizontal acceptance, and reducing the septum thickness from 14 mm to 9 mm to increase the vertical acceptance. The injection kicker system will be made up of two surplus Pbar AP-4 injection kicker magnets. The horizontal aperture is only 41 mm and will likely be one of the limiting apertures of the Delivery Ring. The extraction kicker system will be made up of two Pbar extraction kicker magnets. They have a vertical aperture of 41 mm and will also be one of the limiting apertures of the Delivery Ring.

l_DRkickers

Kickers and Septa

The kickers and septa required for $(g-2)$ operation will need to operate at a much higher frequency than that used for antiproton production, with peak rates increasing as much as a factor of 30. In an effort to make the new kicker systems more economical, existing kicker magnets will be reused. Kickers will be required for injection and extraction from the Delivery Ring as well as for proton removal. Table 4.8 compares kicker parameters for existing Pbar systems to the specifications for the $(g-2)$ injection and proton-removal kickers. The rise and fall time specifications for $(g-2)$ are less strict than what was needed for antiproton production, due to the short bunch length of the muons (and protons). Although the Pbar kicker magnets are suitable for reuse, new power supplies will be needed to operate at the increased rate. Resistive loads for the kickers will need to be cooled with Fluorinert. A single Fluorinert distribution system is planned, with piping bridging the distance between the load resistors from kickers in the 30 and 50 Straight Sections.

The septa and pulsed power supplies used during Pbar operation are not suitable for rapid cycling and cannot be used for $(g-2)$. The septa have no internal cooling to handle the increased heat load from the planned high duty cycle, and the power supplies are not able to charge quickly enough. The Booster-style septum magnets can be modified to have the necessary size and field strength required for use in the injection and proton removal systems, and therefore are the preferred choice. The power supplies used in the Booster to power the septum magnets also appear to be a good fit. Although they are designed to operate at a lower frequency (15 Hz) than the peak needed for $(g-2)$, the lower operating current

Kicker (modules)	Integrated Field (kG-m)	Kick Angle (mrad)	Rise Time 95%/5% (ns)	Fall Time 95%/5% (ns)	Flat Top Time (ns)
Debuncher Extraction (3)	1.34	4.6	150	140	1700
Debuncher Injection (3)	1.81	6.1	180	150	1700
Delivery-Ring Injection (2)	0.57	6.1	n/a	450	450
Delivery-Ring Extraction (2)	0.72	7.0	450	n/a	450
Delivery-Ring Proton Removal (3)	0.57	6.1	450	n/a	1700

Table 4.8: Existing Pbar (top) and future $(g-2)$ (bottom) kicker strength and waveform specifications. `l_DRkickers`

(for 3.1 GeV/c versus 8.89 GeV/c momentum) should more than compensate for changes to the heat load and mechanical stresses due to the increased pulse rate. The Booster septum magnets are slightly shorter than their Pbar counterparts, so the new septa can fit where the Debuncher injection septum presently resides.

Delivery Ring D30 straight section

The Delivery-Ring injection and extraction regions will both be located in the D30 straight section. In both cases, the tight quadrupole spacing in the Delivery Ring creates physical conflicts with existing utilities and ring devices in the areas of elevation change to and from ring level. The existing cable trays on the Debuncher side of the ring will need to be completely dismantled and relocated towards the middle of the tunnel so that the new beamlines can be hung from the ceiling. The extraction line will closely follow the trajectory of the decommissioned AP-4 (Booster to Debuncher) line. The tunnel in this region has an existing stub region that the extraction line will pass through, eliminating the need for civil construction to widen and strengthen the tunnel. Figure 4.28 shows the layout of injection and extraction devices in the D30 straight section.
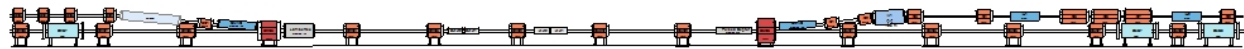

Figure 4.28: D30 straight section, injection on right, extraction on left. `fg:accel_D30straight`

Injection

The M3 line runs above the Delivery Ring in the upstream end of the D30 straight section and ends with a vertical translation into the ring. M3 injection will be achieved with a combination of a C-magnet, magnetic septum, D3Q3 quadrupole, and kicker magnets, which will all provide vertical bends. The septum and C-magnet are both based on existing designs, which reduces overall costs, but modified to improve the aperture. Both magnet designs required modifications in order to attain the $(g-2)$ acceptance goal of 40 π-mm-mr.

The magnetic septum is a modified Booster-style (BSE) magnet, with an increased pole gap and a thinner septum to improve aperture. The BSE magnet has a 1.1-in pole gap, which

will be increased to 1.65 in for the new septum. Similarly, the C-magnet is a larger aperture (2.1 in instead of 1.6 in) and shorter (2.0 m instead of 3.0 m) version of the Main-Injector ICA magnet. An identical C-magnet is used in the extraction region. The descending beam in M3 will pass through the C-magnet first and will be bent upward by 38 mr. The beam will continue well above the center of the D3Q3 quadrupole and receive a 30-mr upward kick. Since the beam is up to 140 mm above the centerline of the quadrupole, a large-bore quadrupole magnet is required in order to provide adequate aperture. The large quadrupole at D3Q3 will be the LQE magnet from the D2Q5 location, which will be replaced by an 8-in quadrupole, as described below. The LQx magnets were designed to have a substantial good-field region that extends between the poles. Similar arrangements with LQ magnets can be found in Pbar at D4Q5 (former AP-2 injection, planned proton removal) and D6Q6 (former Debuncher extraction). The injected beam then passes through the field region of the septum magnet and receives a 37-mr upward bend as required for the necessary trajectory entering the injection kicker magnets. The kicker magnets provide a final 6.1-mr vertical bend to place the injected beam on the closed orbit of the Delivery Ring.

The two-module kicker system is located between the D30Q and D2Q2 magnets. To minimize the horizontal β function and maximize acceptance, the kickers will be located as close to the D2Q2 quadrupole as possible. Spare Pbar injection kicker magnets will be refurbished and reused for muon injection. The magnets are already designed to be oriented vertically, so little additional effort will be required to convert them to their new application. Kicker rise and fall time specifications and power supply information was provided in Table 4.8 and the accompanying text. Figure 4.29 shows the injection devices and their location in the Delivery Ring, along with their bend angles. Due to the large vertical excursion through the top of the D3Q2 magnet, a vertical bump across the injection region will be incorporated to lower the beam and improve the aperture. The quadrupole magnets at D2Q2, D30Q and D3Q4 will be displaced to create the bump by generating steering due to the beam passing off-center through the magnets. To create a 15-mm downward displacement at D3Q2, the magnets will be lowered by 8.1, 11.0, and 4.2 mm respectively. It would be beneficial, but not necessary for 40 π-mm-mr acceptance, to install an existing "extended star chamber" quadrupole at the D3Q2 location. SQD-312, in magnet storage, was previously located at D4Q4 in the Pbar AP-2 injection area and has an extended top lobe in its star chamber.
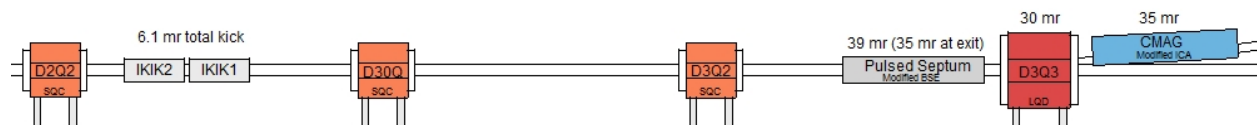

Figure 4.29: Delivery-Ring injection devices. `fg:accel_DRinjection`

Extraction

Extraction from the Delivery Ring takes place in the downstream half of the 30 Straight Section. The extraction channel and the first 60 m of the M4 line will be used for both

Mu2e resonant extraction and $(g - 2)$ single-turn extraction. This arrangement avoids the complexity and additional expense of dual extraction lines in the limited available space. It also eliminates the need to remove potentially highly radioactive objects from the ring when switching between experiments. The ideal extraction configuration will provide enough aperture for both the Mu2e resonantly-extracted proton beam and the $(g - 2)$ muon beam to be transported efficiently through the M4 line.

A Lambertson and C-magnet pair will be used, in conjunction with the intervening D2Q5 quadrupole, to bend the beam upward out of the ring. In the interest of compatibility between $(g - 2)$, Mu2e, and future muon experiments, a Lambertson magnet is required for extraction. The resonant-extraction process used for Mu2e is very restrictive on the size, strength, and location of the electrostatic septa that are required to split the extracted beam. The electrostatic septa must be located on either side of the D2Q3 quadrupole, and are expected to be about 1.5 m in length. In order to achieve the goal of a combined extraction channel and beamline, the $(g - 2)$ extraction kickers must be located in a lattice location that is $n\pi/4$ radians from the Lambertson, where n is an integer, and in an area not already occupied by injection or extraction devices.

The $(g - 2)$ extraction kickers will be located between the D2Q2 and D2Q3 quadrupoles. There will be two kicker modules of approximately 0.85 m length each. During the dedicated period of $(g - 2)$ operation, the kickers will be located as close to the D2Q3 quadrupole as possible in order to minimize the vertical β function and maximize acceptance. The kicker magnets will be repurposed Pbar extraction kicker magnets that have a vertical aperture of 41 mm. The kicker magnets will be powered in series from a single power supply. There is also an alternative layout planned that would allow $(g-2)$ to operate after the Mu2e electrostatic septa are installed. There is only room for a single kicker near the D2Q2 quadrupole in this arrangement, so the kicker inductance would need to be lowered to provide enough bending strength. The relocation of the kicker would also reduce aperture unless the β functions in this region could be suppressed by about 20%. Figure 4.30 shows the layout of the extraction devices for dedicated $(g - 2)$ operation and 40 π-mm-mr acceptance.
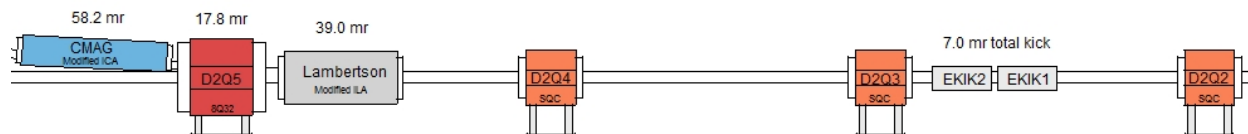

Figure 4.30: Delivery-Ring extraction devices. `fg:accel_DRextraction`

Proton Removal (Abort) System

The proton removal system is an example of both repurposing an otherwise unneeded part of the Antiproton Source and implementing a dual function system that can be used by both $(g - 2)$ and Mu2e. During Mu2e operation, an abort is needed to minimize uncontrolled proton beam loss and to "clean up" beam left at the end of resonant extraction. The proton beam must be removed quickly, by means of kicker magnets, in order to minimize losses in

the ring. The $(g-2)$ experiment can benefit from the removal of protons before they reach the storage ring. The abort system can serve this purpose, as long as the protons sufficiently slip in time to create a gap for the kickers to rise through.

The old Debuncher injection point from the AP-2 line in the D50 straight section will be used for the abort and proton removal systems. Recall that most of the AP-2 line will be removed and replaced with the new M2 line that will merge with the M3 line upstream of the right bend. The downstream end of AP-2, where antiprotons were formerly injected into the Debuncher, can now be used to extract protons from the Delivery Ring. This is made possible by the change in beam direction (as viewed from above) from clockwise to counterclockwise. The existing Pbar injection kicker magnets can be reused, although a new power supply will be needed to operate at the frequency needed to support Mu2e and $(g-2)$. The septum magnet and power supply will also need to be upgraded for the same reason. The new larger-aperture septum magnet will be identical to what was previously described for injection into the Delivery Ring. The section of the AP-2 beamline being repurposed will require the addition of a vertical bending magnet to steer beam into the abort dump located in the middle of the Transport tunnel. Figure 4.31 shows the layout of the abort line.
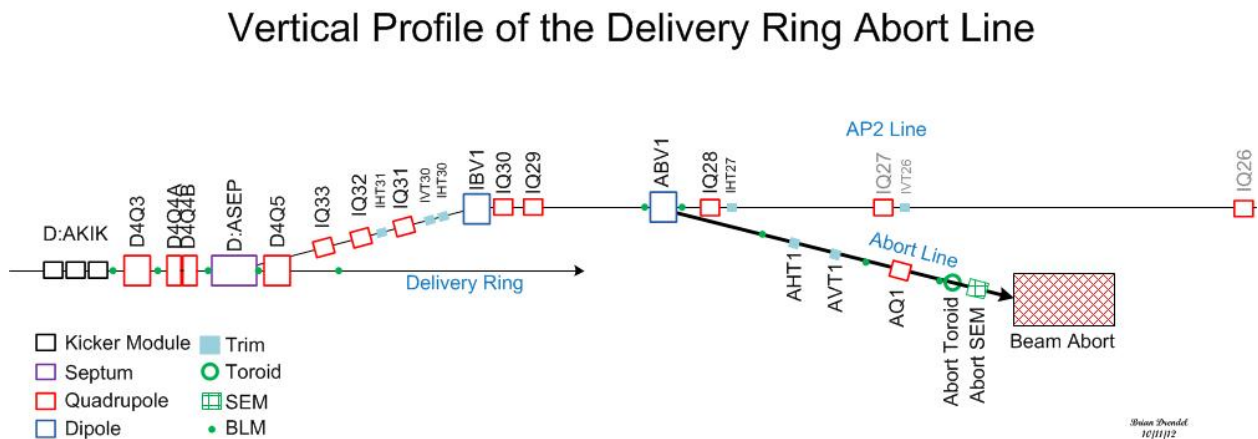

Figure 4.31: Side view of the Delivery Ring Abort/Proton Removal line. `fg:accel_DRabort`

The most economical plan is to power the three kicker magnets in series, which requires only a single power supply. The rise time of the kickers with this configuration is about 450 ns. This rise time is more than adequate for Mu2e operation, because the single 120-ns bunch is very short compared with the 8 GeV proton revolution period of 1695 ns. For $(g-2)$ proton removal, the 450-ns rise time requires several revolutions around the Delivery Ring to provide enough gap between the muons and protons for the kicker to rise through. Table 4.9 lists the separation between the beams and the gap size for different numbers of turns. Seven turns around the Delivery Ring would be required to cleanly remove all of the protons without disturbing the muons. The table is based on the assumptions already stated: that the kicker rise time is 450 ns, the proton and muon bunch lengths are 120 ns and that the kicker should not disturb any of the muons.

As the kicker magnets "fill" during the rising current waveform, the kicker magnetic field and bending strength increase proportionally. Protons are completely removed from the Delivery Ring when the kicker strength is about 85% of what is needed to center beam

	Muon vs. Proton		
	Centroid time difference (ns)	Gap size (ns)	Impact of proton removal kickers
Injection	40	None	Unable to kick protons only
1st turn at Abort	91	None	Unable to kick protons only
2nd turn at Abort	161	41	11% of protons removed
3rd turn at Abort	231	111	29% of protons removed
4th turn at Abort	301	181	48% of protons removed
5th turn at Abort	371	251	66% of protons removed
6th turn at Abort	441	321	84% of protons removed
7th turn at Abort	511	391	Protons cleanly removed
8th turn at Abort	581	461	Protons cleanly removed

Table 4.9: Efficiency of proton-removal system for different number of turns in the Delivery Ring, based on a 120-ns bunch length and 450-ns kicker rise time.

accel_DRturns

in the abort channel. Between 85% and 100% of the nominal kicker strength, some of the protons will be lost on the Abort Septum instead of traveling to the abort. As the kicker strength drops below 85%, an increasing number of protons remain in the Delivery Ring.

In addition to separating the beams to improve removal efficiency, the percentage of protons removed can also be increased by firing the kicker earlier and disturbing part of the muons. Another option is to shorten the rise time of the kickers to 200 ns with the introduction of a second power supply and commensurate doubling of the power-supply cost. With a 200-ns kicker rise time, the gap between beams must be 168 ns or larger (achieved with 4 turns) to remove all of the protons.

A side benefit of the muons taking multiple turns around the Delivery Ring is that virtually all of the pions will have decayed before the muons reach the storage ring. The primary potential problem with this proton removal concept is due to differential decay systematic errors caused by the different muon path lengths as they travel through the Delivery Ring. Although a preliminary analysis indicates that this will not be a significant problem [17], a more thorough analysis is needed.

accel_gm2doc252

Vacuum Systems

The existing vacuum systems in the rings and transport lines have performed very well during Pbar operation. Typical vacuum readings in the Debuncher and transport lines were approximately 1×10^{-8} Torr. The Debuncher has good ion-pump coverage that should generally be adequate for $(g-2)$ operation. Stochastic cooling tanks, kickers and septa that will be removed during the conversion have built-in ion pumps, so some of these pumps may need to be installed in the vacated spaces. Injection and extraction devices should have ion pumps integrated into the design, or there should also be additional pumping capacity added to the surrounding area. Vacuum components from the AP-2 and AP-3 lines should provide most of the needs for the reconfigured M2 and M3 lines. The Accumulator has enough surplus ion pumps and vacuum pipe available to cover part of the needs for the extraction beamlines.

Infrastructure Improvements

Electrical power for the Antiproton Source is provided by Feeder 24, which operated with a power level of about 4.4 MW during Pbar operation. Although the $(g-2)$ power load is expected to be considerably less than what was used in Pbar by virtue of the reduced beam momentum, the Mu2e experiment must also be able to operate the same magnets at 8.89 GeV/c. For Mu2e, most service buildings are expected to use approximately the same amount of power as they did in Pbar operation. The exception is the AP-30 service building, where there will be a large increase in power load from the injection- and extraction-line power supplies. A new transformer may be needed at AP-30 to provide the additional power. A power test was performed on the individual service building transformers to aid in predicting the power needs for Mu2e [18]. Also, since the Accumulator will no longer be used, approximately 1.4 MW will be available for new loads.

Presently, Pbar magnets and power supplies receive their cooling water from the Pbar 95° Low Conductivity Water (LCW) system. The cooling requirements for $(g-2)$ are expected to be lower than for Pbar operation. However, Mu2e will operate at 8.89 GeV/c and create a substantially larger heat load than $(g-2)$. Fortunately, the removal of the heat load from decommissioning the Accumulator and the AP-2 line should be enough to offset the increase from the extraction line and other new loads. The extraction beamlines (M4 and $(g-2)$ lines) will have an LCW stub line connecting to the Debuncher header in the 30 Straight Section. If necessary, it is also possible to design smaller closed-loop systems that heat-exchange with the Chilled Water system. The Chilled Water system has adequate capacity and is already distributed to the Pbar service buildings.

4.5.7   Muon transport to storage ring

ControlsInstrum

4.6   Controls and beam monitoring

:AccelCtrls

4.6.1   Accelerator controls

A well-established controls system allows devices in the former Anitproton-Source ("Pbar"), now Muon, service buildings and tunnel enclosures to receive information such as synchronization signals and to communicate back to other accelerator systems. A map of the service buildings, labeled "AP" for former Antiproton-Source buildings, and "F" for buildings which are part of the F-sector of the Tevatron, is shown in Fig. 4.32. Devices in the new extraction beamlines and MC-1 building will also need to be connected to the controls system.

Figure 4.32: Muon Campus service buildings. `fg:accel_svcbldgs`

CAMAC and links

The existing accelerator service buildings will continue to use the legacy controls infrastructure that is currently in place. These service buildings include all of the Main Injector service buildings, as well as F0, F1, F2, F23, F27, AP0, AP10, AP30 and AP50. Future Muon Campus service buildings, including MC-1 and Mu2e, will be upgraded to a more modern controls infrastructure which will be discussed later in this document. Migration of the existing buildings to the more current controls standard is preferred and is being considered; however, sufficient funding is not available to start the upgrade path and it is believed that the existing infrastructure will be adequate for $(g-2)$ operations.

Computer Automated Measurement and Control (CAMAC) crates exist in each service building and communicate with the control system through a VME-style front-end computer

over a 10 MHz serial link as shown in Fig. 4.33. Both digital and analog status and control of many accelerator devices occur through the CAMAC front ends. There should be no need to install additional CAMAC crates, as there is excess capacity in most of the existing crates. An inventory of existing CAMAC crates in the Muon service buildings shows that about 25% of the slots are unoccupied and could be used for additional CAMAC cards [19]. In addition, further slots have become available that were used to interface devices that became obsolete with the retirement of Collider Run II operations. It is anticipated that there will be ample CAMAC-crate coverage for $(g-2)$ operation in the existing Muon service buildings, and very few crates will need to be added or moved.
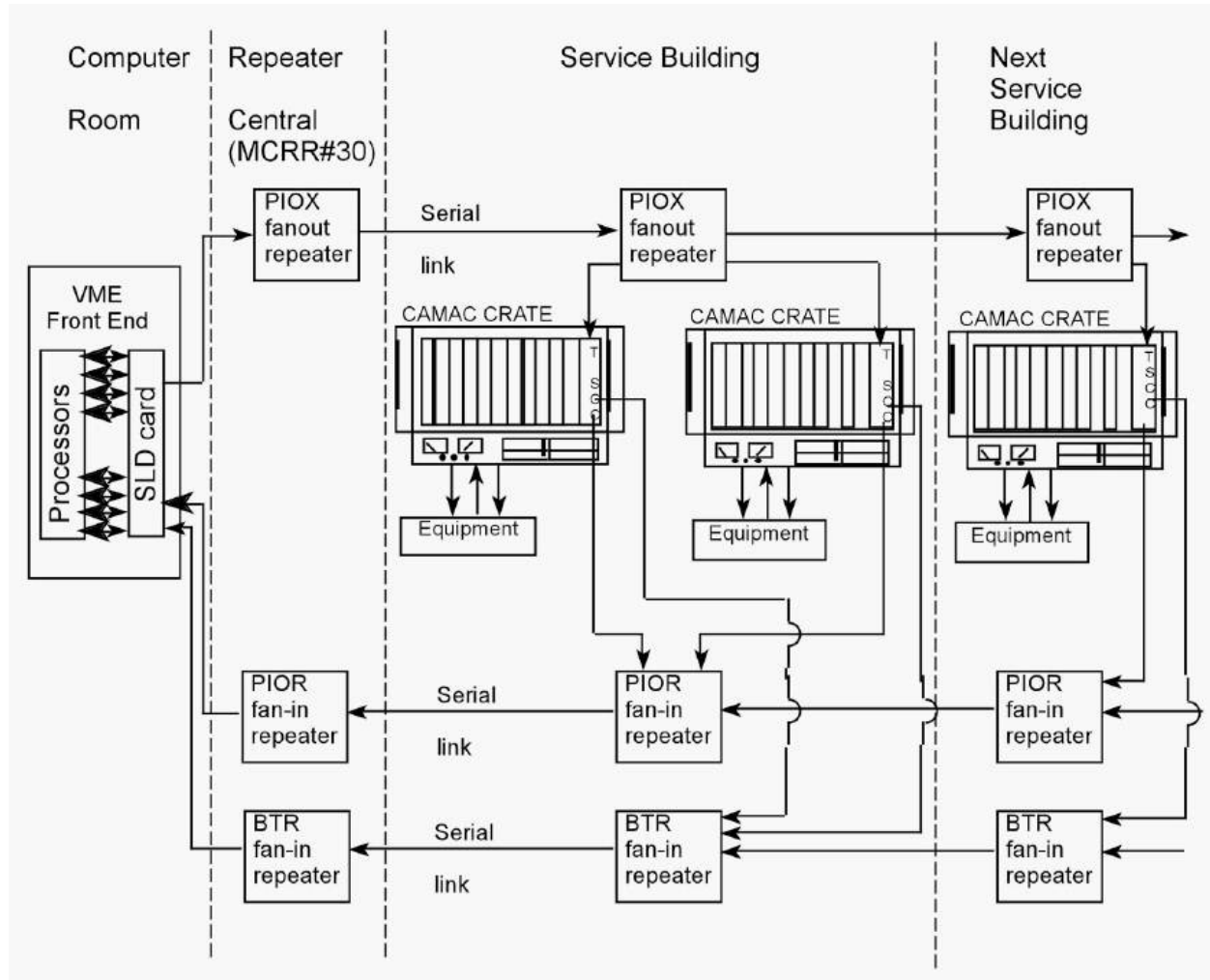

Figure 4.33: Legacy CAMAC crates interfacing VME front ends via serial links provide both analog and digital status and control of accelerator devices, and will continue to be used in existing Muon service buildings.

There are serial links that are distributed through and between the service buildings, via the accelerator enclosures, that provide the necessary communications paths for CAMAC as well as other necessary signals such as clock signals, the beam permit loop, and the Fire and Utilities System (FIRUS). Controls serial links can be run over multimode fiber-optic

cable or copper Heliax cable. Most Muon links that run through accelerator enclosures are run over Heliax, which should function normally in the radiation environment expected for $(g-2)$ operations.
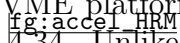
Accelerator device timing that does not require synchronization to the RF buckets will remain on the existing 10 MHz Tevatron Clock (TCLK) system. The existing TCLK infrastructure will remain in existing service buildings and new TCLK link feeds will be run via multimode fiber optic cable from the Mac Room to the new MC-1 and Mu2e service buildings.

Accelerator device timing for devices that require synchronization to the RF buckets will continue to be handled through the Beam Synch Clocks; however, a few changes will be required to maintain functionality. The F0, F1 and F2 service buildings will need both 53 MHz Main Injector beam synch (MIBS) for SY120 operations and 2.5 MHz Recycler beam synch (RRBS) for $(g-2)$ and Mu2e operations. These buildings already support multiple beam synch clocks, so the addition of RRBS will require minimal effort. An obsolete 53 MHz Tevatron beam synch (TVBS) feed in the MI60 control room will be replaced with a 2.5 MHz RRBS feed in order to provide the necessary functionality. The remaining Muon service buildings currently use 53 MHz MIBS, but will require 2.5 MHz RRBS for $(g-2)$ and Mu2e operations. This functionality can be obtained by replacing the MIBS feed at F0 with RRBS and using the existing infrastructure. Further upgrades and cable pulls will only be required if it is later determined that both MIBS and RRBS are required in these service buildings. New beam synch feeds to the $(g-2)$ and Mu2e service building will be run via multimode fiber-optic cable from the Mac Room.

The Delivery-Ring permit loop provides a means of inhibiting incoming beam when there is a problem with the beam delivery system. The Pbar beam permit infrastructure will be used in the existing buildings. The CAMAC 201 and 479 cards, which provide the 50 MHz abort loop signal and monitor timing, will need to be moved from the Mac Room to AP50 to accommodate the addition of the abort kicker at AP50. Existing CAMAC 200 modules in each CAMAC crate can accommodate up to eight abort inputs each. If additional abort inputs are required, spare CAMAC 200 modules will be repurposed from the Tevatron and will only require an EPROM or PAL change. The permit loop will be extended to the MC-1 and Mu2e service buildings via multimode fiber-optic cable from the Mac Room. Abort inputs for these buildings will plug into a Hot-Link Rack Monitor abort card as will be mentioned below.

Operational and permit scenarios are under development. The capability of running beam to the Delivery-Ring dump when Mu2e and $(g-2)$ are down will be needed, as well as the ability to run to either experiment while the other is down.

Hot-Link Rack Monitor

New controls installations will use Hot-Link Rack Monitors (HRMs) in place of CAMAC. A HRM runs on a VME platform that communicates with the control system over Ethernet as shown in Fig. 4.34. Unlike CAMAC, no external serial link is required, minimizing the need for cable pulls between buildings. Each HRM installation provides 64 analog input channels, 8 analog output channels, 8 TCLK timer channels, and 8 bytes of digital I/O. This incorporates the features of multiple CAMAC cards into a single, compact chassis.

Like CAMAC, when additional functionality or controls channels are needed, additional units can be added. As an example, a HRM version of the CAMAC 200 module will be constructed to provide inputs into the Delivery-Ring permit system. One or two HRMs will be installed in both the MC-1 and Mu2e buildings and should provide ample controls coverage for both accelerator and experimental devices.

Figure 4.34: A Hot-Link Rack Monitor is a flexible data acquisition system composed of a remote unit and a PCI Mezzanine card that resides in a VME crate. Each HRM provides provides sixty four 16 bit analog input channels, 8 analog output channels, 8 TCLK timer channels and 8 bytes of digital I/O. HRM.s will eventually replace all of the functionality of CAMAC [20].

HRMs are expected to eventually replace legacy CAMAC systems in the existing buildings. This migration will start by replacing existing 12-bit MADCs and CAMAC 190 cards for analog readings with 16-bit HRM channels. This option was considered for $(g-2)$ operation, but was determined to be impractical considering expected funding, limited legacy Ethernet connectivity in three of the Muon service buildings, and the determination that the existing CAMAC would likely provide adequate performance for $(g-2)$ operations.

Ethernet

Many modern devices have some form of Ethernet user-interface. In addition, many devices and remote front-ends use Ethernet to interface with the control system, instead of using the traditional CAMAC. The results are an increasing demand on the Controls Ethernet. Figure 4.35 is a map of the Muon Controls network. All of the current Muon Ring service buildings have Gigabit fiber-optic connections from the Cross-Gallery computer room to Cisco network switches centrally located in each service building. These will provide ample network bandwidth and connections after the reconfiguration for $(g-2)$ and Mu2e. A central Ethernet switch that fans out to the other Muon Department buildings is currently located in AP10, but will need to be moved to AP30, as will be discussed later in this document.

Ethernet connects between the Muon-Ring service buildings via multimode fiber-optic cable paths that traverse the Rings enclosure on the Accumulator side. The multimode fiber currently in place will remain functional during $(g-2)$ operations. However, in the higher-radiation environments expected during Mu2e operations, these fiber-optic cables will need
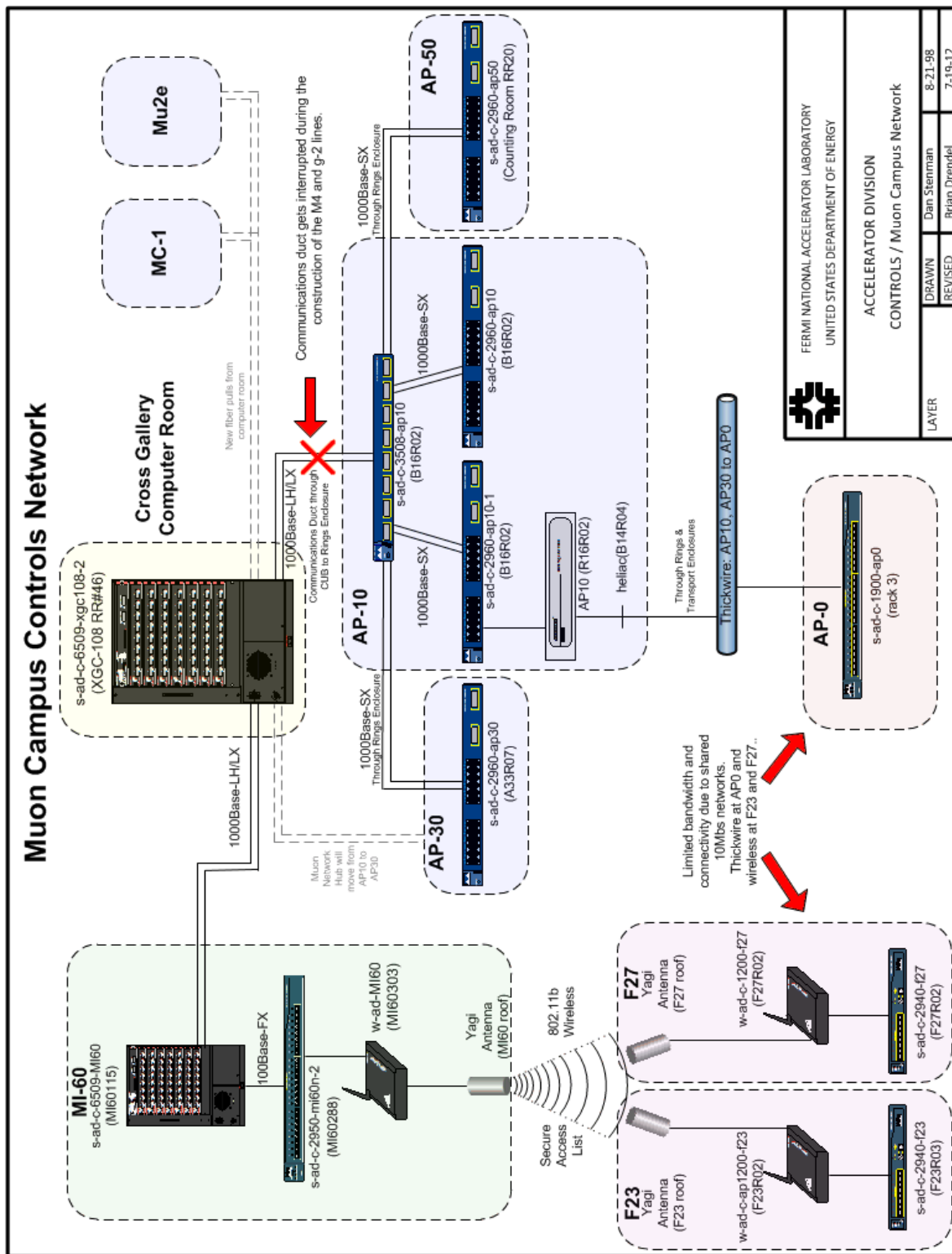
Figure 4.35: Controls Ethernet to the Muon Department service buildings is expected to be adequate for $(g-2)$ operations. The central switch at AP10 will be moved to AP30. Legacy networks at AP0, F23, and F27 have limited bandwidth and connectivity.

to be upgraded to single-mode fiber at a minimum, or to the more costly radiation-hard fiber if radiation rates are too high.

Most beam line service buildings have gigabit fiber connected to centrally located network switches that provide ample network bandwidth and connections. AP0, F23, and F27 are the only three buildings that do not have this functionality. AP0 runs off a 10 Mbps hub that connects to 10Base5 "Thicknet" that runs through the Transport and Rings enclosures back to AP10, while F23 and F27 run off 802.11b wireless from MI60. Both are 10 Mbps shared networks with limited bandwidth and connectivity. It is anticipated that the network in these three buildings may be sufficient for $(g-2)$ operations; however, network upgrade options are being considered, as will be discussed below.

Controls connectivity

Civil construction of the M4 and $(g-2)$ beam line enclosures will result in the removal of the underground controls communication duct that provides the connectivity between the Accelerator Controls NETwork (ACNET) and the Muon Campus [21]. Included in this communication duct is the fiber-optic cable that provides Ethernet connectivity, as well as 18 Heliax cables that provide the controls serial links and other signals including FIRUS. These cables currently connect from this communications duct to the center of the 20 location in the Rings enclosure, and travel through cable trays on the Delivery Ring side to the AP10 service building. After removal of the communications duct, FESS will construct new communications ducts from the existing manholes. These communications ducts will go directly to AP30, MC-1 and Mu2e service buildings without going through accelerator enclosures. See Fig. 4.36 for drawings of the current and future controls connectivity paths.

Restoring connectivity　　When the Heliax and fiber-optic cables are cut during the removal of the above-mentioned communications duct, controls connectivity will be lost. The base plan for restoring both Ethernet and controls-link connectivity is to pull new fiber optic cable from the cross gallery to the manhole outside of Booster Tower West and on to AP30 via the new communications duct. As a result of the new fiber pull, the Ethernet and controls links will fan out from AP30 instead of AP10. This will require some additional controls hardware configuration and labor. Efforts will be made to minimize the disruption by pulling the fiber and staging the new hardware at AP30 before the communication duct is cut. This is especially important for FIRUS which is necessary for monitoring building protection.

More details regarding the base plan and several alternatives, including cutting and splicing the Heliax cable or attempting to keep the fiber and Heliax intact during construction, can be found in Ref. [22].

Establish connectivity to MC-1　　New fiber-optic cable will be pulled from the Mac Room to the MC-1 service building. Single-mode fiber is needed for Ethernet and FIRUS, and multimode fiber is needed for the timing links and the abort-permit loop. A single fiber bundle that contains 72 single-mode fibers and 24 multimode fibers will be pulled to MC-1. The fiber bundle will share a common path with the fiber bundles headed toward AP30 and Mu2e from the Cross Gallery to the manhole by Booster West Tower. All three fiber bundles
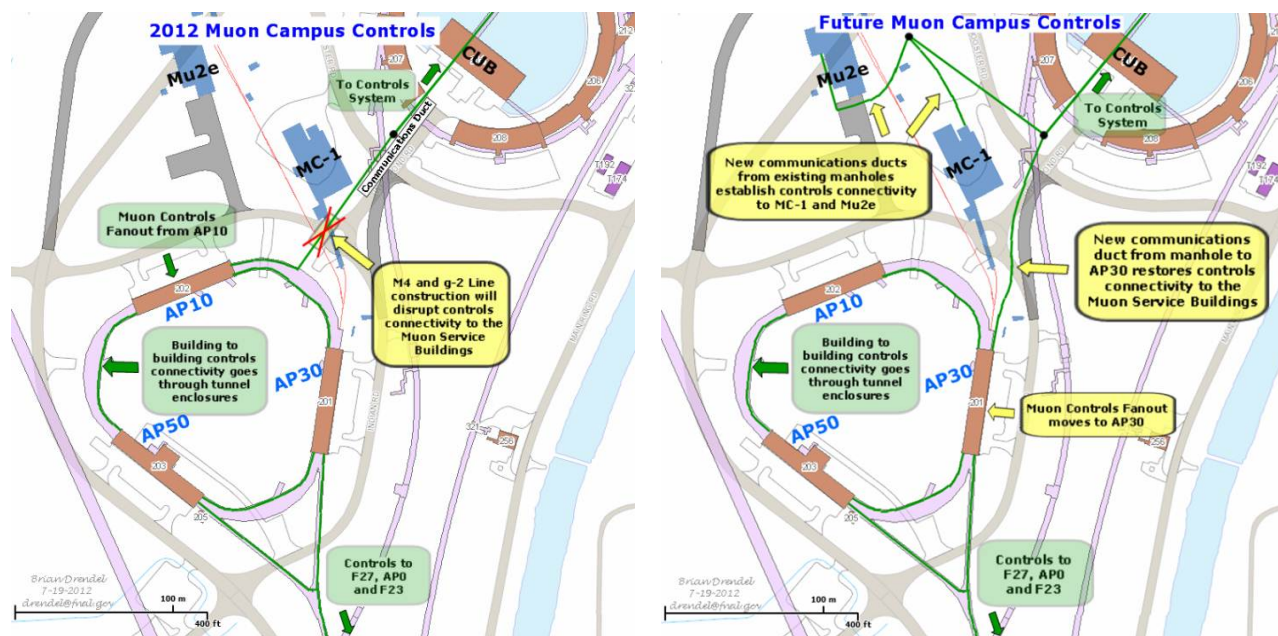
Figure 4.36: Muon campus controls paths. During construction of the M4 and $(g-2)$ beamlines, the communications duct that provides controls connectivity to the Muon Campus will be interrupted. A new communications duct will be built to restore controls connectivity to the Muon service buildings. New controls will need to be established at the MC-1 and Mu2e buildings.

will travel through a single inner duct to the manhole. The Mu2e and MC-1 fiber bundles will then branch off to a second manhole inside a common inner duct, and then separate into the new communication ducts to the Mu2e and MC-1 service buildings. The fiber pulls will provide ample connectivity for all Ethernet and controls signals for both the accelerator and experiment. The $(g-2)$ experiment anticipates requiring network rates approaching 100 MB/sec during production data taking which can be handled easily with the proposed infrastructure.

One alternate solution considered was to pull the new fiber along the existing communications duct until it intersected the extraction-lines enclosure. From there, the fiber could be directed along tunnel-enclosure cable trays to the MC-1 service buildings. Though this option would provide MC-1 cable-pull lengths of approximately the same length as the base option, it was eliminated due to the extra complications of pulling fiber through the tunnel enclosures to both Mu2e and AP-30. In both cases, the expected radiation environment would require a more expensive radiation-hard single-mode fiber. In addition, the CAMAC fiber links only run on multimode fiber, so link and clock repeaters would have to be redesigned to run on single-mode fiber, adding additional expense to the project.

Possible upgrades for legacy networks If the legacy Ethernet networks at AP0, F23, and F27 prove to provide insufficient connectivity or bandwidth for $(g-2)$ operations, they can be most cost-effectively upgraded by replacing the current 10Base5 "Thicknet" with single-mode fiber-optic cable. The path would be from the AP30 service building to the

Rings enclosure, along the cable trays toward the M3 beam line, and down the Transport enclosure. From the Transport enclosure, the fiber-optic cable runs can go to F27 and AP0. An additional fiber-optic cable pull from AP0 through the PreVault enclosure provides a path to F23. The largest issue with this upgrade is that the single-mode fiber-optic cable is susceptible to radiation. If the radiation environment in the accelerator enclosures does not allow for single-mode fiber-optic cable, then radiation-hard fiber-optic cable can be pulled, but at a higher cost. Standard 96-count single-mode fiber costs approximately $1.50/foot, whereas 96-count radiation-hard fiber costs approximately $22/foot. Upgrading to the radiation-hard cable would add approximately $50K to the cost of the cable pull. Other fiber-optic cable path options have been considered, but prove to be more costly to implement.

4.6.2   Accelerator instrumentation

Beam types

Beam monitoring can be divided into distinct zones: primary protons, mixed secondaries, proton secondaries, and muon "secondaries" (actually the dominant source of muons should be from the decay of the pion secondaries, so are technically "tertiary"). The locations of each of these areas are shown in Fig. 4.37. The expected beam properties in each of these areas are shown in Table 4.10.

Beam Type	Particle Species	Beam Momentum (GeV/c)	Number of Particles	RF Bucket (MHz)	Bunch Length (ns)	Transverse Emittance (mm-mrad)
Primary protons	p	8.9	10^{12}	2.515	120	18π
Mixed secondaries	μ^+, π^+, p, e^+	3.1	10^7 to 2×10^8	2.515	120	35π
Proton secondaries	p	3.1	10^7	2.515	120	35π
Muons	μ^+	3.1	$< 10^5$	2.515	120	35π

Table 4.10: Expected properties of primary proton beam, secondary beam off the target, and muon beam from pion decay relevant to instrumentation designed to measure beam. Transverse emittances are 95% normalized.

Primary proton beam   Primary proton beam will traverse the Recycler, P1 stub, P1, P2 and M1 lines. Much of the instrumentation needed to measure the primary proton beam during $(g-2)$ operation already exists, but needs to be modified for use with the faster cycle times and 2.5 MHz RF beam structure. The overall beam intensity is similar to that seen in Pbar stacking operations, and in many cases requires only small calibration changes be made to the instrumentation. Toroids will be used to monitor beam intensity and will be used in conjunction with Beam Loss Monitors (BLMs) to maintain good transmission efficiency in the beamlines. Multiwires and Secondary Emission Monitors (SEMs) will provide beam profiles in both transverse planes. Beam Position Monitors (BPMs) will provide real-time orbit information and will be used by auto-steering software to maintain desired beam positions in the beamlines.
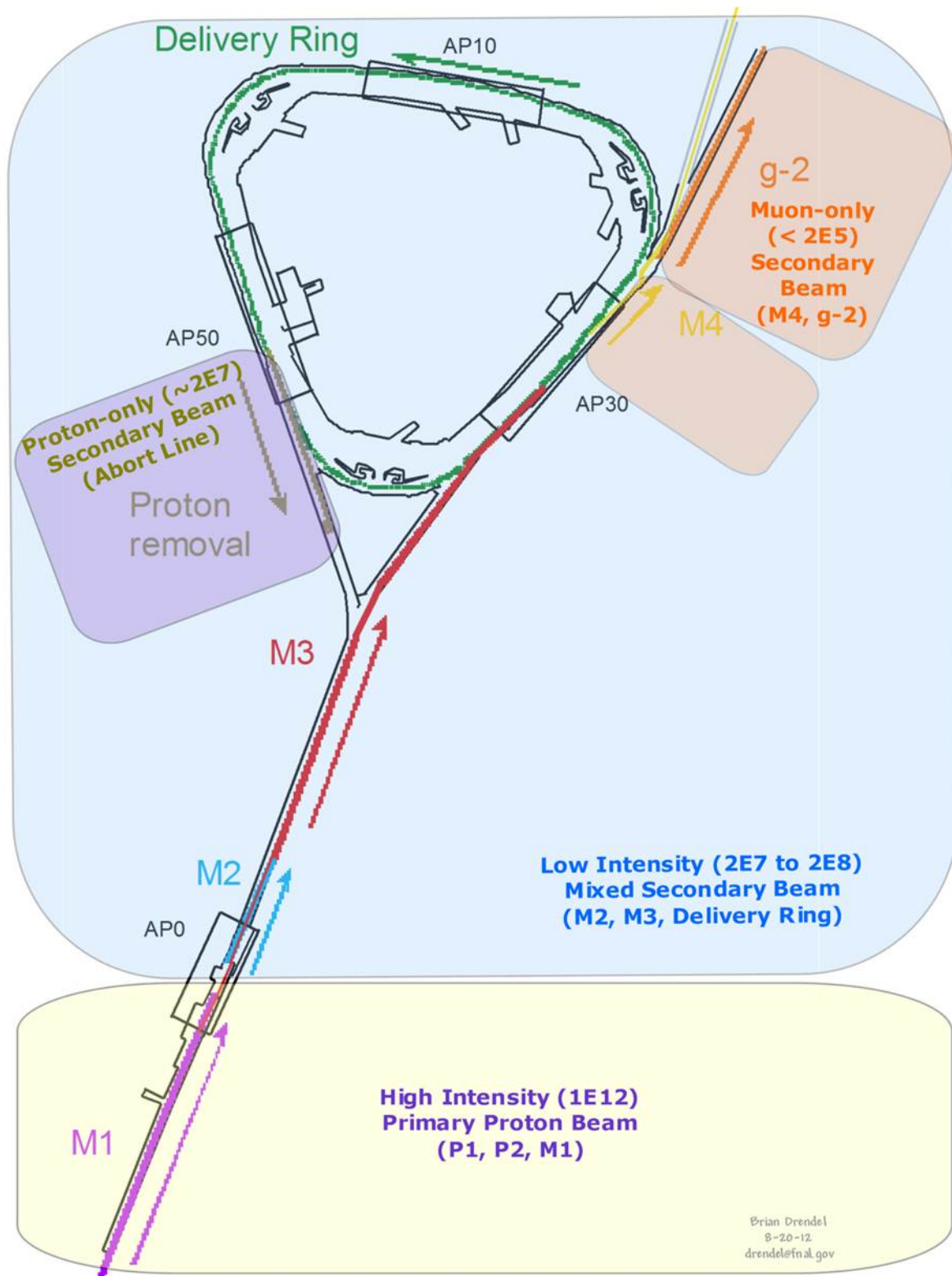
Figure 4.37: Beam monitoring can be divided into four different zones, each with different instrumentation schemes. High-intensity proton beam will be monitored with Toroids, BPMs and BLMs. Low-intensity secondary and proton-only secondary beam will be monitored with Ion Chambers, BPMs and SEMs. Muon-only secondary beam will be monitored with Ion Chambers and SWICs.

cel_instrum

Toroids are beam transformers that produce a signal that is proportional to the beam intensity. There are two toroids in the P1 line, one in the P2 line and two in the M1 line. They will continue to be used in $(g-2)$ operation to measure the primary proton beam. The electronics for these toroids are comprised of legacy analog processing inside of NIM crates. The base plan, due to funding limitations, is to continue to use the legacy electronics. If funding becomes available, the electronics would instead be upgraded to a VME-based processing environment, repurposing electronics from Collider Run II in order to provide cost savings. The existing toroids provide the majority of the required coverage, though the addition of a second toroid in the P2 line and a toroid in the P1 stub is desirable. The present toroid installation locations will be reviewed and modified as needed to provide adequate coverage. One possible change would be to move the upstream P1-line toroid downstream of the P1 line and P1 stub merge so that it could measure the beam injected into the P1 line from the stub. Filters, chokes, and preamps will be added for analog conditioning. Electronics will be modified, where necessary, to calibrate the toroids for $(g-2)$ operations.

Beam line BPMs provide single-pass orbit-position information with sub-millimeter resolution, and will continue to be the primary beam-position devices in the P1, P2 and M1 lines. All BPMs share the Echotek style of electronics which was built as part of the Rapid Transfers Run II upgrade [23], and is the current standard for beam line BPMs. A functional diagram of the BPM hardware is shown in Fig. 4.38. These BPMs were designed to detect 7 to 84 consecutive 53 MHz proton bunches and four 2.5 MHz antiproton bunches for Collider Run II operations. Minimal electronics modifications will be required to measure the single 2.5 MHz bunches of 10^{12} particles expected during $(g-2)$ operations. Two additional BPMs will be installed in the P1 stub.

Beam Loss Monitors are already in place in the P1, P2, and M1 beamlines. Existing ion-chamber detectors will be utilized for Mu2e operation. BLMs will be upgraded to modern BLM log monitor electronics, repurposing unused components from the Tevatron in order to minimize cost. An optional upgrade is being considered that would add snapshot capability to the BLMs. This feature would allow the loss monitors to distinguish losses from individual 15 Hz pulses of beam. However, this option adds significant cost to the BLM system. Two additional BLMs will be installed in the P1 stub.

There are two types of beam profile monitors in the beamlines: multiwires in the P1 and P2 lines, and SEMs in the other beamlines. The profile monitors will primarily be used for commissioning, studies, and documentation of the beamlines. General maintenance will be performed on the hardware and electronics to ensure proper functionality. The current location and wire spacing of the monitors will be reviewed and modified accordingly. Two additional multiwires will be installed in the P1 stub.

Mixed secondaries   Mixed-secondary beam will traverse the M2 and M3 lines, as well as the Delivery Ring. Changes to existing instrumentation are required in these areas as a result of the secondary beam being approximately two orders of magnitude lower in intensity than that during the former Antiproton stacking operations. In addition, 2.515 MHz bunch structure and a faster pulse rate must be taken into consideration. Mu2e beam will have beam intensities four to five orders of magnitude higher than $(g-2)$ operations in the M3 line and Delivery Ring, so design upgrades must take into account the vastly different
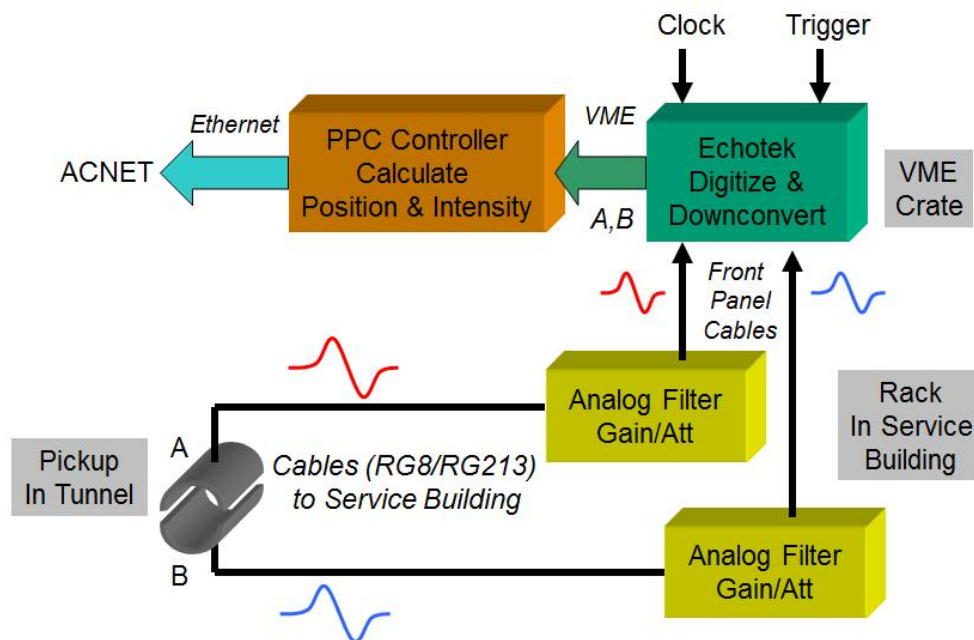
Figure 4.38: BPMs with Echotek processing electronics will be used to measure the transverse beam position of the 2.5MHz primary proton beam in the P1, P2 and M1 lines for $(g-2)$ operations. The BPMs are not sensitive enough to see the low intensity secondary beams downstream of the AP0 target [23].

beam intensities required for both experiments. Beam studies have been conducted in order to help determine what instrumentation best suits the low-intensity secondaries of $(g-2)$ operations [24].

Four toroids are available for use in the secondary beamlines and were the primary intensity-measurement device in these lines during Antiproton operations. These will be used for Mu2e operations; however, beam studies show that even with high gain and careful filtering, we were only able to measure beam intensities at levels one order of magnitude higher than $(g-2)$ operational beam [24], as demonstrated in Fig. 4.39. As a result, toroids will likely not be used during normal $(g-2)$ operations, but may still be used with higher-intensity beams during commissioning and studies periods.

A Direct-Current Current Transformer (DCCT) has been used in the Delivery Ring to measure beam intensity. This device will not function at $(g-2)$ operational intensities and cycle time.

Ion chambers will become the primary beam-intensity measurement device for mixed-secondary beam. They are relatively inexpensive devices that can measure beam intensities with an accuracy of $\pm 5\%$ with as little as 10^5 particles. Ion chambers were used in the AP2 line in the past, and work was done during beam studies to recommission the ion chamber that used to be operational near the end of the AP2 line [24]. For $(g-2)$ operations, one or two ion chambers will be implemented in the M2 line. Ion chambers are also being considered for the M3 line and the Delivery Ring; however, these would need to be installed in a vacuum can with motor controls to allow them to be pulled out of the beam during the
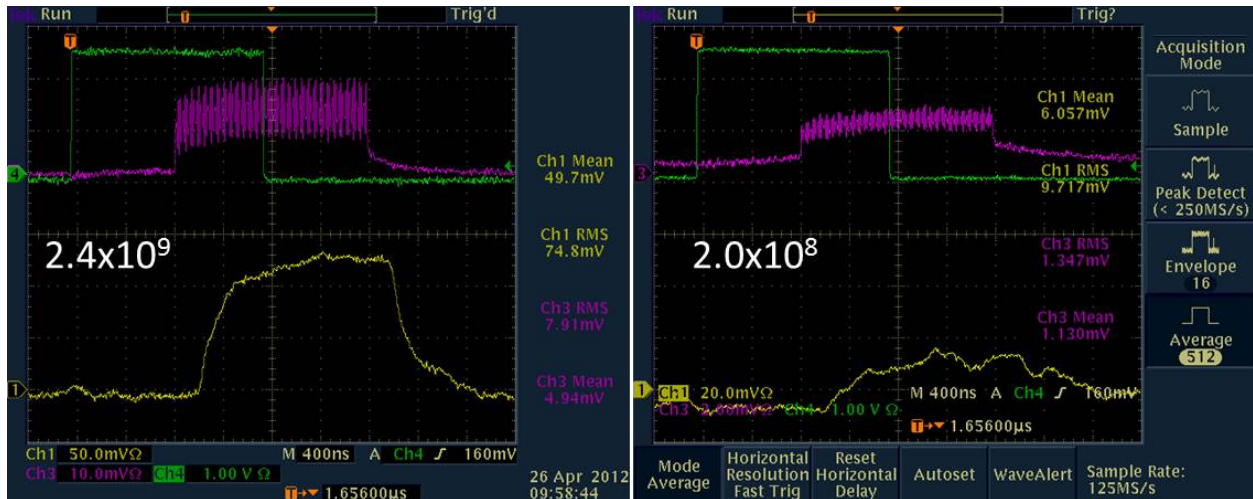
Figure 4.39: The yellow trace on both plots is a calibration test pulse on Toroid 724 in the AP2 line with high-gain preamps and special filtering to look for low-intensity beam. At beam intensities in the low 10^9s, there is an easily-measurable beam signal. However, when the beam intensities are lowered to the level of 10^7-10^8, the $(g-2)$ expected secondary beam intensity range, beam intensities can not be measured.

higher-intensity Mu2e operations. Figure 4.40 shows an ion chamber installation in the AP2 line.

Wall Current Monitors (WCMs) are an alternative intensity-measurement device being considered for mixed-secondary beam. These devices have the advantage of being completely passive, and not requiring a break in the vacuum, which may make them a better fit in the M3 line where we need to stay compatible with the higher intensities of Mu2e operations, and the Delivery Ring where beam circulates for approximately 56 ms in Mu2e operations. New WCM designs are being considered that would provide accurate intensity measurements for secondary beam during $(g-2)$ operations. The design is based on that of a WCM for Mu2e extraction. Each slice of the slow-spilled Mu2e beam is approximately 2×10^7, which is consistent with the intensity that we would expect in the M3 line and Delivery Ring during $(g-2)$ operations.

BPMs were a key diagnostic in Antiproton-Source operation providing sub-millimeter orbit information in the beamlines and Delivery Ring. BPMs are located at each quadrupole, providing ample coverage. There are 34 BPMs in the AP2 line, 28 BPMs in the AP3 line and 120 BPMs in the Delivery Ring; however, it is believed that the BPMs in these areas will not be able to see the low-intensity 2.515 MHz $(g-2)$ secondary beam.

SEMs will be used to measure beam profiles in the M2 and M3 lines, as well as the Delivery Ring. There are eight SEMs in the AP2 line, seven SEMs in the AP3 line, three SEMs in the D/A line, two in the Debuncher, one in the Accumulator and three spares from the former AP4 line to draw from. SEM tunnel hardware will require some maintenance, and locations where SEMs are moved will require new cable pulls. Beam studies showed that special high-gain preamps will be required to measure the low-intensity secondary beam during $(g-2)$ operations [24]. There are only two working high-gain preamps, so additional

Figure 4.40: Fixed-position ion chamber in the AP2 line. The ion chamber is separated from the beam pipe by a vacuum window on each side. Fixed-position ion chambers will only be used in the M2 line. In locations like the M3 line and Delivery Ring that will also see Mu2e beam, the ion chambers will be put inside of vacuum cans and made retractable.

cel_ioncham

preamps will need to be designed and fabricated. Additional SEMs will need to be added to the Delivery Ring from the pool of unused SEMs and spares. A photo of a SEM and its profile display are shown in Fig. 4.41.

BLMs (Fig. 4.42) will be used to help maintain good transmission efficiency through the lines. Both Delivery-Ring and AP3 loss monitors will use the existing hardware and electronics for $(g-2)$ operations, but will be replaced for the higher-intensity Mu2e operations. Care will need to be taken to make a BLM plan that allows for switching back and forth between the two separate BLM systems.

Proton Secondaries   Proton secondaries will extracted to the Delivery Ring abort line and will have a similar beam intensity to that of the Delivery Ring. Existing instrumentation from the downstream AP2 line will be used. A toroid will be used to measure beam intensity for Mu2e operations, but will be out of its operational range for $(g-2)$. If intensity measurement is needed, a retractable ion chamber will be added to the line. Ion chambers, SEMs and BLMs will be used in the same way they are for the mixed secondary lines.

Muon Secondaries   Muon secondaries will traverse the upstream portion of the M4 line and the $(g-2)$ line. The largest technical challenge will be measuring muon secondary beam, which models show should be on the order of 10^5 muons per pulse. This is two or three orders of magnitude smaller than the upstream mixed-secondary beam. Most diagnostics will not work at these beam intensities.
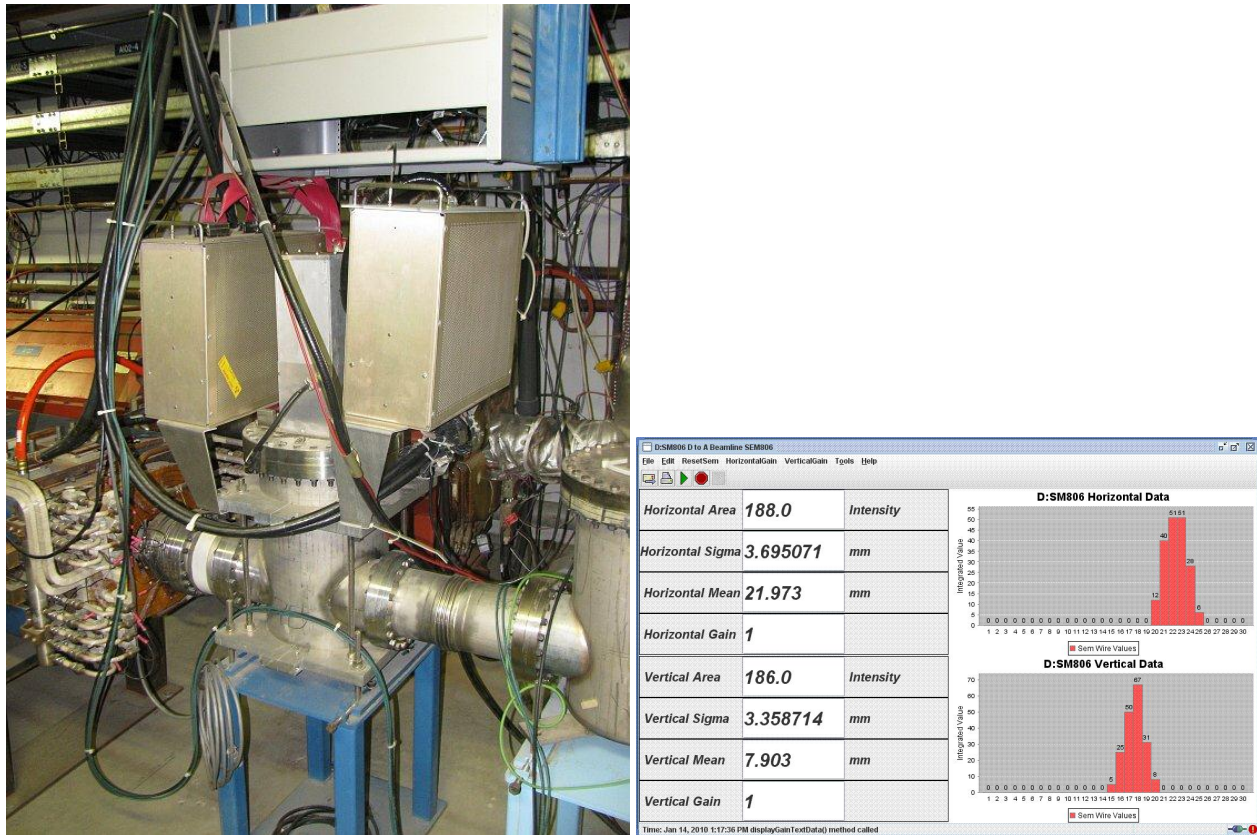
Figure 4.41: SEMs will be used to measure mixed secondary beam profiles. SEM tunnel hardware (left) is pictured. Preamp boxes are mounted next to the vacuum can. The SEM wires can be pulled out of the beam when not in use. SEMs can be used with to measure beam profiles, positions and intensities (right).

Beam intensity will be measured with ion chambers that are designed with three signal foils and four bias foils to increase the signal amplification. This design will allow beam intensity measurements down to 10^5 particles. The ion chamber in the M4 line will need to be retractable in order to be compatible with Mu2e operations, while the $(g - 2)$-line ion chambers can be permanently in the beam path. New ion chambers will be designed and built because there is not a pool of available spares to populate these beamlines. A Wall Current Monitor is another option being considered for beam-intensity measurement in the upstream M4 line. Though this device may be able to measure the Mu2e slow-spill beam intensity, it is not clear if one could be designed that is sensitive enough to see the lower-intensity muon beam expected for $(g - 2)$ operations.

Three options have been considered for measuring beam profiles. The base plan uses Segmented Wire Ion Chambers (SWICs), which are very similar to Multiwires with the exception that the beam goes through $ArCO_2$ gas, which is ionized by the charged-particle beams, creating an amplification that allows measurements of beam intensities down to the 10^4 particle range. This is an order of magnitude lower than the expected $(g - 2)$ operational beam. In addition, SWICs are robust enough to handle particle beams several orders of magnitude higher in intensity than are expected during $(g - 2)$ operations. This
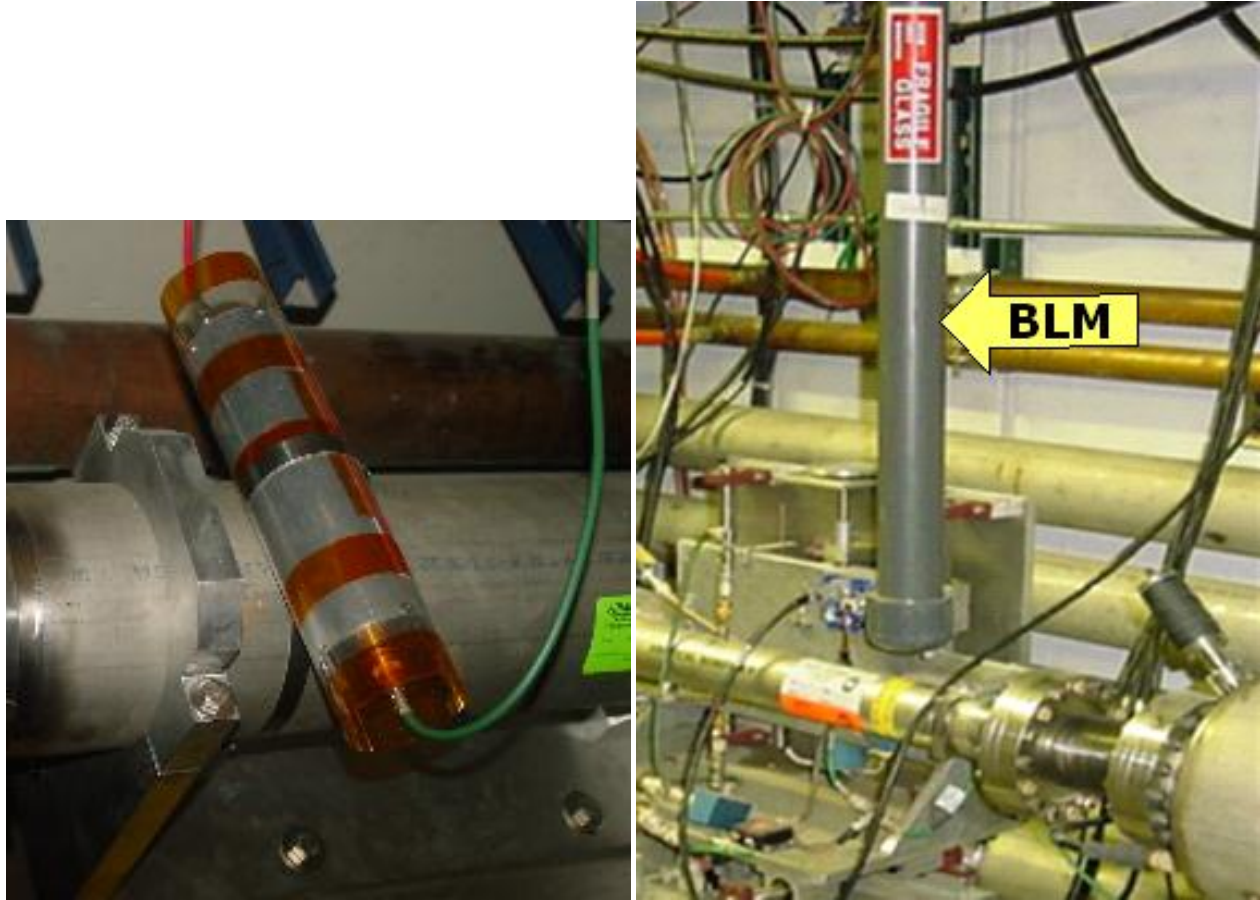
Figure 4.42: Two styles of BLMs will be used. Tevatron-style ion chamber loss monitors (left) will be used in areas of primary beam, and also in the Delivery Ring for Mu2e operations. The Pbar-style ion chamber, which consists of a plastic scintillator and a long light guide connected to a photomultiplier tube shielded from light in PVC, will be used in the Delivery Ring during $(g-2)$ operations.

g:accel_BLM

will provide the flexibility of running higher-intensity protons through the M4 and $g-2$ lines for commissioning and beam studies. The SWICs will need to be retractable since they are a destructive measurement device. Some vacuum cans can be acquired from other systems to minimize the cost; however, the inventory of spare vacuum cans is not sufficient enough to cover all of the SWICs.

A second option that was considered is the Proportional Wire Chamber (PWC). The advantage of the PWC is that it can measure beam down to 10^3 particles, and the wire planes are modular. The major disadvantage is that the wires are easily damaged by higher-intensity pules, limiting the ability to run higher intensity study beam.

The third option that was considered is to design Scintillator Fiber Profile Monitors (SFPMs), which can measure down to 100 particles. These devices are similar to SWICs or PWCs, but the wires are replaced with scintillating fiber. They have been used in the SY120 test-beam lines, and the fibers have been shown to survive long periods of beam operation. The largest disadvantage is that SFPMs cost significantly more than SWICs.

The upstream M4 line will be made compatible with both Mu2e and $(g-2)$ operations. Beam in the M4 line for $(g-2)$ will be at least two orders of magnitude smaller than the individual slices of slow-spilled beam that the line will see in Mu2e operations.

Intensity and profile information will also need to be collected just before and after the inflector, which will likely be achieved with ion chambers and some combination of the profile-measurement devices mentioned above. The two primary factors limiting the instrumentation after the inflector are a much smaller available physical space and potentially lower-intensity beam.

If muon beam profile information cannot be accurately measured with the proposed diagnostics, one option being considered is to develop a tune-up mode. In this mode, protons in the Delivery Ring would not be sent to the abort, but extracted toward $(g-2)$ with the muon beam. This would result in 10^7 particles per pulse in the extraction lines, which is easily measured by ion chambers and SWICs.

Accelerator instrumentation summary

A summary of instrumentation devices which will potentially be used for $(g-2)$ is shown in Table 4.11.

Beamline	Beam type	Intensity	Position	Profile	Loss
Primary protons	P1, P2, M1	toroids	BPMs	multiwires, SEMs	BLMs
Mixed secondaries	M2, M3, DR	ion chambers, WCMs	SEMs	SEMs	BLMs
Proton secondaries	DR abort	ion chambers, WCMs	SEMs	SEMs	BLMs
Muons	M4, $(g-2)$	ion chambers, WCMs	SWICs, PWCs, SFPMs		

Table 4.11: Potential instrumentation to be used in the beamlines for $(g-2)$ operations. `tb:accel_inst`

4.7 Radiation Safety Plan

`t:RadSafety`

4.8 ES&H, Quality Assurance, Value Management

`sct:BS`

References

`accel_PIP` [1] W. Pellico *et al.*, "Proton Source Task Force Report", Beams Doc. 3660 (2010); F. G. Garcia *et al.*, "Fermilab Proton Improvement Plan Design Handbook", Beams Doc 4053 (2012).

`cel_NovaTDR` [2] D.S. Ayres *et al.*, "NOνA Technical Design Report", NOνA Doc 2678 (2007).

`etyieldtest` [3] D. Still *et al.*, "$g - 2$ Yield Beam Study Results – April 2012", $g - 2$ Doc 430 (2012).

`ccel_ioanis` [4] I. Kourbanis, "Bunch Formation for $g - 2$ experiment", $g - 2$ Doc 335 (2012).

`ccel_meiqin` [5] M. Xiao, "Transport from the Recycler Ring to the Antiproton Source Beamlines", Beams Doc 4085 (2012).

`accel_MARS` [6] N. Mokhov, http://www-ap.fnal.gov/MARS.

`rgetmarssim` [7] C. Yoshikawa *et al.*, "Optimization of the Target Subsystem for the New $g - 2$ Experiment", IPAC2012.

`l_striganov` [8] S. Striganov, "Optimization of $g - 2$ Target Parameters", Fermilab Doc GM2-doc-197.

`_g4beamline` [9] Muons, Inc., http://www.muonsinc.com/muons3/G4beamline.

`el_pbrookie` [10] B. Drendel *et al.*, "Antiproton Source Rookie Book", Beams-doc-2872, June 2010.

`accel_ANSYS` [11] ANSYS®, http://www.ansys.com.

`l_lensansys` [12] R. Shultz, "ANSYS Mechanical Simulation for Lithium Lens", Fermilab Doc GM2-doc-362.

`accel_dump` [13] C. Hojvat *et al.*, "The Fermilab Tevatron I Project Target Station For Antiproton Production", Fermilab TM-1175 (March 1983).

`l_transport` [14] D.C. Carey, K.L. Brown, F. Rothacker, FERMILAB-Pub-98/310 (1998).

`l_gm2doc484` [15] $g - 2$ Doc 484 (2012).

`cel_lebedev` [16] V. Lebedev, $g - 2$ Doc 171 (2012).

`l_gm2doc252` [17] $g - 2$ Doc 252 (2012).

`el_mu2e2117` [18] J.P. Morgan, "Power tests for Pbar service buildings", Mu2e Doc 2117 (2012).

cel_pbctrls [19] B. Drendel *et al.*, "Pbar Controls Reference Material", Mu2e-doc-1161, May 2012.

accel_HRM [20] A. R. Franck *et al.*, "HOTLink Rack Monitor", FERMILAB-Conf-01/342/E.

el_commduct [21] B. Drendel *et al.*, "Controls to Mu2e/g-2/Muon and Communications Duct Issues", Mu2e-doc-2069, February, 2012.

l_commduct2 [22] communications duct details and alternative plans

accel_BPM [23] N. Eddy and E. Harms, "Beamline BPM Upgrade", Beams-doc-1279, September 2004.

el_beamtest [24] D. Still *et al.*, "$g - 2$ Yield Beam Tests", G2M-doc-430, July 2012.

Chapter 5

Conventional Facilities

5.1 The MC1 Building

5.2 Beamline Civil Construction

etc.

Chapter 6

ch:SR

The Muon Storage Ring Magnet

6.1 Introduction

As emphasized in Chapter 2, the determination of the muon anomaly a_μ requires a precise measurement of the muon spin frequency in a magnetic field ω_a, and an equally precise measurement of the average magnetic field felt by the ensemble of precessing muons, $\langle B \rangle$. We repeat the spin equation given in Eq. 2.14, since it is central to the design of the storage-ring magnet.

$$\vec{\omega}_a = -\frac{Qe}{m}\left[a_\mu\vec{B} + \left(a_\mu - \left(\frac{m}{p}\right)^2\right)\frac{\vec{\beta}\times\vec{E}}{c}\right].$$

(6.1) eq:omegaa-c

As explained in Chapter 2, the need for vertical focusing and exquisite precision on $\langle B \rangle$ requires that: either the muon trajectories be understood at the tens of parts per billion level, and the magnetic field everywhere be known to the same precision; or the field be as uniform as possible and well-measured, along with "reasonable knowledge" of the muon trajectories. This latter solution was first employed at CERN [1] and significantly improved by E821 at Brookhaven [2]. The uniformity goal at BNL was ±1 ppm when averaged over azimuth, with local variations limited to ≤ 100 ppm.

A photograph of the E821 magnet is shown in Figure 6.1. It is clear from the photo that this "storage ring" is very different from the usual one consisting of lumped elements. This continuous magnet, made up of twelve 30° yoke sections was designed to eliminate the end effects present in lumped magnets, which have large gradients and would make the determination of $\langle B \rangle$ difficult. Furthermore, a small pertubation in the yoke can effect the field halfway around the ring at the ppm level. Thus every effort was made to minimize holes in the yoke, and other pertubations. Thus the only penetrations through the yoke were to permit the muon beam to enter the magnet, and to connect cryogenic services and power to the inflector magnet and to the outer radius coil. Where a hole in the yoke was necessary, extra steel was placed around the hole on the outside of the yoke to compensate for the effect in the magnetic circuit.

Fermilab E989 will use the storage-ring magnet designed and built for Brookhaven E821, with additional shimming to further decrease the local variations in the magnetic field. This requires the relocation of the ring from BNL to Fermilab, which is described in detail in the following chapter. While the magnet steel comes apart and can be moved by conventional
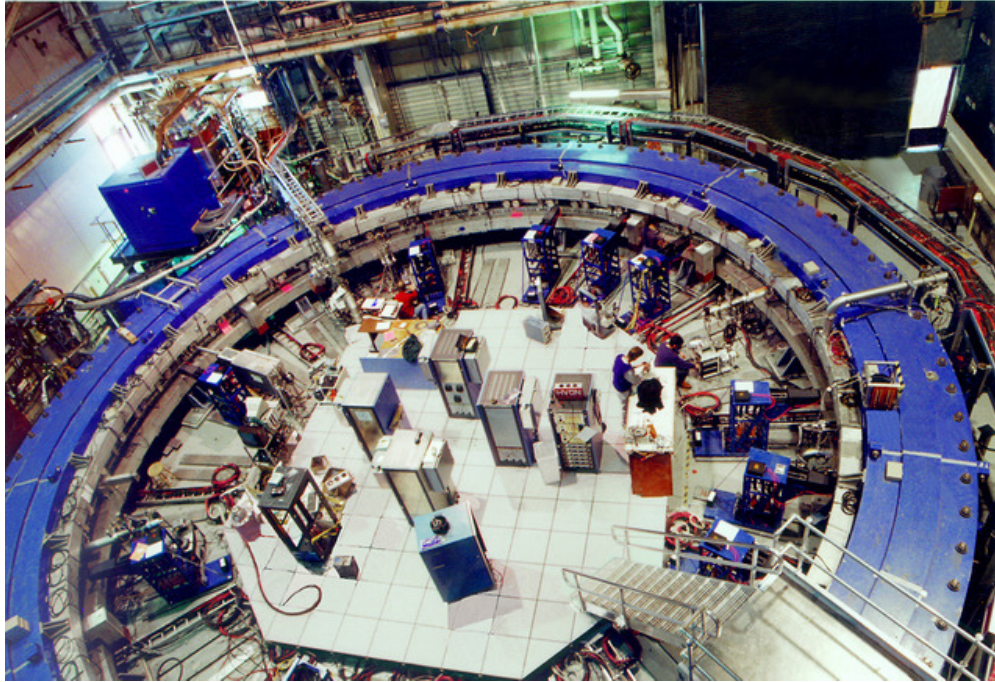
Figure 6.1: The E821 storage-ring magnet at Brookhaven Lab.   `fg:ring-pho`
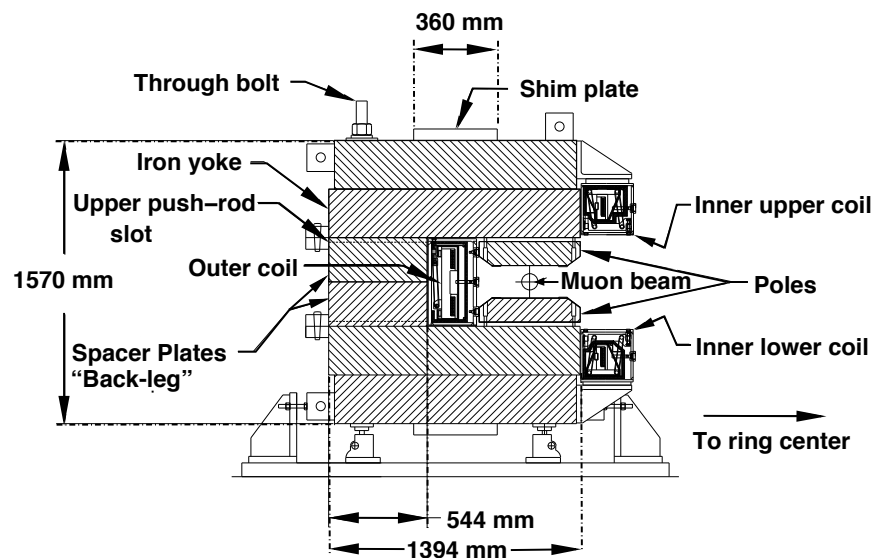

Figure 6.2: Cross section of the E821 storage-ring magnet. The yoke is made up of 12 azimuthal sections, each of which consists of six layers of high quality magnet steel provided by Lukins Steel Corporation. The pole pieces were provided by Nippon Steel Corporation.   `fg:ring-ele`

trucks, the 14.5 m diameter superconducting coils will need to be moved as a package, on a custom designed fixture that can be pulled by a truck to travel by road, and put on a barge to travel by sea, and then again by road to get it to the Fermilab site.

6.2 Design Considerations

The storage ring is built as one continuous superferric magnet, an iron magnet excited by superconducting coils. A cross-section of the magnet is shown in Fig. 6.2. The magnet is C-shaped as dictated by the experiment requirement that decay electrons be observed inside the ring. The field, and hence its homogeneity and stability, are determined dominantly by the geometry, characteristics, and construction tolerances of the iron. Although both copper and superconducting coils were considered, the use of superconducting coils offered the following advantages: thermal stability once cold; relatively low power requirements; low voltage, and hence use of a low-voltage power supply; high L/R time constant value and hence low ripple currents; and thermal independence of the coils and the iron. The main disadvantage was that the coils would have a much larger diameter and smaller height than any previously built superconducting magnet. However, since the E821 magnet team could not identify any fundamental problems other than sheer size, they decided to build superconducting coils.

To obtain the required precision in such a large diameter magnet with an economical design is an enormous challenge. The magnet had to be a mechanical assembly from sub-pieces because of its size. With practical tolerances on these pieces, variations up to several thousand ppm in the magnetic field could be expected from the assembled magnet. To improve this result by two to three orders of magnitude required a design which was a "shimable kit".

Because of the dominant cost of the yoke iron, it was an economic necessity to minimize the total flux and the yoke cross-section. This led to a narrow pole, which in turn conflicts with producing an ultra-uniform field over the 9 cm good field aperture containing the muon beam.

A simple tapered pole shape was chosen which minimized variations in the iron permeability and field throughout the pole. The ratio of pole tip width to gap aperture is only 2/1. This results in a large dependence of the field shape with the field value B. However, since the storage ring is to be used at only one field, $B = 1.45$ T, this is acceptable. Because of dimensional and material property tolerance variation, the compact pole piece increases the necessity for a simple method of shimming.

Experience with computer codes, in particular with POISSON [4], had demonstrated that, with careful use, agreement with experiment could be expected at a level of 10^{-4} accuracy. POISSON is a two-dimensional (2D) or cylindrically symmetric code, appropriate for the essentially continuous ring magnet chosen for the $(g-2)$ experiment. Computational limitations, finite boundary conditions, and material property variations are all possible limitations on the accuracy of "paper" designs.

We will briefly discuss the design features that are relevant to E989, especially to moving the ring, but not repeat all the details given in Danby et al. [3], and in the E821 Design Report [5]. The parameters of the magnet are given in Table 6.2

6.2.1 The Superconducting Coils

The coil design was based on the TOPAZ solenoid at KEK [6]. TOPAZ conductor was used, with pure aluminum stabilizer and niobium-titanium superconductor in a copper matrix.

Table 6.1: Magnet parameters

Design magnetic field	1.451 T
Design current	5200 A
Equilibrium orbit radius	7112 mm
Muon storage region diameter	90 mm
Inner coil radius - cold	6677 mm
Inner coil radius - warm	6705 mm
Outer coil radius - cold	7512 mm
Outer coil radius - warm	7543 mm
Number of turns	48
Cold mass	6.2 metric tons
Magnet self inductance	0.48 H
Stored energy	6.1 MJ
Helium-cooled lead resistance	6 $\mu\Omega$
Warm lead resistance	0.1 mΩ
Yoke height	157 cm
Yoke width	139 cm
Pole width	56 cm
Iron mass	682 metric tons
Nominal gap between poles	18 cm

-parameters

Conductor characteristics are given in Table 6.2.1. At full field the critical temperature of
the outer coil is 6.0 K. The magnet typically operates at 5.0 K. This represents 76% of
the superconductor limit. Each coil block is effectively a very short solenoid with 24 turns,
and one layer. The coils are wound from the inside of the ring so that, when powered,
the coils push out radially against a massive aluminum mandrel. Cooling is indirect with
helium pipes attached to the mandrels. The coil turns, coil stack and insulation are epoxied
together, forming a monolithic block. The coils hang from the cryostat with low heat load
straps, and the shrinkage and expansion of the coils is taken by the straps. The coils are
located using radial stops on the inner radius. For the outer coil the stops transfer the force
from the coil to the cryostat box, and push rods from the iron yoke transfer the force from
the box to the iron (see Fig. 6.3). For the inner coils, pins replace the pushrods.

When the coils are cooled, they contract down onto the radial stops into a scalloped
shape. When powered, the Lorentz force pushes the coils outward, increasing the force
against the mandrel, which provides cooling. This feature, the result of winding on the
inside of the mandrel, reduces the risk of cooling problems even if the coil were to separate
from the mandrel during transport citeyamamoto-pc.

A ground plane insulation band of 0.3 mm thickness was built from a sandwich of three
layers of 50 μm kapton, epoxy coated, between two layers of epoxy-filled fiberglass. The
insulation assembly was fully cured and placed into the mandrel. A 0.1 mm layer of B-stage
epoxy film was placed between the mandrel and kapton laminate, and between the kapton
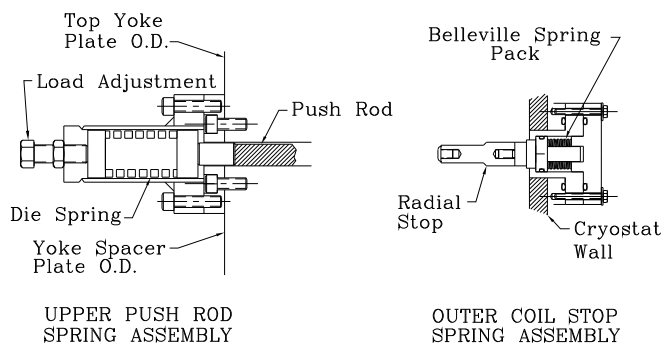laminate and the conductor block after winding. A 4.8 mm thick G-10 piece was placed on

Figure 6.3: The spring-loaded radial stop and push rod. The stops are attached to the cryostat inner wall. The push rods preload the outer cryostat, attaching to the yoke at the outer radius, passing through a radial slot in the yoke to the outer cryostat.

fg:coil-sto

the winding ledge, and on top and on the inner radius of the completed coil block. The insulation protected against a local failure in an insulation layer and against creep failure along a surface. The epoxy-filled fiberglass in the ground plane insulation sandwich improved heat transfer between coil and mandrel.

Table 6.2: Superconductor parameters

|	
Superconductor type	NbTi/Cu
Nominal dimensions	1.8 mm $\times$ 3.3 mm
NbTi/Cu ratio	1:1
Filament 50 μm	
Number of filaments	1400
Twist pitch	27 mm
Aluminum stabilizer type	Al extrusion
Ni/Ti composite dimensions	3.6 mm $\times$ 18 mm
Al/(NbTi + Cu) ratio	10
RRR (Al)	2000-2500
RRR (Cu)	120-140
I_c	8100 A (2.7 T, 4.2 K)

s-conductor

The coil was then wound using a machine that wrapped the superconductor with three overlapping layers of 25 μm of kapton and fiberglass filled with B-stage epoxy, 19 mm in width, laying the conductor into the mandrel with a compressive load as described in Ref. [3]. The wrap was tested at 2000 V DC during the wind. Aluminum covers were added after the coil was wound, and the entire assembly heated to 125° C to cure the epoxy. See Fig. 6.4.

Danby:2001

fg:inner-outer-coil

The outer coil contains two penetrations, one to permit the beam to enter the ring, and one which which could have permitted high voltage to be fed to a proposed electrostatic muon kicker. It was decided at the time to make this "kicker penetration" in the outer coil, but not to make a hole through the magnet yoke until it was shown that this kicker could be built (which was not demonstrated).
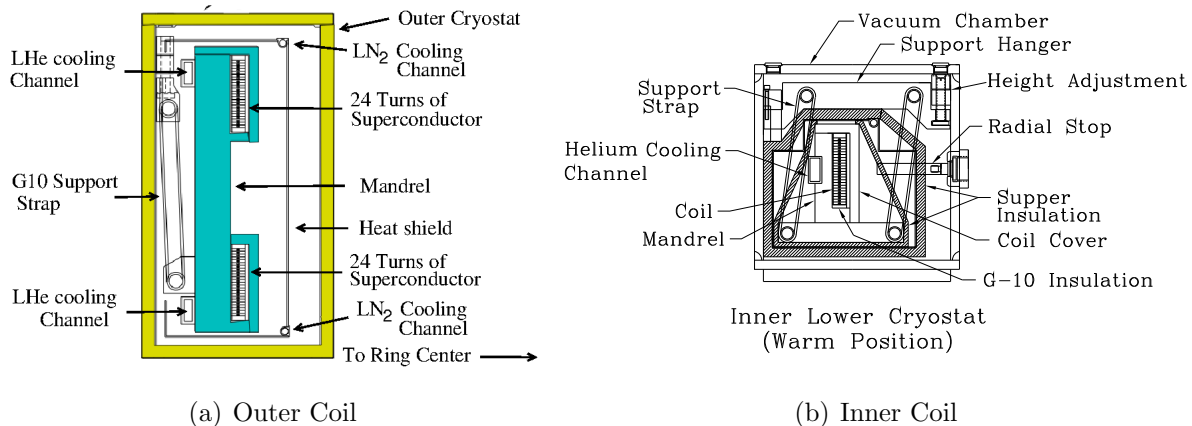
(a) Outer Coil   (b) Inner Coil

Figure 6.4: The outer and inner coil structures. Both are shown in their warm configuration.

The coils are indirectly cooled with two-phase He flowing through channels attached to the mandrel, as shown in Fig. 6.4. The two-phase helium cooling avoids the increase in temperature that would occur in a circuit cooled with single-phase helium. The operating temperature of the coils is within 0.2 K of the coldest temperature in the cooling circuit. The advantages of two-phase cooling are: (1) the helium flows in well-defined flow circuits; (2) the total amount of helium that can be flashed off during a quench is limited to the mass of helium in the magnet cooling tubes; and (3) the location of the helium input and output from the cryostat and the location and orientation of the gas cooled leads are not affected by the cooling system [8].

The key to the operation of a two-phase helium cooling circuit is a helium dewar (the control dewar) that contains a heat exchanger. This heat exchanger sub-cools the helium from the J-T circuit before it enters the magnet cooling circuits. This isobaric cooling provides a higher ratio of liquid to gas with a higher pressure and lower temperature than the refrigerator J-T circuit alone would provide. This feature is important for the long cooling channels in the magnet cooling circuits. The use of a heat exchanger in the control dewar reduces the helium flow circuit pressure drop by a factor of two or more. The control dewar and heat exchanger also have the effect of damping out the oscillations often found in two-phase flow circuits. The helium in the control dewar acts as a buffer providing additional cooling during times when the heat load exceeds the capacity of the refrigerator.

The $(g-2)$ cooling system was originally designed to have three separate cooling circuits: a 218 m long cooling circuit that cools all three mandrels in series, the lead and coil interconnect circuits that are 32 m long (the gas-cooled leads are fed off of this circuit), and a 14 m long cooling circuit for the inflector magnet. Later the cooling system was modified to permit each of the mandrels to be cooled separately. Ultimately, the $(g-2)$ cooling system

operates with parallel cooling circuits for the coils, inflector, and lead cooling. Electrically, the three coils are connected in series so that the two inner coils are in opposition to the outer coil to produce a dipole field between the inner and outer coils. The magnet is powered through a pair of tubular gas-cooled leads developed for this application. Each lead consists of a bundle of five tubes. Each tube in the bundle consists of three nested copper tubes with helium flow between the tubes. The copper tubes used in the leads are made from an alloy with a residual resistance ratio of about 64. The lead length is 500 mm. A typical cool down from 300 to 4.9 K takes about 10 d. Once the control dewar starts to accumulate liquid helium, it takes another day to fill the 1000 l dewar. In operation, the pressure drop across the magnet system is about 0.02 MPa (3.0 psi). We initiated several test quenches and had one unintentional quench when the cooling water was shut off to the compressors. The peak measured pressure during a 5200 A quench was 0.82 MPa (105 psig). Other places in the cooling circuit could have a pressure that is 40% higher. The quench pressure peak occurs 11 s after the start of the quench. The quench pressure pulse is about 12 s long compared to current discharge time constant at 5200 A of 31 s. The outer coil mandrel temperature reaches 38 K after the quench is over. Re-cooling of the magnet can commence within 5 min of the start of the quench. After a full current quench, it takes about 2 h for the outer coil to become completely superconducting. The inner coils recover more quickly.

Table 6.3: Estimates of cryogenic heat leaks

		4.9 K load (W)	80 K load (W)
Magnet system heat load	Outer coil cryostat	52	72
	Two inner coils	108	77
	Inflector	8	5
	Interconnects	11	46
	Magnet subtotal	**179**	**200**
Distribution	Helium piping	19	
	Control dewar	5	
	Interconnects/valves	33	32
	Nitrogen piping		34
	Distribution subtotal	**57**	**66**
Lead gas (1.1 g/s)	Equivalent refrigeration	114	
Total refrigeration		351	266
Contingency		70	51
Cryogenic design	**Operating point**	**421**	**308**

6.2.2 The Yoke Steel

The magnet is constructed with twelve 30° sectors, to limit the size and weight of the individual parts for ease of fabrication and assembly. Each sector, Fig. 6.2, is built up of steel plate and consists of an upper and lower yoke separated by a spacer plate. The sector

mass is about 57,000 kg, including end supports and additional parts, and the complete magnet weighs approximately 680 metric tons.

It is difficult to find suppliers of quality steel who can roll plate steel to the thickness required for the upper and lower yoke plates. To allow the maximum number of steel suppliers to bid, and to reduce the chances of voids through reduction in thickness during the hot-rolling process, these components have been supplied as two separate plates. The plates were welded together at the interface during the machining step. The spacer plate is also made in two pieces to facilitate installation of beam pipes, transfer lines and electrical connections to the outer coil cryostat.

The upper and lower yoke plates and spacer plates are held in place by eight high-strength steel bolts per sector, extending through all of the plates vertically. These bolts are 5 cm in diameter and were tensioned to 80,000 kg each, which is 57% of the yield point. In addition, the three assemblies, the upper yoke plate, spacer plate and lower yoke plate are doweled together to allow ease of disassembly and reassembly while maintaining their horizontal relationship.

A feature of the overall magnetic design is to have the yoke continuous azimuthally. To achieve this, each sector end has four radial projections for bolts to fasten adjacent sector ends to each other. When the sectors are fitted to each other, shimmed, and the bolts tightened, relative motion of adjacent sectors is minimized.

Rolled steel plates are specified for the major pieces of steel used in the yoke plates and spacer plates. These have 0.08% carbon maximum with a minimum of alloying elements and impurities. All rolled plates have been completely inspected ultrasonically for voids and the composition of each plate has been determined by chemical analysis. The background information of each piece was retained by a numbering system stamped into the steel pieces.

The lower horizontal face of the upper yoke plate and the upper horizontal face of the lower yoke plate were milled flat within 130 μm and 1.6 μm finish. The inner radius of each yoke plate machining tolerance was to within ±130 μm of the basic dimension.

Upper and lower surfaces of the spacer plate were milled flat within ±130 μm and parallel within 180 μm, and thickness accurate to ±130 μm. Both inner and outer radii of the spacer plate tolerances were within ±130 μm of the true radius. The as-built vertical yoke gap has an rms deviation of ±90 μm, or 500 ppm of the total air gap of 20 cm, and a full-width spread of ±200 μm.

Azimuthally machining requirements were that the sector ends be perpendicular to the gap faces to within ±0.3 mrad and that the ends be radial to within ±0.2 mrad. The chords between the outer radius corners of the as-machined sectors have an rms deviation of ±0.25 mm and a mean of -0.03 mm. The design azimuthal gap between sectors was 0.5 mm. The as-built azimuthal gaps for the lower yoke average 0.8 mm, with an rms deviation of ±0.2 mm. Spacer plates and upper sectors were matched to the lower sectors to equalize the effective azimuthal gap for the three pieces, weighted by the magnetic reluctance for each sector.

The magnet is intended to move as a single rigid body, as much as possible. The magnet supports are located at the 12 sector joints, and are designed to move the sector pairs together. The ring also sits on low-friction pads, and is held to the floor at only one azimuthal position.
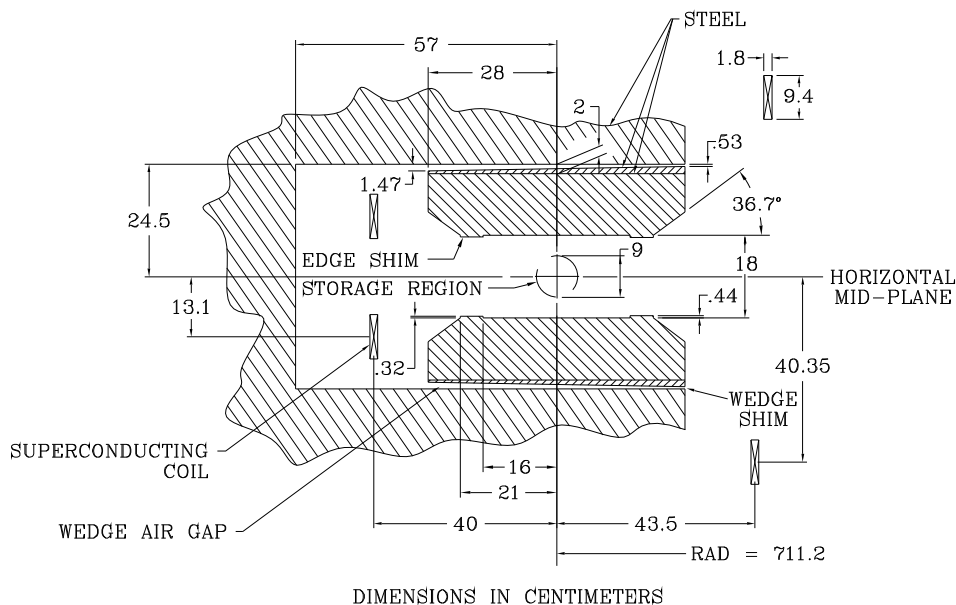
6.2.3   The Pole Pieces and Wedges

Figure 6.5: Cross section view of the magnet gap region.   `fg:poles-de`

The pole pieces are shown in Figs. 6.2 and 6.5. Fig. 6.6 shows the inflector exit and beam vacuum chamber between the poles. The poles directly affect the field quality, while the effect of yoke imperfections is minimized by the air gaps between the yoke and poles. The poles require high-quality steel, with tight machining tolerances on the flatness of the faces which define the storage ring gap. The pole steel was continuous vacuumcast with 0.004% carbon. The tolerance on flatness was 25 μm, which represents 140 ppm of the storage gap. The surface was ground to a 0.8 μm finish (4 ppm). The pole widths were machined to 56 $\pm$0.005 cm, and the thickness to 13.3 $\pm$0.004 cm. The upper and lower faces were machined parallel to 0.005 cm.

In order to control and adjust the pole location and tilt, the poles were constructed in 10° azimuthal sections, compared to the 30° sectors of the yoke. The pole edges that align with the yoke sectors were machined radial, and the middle pole of each sector is interlocking, with a 7° angle from radial. The poles were located azimuthally with 80 μm kapton shims, with the pole edge each 60° in azimuth machined to the correct azimuth. Then kapton was used to electrically isolate the poles from each other to control eddy current effects from field changes, from ramping or quench.

The pole edge-shims were built oversized (4.4 mm thick for the shims on the i.d.; 3.2 mm thick for the o.d. shims) to allow for perturbation adjustment during the magnetic field
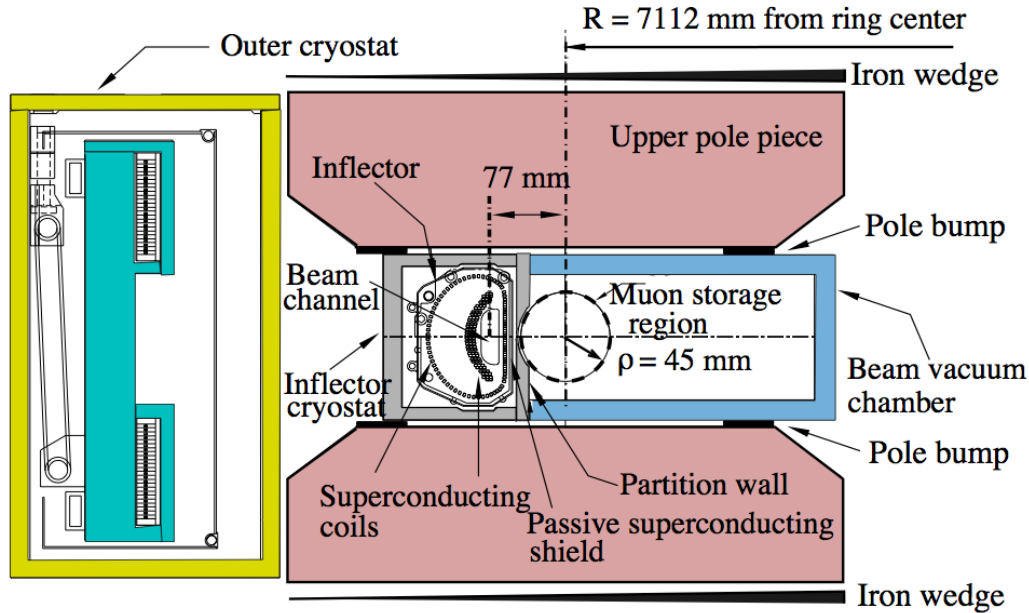
Figure 6.6: The arrangement of the pole pieces, shimming wedges and the inflector cryostat, showing the downstream end of the inflector where the beam exits. The beam is going into the page, and the ring center is to the right.

`fg:pole-out`

shimming. The shim width is 5.0 cm. The edge shims are attached to the poles using flathead iron screws, countersunk into the shims every 12 cm in azimuth. This spacing adequately holds the shims from the unstable magnetic force which attempts to short the gap.

The poles are attached to the yoke plates by steel bolts whose heads are counter-bored deeply into the poles (see Fig. 2). The bolts are located in the tapered region of the poles away from the storage region, and the bolt heads are covered by cylindrical plugs of pole steel.

The as-built storage ring gap with a design value of 18 cm was measured using capacitance devices to ± 1 μm accuracy. The gap height varied by ± 23 μm rms with a full range of 130 μm. The tilts of the poles in the radial direction were measured with a precise bubble level and adjusted to ± 50 μrad. The poles were aligned to be horizontal when powered. This required an initial opening angle of 80 μrad toward the ring center to compensate for the asymmetric closing of the gap, as shown in Fig. 6.7(a). Adjacent poles were matched to ± 10 μm to keep field distortions caused by steps in the iron surface small.

The shimming gaps between the yoke and poles serve three purposes: the gaps decouple the yoke steel from the poles; flat dipole correction coils for each pole are installed in the gaps to adjust the dipole field in azimuth; and the gaps contain iron wedges used to shim the magnetic field. The wedges, sloped radially to provide the C-magnet quadrupole correction, are attached so that they can be adjusted radially. The radial adjustment changes the dipole field locally. The wedges are 9.86 cm wide (azimuthal direction), with 72 per 30° sector. They are 1.65 cm thick on the inner radius, 0.5 cm thick on the outer radius, and are 53 cm long (radial direction). Note that the wedges are rectangular in the $r - \phi$ plane, so that there is

a larger gap azimuthally between the wedges on the outer radius.

A difficulty that we did not anticipate was that the magnetic force direction was quite different at lower field than for full field. The wedge angle is designed to distribute the field lines uniformly radially at full field, with the yoke and wedge iron partly saturated. At lower field, however, the iron is not saturated, and the smaller total gap at the larger radius, where the wedges are thicker, draws more field lines. This leads to a torque on the poles and wedges. To stabilize the wedges, clamps were made from aluminum sheets taped together with the appropriate "anti-wedge" shape. The poles are held in place by the bolts described above, and aluminum/steel laminated spacers are used to hold the poles away from the yokes. At full power the force is 2×10^6 N per pole. The iron lamination in the spacers replaces iron in the wedges that are notched, due to the spacers. There are 24 spacers for each 30° sector, located at the sector ends and at 2.5° azimuthal intervals, on the inner and outer radii of the poles. We measured the torque on a pole during ramp-up (Fig. 6.7(b)) and confirmed calculations that the pole attachments were sufficient.

fg:pole-gap-torque
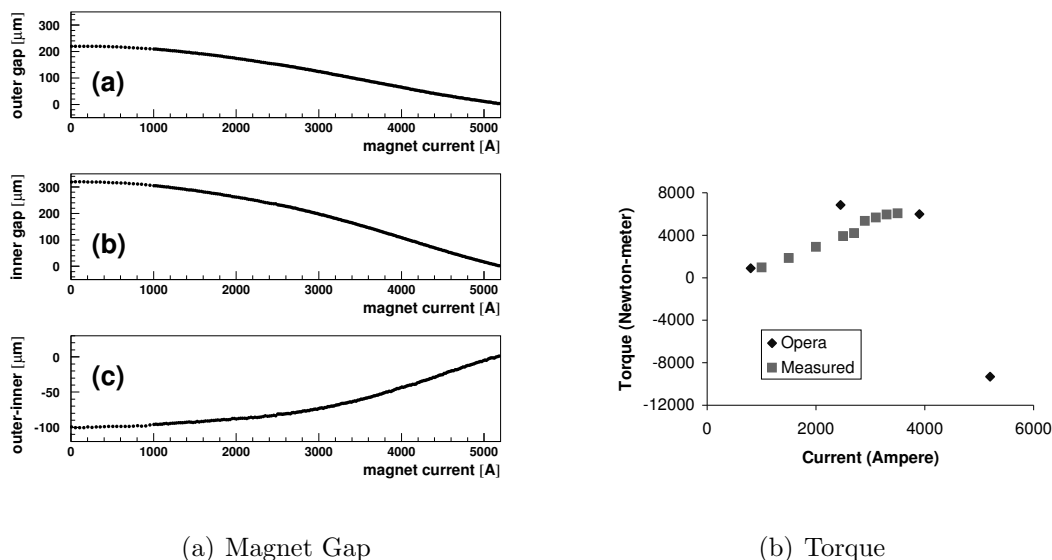
(a) Magnet Gap   (b) Torque

Figure 6.7: (a)The measurement of the storage ring gap as a function of magnet current, using the capacitance device described in the text. The gap was measured at $r = +15$ cm (a), and $r = -15$ cm (b), relative to the center of the storage region. The gap values at full field, 5200 A, have been subtracted. The total gap closure as well as the difference (a)-(b)=(c) is in good agreement with stress calculations. (b)The measured and calculated torque on a pole during ramp-up, with the pole pivoting about the inner radius spacers. At lower current, the outer radius of the pole tries to short the gap, pulling away from the yoke. The torque at full current, 5200 A, is the opposite sign, with the pole pushing against the spacers toward the yoke.

-gap-torque

Another issue that was not appreciated in the design can be understood from Figs. reffg:ring-elevation and 6.6, which has been given the name "the cold cryostat problem". If the vacuum in the outer-diameter cryostat were to become bad, from a liquid helium, liquid nitrogen or

fg:pole-outer-coil-inflector

vacuum leak in the cryogenic system, the cryostat will become cold and shrink radially. Given the close proximity of the pole pieces to the cryostat, serious damage could be done to the magnet if such a vacuum failure goes undetected. If a catastrophic loss of vacuum were to occur, the proceedure was to turn off the LHe as quickly as possible and turn on the Roots Blower and the mechanical vacuum pump at U11. The Fermilab experiment will need to develop a plan on how to mitigate the effects of such an incident.

6.3   Power Supply and Quench Protection

Both persistent mode and power supply excitation were considered. The total flux, $\int \vec{B} \cdot d\vec{s}$, is conserved in persistent mode. However, room temperature changes would result in changes in the effective area. Thus although the flux, is conserved, the magnetic field in the muon storage region is not. Persistent mode would also require a high-current superconducting switch. Power supply excitation with NMR feedback was chosen, although no feedback was used for the 1997 run. This method gives excellent control of the magnetic field and allows the magnet to be turned off and on easily. The power supply parameters are shown in Table 6.3.

Table 6.4: Power supply parameters

Rating	5 V, 6500 A	
Rectifier	480 VAC input, 12 pulse	
	(Two $\pm 15°$, 6 pulse	
	units in parallel)	
Output filter	0.4 F	
Regulator	Low-level system	0.1 ppm stability with
		17 bit resolution
	Power section	Series regulator with
		504 pass transistors
Cooling	Closed loop water system	
	with temperature regulation	
Regulation	Current-internal DCCT	± 0.3 ppm over minutes
		to several hours
	Field-NMR feedback	± 0.1 ppm (limited by
	(current vernier)	the electronics noise floor)
Manufacturer	Bruker, Germany	

field and allows the magnet to be turned off and on easily. The power supply parameters are shown in Table 6.3.

The quench protection design parameters were determined by the requirements of magnetic field stability and protection of the magnet system in case of a quench. When the energy is extracted, eddy currents are set up in the iron which oppose the collapse of the field. This can cause a permanent change in the magnetic field distribution [9]. This is sometimes called the 'umbrellaa effect, since the shape of the change over a pole resembles an umbrella. The eddy currents are minimized if the energy is extracted slowly. There will also be eddy currents in the aluminum mandrels supporting the coils. Electrically, this can be represented by a one turn shorted transformer. These eddy currents will heat the mandrels and can cause the entire coil to become normal. This is called quench-back. This has several beneficial effects. The part of the stored energy that is deposited in the coil is deposited uniformly over the entire coil and mandrel assembly. Also, once quench-back occurs, the energy extraction process is dominated by the quenchback and not by the specifics of where the quench occurred. Therefore, the effects of a quench on the reproducablility of the magnetic field should be minimal.
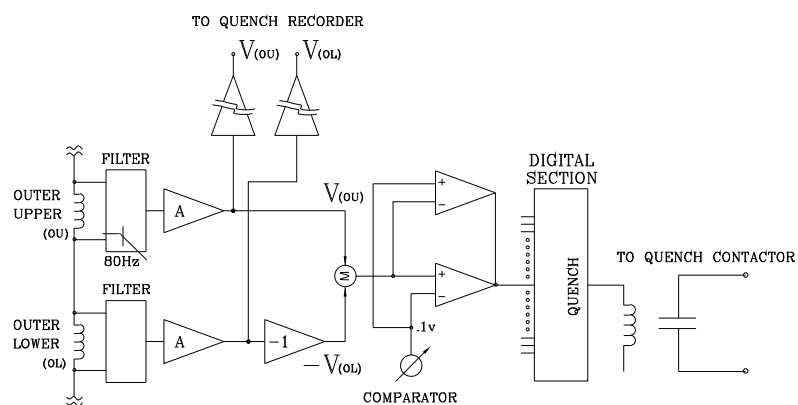

Figure 6.8: Diagram of the quench protection circuit.

The energy extraction system consists of a switch, resistor, and quench detection electronics. An energy extraction resistor of 8 m) was chosen. Including the resistor leads, the room temperature resistance is 8.8 m). This gives an /R time constant of 1 min. The actual time constant varies due to the temperature increase of the coil and dump resistor and the effect of eddy currents in the mandrels during the energy extraction (see below).

This resistance value was calculated to cause quenchback in the outer mandrel within 2 s at full current. The quench protection circuit is shown in Fig. 6.8. The energy extraction trigger for a quench which originates in one of the coils is the voltage difference between matching coils; for example, $V(\text{outer} - \text{upper}) - V(\text{outer} - \text{lower})$. Since the inductance is effectively the same, the voltages should be equal even while charging the magnet, unless a quench develops in one coil. This quench threshold is set at 0.1 V. However, the coil interconnects are thermally coupled together with the helium tubes. It is possible that a quench in an interconnect could propagate to both coils almost simultaneously. Therefore, a voltage threshold of 10 mV was chosen for each interconnect. The outer upper to lower interconnect is only 1 m long. This threshold was set to 5 mV. The thresholds were determined by the requirement that the quench be detected within 0.2 s. The gas-cooled leads develop a voltage of typically 15 mV at full current. If the lead voltage exceeds 30 mV, the energy is extracted.

6.4   Shimming the Magnet

The removable edge shims on the pole surfaces play a major role in the design of the magnet and its eventual actual shimming corrections. As seen in Fig. 3, the edge shims are symmetrically located about the aperture center line. Various symmetric perturbations of the shims produce predictable multipoles. For example, changing equally all four corners produces only sextupole series terms, proportional to even powers of the aperture radius. Increasing the two outside shims and/or decreasing the inside shims produce only normal quadrupole series terms, proportional to odd powers of the aperture radius. This can be extended to up-down and diagonal (skew) asymmetries. These mathematically predictable asymmetries were indeed found to apply to very high accuracy, including linear superpositions for finite permeability, again showing internal consistency in the computations. Finite and realistic permeability was then used, and the amplitudes of the corner shim perturbations were progressively raised. It was found that the multipole description was still correct and increased linearly with amplitude until unrealistically strong edge shims finally gave a breakdown in linearity as well as in the required symmetries. This gave confidence that the computer calculations could be used to get the design optimization on paper, and also to calculate multipole perturbations of the operating magnet, to correct the field to approaching a 1 ppm level.

Wedge-shaped air gaps between the poles and yoke are an important design feature. These air gaps sufficiently isolate the precision poles from the yoke return that field aberations, or multipoles above the dipole term, are minimally affected by reasonable variations in the yoke reluctance (Table 1). Since the poles dominate the field aberations, the highest quality of iron is only required for the poles. Very pure continuous cast steel is used for the poles. This material is typically of 0.004% carbon content. The higher purity increases permeability at the operating field of the magnet compared to conventional AISI 1006 iron (0.07% carbon typically), which is used for the yoke. Even more important is the impact of the purity on inclusions of ferritic or other extraneous material, air bubbles, etc., which are greatly minimized.

This isolation of field aberations from dipole reluctance has an additional very important property. It is necessary to have large holes through the yoke to inject the beam, for inflector

power and cryogens, and for the outer coil leads and cooling. Because of the isolation from the air gaps, no significant effect on multipoles is observed after restoring the reluctance in the region of the holes by adding large iron collars [5].

The air gaps are wedge-shaped, with a larger air gap on the outer radius, closest to the iron return of the C magnet. The slope is calculated to compensate for the gradient due to C magnet asymmetry (Fig. 2), where the field lines would otherwise tend to cross the gap near the return. Calculations showed that a change in wedge angle caused a very pure normal quadrupole adjustment without inducing higher multipoles. A change in the wedge slope by 1 mm over the length of the wedge changes the quadrupole (at 4.5 cm, the edge of the storage volume) by 15 ppm, while the sextupole term changes by 1 ppm, and the higher multipole changes are still smaller. Attempting to make a large quadrupole adjustment by using pole edge shims introduces octupole, roughly half the size of the quadrupole change [5]. Instead, a combination of wedge angle and inside-outside asymmetry in edge shims can null both quadrupole and octupole.

The inner radius coils, required to be away from the midplane to allow observation of decay electrons from the stored muons, were pulled still further vertically away from the midplane in order to have access to the air gaps for shimming. This has the additional advantage of making the hoop force on these large diameter slender inner coils approximately zero.

The final coil design used a single layer of the KEK TOPAZ pure aluminum stabilized superconductor [6] to excite the 20 cm air gap. The iron circuit dominates so strongly that tolerances on coil location are quite reasonable, as discussed below.

Final pole design involved refinements to the edge shims plus adjustments of the location and angle of the taper of the edges of the poles. To first order, to flatten the field, the cross-sectional area of the edge shims is the important parameter. However, in detail the distance of the inner edge of the shims to the center (Fig. 3), chosen to be rfi16 cm, and the shim width of r"5 cm, optimized the field quality by reducing the r6 multipole. This in combination with an edge angle of 36.7° produced a very small r2 sextupole, the r4 term was nulled, and all higher multipole terms were virtually eliminated.

Making the wedge separate from the poles presented some mechanical complications, but resulted in substantial shimming advantages. A change in the air gap, changing the wedge thickness with no change in angle, produces a very strong effect on the local dipole field, essentially proportional to the thickness change divided by the half-gap of 10 cm. This is because the storage ring aperture and air gaps at the base of each pole constitute 93% of the circuit reluctance. However, small vertical movements of the poles have a small effect on the reluctance, since the combined air gap is unchanged (Table 1).

Errors in the precision pole thickness are small compared to the expected variation of up to 200 μm in the distance between the top and bottom yoke plate surfaces adjacent to the poles.

A means of shimming in the air gaps is attractive, since only dipole is affected, and not higher multipoles. The average thickness of the wedges determines dipole, and the wedge angle determines quadrupole, both essentially pure moments. Finally, if the wedges are radially adjustable, a very fine control for dipole exists. Since the wedge angles are approximately 1 50, radial movement by 50 μm changes the gap by 1 μm, finer control than is available otherwise.

At least on paper, and using realistic parameters, a magnet aperture of 9 cm diameter was designed with a uniform field to a ppm level (Fig. 4). Long-wavelength "real world" errors will be greatest for low-order moments, both normal (field vertical on the horizontal midplane) and skew. The shimming techniques described are designed to correct most of these, with surface coils required to correct skew dipole.

Correcting coils on the surface of the poles permit ultimate fine control of static, and slowly varying errors. The surface coils can be used to correct lowest multipoles to tens of ppm, thus providing significant overlap between the iron shimming and the dynamic shimming. These coils have been constructed to generate moments over the entire 360° azimuth. The coils were designed with printed circuit boards, with 2]120 wires running azimuthally around the ring on the top and bottom pole surfaces facing the storage ring gap, and spaced radially 2.5 mm apart, to avoid lumpy effects which generate higher multipoles. Pole surface corrections can be (and have been) added with ferromagnetic material to correct for local effects in the iron geometry. Local current loops may also be used. The 'continuousa ring was built with 10° pole sections, 36 of which form an almost continuous ring. Dipole correction coils are located in the air gaps for each 10° pole.

Strictly speaking, the description of the storage ring field aberations by multipoles assumes no gradients in the beam direction. However, the muon betatron wavelengths are very long so that longitudinal averaging of actual field data is correct to a very good approximation. For example, for a 10° pole section the azimuthal integral of field data can give an average multipole fit to very good accuracy. The pole edge shims or other adjustments can be applied to correct this 10° average.

Computations of a 75 μm crack between the 10° poles show that the dipole field is reduced slightly locally, but the longitudinal integral was independent of both r and y, so the effect was only on the field integral and not on the field aberations. There are limits to averaging out local field irregularities in the poles, one of which is simply that the ability to measure precisely is more difficult with large gradients. Thus, the $(g-2)$ storage ring shimming effort has the goal to make the field as uniform as practical. Fig. 5 shows the magnetic field lines for the design, and the magnet parameters are given in Table 2.

6.5   ES&H, Quality Assurance, Value Management

References

`Bailey79a` [1] Bailey J, et al. Nucl. Phys. B150:1 (1979).

`nnett:2006a` [2] Bennett GW, et al.(The Muon $(g-2)$ Collaboration) Phys. Rev. D, 73:072003 (2006).

`Danby:2001` [3] G.T. Danby, et al., Nucl. Inst and Meth. **A 457**, 151 (2001).

`POISSON` [4] Reference Manual for teh POISSON/SUPERFISH group of codes, LANL, LA-UR-87-126.

`E821DR` [5] Design Report, BNL E821, A New Precision Measurement of the Muon $(g-2)$ Value at the level of 0.35 ppm. 3rd edition, D.H. Brown et al. B.L. Roberts Editor, March 1995.

`mamoto:1984` [6] A. Yamamoto, H. Inoue, H. Hirabayashi, J. Phys. 45 (1984) C1-337.

`yamamoto-pc` [7] A. Yamamoto, private communication.

`Green:1980` [8] M.A. Green et al., Operation of a two-phase cooling system on a large superconducting magnet, Proceeding of the Eighth International Cryogenic Engineering Conference, Genoa, Italy, June 1980, IPC Science and Technology Press, 1980, p. 72.

Chapter 7

Relocation of the E821 Storage Ring Magnet

7.1 Introduction

7.2 Disassembly of the Magnet at BNL

7.3 Shipping the Magnet

7.4 Reassembly of the Magnet at Fermilab

Chapter 8

The Superconducting Inflector Magnet

In this chapter we first introduce the E821 inflector magnet, which is our baseline starting option. We then describe the shortcomings of this magnet and the characteristics that an improved inflector would have, along with the R&D needed to arrive at a new inflector design.

8.1   Introduction to the Inflection Challenges
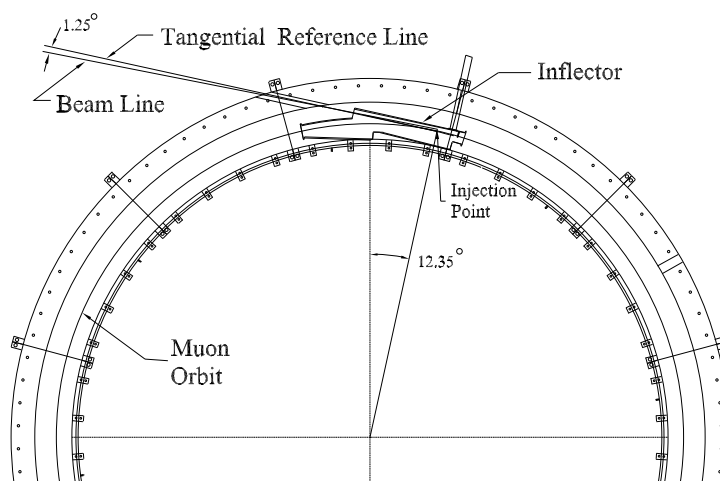
Figure 8.1: Plan view of the beam entering the storage ring.

The usual storage ring is composed of lumped beamline elements such as dipoles, quadrupoles, sextupoles, etc., which leaves space for injection, extraction, and other beam manipulation devices. For the measurement of a_μ, the requirement of ± 1 ppm uniformity on the magnetic field, which in E989 must be known to $\leq \pm 0.07$ ppm, prohibits this usual design. Instead, as described in Chapter 6 the $(g-2)$ storage ring is designed as a monolithic magnet with

141

no end effects. The "C"-magnet construction shown in Fig 6.2 presents several obstacles to transporting a beam into the storage ring: There must be holes through the back-leg of the magnet and through the outer coil cryostat and mandrel for the beam to enter the experiment. These holes must come through at an angle, rather than radially, which complicates the design, especially of the outer-coil cryostat.

A plan view of the beam path entering the storage ring is given in Fig. 8.1. Since the beam enters through the fringe field of the magnet, and then into the main 1.5 T field, it will be strongly deflected unless some magnetic device is present that cancels this field. This device is called the inflector magnet.

The injection beam line is set to a 1.25° angle from the tangential reference line (Fig. 8.1). The inflector is aligned along this reference line and its downstream end is positioned at the injection point. The point where the reference line is tangent to the storage ring circumference is 77 mm radially from the muon central orbit. The main magnet fringe field, upstream of the inflector, bends the incoming beam by about 1.25°, so that the beam enters the inflector nearly parallel to the inflector axis.

The requirements on the inflector magnet are very restrictive:

1. To a good approximation it should null the storage ring field such that the muons are not deflected by the main 1.5 T field.

2. It should be a static device to *prevent time-varying magnetic fields correlated with injection*, which could affect $\int \vec{B} \cdot d\vec{\ell}$ seen by the stored muons and produce an "early to late" systematic effect.

3. It cannot "leak" magnetic flux into the precision shimmed storage-ring field that affects $\int \vec{B} \cdot d\vec{\ell}$ at the sub-ppm level.

4. It cannot contain any ferromagnetic material, which would create problems in satisfying requirement # 3 above.

8.2   The E821 Inflector Design and Operation

Three possible solutions were considered in E821: A pulsed inflector, a superconducting flux exclusion tube, and a modified double $\cos\theta$ magnet. The pulsed inflector proved to be technically impossible at the repetition rate necessary at BNL. Furthermore it violates item 2 above. Naively one could imagine that a superconducting flux exclusion tube would work for this application. However, an examination of Fig. 8.2 shows that in the vicinity of the tube, the magnetic field is perturbed on the order of 10%, or 100,000 ppm [1], an unacceptable level. Attempts to figure out how to mitigate this problem were unsuccessful. This is because the large eddy currents needed to shield the 1.45 T field are large enough to affect the uniformity of the field seen by the muons contained in the red semicircle. However, this principle will re-appear in the discussion of how to shield the 200 G (20 mT) residual magnetic field from the truncated double $\cos\theta$ design.
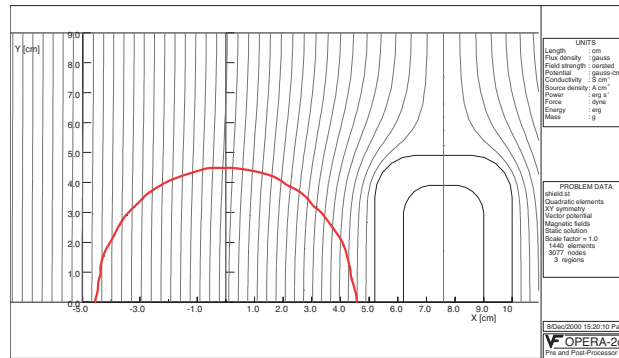
Figure 8.2: The calculated magnetic field outside of a superconducing flux exclusion tube placed in a 1.45 T magnetic field. The red circle is the muon beam storage region. (From Ref. [1])

8.2.1   Magnetic Design of the E821 Inflector

Only the double $\cos\theta$ design[2] satisfied the three criteria listed above. The double $\cos\theta$ design has two concentric $\cos\theta$ magnets with equal and opposite currents, which outside has negligible field from Ampère's law. A double $\cos\theta$ design provides a 1.5 T field close to the storage region, and traps its own fringe field, with a small residual fringe field remaining. However, what is needed for the $(g-2)$ beam channel is a septum magnet. This is achieved by truncating the two $\cos\theta$ distributions along a line of constant vector potential A [2]. The truncation method is shown in Fig. 8.3, taken from Ref. [2], which should be consulted for additional details.

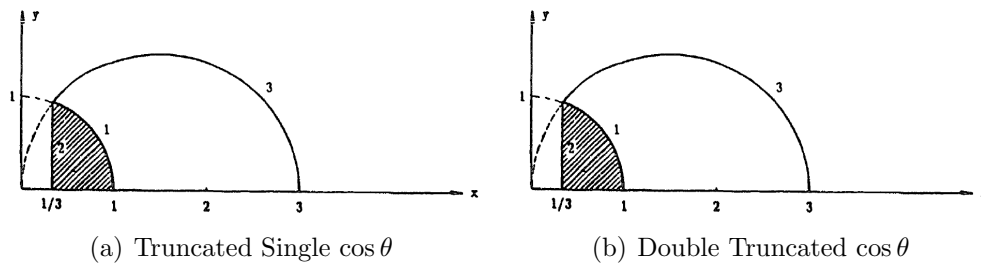| (a) Truncated Single $\cos\theta$ | (b) Double Truncated $\cos\theta$ |

Figure 8.3: (a) The principle of the truncated single $\cos\theta$ magnet. (b) The principle of the truncated double $\cos\theta$ magnet.

Aluminum-stabilized superconductor was chosen for the BNL $(g-2)$ inflector: (a) to minimize the interactions of the incoming pion/muon beam at both upstream and downstream ends of the coil with no open apertures for the beam, and (b) to make the coils and cryostat design compact, so that the conductive cooling (without liquid helium containers surrounding the coils) can be achieved effectively. An existing Al-stabilized superconductor was supplied by Japan KEK (fabricated by Furukawa Co.). This conductor was developed for ASTROMAG (Particle Astrophysics Magnet Facility) [3, 4]. Fig. 8.4 shows the cross-section of this conductor. The basic parameters are listed in Table 8.2.1. From computer
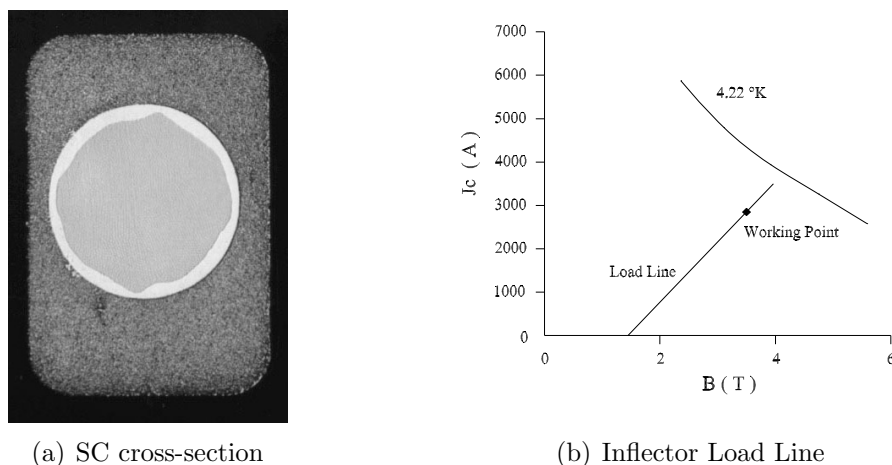
(a) SC cross-section

(b) Inflector Load Line

Figure 8.4: (a) The inflector superconductor cross-section. (b) Superconductor characteristics and the inflector load line in the environment of 1.45 T magnetic field.

`or-loadline`

calculations, the peak field seen by the by the inflector conductor filaments reaches 3.5 T; if the self-field effect [5] is taken into account. This is due to the superposition of the return flux and the main field. Short sample tests were performed at KEK and BNL. The results showed that the critical current of this superconductor is about 3890 A at 4.6 K and 3.5 T. In the $(g-2)$ storage ring, the inflector sees 1.45 T field (from the main magnet) even at zero operating current. From the conductor characteristics, the inflector operates at around 73% of the full load (at 4.6 K). The short sample test data and the inflector load line (in the storage ring field environment) are shown in Fig. 8.4(b).

Table 8.1: Properties of the inflector superconductor.

Configuration (NbTi:Cu:Al)	1:0.9:3.7
Stabilizer	Al (99.997% RRR = 750
Process	Co-extrusion
NbTi/Cu composite	Diameter 1.6 mm monolith
NbTi filament	Diameter 0.02 mm
Number of filaments	3050
Twist pitch	31 mm
Conductor dimension	2×3 mm^2
Insulated conductor dimension	2.3×3.3 mm^2

`l-cond-prop`

The result is a magnet with conductors arranged as shown in Fig. 8.5(a). The conductors are connected in series, with an equal number with current into and out of the page. In Fig. 8.5(a) the current is flowing out of the page in the "D" shaped pattern of conductors, and into the page in the backward "C" shaped arrangement of conductors. So the field from

the inflector magnet is vertical up in the beam channel and downward in the return area. With the main storage ring field vertical in the negative direction, there is no field in the beam channel and $\simeq 3$ T field in the return area. In this design, it is difficult to open up the beam channel because moving the "C" arrangement of conductors to the right would quickly exceed their critical current.
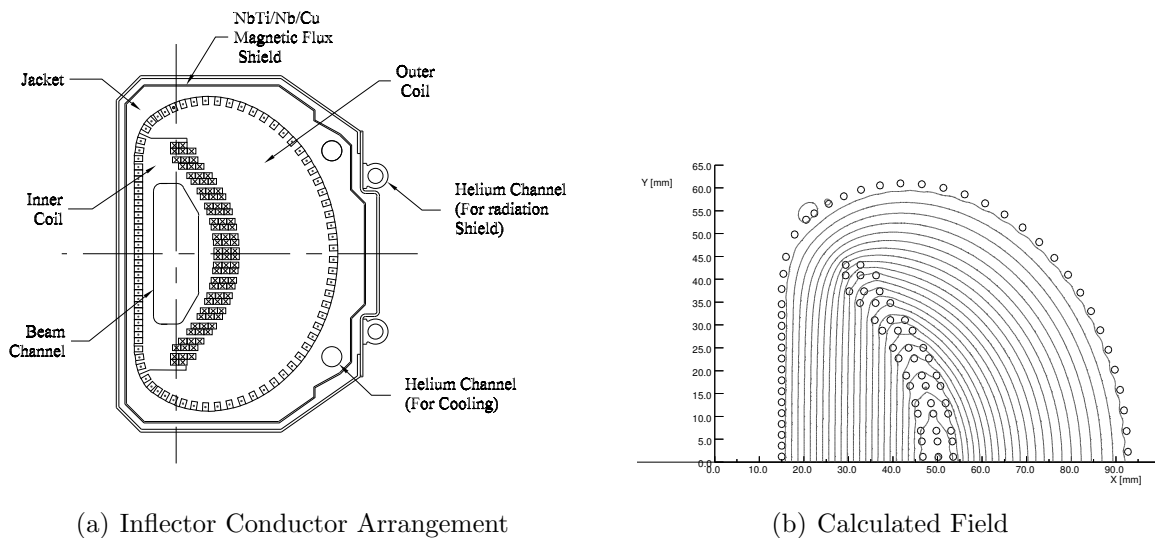

(a) Inflector Conductor Arrangement (b) Calculated Field

Figure 8.5: (a) The arrangement of conductors in the inflector magnet. (b) The magnetic field generated by this arrangement of conductors.

Several additional issues are important, and must be discussed: The interconnects that join the two sets of conductors since all windings are powered in series; and shielding the flux that does leak out of this arrangement of conductors, which can be see to be an issue in Fig. 8.5(b). The latter issue arises because of discrete conductors, rather than a continuous current distribution.

How to wind the ends of the coils was a difficult problem. End-winding configurations were extensively studied by using dummy and real conductors [6]. Fig. 8.6 shows two options. The open-type option leaves the beam channel clear, but end loop support and constraint is much more difficult. The closed-type option forces the incoming beam to penetrate conductor layers, resulting in multiple scattering, but was thought to provides better mechanical and quench stability, and occupies less physical space. Later studies confirmed that the closed-end option gives much less fringe field. A third option, with the upstream end open and the downstream end closed, was also discussed. In that case, the muon storage efficiency would not increase significantly, while the engineering difficulties would remain. The second option, with both ends closed, was chosen.

The coil was wound in two different pieces indicated by "inner" and "outer" coils in Fig. 8.5(a). One end of the coil is shown in Fig. 8.6(a), and the outer coil is shown in Fig. 8.6(b). The choice was made to wind the coil over the beam channel, because this
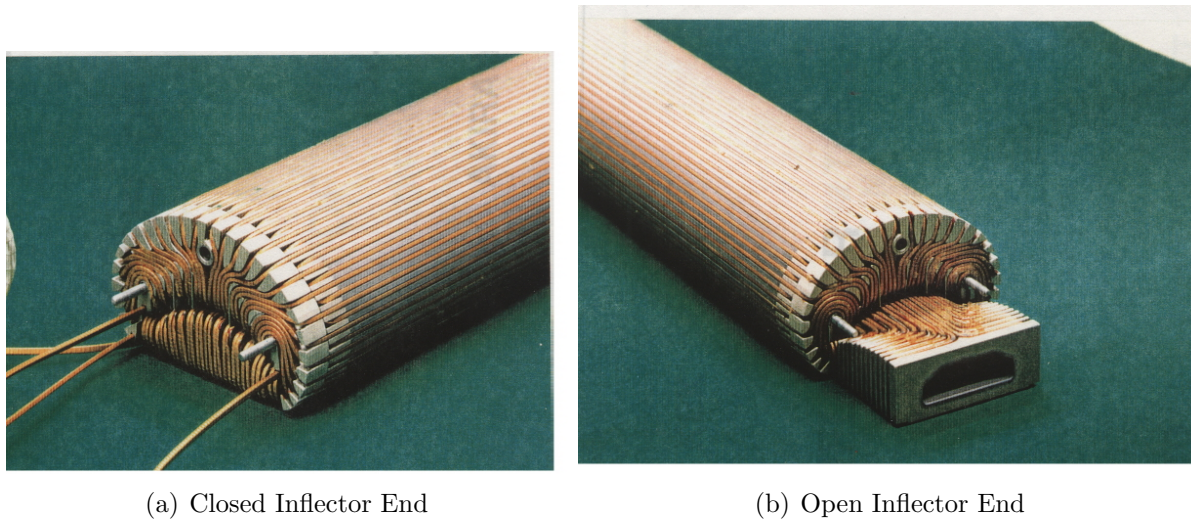
(a) Closed Inflector End   (b) Open Inflector End

Figure 8.6: (a) The prototype closed inflector end. (b) The prototype open inflector end. `fg:infl-ends`

configuration would have less flux leakage, and was thought to be more stable from quenches. However, a 0.5 m prototype was constructed with one open and one closed end, which are shown in Fig. 8.6. This prototype inflector was operated in the earth's field, and then in an external 1.45 T field without incident.

The outer coil has 52 turns many more than the 36 turns in the inner coil (see Fig. 8.7). A difficulty in stacking the end layers for the outer coil was solved by using a double-layer winding scheme. For the first layer, only every other turn was wound on the mandrel. After applying a special outer coil end cap, the remaining turns were then wound and the second layer was formed, as shown in Fig. 8.7. This configuration keeps end loops inside machined grooves, and ensures sufficient mechanical constraint and heat conduction. An aluminum case was designed to serve the following functions: (1) to constrain the conductors along the 1.7 m long surface; (2) to provide sufficient cooling through machined liquid helium paths.

The inner coil and the outer coil are connected in series. The joint is located inside the downstream end of the coils; and is made by soldering the superconductors without removing the aluminum stabilizer. The joint resistance is less than 10 nΩ at 3000 A and 4.2 K. The joined leads were placed inside a U-shaped groove, as shown in Fig. 10, attached to the coil end structure. Cooling tubes run through the extender (aluminum block). One temperature sensor was mounted near the joint to monitor the local ohmic heating.

The geometry of the inflector cryostat is complicated by the proximity of the outer-coil cryostat, the pole pieces and the muon beam. A sketch of the beam path through the outer coil is shown in Fig. 8.8(a). The complicated arrangement where the inflector entrance nests into the concave wall of the inflector cryostat is shown in Fig. 8.8(b). Fig. 8.9 shows the combined inflector cryostat and beam vacuum chamber. The cryostat region and beam region have different vacuums, so the inflector can be cooled, independent of whether the beam vacuum chamber is evacuated or not.

The exit of the inflector magnet is shown in Fig. 6.6, which clearly indicates the accelerator physics issue. The incident beam is contained in the red 18 mm × 56 mm "D"-shaped
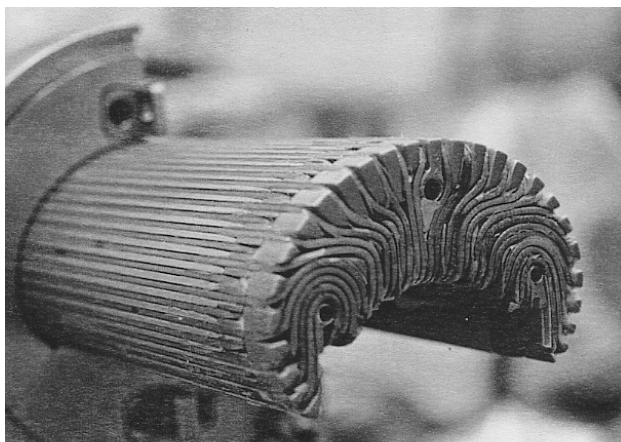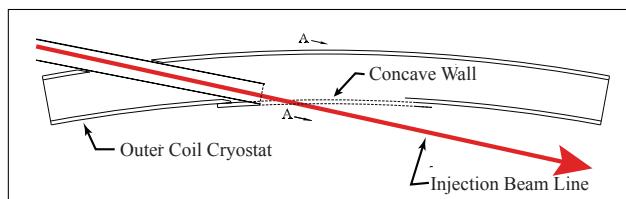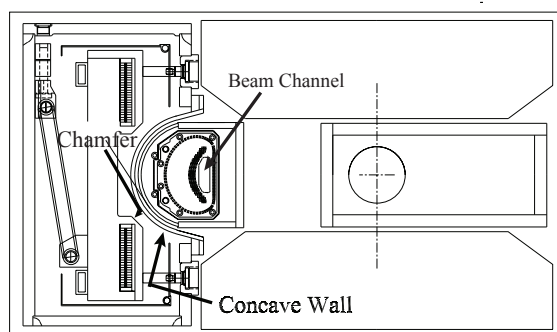
(a) Outer Inflector Coil
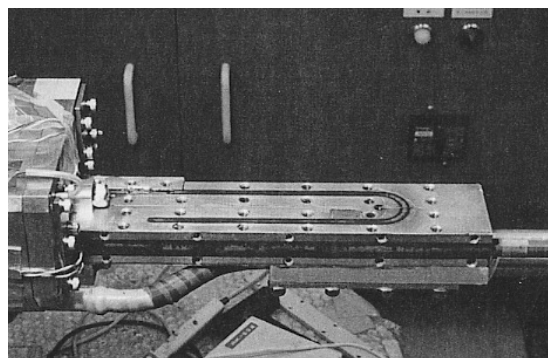
(b) Coil Interconnect

Figure 8.7: (a) The arrangement of conductors in the inflector magnet.(b) The joint and lead holder for the interconnect.

(a) Outer Coil Penetration

(b) Inflector Entrance

Figure 8.8: (a) A plan view of the beam penetration through the outer coil and cryostat. (b) An elevation view of the inflector entrance showing the concave wall of the outer-coil cryostat where the beam exits the outer coil-cryostat.

channel, while the stored beam is confined to a 45 mm diameter circular aperture. Thus it it impossible to match the β or α functions between the ring and the muon beamline. The result is a β wave that causes muon losses after the beam is injected. We return to this, and other issues after we describe the E821 inflector magnet.

8.2.2 Shielding the residual fringe field

Once the coil winding was complete, the effects of the ends on the fringe field needed to be considered. As discussed in Section 3, the closed end option gives much less fringe field. Furthermore, once the winding becomes superconducting, the following effects give possible additional sources of fringe field: (1) Slight variations of the location of the superconducting
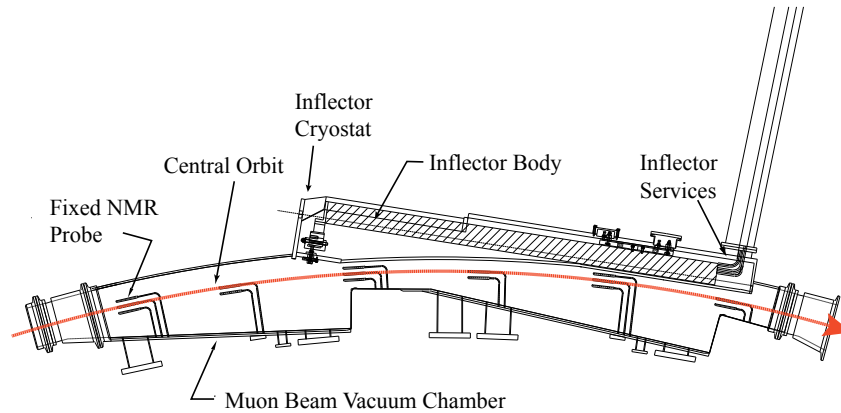
Figure 8.9: Plan view of the combined inflector cryostat-beam vacuum chamber arrangement. The inflector services (power, LHe and sensor wires) go through a radial hole in the back-leg outside of the storage-ring magnet. The NMR fixed probes are in grooves on the outside of the vacuum chambers, above and below the storage region. The red arrow shows the muon beam central orbit.
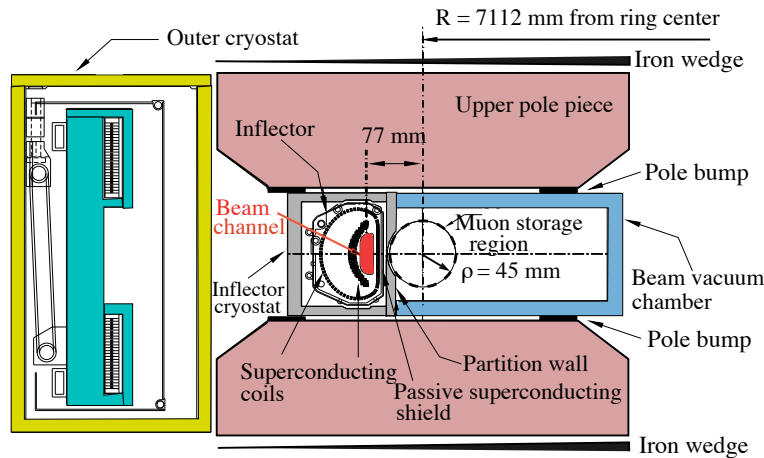

Figure 8.10: The inflector exit showing the incident beam center 77 mm from the center of the storage region. The incident muon beam channel is highlighted in red. (Modified from Fig. 6.6)

core. The center of the conductor could vary by up to a few tenths of a millimeter. (2) Mechanical tolerance on the mandrels. The conductor was insulated by formvar and fiberglass tape, then wound into the machined grooves on the coil mandrels. Winding, assembly, and epoxy resin curing also affect the mechanical tolerances. The tolerance of the superconductor positioning directly affects the field quality. (3) Magnetization effect: During the current ramp, Eddy currents are induced inside each filament. The dipole effects are de-coupled by

the twist pitch of the filaments in the composite [7], but high-order multipoles could still influence the internal (beam channel) and external (storage region) magnetic field. Fringe field measurements were made on the superconducting prototype at room temperature with 20 A current, and at superconducting temperature at full nominal current. The resulting fringe field measurements were consistent [8]. These suggest those sources (1) and (3) are not important. Further detailed computation showed that the magnetization effect, source (3), in the muon storage region is quite small (less than 70 ppm) [9]. Source (2) is the dominant origin of the residual fringe field. At the design current, the maximal fringe field within the muon storage region was about 200 G (1.4%) near the outer edge. The fringe field behaves in such a way that it is a rapidly varying function along the transverse direction, i.e. the radial direction of the storage ring, and essentially gives a negative disturbance. The fringe field of the inflector (prior to the addition of the superconducting shield) is opposite to the main field at the outer radius of the storage ring, and changes sign while crossing the central orbit. The consequence of such a fringe field is severe. The high gradient of the field would be beyond the working range of the NMR probes, so that the magnetic field map of the storage region would be incomplete, directly impacting the error of the measurement precision of the muon magnetic moment. Special measurements in this region are possible, by using Hall probes, or, by varying the NMR reference frequency, trigger time, and excitation amplitude. These methods may reduce the error on the field value, but on the other hand, would introduce an enhanced position error due to two independent field maps, which must be corrected. The residual fringe field had to be further reduced in order to reach the final goal of the $(g - 2)$ experiment, and would be completely unacceptable in E989.

Conventional magneto-static shimming studies to reduce this fringe field were begun, using computer simulations. The iron compensation must be located outside the muon storage region. Its contribution to the central field will be a slowly varying function in this space, which is not able to cancel the larger gradient fringe field to an acceptable level [10]. The best way to eliminate a multipole fringe field is to create an opposite multipole current source with the same magnitude. The best such current source is the super-current generated inside a superconducting material due to the variation of the surrounding field. A method of using SC material to shield the inflector residual fringe field was studied and developed. The fringe field specification was then satisfied.

It was reported that much higher J_c NbTi/Nb/ Cu multi-layer composite sheet (or tubes, cups) were developed at Nippon Steel Corporation. The sheet contains 30 layers NbTi, 60 layers Nb, and 31 layers Cu. The Cu layers greatly improved the dynamic stability against flux jumping [7]. The Nb layers act as barriers, which prevent the diffusion of Ti into Cu. The diffusion could form hard inter-metallic layers and create difficulties for the rolling process. Fig. 13 shows the typical cross section of the sheet. Detailed information and the fabrication procedure are described in [11]. This type of sheet was ideal for the requirement of the inflector shield. A special thin sample sheet was then developed at Nippon Steel Corp. The measured overall critical current density was above 500 A/mm^2 (at 1.5 T, 4.2 K, H$\perp$ NbTi layers). The critical current density J_c of NbTi was about 1200 sim1400 A/mm^2 (at 1.5 T, 4.2 K, $H \perp$ NbTi layers), and above 2000 A/mm^2 (at 1.5 T, 4.2 K; $H \parallel$ NbTi layers).

in 1994, a second superconducting shield was tested on the prototype inflector which was discussed above. The shield was made by a small piece of multi-layer composite sheet (with

thickness of 0.5 mm), which was formed as a sleeve, and glued by epoxy on the downstream part of the prototype. A special cryostat chamber was made to simulate the confined space located around the injection point (as shown in Fig. 8.10), and was placed inside a dipole magnet (AGS type 18D72), which provided the same field (1.45 T) as the $(g-2)$ storage ring. Shielding effects with and without the external magnetic field were studied[13, 14]. This test verified that the heat radiation and flux jump would not be problems, under the indirect cooling system and the slow ramp rate.

Based on the above successful tests, Nippon Steel Corp. developed large, thin pieces of sheet especially for the $(g-2)$ inflector, to cover its 2×0.5 m^2 surface and to fit into the limited space between the storage region and main magnet coil. The shielding result was extremely satisfactory.
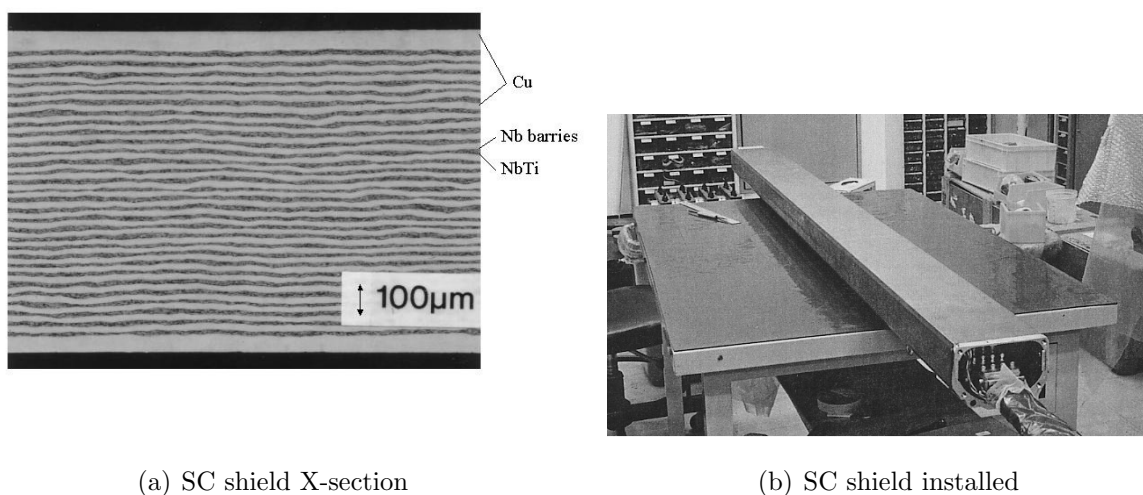
(a) SC shield X-section   (b) SC shield installed

Figure 8.11: (a)Cross section of the multi-layer superconducting shield sheet. (b)The superconducting shield installed around the body of the inflector.

8.2.3   Performance of the E821 Inflector

Two full-size inflectors were produced. In the testing of the first inflector, an accident occurred, where the interconnect shown in Fig. 8.7(b) was damaged. In order to repair it, the superconducting shield was cut to give access to the damaged superconductor. After the repair, an attempt was made to apply a patch to the shield. Unfortunately this attempt was not successful. The resulting fringe field reduced the storage-ring field by 600 ppm over a $1°$ azimuthal angle, resulting in unacceptable magnetic-field gradients for the NMR trolley probes closest to the inflector body. It was also realized that significant fringe field came from the inflector leads. An average field map from the 1999 run using the damaged inflector, and from the 2001 run using the new inflector are shown in Fig. fg:multipoles-99-01. The field in this region had to be mapped by a special procedure following data taking. This large fringe field introduced an additional uncertainty into the measurement of the average field of ±0.20 ppm in the result [12].

An average field map from the 1999 run using the damaged inflector, and from the 2001 run using the new inflector are shown in Fig. fg:multipoles-99-01. The damaged inflector was replaced before the 2000 running period. In the new inflector, the superconducting shield was extended further beyond the downstream end, and the lead geometry was changed to reduce the fringe field due to the inflector leads. Both of these improvements were essential to the excellent shielding obtained from the second inflector. For both the 2000 and 2001 running periods, the fringe field of the inflector was negligible [15, 16]. Bennett:2002,Bennett:2004
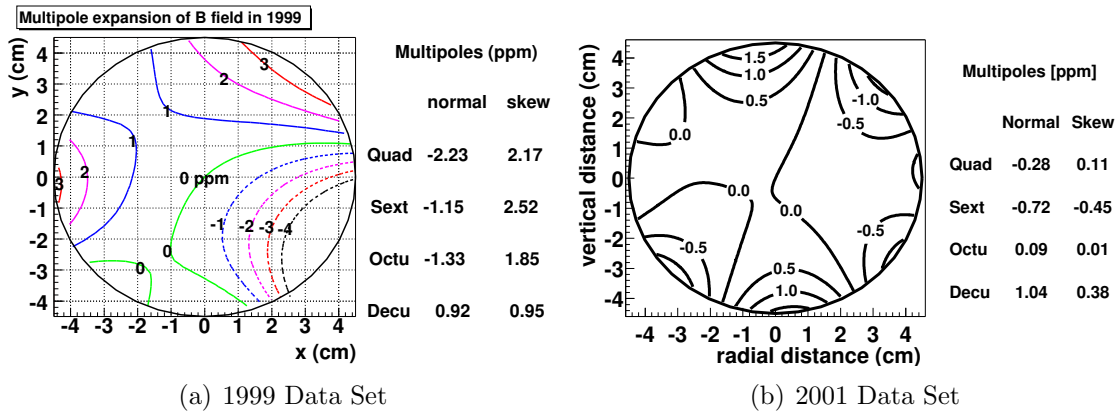

Figure 8.12: The average magnetic field $\langle B \rangle_{azimuth}$ (a) with the damaged inflector (1 ppm contours) (b) and with the second inflector (0.5 ppm contours).

8.2.4 Simulations of Transmission and Muon Storage with the E821 Inflector

H.N. Brown, who designed the E821 beamline concluded from his simulations that the beam lost going through the closed ends was a factor of 1.8. More recent simulations with G2MIGTRACE give a factor of xxx

bla bla bla

Furthermore, the issue raised earlier, the gross mismatch of both the β and α functions between the incident beam and the storage ring resulting from the small inflector aperture also contribute to beam losses. Simulations of a new inflector with an increased aperture which better matches the ring to the beamline show

bla bla bla.

8.3 Lessons for E989 from the E821 Inflector

The most important single lesson from the E821 inflector came from the flux leakage from the damaged inflector, and the realization that the first design of the inflector leads also contributed to this problem (see Fig.8.12) The lesson is clear: *Whatever flux is inside of the inflector must be confined inside of the inflector and not permitted to leak into the storage region.* The ± 0.2 ppm systematic error from this problem would completely saturate the

error budget of E989. The highly localized 600 ppm perturbation at the location of the "repaired" superconducting shield simply could not be shimmed away.

Any new inflector must control the flux leakage. This must be done by utilizing the double $\cos\theta$ principle, which automatically minimizes the leakage by Ampère's law, and by the use of a passive supercondicting shield to eliminate the residual fringe field. Also important is the design of the current-carrying leads, which in the first version of the E821 inflector contributed to the flux leakage problems.

The second issue that is crucial for a new inflector is to open the ends, and to open the size of the beam channel. The muon injection efficiency achieved in E821 was around 2%. Early simulations predicted that it should be 5 - 7%. Opening the ends of the inflector would have doubled the number of stored muons. So it becomes clear that a new open-ended inflector with a larger aperture, perhaps as large as 30 to 40 mm diameter, is desirable and possible. Given the time that will be needed to develop a new inflector, it is impractical to have a new inflector ready by mid-2015 when the shimming program would be ready to install vacuum chambers and the inflector.

A passive superconducting shield, and careful design of the inflector power leads will be an essential feature of this new design.

8.4 Improvements with a New Inflector

8.5 ES&H

References

`amamoto:2002` [1] A. Yamamoto, et al., Nucl. Inst. Meth. **A 491**, 23 (2002).

`rienen:1989` [2] Frank Krienen, Dinesh Loomba and Wuzheng Meng, Nucl. Inst. Meth. **A238**, 5 (1989).

`amamoto:2000` [3] A. Yamamoto, Nucl. Instr. and Meth. A 453 (2000) 445.

`Makida:1991` [4] Y. Makida, et al., IEEE Trans. Magn. 27(2) (1991) 1944.

`Garber:1989` [5] M. Garber, A. Ghosh, W. Samson, IEEE Trans. Magn. 25 (2) (1989) 1940.

`Saito` [6] Y. Saito, et al., Development of beam inflection superconducting magnetevaluation of prototype, Tokin Technical Review, No. 20.

`Wilson:1983` [7] M.N. Wilson, Superconducting Magnets, Oxford Science Publications, Oxford, 1983.

`amamoto:1992` [8] A. Yamamoto, Status of the inflector, Internal Meeting Minutes, 1992; W. Meng, K. Woodle, Superconducting shield test on $(g-2)$ inflector magnet, $(g-2)$ Note, No. 210, 1994.

`Green:1995` [9] M.A. Green, W. Meng, IEEE Trans. Appl. Supercond. 5 (2) (1995) 667.

`Danby:1994` [10] G.T. Danby, W. Meng, W. Sampson, K. Woodle, IEEE Trans. Magn. 30 (4) (1994) 1766.

`Itoh:1993` [11] I. Itoh, T. Sasaki, IEEE Trans. Appl. Supercond. 3 (1993) 177.

`Brown:2001` [12] H.N. Brown, et al, Phys. Rev. Lett. **86** 2227 (2001).

`rienen:1995` [13] F. Krienen, et al., IEEE Trans. Appl. Supercond. **5** (2) (1995) 671.

`Meng:1994` [14] W. Meng, K. Woodle, Superconducting shield test on g-2 inflector prototype, g-2 Note, No. 210, 1994.

`ennett:2002` [15] The $g-2$ Collaboration: G.W. Bennett et al., Phys. Rev. Lett. **89**, 101804 (2002); Erratum-ibid. **89**, 129903 (2002).

`ennett:2004` [16] Bennett GW, et al. (The $g-2$ Collab.) Phys. Rev. Lett. 92:161802 (2004)

Chapter 9

The Physics of Muon Storage

9.1 Beam Dynamics

The behavior of the beam in the $(g-2)$ storage ring directly affects the measurement of a_μ. Since the detector acceptance for decay electrons depends on the radial coordinate of the muon at the point where it decays, coherent radial motion of the stored beam can produce an amplitude modulation in the observed electron time spectrum. Resonances in the storage ring can cause particle losses, thus distorting the observed time spectrum, and must be avoided when choosing the operating parameters of the ring. Care must be taken in setting the frequency of coherent radial beam motion, the "coherent betatron oscillation" (CBO) frequency, which lies close to the second harmonic of $f_a = \omega_a/(2\pi)$. If f_{CBO} is too close to $2f_a$ the difference frequency $f_- = f_{CBO} - f_a$ complicates the extraction of f_a from the data, and can introduce a significant systematic error.

A pure quadrupole electric field provides a linear restoring force in the vertical direction, and the combination of the (defocusing) electric field and the central magnetic field provides a linear restoring force in the radial direction. The $(g-2)$ ring is a weak focusing ring[1, 2, 3] with the field index

$$n = \frac{\kappa R_0}{\beta B_0}, \tag{9.1}$$

where κ is the electric quadrupole gradient. For a ring with a uniform vertical dipole magnetic field and a uniform quadrupole field that provides vertical focusing covering the full azimuth, the stored particles undergo simple harmonic motion called betatron oscillations, in both the radial and vertical dimensions.

The horizontal and vertical motion are given by

$$x = x_e + A_x \cos(\nu_x \frac{s}{R_0} + \delta_x) \quad \text{and} \quad y = A_y \cos(\nu_y \frac{s}{R_0} + \delta_y), \tag{9.2}$$

where s is the arc length along the trajectory, and $R_0 = 7112$ mm is the radius of the central orbit in the storage ring. The horizontal and vertical tunes are given by $\nu_x = \sqrt{1-n}$ and $\nu_y = \sqrt{n}$. Several n - values were used in E821 for data acquisition: $n = 0.137,\ 0.142$ and 0.122. The horizontal and vertical betatron frequencies are given by

$$f_x = f_C \sqrt{1-n} \simeq 0.929 f_C \quad \text{and} \quad f_y = f_C \sqrt{n} \simeq 0.37 f_C, \tag{9.3}$$

where f_C is the cyclotron frequency and the numerical values assume that $n = 0.137$. The corresponding betatron wavelengths are $\lambda_{\beta_x} = 1.08(2\pi R_0)$ and $\lambda_{\beta_y} = 2.7(2\pi R_0)$. It is important that the betatron wavelengths are not simple multiples of the circumference, as this minimizes the ability of ring imperfections and higher multipoles to drive resonances that would result in particle losses from the ring.

The field index, n, also determines the acceptance of the ring. The maximum horizontal and vertical angles of the muon momentum are given by

$$\theta_{\max}^x = \frac{x_{\max}\sqrt{1-n}}{R_0}, \quad \text{and} \quad \theta_{\max}^y = \frac{y_{\max}\sqrt{n}}{R_0}, \tag{9.4}$$ `eq:max-angl`

where $x_{\max}, y_{\max} = 45$ mm is the radius of the storage aperture. For a betatron amplitude A_x or A_y less than 45 mm, the maximum angle is reduced, as can be seen from the above equations.

Resonances in the storage ring will occur if $L\nu_x + M\nu_y = N$, where L, M and N are integers, which must be avoided in choosing the operating value of the field index. These resonances form straight lines on the tune plane shown in Figure 9.1, which shows resonance lines up to fifth order. The operating point lies on the circle $\nu_x^2 + \nu_y^2 = 1$.
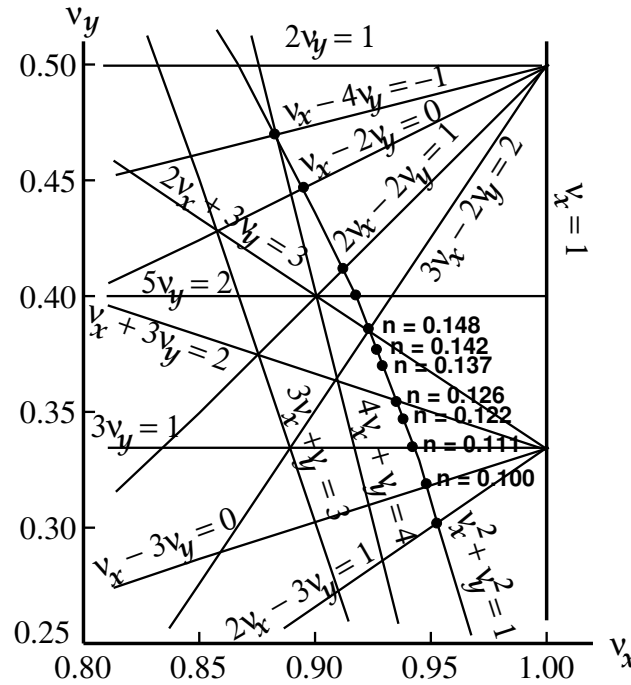

Figure 9.1: The tune plane, showing the three operating points used during our three years `fg:tunepl` of running.

For a ring with discrete quadrupoles, the focusing strength changes as a function of azimuth, and the equation of motion looks like an oscillator whose spring constant changes as a function of azimuth s. The motion is described by

$$x(s) = x_e + A\sqrt{\beta(s)}\cos(\psi(s) + \delta), \tag{9.5}$$

where $\beta(s)$ is one of the three Courant-Snyder parameters.[2] The layout of the storage ring is shown in Figure 9.2. The four-fold symmetry of the quadrupoles was chosen because it provided quadrupole-free regions for the kicker, traceback chambers, fiber monitors, and trolley garage; but the most important benefit of four-fold symmetry over the two-fold used at CERN[4] is that $\sqrt{\beta_{\max}/\beta_{\min}} = 1.03$. The two-fold symmetry used at CERN[4] gives $\sqrt{\beta_{\max}/\beta_{\min}} = 1.15$. The CERN magnetic field had significant non-uniformities on the outer portion of the storage region, which when combined with the 15% beam "breathing" from the quadrupole lattice made it much more difficult to determine the average magnetic field weighted by the muon distribution that appears in the ω_a equation

$$\vec{\omega}_a = -\frac{Qe}{m}\left[a_\mu \vec{B} + \left(a_\mu - \left(\frac{m}{p}\right)^2\right)\frac{\vec{\beta}\times\vec{E}}{c}\right]. \tag{9.6}$$
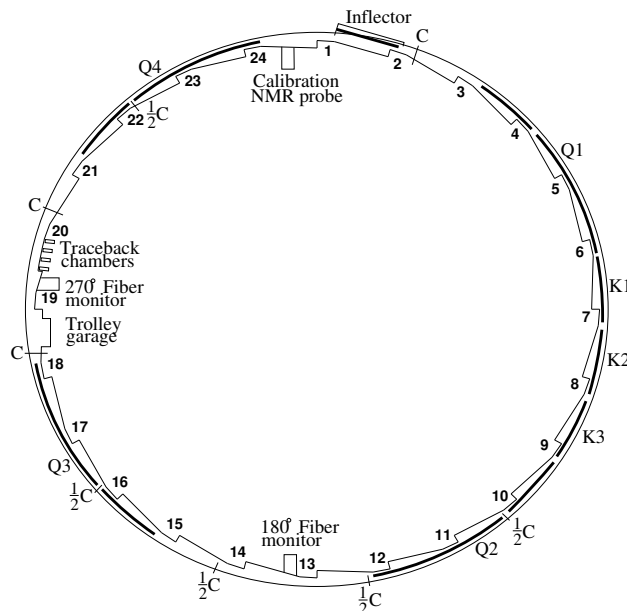
`eq:omegaa-c`

Figure 9.2: The layout of the storage ring, as seen from above, showing the location of the inflector, the kicker sections (labeled K1-K3), and the quadrupoles (labeled Q1-Q4). The beam circulates in a clockwise direction. Also shown are the collimators, which are labeled "C", or "$\frac{1}{2}$C" indicating whether the Cu collimator covers the full aperture, or half the aperture. The collimators are rings with inner radius: 45 mm, outer radius: 55 mm, thickness: 3 mm. The scalloped vacuum chamber consists of 12 sections joined by bellows. The chambers containing the inflector, the NMR trolley garage, and the trolley drive mechanism are special chambers. The other chambers are standard, with either quadrupole or kicker assemblies installed inside. An electron calorimeter is placed behind each of the radial windows, at the postion indicated by the calorimeter number.

`fg:ring`

The detector acceptance depends on the radial position of the muon when it decays, so that any *coherent* radial beam motion will amplitude modulate the decay $e^\pm$ distribution.

The principal frequency will be the "Coherent Betatron Frequency,"

$$f_{\text{CBO}} = f_C - f_x = (1 - \sqrt{1-n})f_C \simeq 470 \text{ kHZ}, \qquad (9.7)$$ `eq:cbo`

which is the frequency at which a single fixed detector sees the beam coherently moving back and forth radially. This CBO frequency is close to the second harmonic of the $(g-2)$ frequency, $f_a = \omega_a/2\pi \simeq 228$ Hz.

An alternative way of thinking about the CBO motion is to view the ring as a spectrometer where the inflector exit is imaged at each successive betatron wavelength, λ_{β_x}. In principle, an inverted image appears at half a betatron wavelength; but the radial image is spoiled by the $\pm 0.3\%$ momentum dispersion of the ring. A given detector will see the beam move radially with the CBO frequency, which is also the frequency at which the horizontal waist precesses around the ring. Since there is no dispersion in the vertical dimension, the vertical waist (VW) is reformed every half wavelength $\lambda_{\beta_y}/2$. A number of frequencies in the ring are tabulated in Table 9.1 `tb:freq`

Table 9.1: Frequencies in the $(g-2)$ storage ring, assuming that the quadrupole field is uniform in azimuth and that $n = 0.137$.

Quantity	Expression	Frequency	Period
f_a	$\frac{e}{2\pi mc}a_\mu B$	0.228 MHz	4.37 μs
f_c	$\frac{v}{2\pi R_0}$	6.7 MHz	149 ns
f_x	$\sqrt{1-n}f_c$	6.23 MHz	160 ns
f_y	$\sqrt{n}f_c$	2.48 MHz	402 ns
f_{CBO}	$f_c - f_x$	0.477 MHz	2.10 μs
f_{VW}	$f_c - 2f_y$	1.74 MHz	0.574 μs

`tb:freq`

The CBO frequency and its sidebands are clearly visible in the Fourier transform to the residuals from a fit to the five-parameter fitting function Equation 2.20, `eq:fivep` and are shown in Figure 9.3. `fg:fourier` The vertical waist frequency is barely visible. In 2000, the quadrupole voltage was set such that the CBO frequency was uncomfortably close to the second harmonic of f_a, thus placing the difference frequency $f_- = f_{CBO} - f_a$ next to f_a. This nearby sideband forced us to work very hard to understand the CBO and how its related phenomena affect the value of ω_a obtained from fits to the data. In 2001, we carefully set f_{CBO} at two different values, one well above, the other well below $2f_a$, which greatly reduced this problem.

9.1.1   Monitoring the Beam Profile `sct:mubeam`

Three tools are available to us to monitor the muon distribution. Study of the beam debunching after injection yields information on the distribution of equilibrium radii in the storage ring. The FSDs provide information on the vertical centroid of the beam. The wire chamber system and the fiber beam monitors, described above, also provide valuable information on the properties of the stored beam.
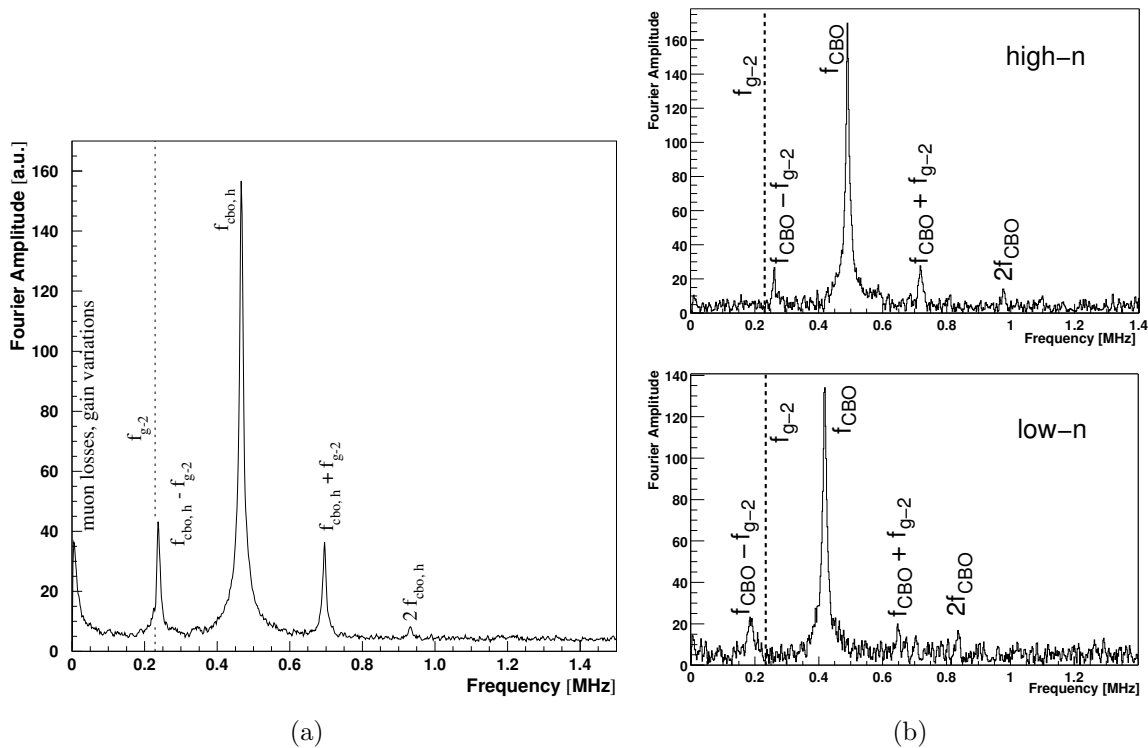
(a) (b)

Figure 9.3: The Fourier transform to the residuals from a fit to the five-parameter function, showing clearly the coherent beam frequencies. (a) is from 2000, when the CBO frequency was close to $2\omega_a$, and (b) shows the Fourier transform for the two n-values used in the 2001 run period.

fg:fourier

The beam bunch that enters the storage ring has a time spread with $\sigma \simeq 23$ ns, while the cyclotron period is 149 ns. The momentum distribution of stored muons produces a corresponding distribution in radii of curvature. The distributions depend on the phase-space acceptance of the ring, the phase space of the beam at the injection point, and the kick given to the beam at injection. The narrow horizontal dimension of the beam at the injection point, about 18 mm, restricts the stored momentum distribution to about $\pm 0.3\%$. As the muons circle the ring, the muons at smaller radius (lower momentum) eventually pass those at larger radius repeatedly after multiple transits around the ring, and the bunch structure largely disappears after 60 μs . This de-bunching can be seen in Figure 9.4 where the signal from a single detector is shown at two different times following injection. The bunched beam is seen very clearly in the left figure, with the 149 ns cyclotron period being obvious. The slow amplitude modulation comes from the $(g-2)$ precession. By 36 μs the beam has largely de-bunched.

Only muons with orbits centered at the central radius have the "magic" momentum, so knowledge of the momentum distribution, or equivalently the distribution of equilibrium radii, is important in determining the correction to ω_a caused by the radial electric field used for vertical focusing. Two methods of obtaining the distribution of equilibrium radii from
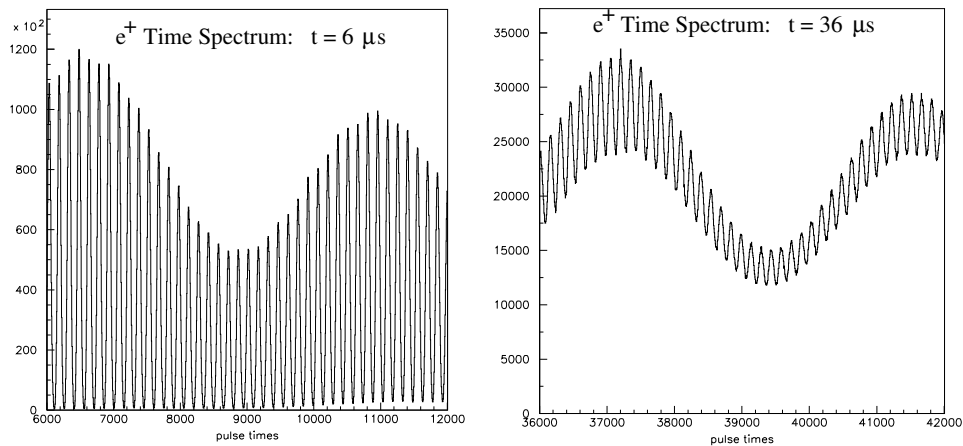
Figure 9.4: The time spectrum of a single calorimeter soon after injection. The spikes are
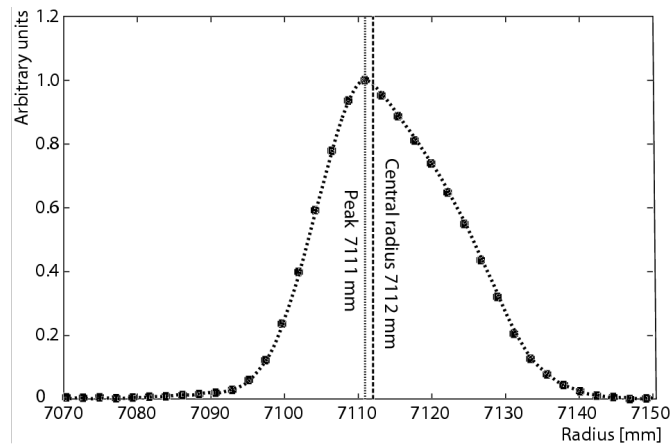separated by the cyclotron period of 149 ns.

fg:fastrot

Figure 9.5: The distribution of equilibrium radii obtained from the beam de-bunching. The
solid circles are from a de-bunching model fit to the data, and the dotted curve is obtained
from a modified Fourier analysis.

fg:rdist

the beam debunching are employed in E821. One method uses a model of the time evolution
of the bunch structure. A second, alternative procedure uses modified Fourier techniques[9].
The results from these analyses are shown in Figure 9.5. The discrete points were obtained
using the model, and the dotted curve was obtained with the modified Fourier analysis.
The two analyses agree. The measured distribution is used both in determining the average
magnetic field seen by the muons and the radial electric field correction discussed below.

The scintillating-fiber monitors show clearly the vertical and horizontal tunes as expected.
In Figure 9.6, the horizontal beam centroid motion is shown, with the quadrupoles powered
asymmetrically during scraping, and then symmetrically after scraping. A Fourier transform
of the latter signal shows the expected frequencies, including the cyclotron frequency of
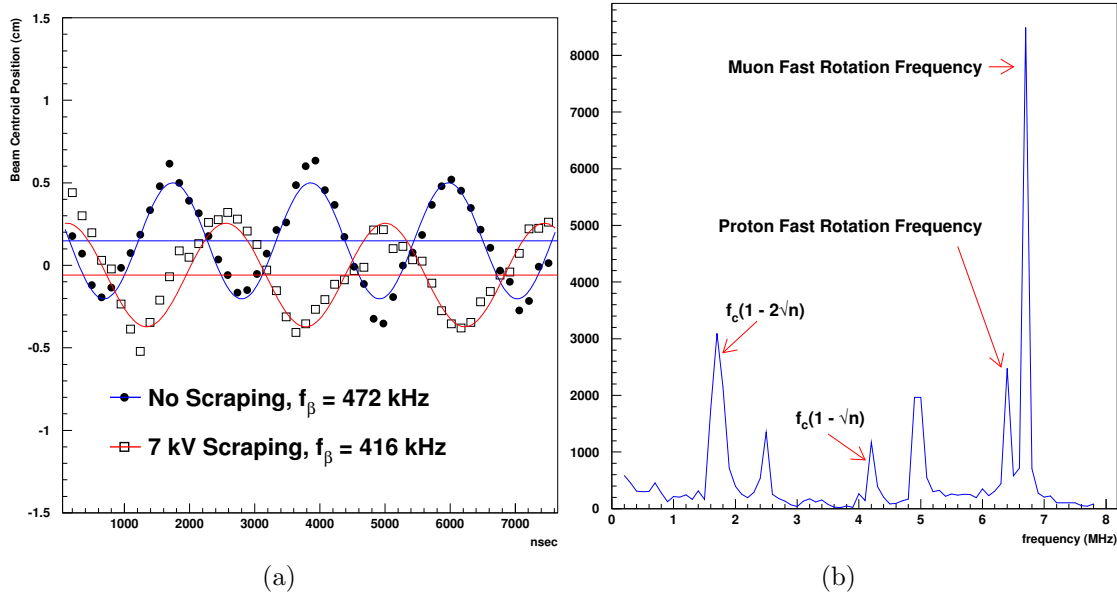protons stored in the ring. The traceback system also sees the CBO motion.

Figure 9.6: (a) The horizontal beam centroid motion with beam scraping and without, using data from the scintillating fiber hodoscopes; note the tune change between the two. (b) A Fourier transform of the pulse from a single horizontal fiber, which shows clearly the vertical waist motion, as well as the vertical tune. The presence of stored protons is clearly seen in this frequency spectrum.

9.1.2 Corrections to ω_a: Pitch and Radial Electric Field

`sct:p-E`

In the simplest case, the rate at which the spin turns relative to the momentum is given by

$$\omega_a = \omega_S - \omega_C = -\left(\frac{g-2}{2}\right)\frac{Qe}{m}B = -a\frac{Qe}{m}B \tag{9.8}$$

`eq:diffreq`

The spin equation modified by the presence of an electric field was introduced earlier, with the assumption that the velocity is transverse to the magnetic field, and that all muons are at γ_{magic}. Neither of these assumptions are valid, since the vertical betatron motion must be included, and the momentum acceptance of $\pm 0.5\%$ means the muon ensemble has a range of momenta. Corrections for these two effects were the only corrections made to the data In E821. In the 2001 data set, the electric field correction for the low n-value data set was $+0.47 \pm 0.05$. The pitch correction was $+0.27 \pm 0.04$. These are the <u>only</u> corrections made to the ω_a data.

We sketch the derivation for E821 and E989 below[6]. For a general derivation the reader is referred to References [7, 8].

Without the assumption that $\vec{\beta} \cdot \vec{B} = 0$ the cyclotron and spin rotation frequencies become:

$$\vec{\omega}_C = -\frac{q}{m}\left[\frac{\vec{B}}{\gamma} - \frac{\gamma}{\gamma^2 - 1}\left(\frac{\vec{\beta} \times \vec{E}}{c}\right)\right], \tag{9.9}$$

`eq:cyc-E`

and the spin precession frequency becomes[5]

$$\vec{\omega}_S = -\frac{q}{m}\left[\left(\frac{g}{2}-1+\frac{1}{\gamma}\right)\vec{B} - \left(\frac{g}{2}-1\right)\frac{\gamma}{\gamma+1}(\vec{\beta}\cdot\vec{B})\vec{\beta} - \left(\frac{g}{2}-\frac{\gamma}{\gamma+1}\right)\left(\frac{\vec{\beta}\times\vec{E}}{c}\right)\right]. \qquad (9.10) \quad \boxed{\texttt{eq:fullfreq}}$$

Substituting for $a_\mu = (g_\mu - 2)/2$, we find that the spin difference frequency is

$$\vec{\omega}_a = -\frac{q}{m}\left[a_\mu\vec{B} - a_\mu\left(\frac{\gamma}{\gamma+1}\right)(\vec{\beta}\cdot\vec{B})\vec{\beta} - \left(a_\mu - \frac{1}{\gamma^2-1}\right)\frac{\vec{\beta}\times\vec{E}}{c}\right]. \qquad (9.11) \quad \boxed{\texttt{eq:Ediffreq}}$$

If $\vec{\beta}\cdot\vec{B} = 0$, this reduces to

$$\vec{\omega}_a = -\frac{q}{m}\left[a_\mu\vec{B} - \left(a_\mu - \frac{1}{\gamma^2-1}\right)\frac{\vec{\beta}\times\vec{E}}{c}\right]. \qquad (9.12) \quad \boxed{\texttt{eq:omega}}$$

For $\gamma_{\mathrm{magic}} = 29.3$ ($p_\mu = 3.09$ GeV/c), the second term vanishes; and the electric field does not contribute to the spin precession relative to the momentum. The spin precession is independent of muon momentum; *all* muons precess at the same rate. Because of the high uniformity of the B-field, a precision knowledge of the stored beam trajectories in the storage region is not required.

First we calculate the effect of the electric field, for the moment neglecting the $\vec{\beta}\cdot\vec{B}$ term. If the muon momentum is different from the magic momentum, the precession frequency is given by

$$\omega_a' = \omega_a\left[1 - \beta\frac{E_r}{B_y}\left(1 - \frac{1}{a_\mu\beta^2\gamma^2}\right)\right]. \qquad (9.13)$$

Using $p = \beta\gamma m = (p_m + \Delta p)$, after some algebra one finds

$$\frac{\omega_a' - \omega_a}{\omega_a} = \frac{\Delta\omega_a}{\omega_a} = -2\frac{\beta E_r}{B_y}\left(\frac{\Delta p}{p_m}\right). \qquad (9.14)$$

Thus the effect of the radial electric field reduces the observed frequency from the simple frequency ω_a given in Equation 9.8. Now $\boxed{\texttt{eq:diffreq}}$

$$\frac{\Delta p}{p_m} = (1-n)\frac{\Delta R}{R_0} = (1-n)\frac{x_e}{R_0}, \qquad (9.15)$$

where x_e is the muon's equilibrium radius of curvature relative to the central orbit. The electric quadrupole field is

$$E = \kappa x = \frac{n\beta B_y}{R_0}x. \qquad (9.16)$$

We obtain

$$\frac{\Delta\omega}{\omega} = -2n(1-n)\beta^2\frac{xx_e}{R_0^2 B_y}, \qquad (9.17)$$

so clearly the effect of muons not at the magic momentum is to lower the observed frequency. For a quadrupole focusing field plus a uniform magnetic field, the time average of x is just x_e, so the electric field correction is given by

$$C_E = \frac{\Delta\omega}{\omega} = -2n(1-n)\beta^2\frac{\langle x_e^2\rangle}{R_0^2 B_y}, \qquad (9.18)$$

where $\langle x_e^2 \rangle$ is determined from the fast-rotation analysis (see Figure 9.4). The uncertainty on $\langle x_e^2 \rangle$ is added in quadrature with the uncertainty in the placement of the quadrupoles of $\delta R = \pm 0.5$ mm (± 0.01 ppm), and with the uncertainty in the mean vertical position of the beam, ± 1 mm (± 0.02 ppm). For the low-n 2001 sub-period, $C_E = 0.47 \pm 0.054$ ppm.
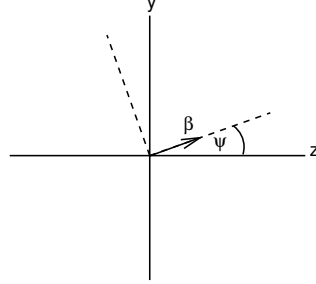

Figure 9.7: The coordinate system of the pitching muon. The angle ψ varies harmonically. The vertical direction is $\hat{y}$ and $\hat{z}$ is the azimuthal (beam) direction.

The vertical betatron oscillations of the stored muons lead to $\vec{\beta} \cdot \vec{B} \neq 0$. Since the $\vec{\beta} \cdot \vec{B}$ term in Equation 9.10 is quadratic in the components of $\vec{\beta}$, its contribution to ω_a will not generally average to zero. Thus the spin precession frequency has a small dependence on the betatron motion of the beam. It turns out that the only significant correction comes from the vertical betatron oscillation; therefore it is called the pitch correction (see Equation 9.11). As the muons undergo vertical betatron oscillations, the "pitch" angle between the momentum and the horizontal (see Figure 9.7) varies harmonically as $\psi = \psi_0 \cos \omega_y t$, where ω_y is the vertical betatron frequency $\omega_y = 2\pi f_y$, given in Equation 9.3. In the approximation that all muons are at the magic γ, we set $a_\mu - 1/(\gamma^2 - 1) = 0$ in Equation 9.11 and obtain

$$\vec{\omega}_a' = -\frac{q}{m}\left[a_\mu \vec{B} - a_\mu \left(\frac{\gamma}{\gamma+1}\right)(\vec{\beta} \cdot \vec{B})\vec{\beta}\right], \qquad (9.19)$$

where the prime indicates the modified frequency as it did in the discussion of the radial electric field given above, and $\vec{\omega}_a = -(q/m)a_\mu \vec{B}$. We adopt the (rotating) coordinate system shown in Figure 9.7, where $\vec{\beta}$ lies in the zy-plane, z being the direction of propagation, and y being vertical in the storage ring. Assuming $\vec{B} = \hat{y}B_y$, $\vec{\beta} = \hat{z}\beta_z + \hat{y}\beta_y = \hat{z}\beta\cos\psi + \hat{y}\beta\sin\psi$, we find

$$\vec{\omega}_a' = -\frac{q}{m}[a_\mu \hat{y}B_y - a_\mu \left(\frac{\gamma}{\gamma+1}\right)\beta_y B_y(\hat{z}\beta_z + \hat{y}\beta_y)]. \qquad (9.20)$$

The small-angle approximation $\cos\psi \simeq 1$ and $\sin\psi \simeq \psi$ gives the component equations

$$\omega_{ay}' = \omega_a \left[1 - \left(\frac{\gamma-1}{\gamma}\right)\psi^2\right] \qquad (9.21)$$

and

$$\omega_{az}' = -\omega_a \left(\frac{\gamma-1}{\gamma}\right)\psi. \qquad (9.22)$$

Rather than use the components given above, we can resolve ω_a' into components along the coordinate system defined by $\vec{\beta}$ (see Figure 9.7) using the standard rotation formula. The transverse component of ω' is given by

$$\omega_\perp = \omega_{ay}' \cos\psi - \omega_{az}' \sin\psi. \tag{9.23}$$

Using the small-angle expansion for $\cos\psi \simeq 1 - \psi^2/2$, we find

$$\omega_\perp \simeq \omega_a \left[1 - \frac{\psi^2}{2}\right]. \tag{9.24}$$

As can be seen from Table 9.1, the pitching frequency ω_y is an order of magnitude larger than the frequency ω_a, so that in one $g-2$ period $\omega_\parallel$ oscillates more than ten times, thus averaging out its effect on ω_a' so $\omega_a' \simeq \omega_\perp$. Thus

$$\omega_a \simeq -\frac{q}{m} a_\mu B_y \left(1 - \frac{\psi^2}{2}\right) = -\frac{q}{m} a_\mu B_y \left(1 - \frac{\psi_0^2 \cos^2\omega_y t}{2}\right). \tag{9.25}$$

Taking the time average yields a pitch correction

$$C_p = -\frac{\langle \psi^2 \rangle}{2} = -\frac{\langle \psi_0^2 \rangle}{4} = -\frac{n}{4} \frac{\langle y^2 \rangle}{R_0^2}, \tag{9.26}$$

where we have used Equation 9.4 $\langle \psi_0^2 \rangle = n \langle y^2 \rangle / R_0^2$. The quantity $\langle y_0^2 \rangle$ was both determined experimentally and from simulations. For the 2001 period, $C_p = 0.27 \pm 0.036$ ppm, the amount the precession frequency is lowered from that given in Equation 9.6 because $\vec{\beta} \cdot \vec{B} \neq 0$.

We see that both the radial electric field and the vertical pitching motion *lower* the observed frequency from the simple difference frequency $\omega_a = (e/m)a_\mu B$, which enters into our determination of a_μ using Equation 2.25. Therefore our observed frequency must be *increased* by these corrections to obtain the measured value of the anomaly. Note that if $\omega_y \simeq \omega_a$ the situation is more complicated, with a resonance behavior that is discussed in References [7, 8].

9.2   General Feature of Muon Storage

9.3   Muon Injection

9.4   Beam Scraping

9.5   Coherent Beam Motion

References

`wied` [1] H. Wiedemann, *Particle Accelerator Physics* Vol. 1, Springer-Verlag, (1993) p. 54.

`edwards` [2] D.A. Edwards and M.J. Syphers, *An Introduction to the Physics of High Energy Accelerators*, John Wiley & Sons, (1993) p. 75.

`cp` [3] F. Combley and E. Picasso, Phys. Rept. **14**, 1 (1974).

`cern3b` [4] J. Bailey, et al., Nucl. Phys. **B150**, 1 (1979).

`TBMT` [5] L. H. Thomas, Phil. Mag. **3**, 1 (1927); V. Bargmann, L. Michel, and V. L. Telegdi, Phys. Rev. Lett. **2**, 435 (1959).

`paley` [6] We follow the approach given by J.M. Paley, Ph.D. Dissertation, Boston University, 2004.

`fp` [7] F.J.M. Farley and E. Picasso, in Quantum Electrodynamics, Adv. Series on Dir. in H.E.P., V7, T. Kinoshita, ed., World Scientific, 479, (1990).

`arley-pitch` [8] F.J.M. Farley, Phys.Lett. **B 42**, 66 (1972), and J.H. Field, and G. Fiorentini, Nuovo Cimento, **21 A**, 297 (1974).

`orlov` [9] Y. Orlov, et al., Nucl. Instrum. Meth. **A482**, 767 (2002).

Chapter 10

The Electrostatic Quadrupoles

Chapter 11

The Fast Muon Kicker

11.1 Requirements for the E989 Kicker

11.2 Limitations of the E821 Kicker

11.3 New Kicker Design

11.3.1 New Pulseforming Network

11.3.2 New Kicker Plate Design

11.3.3 Kicker R&D at Cornell

References

nim-kicker [1] Efstathiadis E, et al. *Nucl. Inst. and Methods Phys. Res.* A496:8-25 (2002)

Chapter 12

The Precision Magnetic Field: ω_p

12.1 Introduction and Specifications

The requirement for total uncertainty on the magnetic field in E989 is ± 0.7 ppm, roughly a factor of three smaller than was achieved in E821. E989 will use the same principles that were employed in E821, but improved to reduce the systematic errors to the needed level. As a basis for discussion, the systematic errors from E821 are listed below in Table 12.1.

Table 12.1: Systematic errors for the magnetic field for the different run periods. [†]Higher multipoles, trolley temperature and its power supply voltage response, and eddy currents from the kicker.

Source of errors	R99 [ppm]	R00 [ppm]	R01 [ppm]
Absolute calibration of standard probe	0.05	0.05	0.05
Calibration of trolley probes	0.20	0.15	0.09
Trolley measurements of B_0	0.10	0.10	0.05
Interpolation with fixed probes	0.15	0.10	0.07
Uncertainty from muon distribution	0.12	0.03	0.03
Inflector fringe field uncertainty	0.20	–	–
Others †	0.15	0.10	0.10
Total systematic error on ω_p	0.4	0.24	0.17
Muon-averaged field [Hz]: $\widetilde{\omega}_p/2\pi$	61 791 256	61 791 595	61 791 400

Nuclear magnetic resonance (NMR) is at the heart of the measurement and control system, since it alone provides the means to measure magnetic fields to the tens of parts per billion (ppb). A central elemen of the system is a field-mapping trolley, shown in Fig. 12.1(a) that mapped the field at several thousand points around the ring. This trolley contains 17 NMR probes arranged in concentric circles as shown in Fig. 12.1(b).

There are four major tasks required from the NMR system: Mapping the field when the beam is off; Monitoring the field when data are being collected; Providing feedback information to the storage ring power supply; Providing an absolute calibration to the Larmor frequency of the free proton.
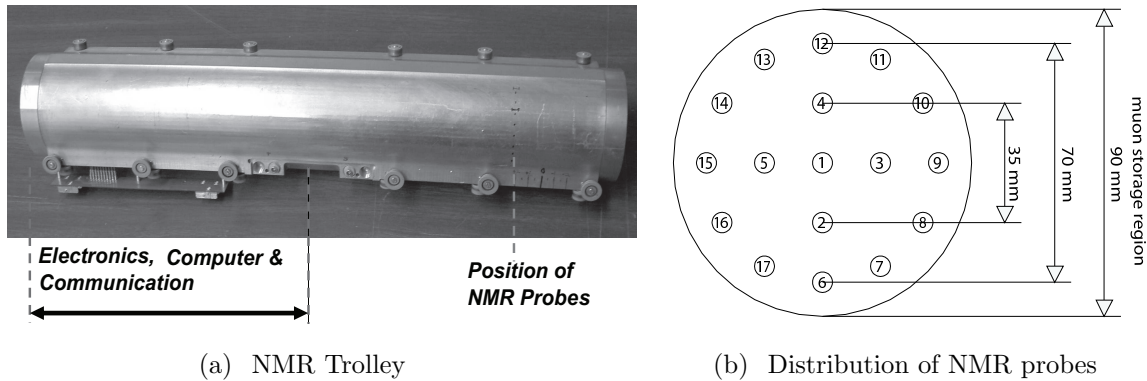
(a) NMR Trolley

(b) Distribution of NMR probes

Figure 12.1: (a)Photograph of the NMR trolley, which measures the magnetic field in the storage ring. The array of 17 NMR probes, which are located inside the trolley housing, 82(1) mm behind the front of the trolley. Electronics occupies the back part of the device. At the location of the probes, the field perturbation by these materials is less than 2 ppm and is accounted for by the calibration method. (b)The probe numbers and placement are given by the schematic.

:trolleypos

12.2   Field Measurement and Control

Monitoring of the magnetic field

The magnetic field is measured and monitored by pulsed Nuclear Magnetic Resonance of protons in water samples [2]. The free induction decay (FID) is picked up by the coil L_S in Fig. 12.2 after a pulsed excitation rotates the proton spin in the sample by 90° to the magnetic field. The proton response signal at frequency f_{NMR} is measured by counting its zero crossings within a well-measured time period the length of which is automatically adjusted to approximately the decay time $(1/\mathrm{e})$ of the FID. It is mixed with a stable reference frequency and filtered to arrive at the difference frequency f_{FID} chosen to be typically in the 50 kHz region. The reference frequency of $f_{\mathrm{ref}} = 61.74$ MHz is obtained from a frequency synthesizer, which is phase locked to a LORAN C secondary frequency standard [5], and it is chosen such that always $f_{\mathrm{ref}} < f_{\mathrm{NMR}}$. The very same LORAN C device also provides the time base for the ω_a measurement. The relationship between the actual field B_{real} and the field corresponding to the reference frequency is given by

$$B_{\mathrm{real}} = B_{\mathrm{ref}}\left(1 + \frac{f_{\mathrm{FID}}}{f_{\mathrm{ref}}}\right). \tag{12.1}$$

eq:Bfield-n

The field measurement process has three aspects: calibration, monitoring the field during data collection, and mapping the field. The probes used for these purposes are shown in Fig. 12.2 To map the field, an NMR trolley [4] was built with an array of 17 NMR probes arranged in concentric circles, as shown in Fig. 2.4 While it would be preferable to have information over the full 90-mm aperture, space limitations inside the vacuum chamber, which can be understood by examining Figs. 2.4, prevent a larger diameter trolley.

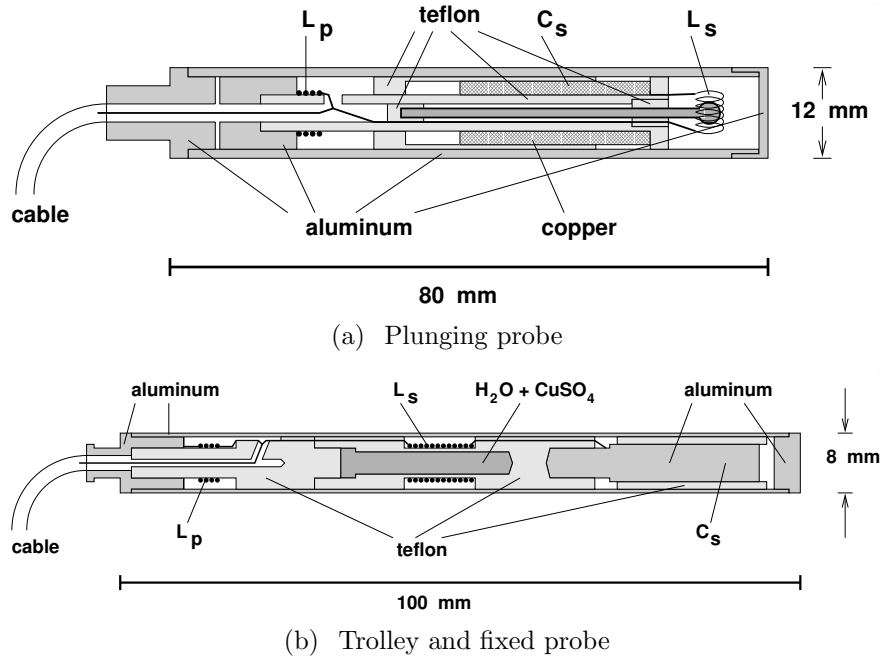(a) Plunging probe



(b) Trolley and fixed probe

Figure 12.2: (a) Plunging probe, which can be inserted into the vacuum at a specially shimmed region of the storage ring to transfer the calibration to the trolley probes. (b) The standard probes used in the trolley and as fixed probes. The resonant circuit is formed by the two coils with inductances L_s and L_p and a capacitance C_s made by the Al-housing and a metal electrode.

fg:probes

(a) Absolute calibration probe
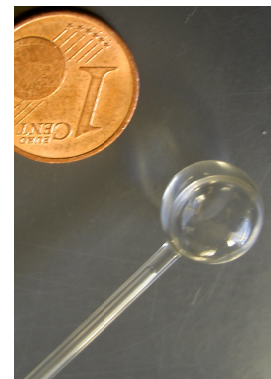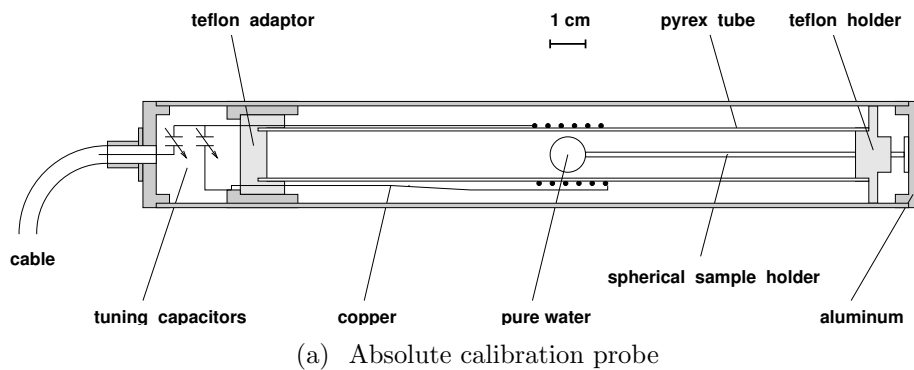
(b) Spherical Pyrex container

Figure 12.3: The different NMR probes. (a) Absolute probe featuring a spherical sample of water. This probe and all its driving and readout electronics are the very same devices employed in reference [13] to determine λ, the muon-to-proton magnetic-moment ratio. (b) The spherical Pyrex container for the absolute probe.

ixed-probes

The trolley is built from non-magnetic materials and has a fully functional CPU on-board which controls a full FID excitation and zero crossing counting spectrometer. It is pulled around the storage ring by two cables, one in each direction circling the ring. One of these cables is a thin co-axial cable with only copper conductors and Teflon dielectric and outside protective coating (Suhner 2232-08). It carries simultaneously the dc supply voltage, the reference frequency $f_{\rm ref}$ and two-way communication with the spectrometer via RS232 standard. The other cable is non-conducting nylon (fishing line) to eliminate pickup from the pulsed high voltage on the kicker electrodes.

During muon decay data-collection periods, the trolley is parked in a garage (see Fig. 9.2) in a special vacuum chamber. Every few days, at *random times*, the field is mapped using the trolley. During mapping, the trolley is moved into the storage region and over the course of 2 hours is pulled around the vacuum chamber, measuring the field at some 100,000 points by continuously cycling through the 17 probes while moving. Data were recorded in both possible directions of movement. During the approximately three-month data-collection runs, the storage-ring magnet remains powered continuously for periods lasting from five to twenty days; thus the conditions during mapping are identical to those during the data collection.

To cross calibrate the trolley probes, a two-axis non-magnetic manipulator made from aluminum and titanium only, including titanium bellows, and driven by non-magnetic piezo motors was developed. It was placed at one location in the ring and it permits a special NMR plunging probe, or an absolute calibration probe with a spherical water sample [3], to plunge into the vacuum chamber. In this way the trolley probes can be calibrated by transferring the absolute calibration from the calibration probe shown in Fig. 12.2 to individual probes in the trolley. These measurements of the field at the same spatial point with the plunging, calibration and trolley probes provide both relative and absolute calibration of the trolley probes. During the calibration measurements before, after and occasionally randomly during each running period, the spherical water probe is used to calibrate the plunging probe, and with this then the trolley probes. The absolute calibration probe provides the calibration to the Larmor frequency of the free proton [7], which is called ω_p below.

To monitor the field on a continuous basis during data collection, a total of 378 NMR probes are placed at fixed locations in grooves machined into the outside upper and lower surfaces of the vacuum chamber around the ring. Of these, about half provide useful data for monitoring the field with time. Some of the others are noisy, or have cables damaged over the years or other problems, but a significant number of fixed probes are located in regions near the pole-piece boundaries where the magnetic gradients are sufficiently large to reduce the free-induction decay time in the probe, limiting the precision on the frequency measurement. The number of probes at each azimuthal position around the ring alternates between two and three, at radial positions arranged symmetrically about the magic radius of 7112 mm. Because of this geometry, the fixed probes provide a good monitor of changes in the dipole and quadrupole components of the field around the storage ring.

Initially the trolley and fixed probes contained cylindrical water samples. Over the course of the experiment, the water samples in many of the probes were replaced with petroleum jelly. The jelly has several advantages over water: Low evaporation, favorable relaxation times at room temperature, a proton NMR signal almost comparable to that from water, and a chemical shift (and the accompanying NMR frequency shift) with a temperature

coefficient much smaller than that of water, and thus negligible for our experiment.

The magnetic field data consist of three separate sets of measurements: The calibration data taken before, after, and occasionally during each running period; maps of the magnetic field obtained with the NMR trolley at intervals of a few days at random hours; and the field measured by each of the fixed NMR probes located in the vacuum chamber walls. For the latter measurements groups of 20 probes were connected via one of 20 analog multiplexers to one of 20 readout channels, each consisting of a frequency mixer and a custom-designed FID zero crossing counting device [2]. The plunging probe and the calibration probe [3] were also connected to one of the multiplexer inputs. The probes of each group were sequentially excited and their FID was read in full cycles repeated approximately every 5 seconds all throughout the experimental periods and whenever the magnet was energized. The data taken concurrent with the muon spin-precession data were tied to the field mapped by the trolley, which were used to determine the average magnetic field in the storage ring, and subsequently the value of ω_p to be used in Eq. (2.25).

Calibration of the trolley probes

The errors arising from the cross-calibration of the trolley probes with the plunging probes are caused both by the uncertainty in the relative positioning of the trolley probe and the plunging probe, and by the local field inhomogeneity. At this point in azimuth, trolley probes are fixed with respect to the frame that holds them, and to the rail system on which the trolley rides. The vertical and radial positions of the trolley probes with respect to the plunging probe are determined by applying a sextupole field and comparing the change of field measured by the two probes. The field shimming at the calibration location minimizes the error caused by the relative-position uncertainty, which in the vertical and radial directions has an inhomogeneity less than 0.2 ppm/cm, as shown in Fig. 12.4(b). The full multipole components at the calibration position are given in Table 12.2, along with the multipole content of the full magnetic field averaged over azimuth. For the estimated rms 1 mm-position uncertainty, the uncertainty on the relative calibration is less than 0.02 ppm.

The absolute calibration utilizes a probe with a spherical water sample (see Figs. 12.2(a), 12.2(b)) [3]. The Larmor frequency of a proton in a spherical water sample is related to that of the free proton through [43, 8]

$$f_{\mathrm{L}}(\mathrm{sph} - \mathrm{H_2O}, T) = [1 - \sigma(\mathrm{H_2O}, T)]\, f_{\mathrm{L}}(\mathrm{free}), \tag{12.2}$$

where $\sigma(\mathrm{H_2O}, T)$ is from the diamagnetic shielding of the proton in the water molecule, determined from [7]

$$\sigma(\mathrm{H_2O}, 34.7^\circ C) = 1 - \frac{g_p(\mathrm{H_2O}, 34.7^\circ C)}{g_J(H)} \frac{g_J(H)}{g_p(H)} \frac{g_p(H)}{g_p(\mathrm{free})} \tag{12.3}$$

$$= 25.790(14) \times 10^{-6}. \tag{12.4}$$

The g-factor ratio of the proton in a spherical water sample to the electron in the hydrogen ground state ($g_J(H)$) is measured to 10 parts per billion (ppb) [7]. The ratio of electron to proton g-factors in hydrogen is known to 9 ppb [9]. The bound-state correction relating the g-factor of the proton bound in hydrogen to the free proton are calculated in References [10, 11].

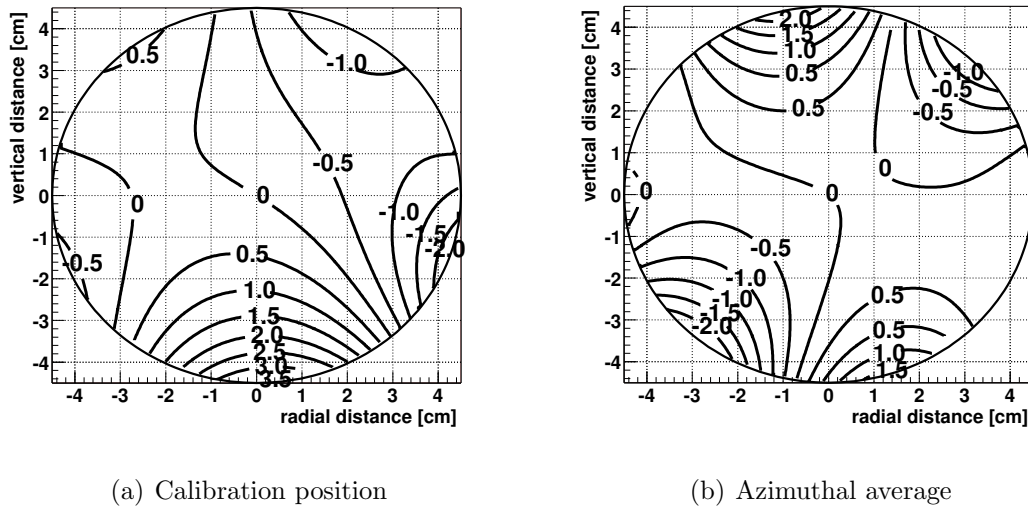(a) Calibration position   (b) Azimuthal average

Figure 12.4: Homogeneity of the field (a) at the calibration position and (b) for the azimuthal average for one trolley run during the 2000 period. In both figures, the contours correspond to 0.5 ppm field differences between adjacent lines.

The temperature dependence of σ is corrected for using $d\sigma(\mathrm{H_2O}, T)/dT = 10.36(30) \times 10^{-9}/°\mathrm{C}$ [12]. The free proton frequency is determined to an accuracy of 0.05 ppm.

The fundamental constant $\lambda_+ = \mu_{\mu^+}/\mu_p$ (see Eq. (2.25)) can be computed from the hyperfine structure of muonium (the $\mu^+ e^-$ atom) [8], or from the Zeeman splitting in muonium [13]. The latter experiment used the very same calibration probe as well as the essential NMR field monitoring and mapping devices and techniques, including all the driving and readout electronics, as we used in our $(g-2)$ experiment. The magnetic environments of the two experiments were slightly different, so that perturbations of the probe materials on the surrounding magnetic field differed by a few ppb between the two experiments, which can be neglected at our level of accuracy. We have therefore a direct robust link of our magnetic field to the muon magneton (proton NMR has only the role of a fly wheel), which is independent of possible future changes in fundamental constants in the regular adjustment procedures [8], unless the muon magneton will be remeasured experimentally.

The errors in the calibration procedure result both from the uncertainties on the positions of the water samples inside the trolley and the calibration probe, and from magnetic field inhomogeneities. The precise location of the trolley in azimuth, and the location of the probes within the trolley, are not known better than a few mm. The uncertainties in the relative calibration resulting from position uncertainties are 0.03 ppm. Temperature and power-supply voltage dependences contribute 0.05 ppm, and the paramagnetism of the $\mathrm{O_2}$ molecules in the air-filled trolley causes an experimentally verified 0.037 ppm shift in the field.

Table 12.2: Multipoles at the outer edge of the storage volume (radius = 4.5 cm). The left-hand set are for the plunging station where the plunging probe and the calibration are inserted. The right-hand set are the multipoles obtained by averaging over azimuth for a representative trolley run during the 2000 period.

| Multipole | Calibration | | Azimuthal Averaged | |
[ppm]	Normal	Skew	Normal	Skew
Quadrupole	-0.71	-1.04	0.24	0.29
Sextupole	-1.24	-0.29	-0.53	-1.06
Octupole	-0.03	1.06	-0.10	-0.15
Decupole	0.27	0.40	0.82	0.54

:multipoles

Mapping the magnetic field

During a trolley run, the value of B is measured by each probe at approximately 6000 locations in azimuth around the ring. The magnitude of the field measured by the central probe is shown as a function of azimuth in Fig. 12.5 for one of the trolley runs. The insert shows that the fluctuations in this map that appear quite sharp are in fact quite smooth, and are not noise. The field maps from the trolley are used to construct the field profile averaged over azimuth. This contour plot for one of the field maps is shown in Fig. 12.4(b). Since the storage ring has weak focusing, the average over azimuth is the important quantity in the analysis. Because the recorded NMR frequency is only sensitive to the magnitude of B and not to its direction, the multipole distributions must be determined from azimuthal magnetic field averages, where the field can be written as

$$B(r, \theta) = \sum_{n=0}^{n=\infty} r^n \left(c_n \cos n\theta + s_n \sin n\theta \right), \tag{12.5}$$

eq:mult-dec

where in practice the series is limited to 5 terms.

Tracking the magnetic field in time

During data-collection periods the field is monitored with the fixed probes. To determine how well the fixed probes permitted us to monitor the field felt by the muons, the measured field, and that predicted by the fixed probes is compared for each trolley run. The results of this analysis for the 2001 running period is shown in Fig. 12.6. The rms distribution of these differences is 0.10 ppm.

sct:avB ### Determination of the average magnetic field: ω_p

The value of ω_p entering into the determination of a_μ is the field profile weighted by the muon distribution. The multipoles of the field, Eq. (12.5), are folded with the muon distribution,

$$M(r, \theta) = \sum [\gamma_m(r) \cos m\theta + \sigma_m(r) \sin m\theta], \tag{12.6}$$

to produce the average field,

$$\langle B \rangle_{\mu-\text{dist}} = \int M(r, \theta) B(r, \theta) r dr d\theta, \tag{12.7}$$
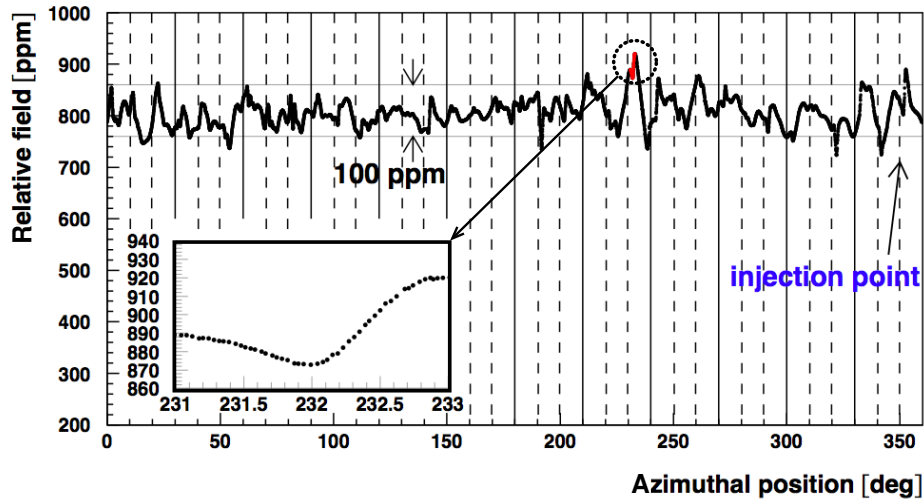
Figure 12.5: The magnetic field measured at the center of the storage region vs. azimuthal position. Note that while the sharp fluctuations appear to be noise, when the scale is expanded the variations are quite smooth and represent true variations in the field.
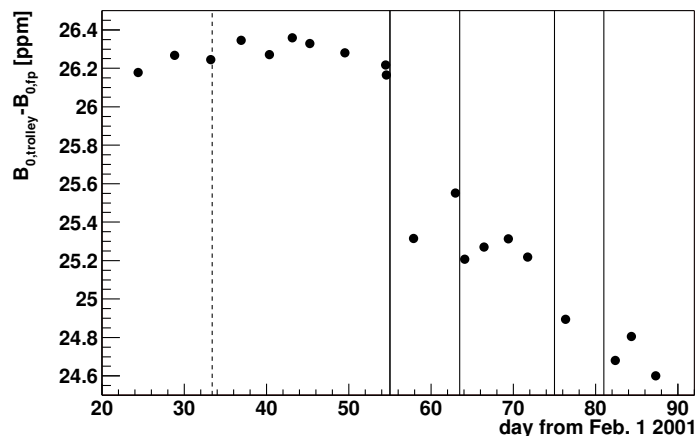
eld_azimuth

Figure 12.6: The difference between the average magnetic field measured by the trolley and that inferred from tracking the magnetic field with the fixed probes between trolley maps. The vertical lines show when the magnet was powered down and then back up. After each powering of the magnet, the field does not exactly come back to its previous value, so that only trolley runs taken between magnet powerings can be compared directly.

fg:Btrack

where the moments in the muon distribution couple moment-by-moment to the multipoles of $\vec{B}$. Computing $\langle B \rangle$ is greatly simplified if the field is quite uniform (with small higher multipoles), and the muons are stored in a circular aperture, thus reducing the higher moments of $M(r, \theta)$. This worked quite well in E821, and the uncertainty on $\langle B \rangle$ weighted by the muon distribution was ± 0.03 ppm.

The weighted average was determined both by a tracking calculation that used a field map and calculated the field seen by each muon, and also by using the quadrupole component of the field and the beam center determined from a fast-rotation analysis to determine the average field. These two agreed extremely well, vindicating the choice of a circular aperture and the ± 1 ppm specification on the field uniformity, that were set in the design stage of the experiment. [1]

Summary of the magnetic field analysis

The limitations on our knowledge of the magnetic field come from measurement issues, i.e. systematics and not statistics, so in E821 the systematic errors from each of these sources had to be evaluated and understood. The results and errors are summarized in Table 12.1.

^{3}He Probe

An alternative absoluted calibration probe being considered will contain polarized ^{3}He. Such a probe has the advantage that the NMR frequency does not depend on the shape of the ^{3}He volume, unlike the water sample which has to be spherical, and depends on a number of external quantities discussed above.

12.3   ES&H, Quality Assurance, Value Management

References

`ett06-mu-fc` [1] G. Bennett, *et al.*, (Muon ($g - 2$) Collaboration), Phys. Rev. **D73**, 072003 (2006).

`nmr-fc` [2] R. Prigl, *et al.*, Nucl. Inst. Methods Phys. Res. **A374** 118 (1996).

`fei-fc` [3] X. Fei, V. Hughes and R. Prigl, Nucl. Inst. Methods Phys. Res. **A394**, 349 (1997).

`rossmann-fc` [4] A. Grossmann, doctoral thesis, University of Heidelberg (1998)

`loran-fc` [5] LORAN-C User Handbook, OMDTPUB P16562.6, available at http://www.navcen.uscg.gov/loran/handbook/h-book.htm

`abragam-fc` [6] see A. Abragam, "Principles of Nuclear Magnetism", Oxford U. Press, (1961), pps. 173-178.

`phillips-fc` [7] W.D. Phillips *et al.*, Metrologia **13**, 179 (1979).

`mohr-mu-fc` [8] P.J. Mohr and B.H. Taylor, Rev. Mod. Phys. **77**, 1 (2005).

`winkler-fc` [9] P.F. Winkler, D. Kleppner, T. Myint, and F.G. Walther, Phys. Rev. **A5**, 83 (1972).

`lamb41-fc` [10] W.E. Lamb Jr., Phys. Rev. **60**, 817 (1941).

`grotch-fc` [11] H. Grotch and R.A. Hegstrom, Phys. Rev. **A4**, 59 (1971).

`british-fc` [12] B.W. Petley *et al.*, Metrologia **20**, 81 (1984).

`lambda-fc` [13] W. Liu et. al., Phys. Rev. Lett. **82**, 711 (1999); D.E. Groom, et al, (Particle Data Group), Eur. Phys. J. **C15**, 1 (2000).

Chapter 13

Determination of ω_a
[ch:wa]

13.1 Introduction

13.1.1 The E821 measurements

13.1.2 Requirements for E989

13.2 The Calorimeters

13.3 Detector Electronics

13.4 ES&H, etc.

Chapter 14

Search for the muon EDM, d_μ

Chapter 15

Data Acquision and Slow Controls

ChapterRisk Analysis

Chapter 16

Safeguards and Security

Chapter 17

Stakeholder Input

Chapter 18

Life Cycle Costs

Chapter 19

Cost, Schedule and Scope

Chapter 20

Work Breakdown Structure